Wiley Series in Pure and Applied Optics

The Wiley Series in Pure and Applied Optics publishes outstanding books in the field of optics. The nature of these books may be basic ("pure" optics) or practical ("applied" optics). The books are directed towards one or more of the following audiences: researchers in universities, government, or industrial laboratories; practitioners of optics in industry; or graduate-level courses in universities. The emphasis is on the quality of the book and its importance to the discipline of optics.

Optical Signal Processing

ANTHONY VANDERLUGT
North Carolina State University
Raleigh, North Carolina

A Wiley-Interscience Publication

John Wiley & Sons, Inc.

New York / Chichester / Brisbane / Toronto / Singapore

I acknowledge the influence that a group of people at the University of Michigan had on my early career. Professor L. J. Cutrona first introduced me to the wonderful world of coherently illuminated optical systems, Emmett Leith shared his knowledge of how optical systems could perform computational algorithms, and Bill Brown mentored me on the finer points of presenting and disseminating scientific results, as well as showing me how to secure research contracts. Many others at the University of Michigan contributed to my understanding of optical signal processing. Of these, Carmen Palermo deserves special thanks. His professional career and mine intertwined at diverse times and places for nearly three decades. His continued interest and commitment to optical signal processing, as well as his continuing friendship, are much appreciated. My thanks also go to Professor H. H. Hopkins for teaching me much of what I know about optics and for his hospitality during our two-year stay at the University of Reading in England.

On a personal note, I thank Taibi Kahler for sharing his keen insights into personality types and for showing me how to identify and meet my needs. His ideas have contributed significantly to improving my quality of life. Marilyn, Beth, and Rob have provided a family support system that I value greatly. I have learned much from Marilyn's personal quest for excellence; thank you for your encouragement, enthusiasm, and love.

ANTHONY VANDERLUGT

Cary, North Carolina
November 1991

Contents

Optical Signal Processing

1

Basic Signal Parameters

1.1. INTRODUCTION

The roots of optical signal processing date back to the work of Fresnel and Fraunhofer nearly 200 years ago. But the connection between optics and information theory did not take shape until the 1950's. In 1953, Norbert Wiener published a paper in the *Journal of the Optical Society of America* entitled "Optics and the Theory of Stochastic Processes" (1). That same issue contained articles by Elias on "Optics and Communication Theory" (2), and by Fellgett on "Concerning Photographic Grain, Signal-to-Noise Ratio, and Information" (3). Other interesting papers of that decade include those written by Linfoot on "Information Theory and Optical Imagery" (4), by Toraldo on "The Capacity of Optical Channels in the Presence of Noise" (5), and the seminal paper by O'Neill on "Spatial Filtering in Optics" (6). These papers represent the early infusion of information theory into classical optics.

A powerful feature of a coherently illuminated optical system is that the Fourier transform of a signal exists in space. As a result, we can implement filtering operations directly in the Fourier domain. This feature was anticipated in papers by Fresnel, Fraunhofer, and Kirchhoff, and had been demonstrated, before the turn of this century, by Abbe in connection with his work on images produced by microscopes.

It is one thing, of course, to recognize that images can be changed by modifying their spectral content; it is another matter to implement the change. In their image-processing work, Marechal (7) and O'Neill (6) used elementary spatial filters to illustrate the principles of optical spatial filtering and to perform mathematical operations such as differentiation and integration. Such was the status of optical signal processing in the early 1960's.

A major impetus to optical signal processing was the need to process data generated by synthetic aperture radar systems. These radar systems were a significant departure from conventional ones because they proved that a small antenna, when used appropriately, provides better resolution than that achieved by a large one. This result, at first glance, is surprising. No physical principles are violated, however, because the small antenna *samples and stores* the radar returns as a means to synthesize a large antenna. To display the radar maps, we need to process the two dimensionally formatted radar returns; because digital computers could not handle the computational load, powerful new signal-processing tools were required.

Photographic film stored the extensive information collected by the radar system. Range information was stored across the film and azimuth information was stored along the film. When the film was illuminated with coherent light, the desired radar map was created by the propagation of light through free space, coupled with the use of some special lenses (see Chapter 5, Section 5.6, for more details). Generating radar maps was the first routine use of optical processing and was the first application for which the matched spatial filter included complicated phase functions such as lenses. It is hard to overestimate the influence that radar processing had on optical signal processing and holography. The classic paper by Cutrona, Leith, Palermo, and Porcello on "Optical Data Processing and Filtering Systems" (8) is important because it presented the basic concepts in a remarkably complete way.

To expand the capabilities of optical filtering to more general operations, such as matched filtering for pattern recognition, we needed to construct filters for which amplitude and phase responses were arbitrary. A solution to the difficult problem of recording the phase information was developed in the early 1960's (9). Because every sample of an input object contributes light to every sample in the matched filter, these two planes are globally interconnected. The computational power of such systems is high because many complex multiplications and additions are performed in parallel. The performance of pattern-recognition systems from that decade has yet to be exceeded.

1.2. CHARACTERIZATION OF A GENERAL SIGNAL

Optical signal processing is based on the same fundamental principles used with other signal-processing technologies. In the remainder of this chapter, we briefly review these fundamentals, primarily to establish the linkage in terminology between spatial and temporal signal processing. We do so without rigor; the reader is invited to consult communication and signal-processing texts for more details. For many readers, the descriptions given here are reminders of what they already know, but possibly never connected with spatial signals. A signal is a signal is a signal...

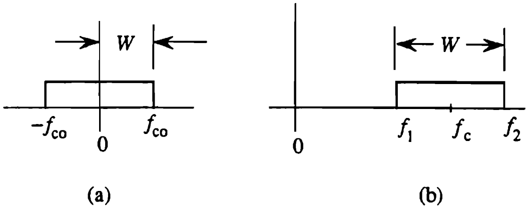

Figure 1.1. Signal spectra: (a) baseband spectrum and (b) bandpass spectrum.

1.2.1. By Bandwidth

One way to characterize a signal $f(t)$ is by its bandwidth. Suppose that all the signal energy is contained in a temporal frequency band W. That is, the signal contains no frequencies higher than $f_{co} = W$, where f_{co} is the *cutoff frequency* and W is the *bandwidth* of the signal. If the two-sided spectrum of a signal occupies the frequency range from $-W$ to W, as illustrated in Figure 1.1(a), it is a *baseband* signal. If the signal has energy only in a band of frequencies $W = f_2 - f_1$, it is a *bandpass* signal, as shown in Figure 1.1(b).

1.2.2. By Time

Signals are generally bounded in time, either because they are generated with a finite time duration, or because we restrict the time duration while processing the signal. For example, we sometimes segment a long-duration signal into shorter segments of duration T for spectrum analysis or correlation. This *time duration* T, as shown in Figure 1.2, is an important signal-processing parameter.

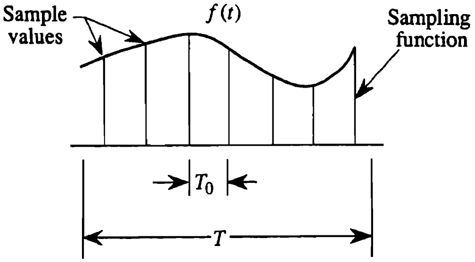

Figure 1.2. Sampling of an analog signal.

1.2.3. By Sample Interval

The sampling theorem states that a signal bandlimited to a frequency range $|f| \leq W$ can be accurately represented by its sample values if the signal is sampled at time intervals T_0, where

$$T_0 = \frac{1}{2f_{co}} = \frac{1}{2W}. \tag{1.1}$$

The signal must be sampled at the *Nyquist sampling rate* $R = 1/T_0$ so that each period of the highest frequency in the signal is sampled twice. Clearly, the sampling rate is just twice the signal bandwidth: $R = 2W$. In Figure 1.2 we show the signal $f(t)$ and a few of the sampling positions spaced at intervals of T_0.

1.2.4. By Number of Samples

If the signal is bounded in time T and in bandwidth W, the total *number of samples* needed to accurately represent the signal is

$$N = \frac{T}{T_0} = 2TW. \tag{1.2}$$

The product TW is generally called the *time bandwidth product* of a signal and is a standard measure of its complexity. For example, a signal with low frequencies and a short time duration contains less information than one with high frequencies and a long time duration. The time bandwidth product is therefore a strong indicator of the computational intensity of a processing operation.

It is not possible, in theory, for a signal to be bounded in both the time and frequency domains. Nevertheless, the assumption is reasonably accurate, in practice, for the purpose of characterizing signals by these two parameters.

1.2.5. By Number of Amplitude Levels or Signal Features

Binary signals have just two amplitude or phase states. We require $n = 2^r$ levels, however, to represent analog signals with an adequate degree of accuracy. For example, we may quantize each sample of an audio signal to at least $r = 16$ bits in amplitude to achieve a sufficient number of signal levels. Two-dimensional signals, such as images, may require n amplitude levels, generally referred to as the *gray scale*. Furthermore, we may require c colors, h hues, s saturation levels, and p polarizations to fully represent the image. We therefore require $g = nchsp$ values to characterize each sample.

1.2.6. By Degrees of Freedom

Because each sample may require g values to determine its state, a signal has *gN degrees of freedom*.

1.3. THE SAMPLE FUNCTION

Although optical signals are generally handled in analog form throughout the system, we introduce the sampling theorem for a variety of reasons. First, the sampling theorem provides a convenient way to characterize the complexity of an analog signal, such as an image, in terms of the required number of samples, generally called *pixels*. Optical images, in contrast to time signals, do not have a fixed underlying metric. For example, images can be magnified or demagnified, thereby changing their areas and their spatial frequency bandwidths, but the number of samples remains the same. Second, the Fourier transform of an optical signal exists in space and is often detected directly by a photodetector array. Because the elements of the array sample the spectrum, we need to understand how the sampling process affects the accuracy with which the spectrum is measured. Third, some images are originally sampled by collection devices, such as solid-state cameras, which contain two-dimensional photodetector arrays. In these cases, the input signals to the optical system have already been sampled and we must account for the impact of sampling on subsequent processing operations. Fourth, we frequently use point sources in optical systems. Throughout this book, we treat a point source as a bandlimited signal containing exactly one sample. Finally, the sampling theorem, when associated with bandlimited signals whose duration in time or space is finite, leads to the optical invariant that is important for the analysis and design of optical systems.

Consider a signal $f(t)$, whose spectrum is $F(f)$, bandlimited to the range $|f| \leq W$. This signal, when sampled by an infinite train of delta functions, is represented by

$$f_s(t) = f(t) \sum_{n=-\infty}^{\infty} \frac{1}{T_0}\delta(t - nT_0), \tag{1.3}$$

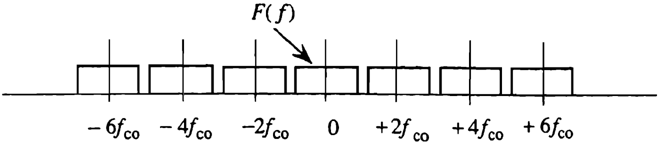

Figure 1.3. Spectrum of the sampled analog signal.

so that the spectrum of the sampled signal becomes

$$F_s(f) = F(f) * \sum_{n=-\infty}^{\infty} \delta(f - 2nf_{\text{co}}), \tag{1.4}$$

where $*$ indicates convolution, and the factor $1/T_0$ in Equation (1.3) ensures conservation of the integrated area between the function $F(f)$ and its sampled representation $F_s(f)$. The spectrum $F_s(f)$ is shown in Figure 1.3 with the baseband spectrum $F(f)$ centered at $f = 0$; replicas of $F(f)$ are centered at $f = \pm 2f_{\text{co}}$, $\pm\ 4f_{\text{co}}$ and other even multiples of the cutoff frequency.

The signal $f(t)$ can be recovered from the sampled signal $f_s(t)$ by passing $f_s(t)$ through a low-pass filter whose frequency response $\text{rect}(f/2W)$ is equal to one for $|f| \leq W$ and equal to zero elsewhere, as shown in Figure 1.4. The filter, whose impulse response is $h(t)$, admits only the central spectral components $F(f)$ from the sampled signal

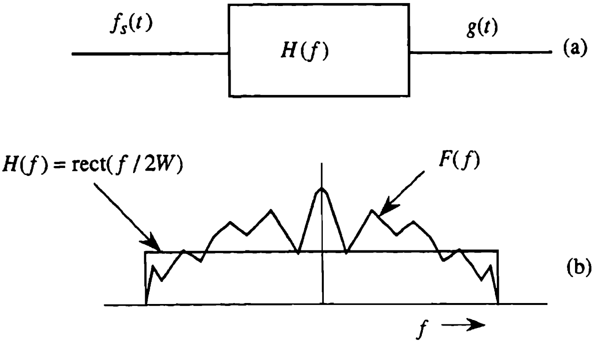

Figure 1.4. Filtering operation and spectrum of a bandlimited signal.

spectrum $F_s(f)$. The impulse response of the filter is

$$
\begin{aligned}
h(t) &= \int_{-\infty}^{\infty} H(f) e^{j2\pi,}\, df \\
&= \int_{-\infty}^{\infty} \operatorname{rect}(f/2W) e^{j2\pi f t}\, df \\
&= \int_{-W}^{W} e^{j2\pi f t}\, df \\
&= (2W)\operatorname{sinc}(2Wt) = (1/T_0)\operatorname{sinc}(t/T_0),
\end{aligned}
\tag{1.5}
$$

where $2W = 1/T_0$ is a scaling factor similar to that used in Equation (1.3), and where

$$\operatorname{sinc}(x) \equiv \frac{\sin(\pi x)}{\pi x}. \tag{1.6}$$

The sinc function, as defined by Equation (1.6) and shown in Figure 1.5, is generally called the *interpolation function* because it allows an interpolation between the sample intervals T_0 to recover $f(t)$ for all time.

As we noted before, concepts associated with the sampling theorem help in understanding optical signal processing, even if the signals are in an analog form. To cover the wide range of uses discussed at the beginning of this section, we refer to the interpolation function as the *sample function*. We therefore distinguish among the sampling function which is the train of delta functions shown in Figure 1.2, the sample function which is the sinc function wrapped around each delta function as shown in Figure 1.5, and the sampled values which are the values of the sampled signal $f_s(t)$.

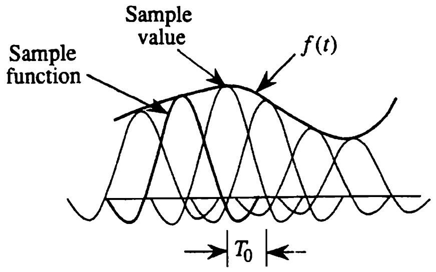

Figure 1.5. Sample function as an interpolator.

1.4. EXAMPLES OF SIGNALS

The bandwidths of commonly encountered signals vary over a considerable range:

• Underwater sound	4 Hz
• Speech (phone quality)	3,000 Hz
• Audio range	20,000 Hz
• Color television	6,000,000 Hz
• Wideband communication system	100,000,000 Hz
• Color motion picture	5,000,000,000 Hz
• Visible spectrum (blue to red)	10,000,000,000,000 Hz

The bandwidth of the visible spectrum is extremely wide relative to that of any of the listed signals, implying enormous signal-processing potential. This wide bandwidth is, in part, why optics is useful for performing communication and signal-processing functions.

The complexity of an analog signal-processing operation is typically proportional to $N = 2TW$. For example, if we compute the Fourier transform of each of the listed signals for a one-second interval, the complexity becomes significantly higher as we progress down the list. For example, the audio signal requires a 40,000-point FFT to determine the frequency content of the signal to a resolution of 1 Hz or a 4,000-point FFT to resolve frequencies to 10 Hz. For *real-time* operation the computational complexity is generally very high. Correlation, for example, requires that we perform $2TW$ multiplications and additions in the time interval T_0 so that the computational rate, in operations per second, is

$$R = \frac{2TW}{T_0} = 4TW^2, \qquad (1.7)$$

which increases as the *square* of the bandwidth. Hence, it is difficult to process wideband signals in real time without using the power of optical processing.

1.5. SPATIAL SIGNALS

The signals cited above are all one-dimensional time signals. Pictorial signals, however, generally originate as three-dimensional signals; for example, a motion picture is a function of two space variables and a time

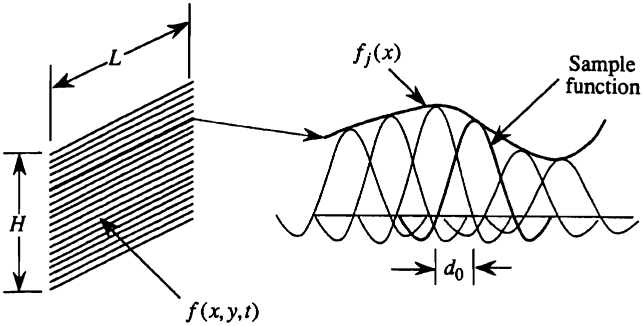

Figure 1.6. Raster-scanned image.

variable. For transmitting such images, we convert the three-dimensional signal $f(x, y, t)$ to a one-dimensional time signal $r(t)$ through a raster-scanning operation, which is easily visualized as a sampling operation in both spatial coordinates. A television receiver converts $r(t)$ to the same format as the original signal $f(x, y, t)$. A holographic or stereographic movie is an example of a four-dimensional signal $f(x, y, z, t)$.

We use spatial frequencies to describe spatial signals such as images, similar to our use of temporal frequencies for describing time signals. We encounter spatial frequencies every day, but may not recognize them as such. For example, the regular pattern of lines in a screen, a checkerboard, a piece of cloth, or a cornfield form spatial frequencies in different spatial directions. Irregular spatial frequencies are evident in water surface waves and most street patterns.

Figure 1.6 shows a raster-scanned signal $f(x, y, t)$ such as that produced by a single frame of a television signal. The signal has length L, height H, and exists for a time duration T_f. To illustrate the fundamental concepts, we select the jth line and display it as $f_j(x)$. This signal, whose highest *spatial frequency* is α_{co}, requires a *sampling interval* d_0, where

$$d_0 = \frac{1}{2\alpha_{co}}. \tag{1.8}$$

In general, we use α and β to indicate spatial frequencies, expressed in cycles/millimeter, in the x and y directions; they are the optical equivalents of a temporal frequency f. In turn, the sample interval d_0 is equivalent to the temporal sample interval T_0.

The number of samples in the x direction is $N_x = L/d_0 = 2\alpha_{co}L$. The *length bandwidth product* of the spatial signal in the x direction is the product of the length of the spatial signal and the cutoff spatial frequency: LBP $= \alpha_{co}L$. The number of samples in the y direction is $N_y = H/d_0 = 2\beta_{co}H$, where HBP $= \beta_{co}H$ is the *height bandwidth product* of the spatial signal in the y direction. We therefore need a total of $N = N_xN_y$ samples, sometimes called pixels, to accurately represent the image. The product of the length and height bandwidth products gives the overall *space bandwidth product*: SBP = (LBP)(HBP) $= \alpha_{co}\beta_{co}LH$.

If $f(x, y)$ is a bandlimited signal, the appropriate sample function is the product sinc(x/d_0)sinc(y/d_0), in the same sense that sinc(t/T_0) is the appropriate sample function for time signals. We can therefore represent the signal on the jth scan line as

$$f_j(x) = \sum_{n=-\infty}^{\infty} a_n \operatorname{sinc}\left[\frac{x - nd_0}{d_0}\right] \operatorname{rect}\left(\frac{x}{L}\right), \tag{1.9}$$

where the real-valued a_n are the sampled values, sinc(x/d_0) is the sample function, and the rect function defines the region occupied by the signal. An alternative and completely equivalent way to represent $f_j(x)$ is by using exponential functions:

$$f_j(x) = \sum_{n=-\infty}^{\infty} b_n e^{j2\pi n\alpha_0 x} \operatorname{rect}(n\alpha_0/2\alpha_{co}), \tag{1.10}$$

where the b_n are complex-valued weights for the exponential functions, $\alpha_0 = 1/L$ is the lowest, or fundamental spatial frequency contained in the signal, and the rect function shows that the signal is bandlimited by the cutoff frequency α_{co}. Either Equation (1.9) or Equation (1.10) is an appropriate way to represent the signal; which is most useful depends on the particular signal or signal-processing application.

PROBLEMS

1.1. A baseband time signal has a bandwidth of 6 MHz. What is the proper sampling interval T_0? If each sample is characterized by one of 32 voltage levels, calculate the degrees of freedom if the signal duration is 100 ms.

1.2. We record a 6-MHz bandwidth baseband video signal onto photographic film using a raster-scanned format. If the film resolution is 2 μ × 2 μ (equivalent to the spatial sampling interval), calculate the area required to store 30 minutes of information. Assume a square recording format and that the film can support the required 32 information levels at each sample position.

1.3. For the parameters given in Problem 1.2, what is the highest spatial frequency required of the film? Calculate the two-dimensional space bandwidth product of the stored signal and the time bandwidth product of the time signal.

1.4. Find the required sample interval and the optimum sampling function in the frequency domain if the signal is limited to a time duration from $|t| \leq T$. The bandwidth of the signal is not constrained in any way. Hint: This problem is the dual of the sampling theorem in the space or time domains.

2

Geometrical Optics

2.1. INTRODUCTION

The main emphasis in this book is on physical optics, which describes how light interacts to produce diffraction effects useful in optical signal processing. Although most of the results in this chapter can be obtained from physical optics, we first provide a working knowledge of geometrical optics because it often provides the same results through more straightforward calculations. Geometrical optics is the characterization of optical systems based on an assumption that the wavelength of light is zero and that light travels only along ray paths.

As it turns out, we cannot isolate a single ray. If we attempt to do so, we find that the harder we try, the more difficult it becomes. In both Figure 2.1(a) and Figure 2.1(b) we successfully introduce apertures that reduce the spatial extent of the incident light beam. Figure 2.1(c), however, shows that a further reduction in the size of the aperture does not isolate a ray; in fact, light actually diverges after the aperture. The finite wavelength of light causes this spreading action or *diffraction*, as discussed extensively in Chapter 3, and is the foundation on which much of optical signal processing is built. In this chapter we proceed as though we can actually isolate a ray.

2.2. REFRACTIVE INDEX AND OPTICAL PATH

The velocity c of light in vacuum is approximately $3(10^8)$ m/sec. The velocity v of light in any other medium, however, is lower than c. The inverse relative velocity $n = c/v$ is the *refractive index* of the medium for monochromatic light of wavelength λ. Frequency, wavelength, and velocity are connected by the relationship $v = \lambda f$. Because the frequency of light remains unchanged in passing from a medium whose refractive index is n_1

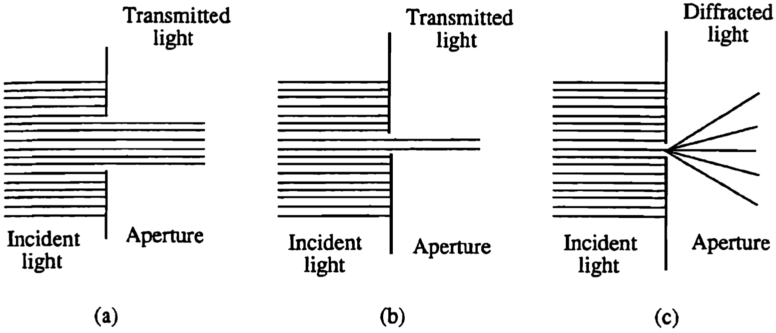

Figure 2.1. Effect of an aperture on a bundle of rays of light: (a) large aperture, (b) small aperture, (c) pinhole aperture.

into a medium of index n_2, we find that

$$v_1 = \lambda_1 f,$$
$$v_2 = \lambda_2 f, \tag{2.1}$$

from which we conclude that

$$n_1\lambda_1 = n_2\lambda_2, \tag{2.2}$$

so that the wavelength shortens when light passes into a medium with a higher refractive index, often called a more *dense* medium.

The index of refraction is generally a function of the wavelength of light. The *dispersive power* of a medium is defined as $(n_b - n_r)/(n_y - 1)$, where n_b is the refractive index for blue light, n_r is the refractive index for red light, and n_y is the refractive index for yellow light. This second-order property of the index of refraction is generally not important for us because we mostly study optical signal-processing systems for which light is monochromatic. We therefore use λ and n, without color-referenced subscripts, to indicate wavelength and refractive index.

A distance, multiplied by the appropriate refractive index, is defined as the *optical path*. By convention, we use brackets to indicate an optical path [OP] or an optical path difference [OPD]. In a time interval t_0, a light disturbance always traverses the same optical path length. For example, consider light entering media of refractive indices n_1 and n_2. The distances traveled in time t_0 are $D_1 = v_1 t_0$ and $D_2 = v_2 t_0$, from which we conclude that $n_1D_1 = n_2D_2 = [\mathrm{OP}]$ so that the optical paths are equal. In a similar way we can show that if light arrives at a point via two paths, the *phase difference* between them is simply the optical path difference expressed in wavelengths of light, multiplied by 2π radians:

$$\Delta\phi = \frac{2\pi}{\lambda}[\mathrm{OPD}], \tag{2.3}$$

where $[\mathrm{OPD}] = [\mathrm{OP}_2 - \mathrm{OP}_1]$ is the optical path difference and λ is the wavelength in the medium.

A surface on which all light rays have the same phase is called a *wavefront*. At each point on an arbitrary wavefront we construct *wave normals* as suggested in Figure 2.2. As an example, if the medium is *isotropic*, which means that the index of refraction is the same in all directions, a point source emits light into expanding spherical wavefronts. In this case, the times of flight from the source to every point on the wavefront surface are equal. Furthermore, all the wavefront normals are rays that have the point source as their common origin. The use of rays is most convenient for the study of geometrical optics, whereas we use wavefronts to develop the theories of interference, diffraction, and lens aberrations.

Energy is transported along ray paths; the rays, in an isotropic medium, are normal to the wavefront. In an *anisotropic* medium, for which the indices of refraction are not the same in all directions, the rays still define the directions in which energy propagates; they are not, however, generally normal to the wavefront.

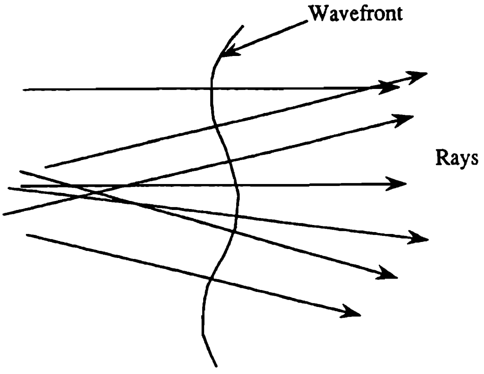

Figure 2.2. Rays are surface normals to wavefronts.

2.3. BASIC LAWS OF GEOMETRICAL OPTICS

The basic laws of geometrical optics are the laws of reflection and refraction, Snell's law, and Fermat's principle. These laws provide the basic tools for tracing rays through a system consisting of optical elements such as mirrors, prisms, and lenses.

2.3.1. Law of Reflection

We first examine how a wavefront changes when it is *reflected* at a surface. Consider a plane wave AB, incident on the reflective surface S shown in Figure 2.3. The refractive index of the medium is n_1. An incident ray, associated with the wavefront at A, arrives at the *angle of incidence* I_1 with respect to the surface normal. Note, too, that the incident wavefront AB forms an angle I_1 with respect to the surface S. At some time t_0, the wavefront has advanced so that it has just arrived at point C. The time of flight is

$$t_0 = \frac{BC}{v_1} = \frac{BC}{c/n_1} = \frac{n_1 BC}{c} = \frac{\text{optical path}}{\text{velocity of light in vacuum}}. \tag{2.4}$$

When t_0 seconds have elapsed, we know that the energy arriving at point A has been reflected, but we do not know the direction. To find the direction, we construct a circle of radius $n_2 AD = n_1 BC$, with center at A,

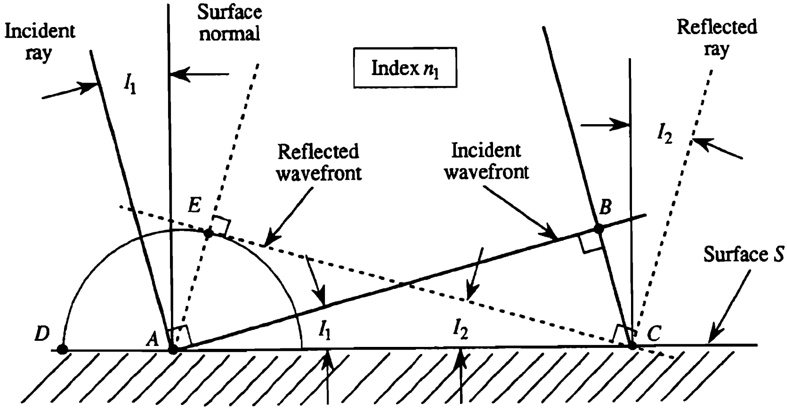

Figure 2.3. Law of Reflection.

where $n_2 = n_1$ refers to the index of refraction after the wavefront is reflected. Because the reflected wavefront must be tangent to this circle, the angle that EC makes with respect to the surface is the *angle of reflection* I_2, and the optical path $[AE]$ is equal to $n_2 AD = n_1 BC$. As the incident and reflected rays are in the same medium, we use the fact that $n_1 = n_2$ to obtain the result that

$$|I_1| = |I_2|. \qquad (2.5)$$

The absolute value signs used in Equation (2.5) allow for the possibility that I_2 is equal to $-I_1$; we address the sign conventions for angles in Section 2.5.1. The *law of reflection* states that the magnitude of the angle of reflection is equal to that of the angle of incidence. The incident and reflected rays are therefore equally inclined relative to the normal of the reflecting surface. They are also in the same plane; that is, the reflected ray is in the plane defined by the incident ray and the surface normal.

2.3.2. Law of Refraction

When light passes through a surface separating media of different refractive indices, rays are *refracted* so that they change directions. The development of the law of refraction is similar to that for the law of reflection. A wavefront AB arrives at a surface S shown in Figure 2.4. The refractive

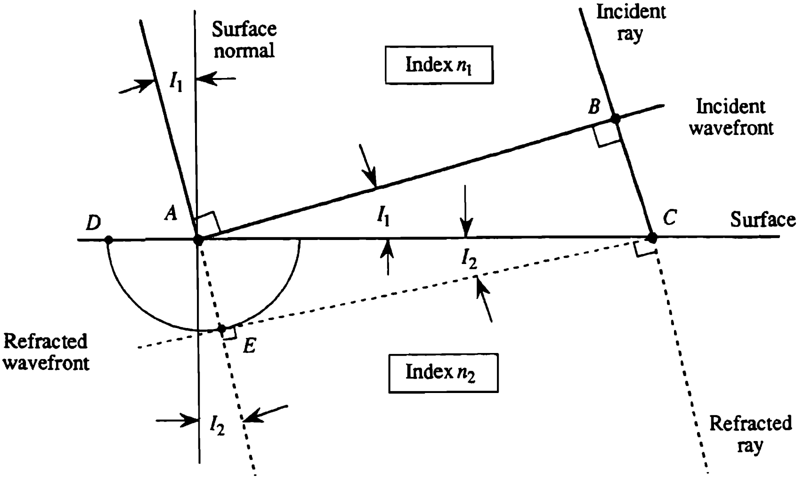

Figure 2.4. Law of Refraction.

indices of the two media are n_1 and n_2. At time $t_0 = BC/v_1$, the wavefront has just arrived at point C. During this same time interval, the wavefront element entering at A, with incidence angle I_1 to the surface normal, has traveled an optical path $n_2 AD = n_1 BC$. The new wavefront must be tangent to the circle of radius $n_2 AD$. From the diagram we find that

$$\sin I_1 = \frac{BC}{AC} \quad \text{and} \quad \sin I_2 = \frac{AD}{AC}, \tag{2.6}$$

or that

$$AD \sin I_1 = BC \sin I_2. \tag{2.7}$$

Because equal optical paths are traveled in equal time, we find that $n_1 BC = n_2 AD$ and that

$$\boxed{n_1 \sin I_1 = n_2 \sin I_2,} \tag{2.8}$$

which relates the angle of incidence to the angle of refraction. When $n_2 > n_1$ we find that $I_2 < I_1$. Thus, in passing into a denser medium, a ray is bent toward the surface normal. The *law of refraction*, as given in Equation (2.8), is also known as *Snell's law* and is the foundation on which geometrical optics is based.

2.3.3. Fermat's Principle

The laws governing the behavior of rays are combined in Fermat's principle. *Fermat's principle* states that the time of flight for a light packet traveling from one point to another along a ray is, to a first approximation, equal to the time of flight experienced by light packets on nearby rays; that is, *the time of flight has a stationary value*. Fermat originally stated that the time of flight, and therefore the optical path, is a *minimum*; however, the actual time of flight may be a maximum, a minimum, or neither, as we show shortly.

Consider the path of a ray in Figure 2.5 from point P_1 in a medium of index n_1 to the point P_2 in a medium of index n_2, where $n_1 < n_2$. The intersection point at the surface is found when the path length, or time of flight, has a *stationary value*. The total time to travel from P_1 to P_2 is

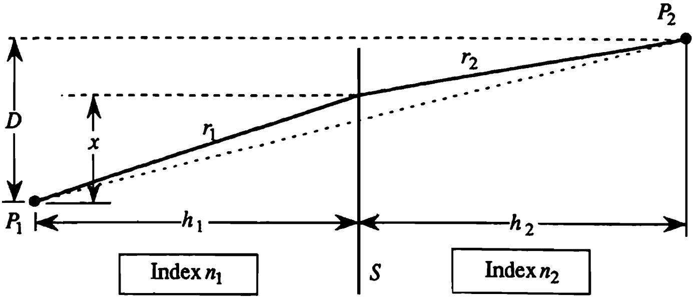

Figure 2.5. Fermat's principle.

$$t_{12} = t_1 + t_2 = \frac{r_1}{v_1} + \frac{r_2}{v_2}$$

$$= \frac{\sqrt{h_1^2 + x^2}}{v_1} + \frac{\sqrt{h_2^2 + (D - x)^2}}{v_2}. \tag{2.9}$$

When t_{12} is at a stationary value, the partial derivative $\partial t_{12}/\partial x$ is zero:

$$\frac{\partial t_{12}}{\partial x} = \frac{\frac{1}{2}(2x)}{v_1\sqrt{h_1^2 + x^2}} + \frac{\frac{1}{2}(-2)(D - x)}{v_2\sqrt{h_2^2 + (D - x)^2}} = 0, \tag{2.10}$$

from which we conclude that

$$\frac{n_1 x}{r_1} = \frac{n_2(D - x)}{r_2}, \tag{2.11}$$

which implies that

$$n_1 \sin I_1 = n_2 \sin I_2. \tag{2.12}$$

Snell's law, as shown by Equation (2.12), is therefore implicitly contained in Fermat's principle.

Figure 2.6 shows several examples in which the ray paths are at their stationary values, not necessarily at their minimum or maximum values. In each case, we consider light traveling from point P_1 to point P_2. The true

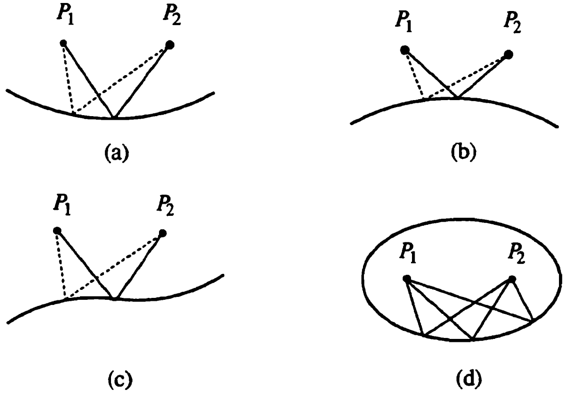

Figure 2.6. Ray Paths: (a) maximum length path, (b) mi imum length path, (c) inflection length path, and (d) equal length path.

ray paths are shown as solid lines, and candidate ray paths are shown as dotted lines. Aside from the obvious fact that the direct path from P_1 to P_2 is a minimum in all cases, we are concerned with the paths of rays that reflect from the surfaces. The reflected path is a *maximum* in Figure 2.6(a); the path is a *minimum* in Figure 2.6(b); the path is at an *inflection point* in Figure 2.6(c); the paths are all *equal* in Figure 2.6(d), because P_1 and P_2 are the foci of an ellipsoid.

2.3.4. The Critical Angle

When a ray passes from a less dense medium into one that is more dense, the ray is bent *toward* the normal. When the ray propagates in the opposite direction, the ray bends *away* from the normal. Figure 2.7 shows that ray *AB*, in a medium of index n_1, has an angle of incidence I_1 with respect to the surface normal. When I_2 reaches 90°, Snell's law shows that ray *AB* cannot enter the less dense medium and is completely reflected at the surface. The angle at which *total internal reflection* occurs is called the *critical angle* I_c:

$$I_c = \sin^{-1}\left(\frac{n_2}{n_1}\right). \tag{2.13}$$

As an example, suppose that $n_1 = 1.5$ and $n_2 = 1.0$; the critical angle I_c for which total internal reflection occurs is then $I_c = \sin^{-1}(1/1.5) = 41.8°$

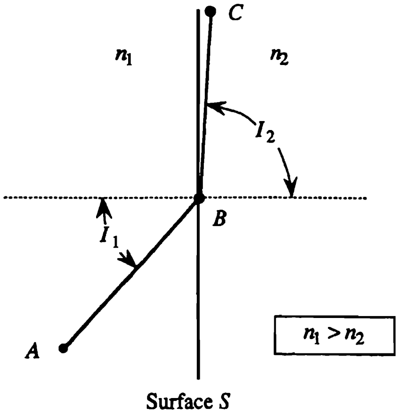

Figure 2.7. Critical angle.

Although Equation (2.13) shows that rays whose incidence angles are beyond the critical angle I_c cannot penetrate into the less dense medium, Snell's law shows that rays can always penetrate into a more dense material. Total internal reflection is found in many common optical systems, such as in the prisms used in cameras and binoculars.

2.4. REFRACTION BY PRISMS

Prisms are sometimes used in optical signal-processing systems to bend a set of parallel rays, perhaps for folding the system to make it more compact. Sometimes the magnification of a prism is used to change the size of a light beam, such as that produced by an injection laser diode, in only one dimension.

2.4.1. Minimum Deviation Angle

A symmetric prism, shown in Figure 2.8, is constructed from a material whose index of refraction is n_2; the medium on either side of the prism is air, with index $n_1 = n_3 = 1$. The entrance ray forms the angle I_1 with respect to the normal. We apply Snell's law to the incident and refracted rays at each surface of the prism:

$$\begin{aligned} n_1 \sin I_1 &= n_2 \sin I_2 \\ n_2 \sin I_3 &= n_3 \sin I_4. \end{aligned} \tag{2.14}$$

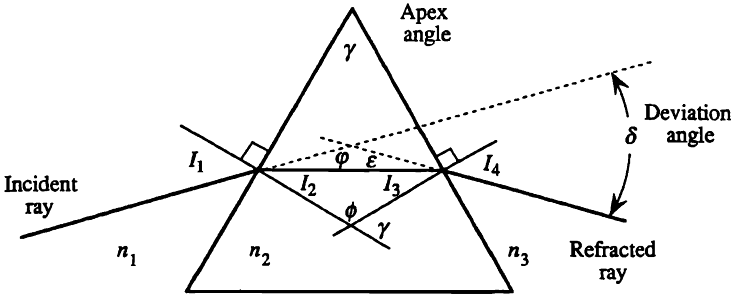

Figure 2.8. Refraction of a ray by a prism.

From Figure 2.8 we see that $I_2 + I_3 = \gamma$, where γ is the apex angle of the prism.

The *deviation angle* δ is the amount by which the entrance ray is bent in passing through the prism. From the diagram, we find that the deviation angle is

$$\begin{aligned}\delta &= \varphi + \varepsilon \\ &= I_1 - I_2 + I_4 - I_3 \\ &= I_1 - I_2 + I_4 - (\gamma - I_2) \\ &= I_1 + I_4 - \gamma. \end{aligned} \tag{2.15}$$

The deviation angle is therefore not a direct function of the internal angles I_2 and I_3. We use Equation (2.14) in Equation (2.15) to find that

$$\begin{aligned}\delta &= I_1 - \gamma + \sin^{-1}[n_2 \sin I_3] \\ &= I_1 - \gamma + \sin^{-1}[n_2 \sin(\gamma - I_2)] \\ &= I_1 - \gamma + \sin^{-1}\left[n_2 \sin\left\{\gamma - \sin^{-1}\left(\frac{\sin I_1}{n_2}\right)\right\}\right]. \end{aligned} \tag{2.16}$$

The result given by Equation (2.16) is valid for all angles of incidence, provided that the ray striking the second surface is not at, or beyond, the critical angle. The condition for avoiding total internal reflection is that

$$n_2 \sin\left\{\gamma - \sin^{-1}\left(\frac{\sin I_1}{n_2}\right)\right\} < 1. \tag{2.17}$$

A plot of the deviation angle δ, as a function of I_1, reveals that the *minimum deviation angle* occurs when $I_1 = I_4$ so that the entrance and exit rays make equal angles with the surfaces of the prism. Under this condition $\delta_{\min} = 2I_1 - \gamma$, as can be seen from Equation (2.15), and the aberrations introduced by the prism are minimized, as we show in Section 2.9.

When the apex angle is small, the prism is called a *thin prism*. Furthermore, if the angle of incidence is small, we replace the sines of the angles by the angles themselves in Equation (2.16). The expression for the deviation angle is therefore simplified considerably:

$$\boxed{\delta = (n_2 - 1)\gamma,} \tag{2.18}$$

and we see that the deviation angle is not a function of the angle of incidence.

We sometimes refer to the *power* of a prism defined as the deflection of a ray, in millimeters, at a distance of one meter; the unit of measurement is a *prism diopter*. A prism whose power is one prism diopter deflects a ray 10 mm at a distance of 1 m from the prism.

2.4.2. Dispersion by a Prism

The refractive index of an optically transparent material is dependent on the wavelength of light. As the index is typically higher for blue than for red wavelengths, blue wavelengths are bent more toward the normal within the prism and are bent even further away from the normal when they exit the prism, a phenomenon called *dispersion*. Dispersion explains why white light separates into its color spectrum, as reported by Newton. Also, since the dispersion is generally not linear ($\partial^2 n/\partial\lambda^2 \neq 0$), the spectrum is typically spread more in the blue region than in the red region.

2.4.3. Beam Magnification by a Prism

Prisms can be configured so that the magnification is different in orthogonal directions; this condition is called *anamorphic magnification*. Consider the prism shown in Figure 2.9, for which light is incident normal to the entrance face. As there is no ray deviation at the first surface, we apply Snell's law immediately to the second surface:

$$n_2 \sin I_2 = n_3 \sin I_3. \tag{2.19}$$

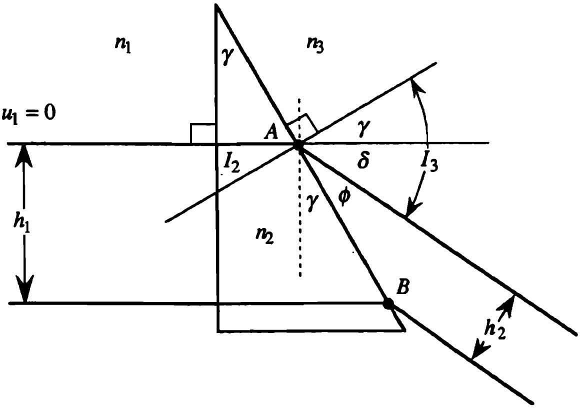

Figure 2.9. Beam magnification by a prism.

As $n_3 = 1$ and $I_2 = \gamma$, we find that $\sin I_3 = n_2 \sin \gamma$. Thus, we find that

$$\begin{aligned} I_3 &= \sin^{-1}[n_2 \sin \gamma], \\ &= \delta + \gamma, \end{aligned} \tag{2.20}$$

from which we conclude that the deviation angle is

$$\delta = \sin^{-1}[n_2 \sin \gamma] - \gamma. \tag{2.21}$$

The result given by Equation (2.21) is valid only when $n_2 \sin \gamma < 1$ so that internal reflection at the second surface is avoided.

The beam magnification of the prism is $M = h_2/h_1$. From Figure 2.9 we see that

$$\begin{aligned} h_1 &= AB \cos \gamma \\ h_2 &= AB \sin \phi, \end{aligned} \tag{2.22}$$

so that the beam magnification is $M = \sin \phi/\cos \gamma$. Because $\phi = 90° - \gamma - \delta$, we find that

$$M = \frac{\cos[\sin^{-1}(n_2 \sin \gamma)]}{\cos \gamma}. \tag{2.23}$$

After using some trigonometric substitutions and algebraic manipulations, we find an alternative form for the magnification:

$$\boxed{M = \frac{\sqrt{1 - n_2^2 \sin^2 \gamma}}{\sqrt{1 - \sin^2 \gamma}},} \tag{2.24}$$

valid for $n_2 \sin \gamma < 1$ so that total internal reflection is avoided. The magnification is always less than 1 when light travels from left to right, as shown in Figure 2.9.

We solve Equation (2.24) to find the required apex angle γ in terms of M and n_2:

$$\sin \gamma = \sqrt{\frac{1 - M^2}{n_2^2 - M^2}} \tag{2.25}$$

Large changes in the beam size are obtained with prisms of modest parameters, as shown in the following table. We calculate the exit angle I_3 with respect to the surface normal, as a function of increasing the apex angle of the prism; in all cases the refractive index is $n_2 = 1.70$:

γ	I_3	M
30	58.2	0.61
35	77.2	0.27
36	87.7	0.05

Because the magnification changes rapidly as $\gamma \rightarrow 36°$, it is a sensitive function of manufacturing errors in the apex angle or of errors in the refractive index of the prism. Because the exit angle is close to grazing at the exit face when the magnification is small, we risk total internal reflection; we reduce this risk by rotating the prism slightly toward the minimum deviation angle. In general it is better to use two or more prisms in series when a large change in the beam size is needed to avoid the most sensitive operating configuration for any one prism.

Magnifications greater than 1 are most easily handled by initially assuming that the magnification is less than 1. We use the relationships developed here and then reverse the prism configuration relative to the direction in which light travels. Although the relationships developed in this section are valid only when light enters normal to the entrance face of the prism, similar relationships can be developed for arbitrary incidence angles.

2.4.4. Counter-Rotating Prisms

An equivalent prism having a variable deviation angle is implemented by using two prisms, each with an apex angle γ, as shown in Figure 2.10. When the prisms are rotated so that their powers add, as shown in Figure 2.10(a), the equivalent deviation angle is 2δ. When the prisms are counter rotated so that their powers subtract, as shown in Figure 2.10(b), the equivalent deviation angle is zero. A pair of such prisms is therefore useful to bend light through an arbitrary angle ranging from zero to 2δ. The prisms are generally mounted so that the second prism is rotated relative to the first to obtain the desired deviation angle. The entire prism assembly is then rotated so that the deviation occurs in the desired plane.

2.4.5. The Wobble Plate

A parallel plate of glass can be used to slightly displace a beam of light. Figure 2.11 shows a glass plate of thickness z_{12} and index of refraction n_2. By straightforward calculations (see Problem 2.5), the displacement for small angles of incidence is

$$h = \frac{z_{12} I_1 (n_2 - 1)}{n_2}. \tag{2.26}$$

Fine control over ray displacements is obtained by such a *wobble plate*, without deviating the angles of the incident rays.

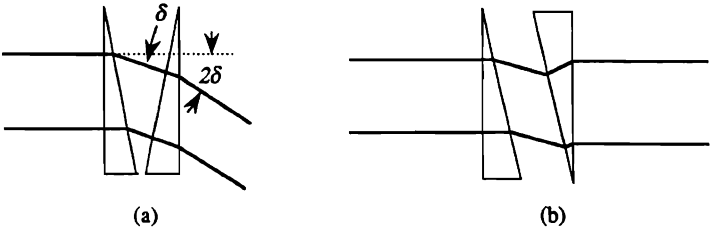

Figure 2.10. Counter-rotating prisms: (a) prism powers adding and (b) prism powers subtracting.

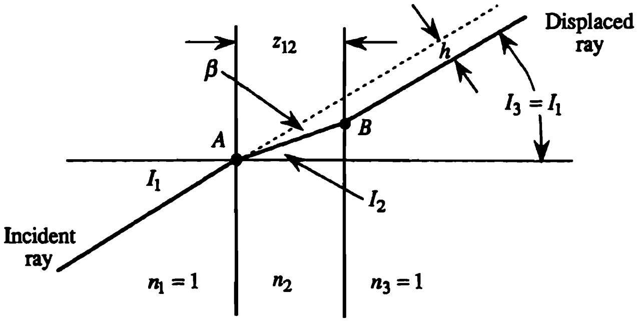

Figure 2.11. Displacement of a ray by a plane parallel plate.

2.5. THE LENS FORMULAS

Snell's law is the basic method for tracing rays through optical elements with curved surfaces. To obtain the key relationships we must first establish a sign convention. Unfortunately, no sign convention is used uniformly in all optics texts. The sign convention can be chosen freely, however, provided that it is used consistently throughout all calculations.

We want our sign convention to be consistent with our notion of positive and negative *temporal* frequencies, as well as with our notion of positive and negative *spatial* frequencies. The sign convention also influences the sign of the kernel function in the temporal and spatial Fourier-transform relationships. As a result of these requirements, we establish a sign convention that unifies the results from geometrical optics, physical optics, and Fourier-transform theory.

2.5.1. The Sign Convention

To illustrate the sign convention, consider the simple situation shown in Figure 2.12, in which a ray passes through plane P_0 at a height h_0 and at an angle u_0 with respect to the optical axis. We focus our attention at the first origin, the point O at plane P_0, and use the sign conventions of coordinate geometry. The basic sign conventions are

- Heights above the optical axis are positive; those below the axis are negative.
- Distances to the right of the *current origin* are positive; distances to the left of the current origin are negative.

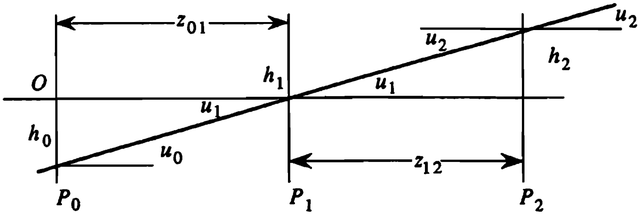

Figure 2.12. Sign convention for rays and distances.

- The *acute* angle that a ray makes with the axis, as measured *from the axis to the ray*, is positive if the rotation is counterclockwise; acute angles are negative if the rotation is clockwise. As shown, u_0, u_1, and u_2 are each positive. All angles are measured in radians.

Much of geometrical optics deals with rays that are nearly parallel to the optical axis; these rays are called *paraxial rays* and the approximations $\sin u \approx \tan u \approx u$ are valid. In the following development, we use the angles themselves as a substitute for the sines or the tangents of the angles; we use the trigonometric functions of finite angles, whenever necessary, for computational accuracy.

We illustrate how the sign convention works by starting with plane P_0 as our current origin and find that

$$h_1 = h_0 + u_0 z_{01}, \tag{2.27}$$

where u_0 is the paraxial angle of the ray between P_0 and P_1 and z_{01} is the distance from P_0 to P_1. From the diagram we note that $h_1 = 0$ so that

$$h_0 = -u_0 z_{01}. \tag{2.28}$$

Because z_{01} is positive and h_0 is negative, u_0 must be positive, as claimed, to satisfy our sign convention. Similarly, by shifting our current origin to plane P_1, we find that

$$h_2 = h_1 + u_1 z_{12}, \tag{2.29}$$

and, since $h_1 = 0$, we conclude that

$$h_2 = u_1 z_{12}. \tag{2.30}$$

Again, as both z_{12} and u_1 are positive, h_2 is positive as required by the sign convention.

The *transfer equation* that allows us to trace the ray heights through a system has the general form

$$\boxed{h_{n+1} = h_n + u_n z_{n,n+1},} \tag{2.31}$$

which is used to calculate the ray intersection heights at successive planes in an optical system. The current origin for which Equation (2.31) applies is at plane P_n.

2.5.2. Refraction at a Curved Surface

Consider the refraction of a ray at a curved surface of radius R_1 that delineates regions of refractive indices n_1 and n_2, as shown in Figure 2.13. The *curvature* of the surface is $c_1 = 1/R_1$. An auxiliary sign convention is that the curvature of a convex surface, as viewed from the direction that the ray travels, is positive; the curvature of a concave surface is negative. For the moment, we assume that the refractive index is n_2 everywhere to the right of the spherical surface intersecting the points O and P; the vertex of the sphere defines the position of plane P_1. Based on our sign

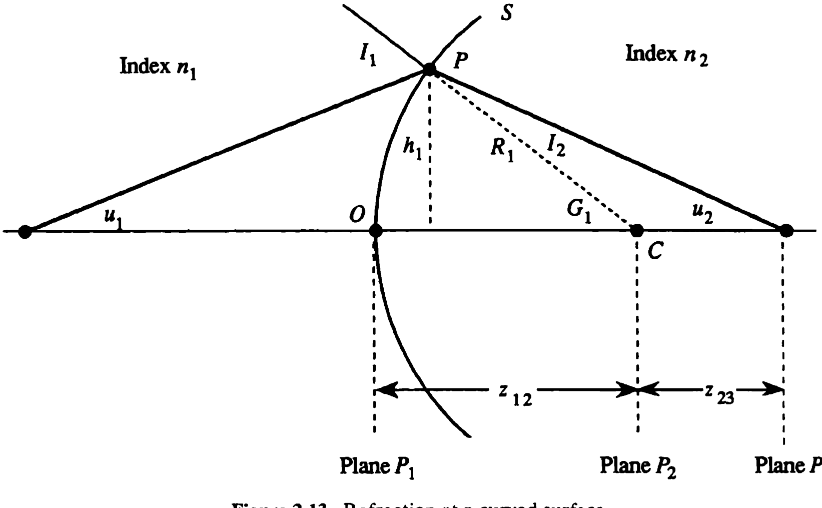

Figure 2.13. Refraction at a curved surface.

convention, we see that u_1 is positive, u_2 is negative, and h_1 is positive. The angle G_1 of the *normal to the surface* is given by the angle OCP. Because we use the same sign convention for wavefront normals as for rays, G_1 is negative.

We begin by setting our current origin at the vertex of the surface and applying Snell's law to the ray as it intersects the surface S:

$$n_1 I_1 = n_2 I_2, \tag{2.32}$$

where we use the paraxial ray approximation. Although all the angles are small in practice, we exaggerate them in our figures for clarity. From the sketch we see that the angle of incidence is equal to the sum of the angles u_1 and G_1. Because G_1 is negative, we find that

$$I_1 = u_1 - G_1. \tag{2.33}$$

The sign of the angle of incidence is dictated by the ray and normal angles so that relationship (2.33) is not overspecified. As shown, I_1 is positive because u_1 is positive and G_1 is negative. In a similar fashion, we find that

$$I_2 = u_2 - G_1. \tag{2.34}$$

The sign of I_2 is also positive because, although both u_2 and G_1 are negative, $|G_1| > |u_2|$. We use these values for the angles of incidence and refraction in Equation (2.32) to find that

$$n_1(u_1 - G_1) = n_2(u_2 - G_1). \tag{2.35}$$

As $G_1 = -h_1/R_1 = -h_1 c_1$, we find that

$$\boxed{n_2 u_2 = n_1 u_1 - h_1 c_1 (n_2 - n_1),} \tag{2.36}$$

which is the *refraction equation* for a surface in its generalized form. The quantity $c_1(n_2 - n_1)$ is the *power of the surface* and is denoted by K_1. The power of a surface is expressed in *diopters* when the curvature is expressed in reciprocal meters. From Equation (2.36) we see that when $c_1 = 0$ the curved surface degenerates into a flat surface and Equation (2.36) reduces to Snell's law, as expected, because the power of the surface is then zero. Also, if $n_2 = n_1$, the power of the surface is zero for all values of c_1. This trivial situation simply shows that an optical surface cannot be defined when $n_2 = n_1$.

2.5.3. The Refraction Equation for Combined Surfaces

The refraction equation for a surface can be applied repeatedly to successive surfaces to develop the refraction equation for a lens. Suppose that the ray encounters a second surface of curvature c_2 separating a region of index n_2 from a region of index n_3, as shown in Figure 2.14. We apply the transfer equation (2.31) to find the height at which the ray penetrates the second surface of the lens:

$$h_2 = h_1 + u_1 z_{12}, \tag{2.37}$$

where z_{12} is the distance between the vertices of the two surfaces of the lens. In Section 2.5.6 we define the principal planes of a thin lens, whose parameters allow us to set h_2 equal to h_1. With $h_2 = h_1 = h$, we apply the refraction equation directly at the second surface of the lens to find that

$$n_3 u_3 = n_2 u_2 - h c_2 (n_3 - n_2). \tag{2.38}$$

We substitute the value of $n_2 u_2$ from Equation (2.36) into Equation (2.38) to find that

$$\boxed{n_3 u_3 = n_1 u_1 - h\left[c_2(n_3 - n_2) + c_1(n_2 - n_1)\right].} \tag{2.39}$$

The result given by Equation (2.39) is the most general statement of the refraction equation for lenses and can be used in all situations. It is valid for glass lenses in air or, as sometimes used in medical instruments, for air lenses in glass.

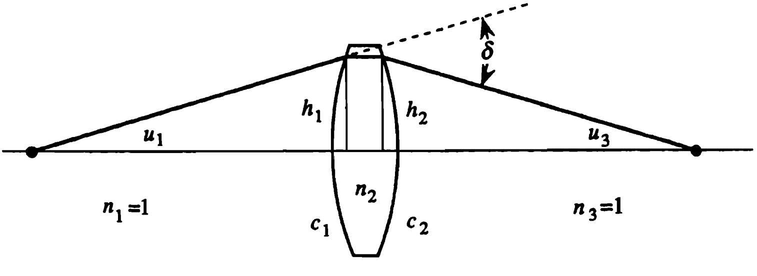

Figure 2.14. Ray trace for a thin lens.

The power of the lens is the sum of the powers of the two surfaces:

$$K = K_1 + K_2 = c_1(n_2 - n_1) + c_2(n_3 - n_2). \qquad (2.40)$$

For the special situation of a glass lens in air, as sketched in Figure 2.14, $n_1 = n_3 = 1$ is the refractive index for the two air spaces and n_2 is the refractive index of the lens. We find that Equation (2.39) then yields

$$u_3 = u_1 - h(c_1 - c_2)(n_2 - 1), \qquad (2.41)$$

which is the refraction equation for a thin lens in terms of the constructional parameters of the lens.

The *power* of a thin lens of index n_2, embedded in air, and with surface curvatures c_1 and c_2, is given by

$$\boxed{K = (c_1 - c_2)(n_2 - 1).} \qquad (2.42)$$

As c_2 is negative and $n_2 > 1$, the power of the lens is positive. The *deviation* of the ray is given by $\delta = u_1 - u_3$, which is equal to hK, the product of the power of the lens and the ray height. The ray at the maximum height, called the *marginal ray*, is bent the most, whereas the axial ray is not deviated because $h = 0$.

2.5.4. The Condenser Lens Configuration

A condenser lens configuration occurs when all incident rays are parallel, as shown in Figure 2.15(a). The refraction equation, using the lens as our current origin, states that

$$u_3 = u_1 - hK, \qquad (2.43)$$

so that, for $u_1 = 0$, we find that

$$u_3 = -hK. \qquad (2.44)$$

As $u_3 = -h/z_{23}$ for small angles, we find that $z_{23} = 1/K = F$, which is the focal length of the lens. Thus, a thin lens *condenses* a bundle of parallel rays at a distance equal to its focal length. This plane is called the *back focal plane* of the lens.

Parallel rays entering the lens at an off-axis angle also focus at the back focal plane of the lens. Consider the upper entrance ray in Figure 2.16,

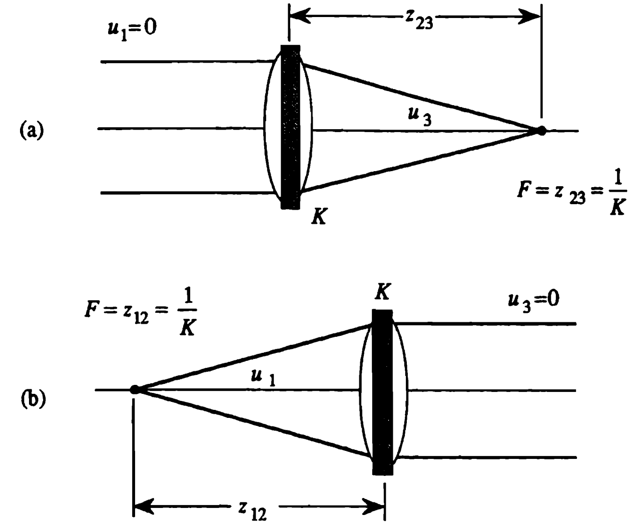

Figure 2.15. Thin lenses: (a) condenser and (b) collimator.

which makes an angle u_1 with respect to the optical axis. By the refraction equation we find that

$$u_3 = u_1 - h_2K, \tag{2.45}$$

where h_2 is the height of the ray at the lens. By the transfer equation, we find that

$$h_3 = h_2 + u_3z_{23}, \tag{2.46}$$

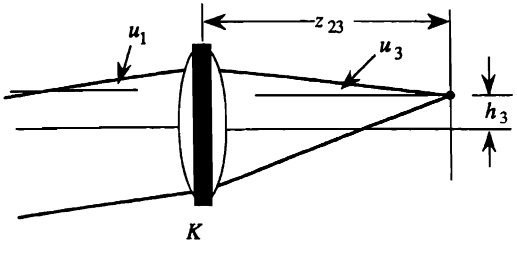

Figure 2.16. Imaging of an off-axis bundle of rays.

where the distance from the lens to the image plane is undetermined for the moment. The focal plane is found by tracing a second ray through the lens. The ray passing through the center of the lens is a convenient one to trace; for it, we find that

$$h_3 = u_1 z_{23}. \tag{2.47}$$

The parallel rays entering the lens are due, in effect, to an object sample at infinity. Because the image of a sample requires that all rays intersect, we require that the values of h_3 from Equation (2.46) and Equation (2.47) must be equal so that

$$\begin{aligned} u_1 z_{23} &= h_2 + u_3 z_{23} \\ &= h_2 + (u_1 - h_2 K) z_{23} \\ &= u_1 z_{23} + h_2 - h_2 K z_{23}, \end{aligned} \tag{2.48}$$

which, in turn, shows that z_{23} must be equal to F. This argument is easily extended to show that all parallel rays focus to a single point at the back focal plane of the lens.

2.5.5. The Collimating Lens Configuration

Suppose that we want to create parallel rays for which $u_3 = 0$, as shown in Figure 2.15(b). The refraction equation, as applied at the plane of the lens, becomes $u_1 = hK$. In a fashion similar to that shown in Section 2.5.4, we find that $z_{12} = 1/K = F$ so that the lens *collimates* a point source of light located at the *front focal plane* of the lens. Also, by using equations similar to those developed above, we find that light from any off-axis object sample, at the front focal plane, produces a parallel beam of light that propagates at an off-axis angle. A lens system is therefore *bilateral* so that its operation on rays traveling in one direction is the same as its operation on rays traveling in the opposite direction.

2.5.6. Principal Planes

In our derivation of the refraction formula, we assumed that $h_2 = h_1$ at the surfaces of the lens. In the case of thick lenses, where the assumption does not hold, we can still retain the formalism that $h_2 = h_1$ by introducing the concept of the principal planes of a lens. The first principal plane is found by tracing a ray from the front focal point O_1, as shown in

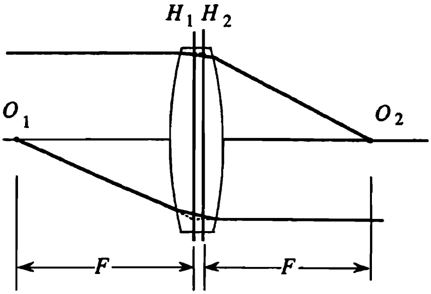

Figure 2.17. Principal planes for a thin lens.

Figure 2.17, to the lens surface. This ray exits the lens, parallel to the axis, at some point on the second surface of the lens, which establishes its height from the axis. We extend these two rays to their intersection point to define the position of plane H_1, called the *first principal plane* of the lens.

We follow a similar procedure for an entrance ray parallel to the axis, which passes through the back focal point O_2 after refraction. The intersection of these two rays defines the positions of plane H_2 and establishes the *second principal plane* of the lens. The principal planes provide the following properties for simplifying the representation of a lens:

- The front and back focal lengths of the lens are measured from the principal planes H_1 and H_2, respectively. For some lenses, principal plane H_2 may occur before principal plane H_1, generally referred to as a *crossover* of the principal planes.
- The principal planes are *unit magnification planes* because the magnification between them is $M = +1$. Thus, any ray that intersects plane H_1 at some height h_1 is transferred to plane H_2 at the *same* height h_1, where the entire bending action of the refraction equation is applied.
- Based on unit magnification, we collapse the space between H_1 and H_2 to represent the lens as a true thin lens with a single plane where all of the power of the lens is concentrated.

Principal planes may become curved surfaces for lenses with high relative apertures or for special lenses such as wide-angle lenses. The principal planes are generally flat for the types of lenses encountered in optical signal processing.

2.5.7. Thin-Lens Systems

We now generalize the refraction equation for a two-lens system, as shown in Figure 2.18(a), to find the equivalent power of a lens pair. Suppose that a parallel ray, for which $u_1 = 0$, enters the first lens at height h_1. This ray is bent by the first lens of power K_1 and intercepts the second lens at height h_2. The second lens bends the ray to its final value u_3 and the ray intercepts the axis at plane P_3. Suppose that we want to replace these two lenses with one having the equivalent power necessary to bend the incoming ray to the *same final angle* u_3, as shown in Figure 2.18(b). The first principal plane of the equivalent lens lies in the same plane as the first principal plane of the first lens of the pair. Although the equivalent lens *must* produce the same angle u_3 as the two-lens system, we do not require that the distances from the first principal planes to the focal planes be the same.

We begin by noting, from Figure 2.18(a), that

$$u_2 = u_1 - h_1 K_1 \tag{2.49}$$

by virtue of the refraction equation, that

$$h_2 = h_1 + u_2 z_{12} \tag{2.50}$$

by virtue of the transfer equation, and that

$$u_3 = u_2 - h_2 K_2 \tag{2.51}$$

by virtue of a second application of the refraction equation. We substitute

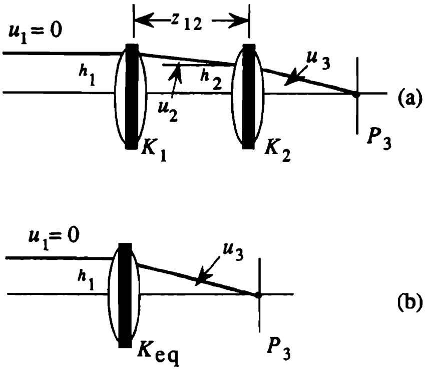

Figure 2.18. Ray traces: (a) two-lens system and (b) single-lens equivalent.

Equations (2.50) and (2.49) into Equation (2.51) to obtain

$$u_3 = (u_1 - h_1K_1) - [h_1 + (u_1 - h_1K_1)z_{12}]K_2. \tag{2.52}$$

Because $u_1 = 0$, we find that

$$u_3 = -h_1[K_1 + K_2 - z_{12}K_1K_2]. \tag{2.53}$$

For the equivalent lens shown in Figure 2.18(b), we see that

$$u_3 = -h_1K_{\text{eq}}. \tag{2.54}$$

By comparing Equation (2.53) with Equation (2.54) we see that the *equivalent power* of the two-lens system is

$$\boxed{K_{\text{eq}} = K_1 + K_2 - z_{12}K_1K_2,} \tag{2.55}$$

where K_1 and K_2 are the powers of the individual lenses and z_{12} is the distance between the two lenses. In this development, the sign of z_{12} is positive. The result given in Equation (2.55) is extremely useful for finding the proper geometric arrangement for two lenses to obtain a lens whose equivalent power is different from that of either lens.

To illustrate the use of the equivalent lens concept, consider the situation for two positive lenses. The maximum power is obtained when z_{12} is zero so that the two thin lenses are in contact and the equivalent focal power is

$$K_{\text{eq}} = K_1 + K_2, \tag{2.56}$$

in a fashion analogous to how the powers of the surfaces of the lenses add. A special case is obtained when $z_{12} = F_1$ so that the second lens is positioned at the back focal plane of the first lens. We then find that $K_{\text{eq}} = K_1$, which means that the lens with power K_2 has no contribution to the overall power; this lens is in a "no power plane." Such lenses are sometimes used as field lenses to help contain ray bundles, without contributing to image quality.

Because the power varies from $K_{\text{max}} = K_1 + K_2$ to $K_{\text{min}} = K_1$, each lens must have a focal length longer than the one we wish to synthesize. Also, given two lenses of powers K_1 and K_2, we obtain the largest range of powers when the lower-power lens is the first lens of the pair. This arrangement also tends to minimize the aberrations of the combination because the *relative apertures*, defined as the ratio of the lens aperture to its focal length, are more nearly equal for the two lenses.

There are no restrictions on the value of z_{12} or on the signs of the powers of the lenses *provided that u_3 has the proper numerical value and sign at the output of the equivalent lens*. For example, if the separation between the lenses is so large that the equivalent power is negative, we find that the ray angle u_3, for a parallel entrance ray a distance h_1 above the axis, must be negative, violating the constraint. Note that the equivalent power for a pair of negative lenses is always negative, independent of the value of z_{12}. If one lens is positive and one is negative, the constrained value of z_{12} is a function of the values of K_1 and K_2. Finally, we note that the total power of the two-lens system is zero when $z_{12} = F_1 + F_2$, a case that we now consider in more detail.

2.5.8. Afocal or Telescopic Configurations

In optical signal-processing systems we often consider signals that are in either the front or the back focal plane of the lens. Using these planes considerably simplifies the mathematical analysis of the system, with little loss of generality, and offers opportunities to reduce aberrations in a laboratory system (see Section 2.9). Furthermore, the plane under consideration may be simultaneously the back focal plane of one lens and the front focal plane of the next lens in cascaded systems.

For example, plane P_1, as shown in Figure 2.19(a), is the back focal plane of the lens whose power is K_1 and is simultaneously the front focal plane of the lens whose power is K_2. When arranged as shown, these two lenses are in an *afocal* or *telescopic configuration*. Such a configuration causes no net bending of the incident and exit rays, as shown by the fact that, for an *arbitrary* entrance ray at an angle u_1, we have

$$u_3 = u_1 - h_{\text{eq}} K_{\text{eq}}. \tag{2.57}$$

Because $K_{\text{eq}} = K_1 + K_2 - z_{12} K_1 K_2$ is the equivalent power of the lens pair and because $z_{12} = F_1 + F_2$ is the distance between the lenses, we find that

$$\begin{aligned} u_3 - u_1 &= -h_{\text{eq}}[K_1 + K_2 - (F_1 + F_2)K_1K_2] \\ &= -h_{\text{eq}}\left[K_1 + K_2 - \left\{\frac{1}{K_1} + \frac{1}{K_2}\right\}K_1K_2\right] \\ &= -h_{\text{eq}}\left[K_1 + K_2 - \left\{\frac{K_1 + K_2}{K_1K_2}\right\}K_1K_2\right] = 0, \end{aligned} \tag{2.58}$$

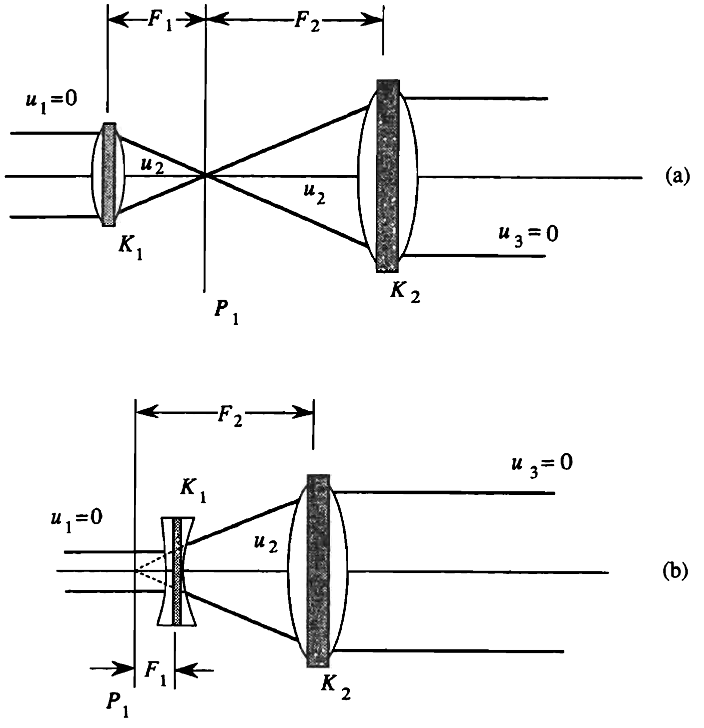

Figure 2.19. Cascaded lenses in afocal arrangements: (a) positive lenses and (b) negative/positive lenses.

so that $u_3 = u_1$. The name *telescopic* derives from the property of a telescope, which accepts parallel light at a given angle and produces parallel light, generally with some beam magnification, at the same angle.

The telescopic condition arises whenever $z_{12} = F_1 + F_2$. The net power of the system is therefore zero, and rays are not bent in traversing the system. There are two generic telescopic configurations that result according to the signs associated with the focal lengths of the two lenses. In the first configuration, shown in Figure 2.19(a), it is clear that the two lenses are separated by the sum of their focal lengths. In the second configuration, shown in Figure 2.19(b), the first lens has a negative power, but the two lenses are still separated by the sum of their focal lengths and plane P_1 is a common focal plane for both lenses. There are two other telescopic configurations that provide magnifications less than one; these configurations are simply those of Figure 2.19(a) and Figure 2.19(b) with the lenses interchanged. The total length of the system and the sign of the magnification depend on the signs of the focal lengths of the two lenses.

2.6. THE GENERAL IMAGING CONDITION

So far we have considered some special conditions in which either the object or the image is at infinity; these are called *infinite conjugate* imaging conditions. A more general condition arises when an object at plane P_1 is imaged at plane P_3, as shown in Figure 2.20. Both planes are at finite distances from the lens, resulting in a *finite conjugate* imaging condition. With the lens as the current origin, z_1 and z_3 indicate the distances of these planes from the lens. A sample in the object plane, a height h_1 above the axis, generates a family of rays that produces a wavefront W_1 normal to all the rays. In a well-corrected system, Fermat's principle states that the optical paths traveled by all rays are equal. Therefore wavefront W_2 is also normal to the ray family on the image side; the image occurs at plane P_3, a height h_3 below the optical axis. For all conjugate-ray pairs the refraction equation states that

$$u_3 = u_1 - hK, \tag{2.59}$$

where h is the height at which the ray intercepts the lens. When we divide all terms in Equation (2.59) by h, we find that

$$\frac{u_3}{h} = \frac{u_1}{h} - K. \tag{2.60}$$

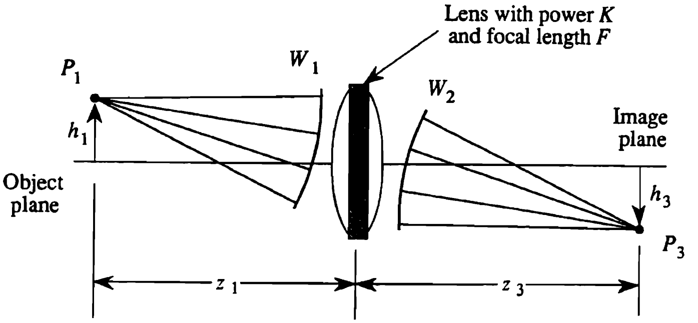

Figure 2.20. General imaging condition.

For the sample located on the optical axis at plane P_1, we find that $u_3 = -h/z_3$ and $u_1 = -h/z_1$, so that

$$-\frac{1}{z_1} + \frac{1}{z_3} = \frac{1}{F}, \tag{2.61}$$

which is commonly referred to as the *lens equation*. Thus, if we know the value of F and the value of either z_1 or z_3, we can determine the remaining unknown distance. Remember that Equation (2.61) is valid only for a thin lens in air. The more general result, as given by Equation (2.39), is always valid.

2.6.1. Ray Tracing

To analyze the image quality produced by an optical system, we trace many rays from an object sample through the system and require that they all fall within a specified distance from the true image sample position. However, only a few rays are required to determine the positions of the object and image planes relative to the lens. The trick is to select the most useful ones.

Throughout this section, we treat axial distances as having positive magnitudes and account for their negative values by compensating for the signs in the equations. We do this because we need to shift the current origin several times to derive general results. The sign of an axial distance may therefore be both positive and negative, depending on the position of the current origin, and ambiguities could arise when making the final calculations. This procedure is not necessary, of course, when we numerically calculate ray positions because the calculations are completed at each surface before we proceed to the next surface.

We begin by selecting a ray parallel to the optical axis, as shown in Figure 2.21(a), for which $u_1 = 0$. This ray starts from an object sample at plane P_1 located a height h_1 above the axis. We use the transfer equation to find the ray height at the lens plane P_3:

$$\begin{aligned} h_3 &= h_1 + (z_{12} + z_{23})u_1 \\ &= h_1. \end{aligned} \tag{2.62}$$

The refraction equation for a lens in air states that

$$\begin{aligned} u_3 &= u_1 - h_3K \\ &= -h_3K = -h_1K, \end{aligned} \tag{2.63}$$

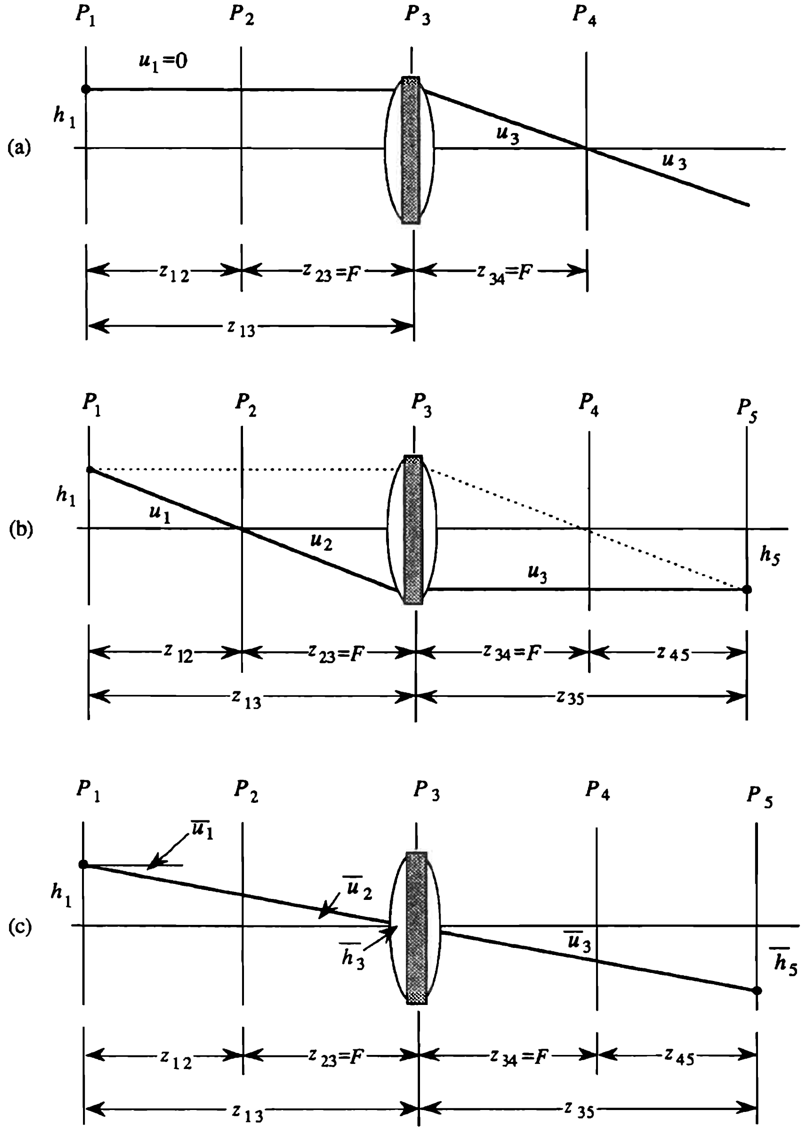

Figure 2.21. Three convenient rays for finding the position of the image plane and the object magnification: (a) input parallel ray, (b) output parallel ray, and (c) principal pupil ray.

where K is the power of the thin lens. This parallel input ray crosses the axis at plane P_4, located a distance z_{34} from the lens. The position of plane P_4 is found by solving the equation

$$h_4 = h_3 + u_3 z_{34} = 0, \tag{2.64}$$

from which we deduce that

$$z_{34} = -\frac{h_1}{u_3} = \frac{1}{K} = F, \tag{2.65}$$

where F is the focal length of the lens. Plane P_4 is therefore the back focal plane of the lens; all parallel rays entering the lens focus at this plane, as we showed in Section 2.5.4. At this stage of the analysis, we do not know the position of the image plane P_5, nor the image height h_5. We therefore temporarily extend the ray from P_3 through plane P_4 for an arbitrary distance to the right of plane P_4.

A second ray uniquely determines the position of image plane P_5 and the image height h_5. The bilateral nature of the lens suggests that we select a ray, passing from the sample h_1 in P_1 through the front focal point of the lens, as shown in Figure 2.21(b). Tracing this ray forward through the system is the same as tracing the previous ray backwards. Because this ray passes through the front focal plane of the lens, $h_2 = 0$, and we apply the transfer equation to find u_1:

$$h_2 = h_1 + u_1 z_{12} = 0, \tag{2.66}$$

so that $u_1 = -h_1/z_{12}$. This ray intercepts plane P_3 at a height

$$h_3 = h_2 + u_2 z_{23}, \tag{2.67}$$

where $z_{23} = F$ is the focal length of the lens. But the intersection height $h_2 = 0$ so that $u_2 = u_1 = -h_1/z_{12}$ and

$$h_3 = \frac{-h_1 z_{23}}{z_{12}} = \frac{-h_1 F}{z_{12}}. \tag{2.68}$$

We apply the refraction equation at plane P_3 to find that

$$\begin{aligned} u_3 &= u_2 - h_3 K \\ &= -\frac{h_1}{z_{12}} - \left[\frac{-h_1 F}{z_{12}}\right] K = 0, \end{aligned} \tag{2.69}$$

so that the second ray is rendered parallel to the optical axis by the collimating action of the lens.

The intersection of the second ray with the extension of the first ray defines the position of the image plane P_5. For the second ray, we find that

$$h_5 = h_4 = h_3 = \frac{-h_1 F}{z_{12}}, \tag{2.70}$$

which gives the height of the image sample.

The distance z_{45} can now be found from the transfer equation

$$\begin{aligned} h_5 &= h_4 + u_3 z_{45} = u_3 z_{45} \\ &= -h_1 K z_{45}. \end{aligned} \tag{2.71}$$

We use Equation (2.70) in Equation (2.71) to find that

$$-\frac{h_1 F}{z_{12}} = -h_1 K z_{45}, \tag{2.72}$$

which is rearranged as

$$z_{12} z_{45} = F^2, \tag{2.73}$$

to obtain *Newton's formula* for relating the distances of the object and image plane from the focal planes of the lens.

2.6.2. Lateral Magnification

The *lateral magnification M* is given by the ratio of the image height to the object height, as shown in Figure 2.21(b). From similar triangles, we find that

$$M = \frac{h_5}{h_1} = \frac{-F}{z_{12}}, \tag{2.74}$$

which is the ratio of the focal length of the lens to the distance from the front focal plane to the object plane. We can also express the magnification in terms of the object to lens distance z_{13}:

$$z_{13} = z_{12} + z_{23} = z_{12} + F \tag{2.75}$$

so that

$$M = \frac{-F}{z_{13} - F}. \tag{2.76}$$

Three special cases are of interest. In the first case, $z_{13} \to F$, which means that the object plane approaches the front focal plane of the lens. In this case, $M \to -\infty$ so that the lateral magnification is infinite and the lens acts as the collimator shown in Figure 2.15(b). In the second case, $z_{13} = 2F$ so that $M = -1$ and the object and the image planes are symmetrically located two focal lengths from the lens. The modulus of the magnification is unity, with the negative sign implying a reversal of the image coordinate system in passing from plane P_1 to plane P_5. The image is therefore rotated 180° with respect to the object. In the third case, $z_{13} \to \infty$ so that $M \to -1/\infty = 0$, and the lens acts as the condenser shown in Figure 2.15(a). The rays on the object side of the lens are therefore parallel and the image is formed at the back focal plane of the lens.

We also express the magnification in terms of the parameters on the image side of the lens. From similar triangles, we find that

$$M = \frac{h_5}{h_1} = \frac{-z_{45}}{F} = \frac{F - z_{35}}{F}. \tag{2.77}$$

Arguments similar to those given in the previous paragraph are applied to Equation (2.77) to determine the position of the image plane for various values of the magnification.

2.6.3. The Principal Pupil Ray

Another easy ray to trace is the *principal pupil ray*, which is midway between the two marginal rays and passes through the center of the lens as shown in Figure 2.21(c). The angles and intersection heights of principal pupil rays are usually indicated by an overbar; they obey, of course, the same laws of propagation as do other rays. For the principal pupil ray we have

$$\bar{u}_1 = \frac{-h_1}{z_{12} + z_{23}} = \bar{u}_2. \tag{2.78}$$

At plane P_3 we have

$$\bar{u}_3 = \bar{u}_2 - \bar{h}_3 K. \tag{2.79}$$

But $\bar{h}_3 = 0$ by construction so that $\bar{u}_3 = \bar{u}_2 = \bar{u}_1$, which shows that the ray is not bent as it passes through the center of the lens. It therefore arrives at plane P_5 at a height

$$\begin{aligned}\bar{h}_5 = h_5 &= \bar{h}_3 + (z_{34} + z_{45})\bar{u}_3 \\ &= 0 + \left[-h_1 \frac{z_{34} + z_{45}}{z_{12} + z_{23}}\right] \\ &= \frac{-h_1 z_{35}}{z_{13}}.\end{aligned} \tag{2.80}$$

The magnification is $M = h_5/h_1 = -z_{35}/z_{13}$, which is an alternative, and perhaps the easiest, way to obtain the magnification. The magnification is simply the ratio of image to object distance. If $z_{35} > z_{13}$, the magnitude of the magnification is greater than 1; if $z_{35} < z_{13}$ the corresponding magnitude is less than 1.

These three rays are useful for determining the image position and magnification when the object position and the lens focal length are known. Any two of the three rays are sufficient; we generally choose whichever pair is most convenient for a particular system. These rays do not, however, reveal anything about the detailed structure of the image in terms of the required sampling distance for the object or about the spatial resolution of the lens. We now show how we can trace some rays that are associated with object and image resolution and combine them with those traced so far to develop an important result: the optical invariant.

2.7. THE OPTICAL INVARIANT

Suppose that the object has a sampling interval d_0, the distance between the delta functions of the sampling function, for a signal bandlimited to α_{co}, as discussed in Chapter 1. Further, each sample in the object between $-h_1$ to h_1, shown in Figure 2.22, diffracts light rays over a range of angles bounded by $\pm u_1$. For the moment we concern ourselves with only those rays produced by the sample located at O_1 at plane P_1 and use the refraction equation to establish the position of the image plane P_5. We begin by finding a relationship between u_1 and u_5. From plane P_2, the

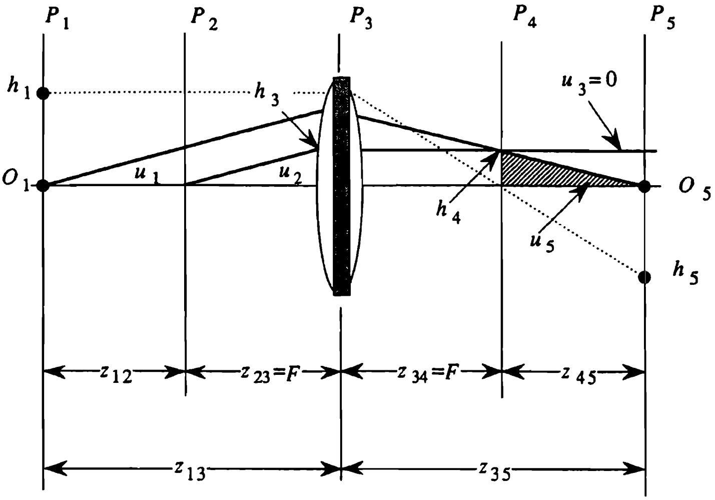

Figure 2.22. Rays necessary to determine the optical invariant.

front focal plane of the lens, we construct a parallel ray with the same angle $u_2 = u_1$ as the marginal ray from sample O_1. As $h_2 = 0$ at plane P_2 for this ray, we find that

$$\begin{aligned} h_3 &= h_2 + u_2 z_{23} \\ &= u_2 z_{23}. \end{aligned} \tag{2.81}$$

The refraction equation requires that

$$\begin{aligned} u_3 &= u_2 - h_3 K \\ &= \frac{h_3}{z_{23}} - h_3 K = 0. \end{aligned} \tag{2.82}$$

This ray is therefore parallel to the optical axis and it intercepts plane P_4 at a height $h_4 = h_3$; as before, we extend this ray to infinity on the image side of the lens. Because parallel rays on the object side of the lens focus at plane P_4, the ray originating from the sample O_1 also intersects plane P_4 at height h_4. From the shaded triangle we see that

$$h_4 = u_5 z_{45}. \tag{2.83}$$

But because $h_4 = h_3 = z_{23}u_1$, we further find that

$$u_1 z_{23} = -u_5 z_{45}, \tag{2.84}$$

which relates the image ray bundle angle u_5 to the object ray bundle angle u_1.

We now find a relationship between h_1 and h_5. By tracing the dotted ray through the lens, we see by inspection that

$$M = \frac{h_5}{h_1} = \frac{-z_{45}}{z_{34}}. \tag{2.85}$$

We solve Equation (2.85) for z_{45} and use this value in Equation (2.84) to find that

$$u_1 z_{23} = u_5 \left[\frac{h_5 z_{34}}{h_1} \right]. \tag{2.86}$$

As $z_{23} = z_{34} = F$ is the focal length of the lens, we further simplify Equation (2.86) to show that $h_1 u_1 = h_5 u_5$. We developed this result on the assumption that $n_1 = n_5$. The more general and complete result, for arbitrary indices of refraction on either side of the lens, is that

$$\boxed{n_1 h_1 u_1 = n_5 h_5 u_5.} \tag{2.87}$$

This relationship is variously known as Helmholtz's equation, Lagrange's equation, or Smith's equation; it is becoming more universally known as the *optical invariant*.

For a given system, the value of the *optical invariant is the same for all image planes*, provided that no information is lost due to aperture stops and that the system is free from aberrations. For example, a periscope has many intermediate image planes between the object plane and the final image plane; the optical invariant has the same value at each of these planes, even though the image sizes may be different.

The optical invariant is valuable for quickly sketching the geometry of an optical system, for double-checking mathematical calculations, and for showing why the brightness at any set of conjugate planes is fixed. The optical invariant is an important and quick way to check whether an optical system is feasible and how difficult it is to design. Some examples of how the optical invariant is used are given in the following sections.

2.7.1. Magnification Revisited

The optical invariant provides a useful alternative method for calculating the magnification of a system. Because the lateral magnification is defined as $M = h_5/h_1$, we use Equation (2.87) to show that

$$M = \frac{n_1 u_1}{n_5 u_5} \tag{2.88}$$

is an alternative expression for the lateral magnification. As h_5 is negative and h_1 is positive, the magnification is negative for the system shown in Figure 2.22, as confirmed by the fact that u_1 is positive and u_5 is negative. We see that $|n_5 u_5| > |n_1 u_1|$ when $|M| < 1$. For the typical case of $n_5 = n_1 = 1$, Equation (2.88) states that the angle u_5 is inversely proportional to the magnification. Because an image that is smaller than the object has smaller sample spacings, the maximum value of the included angle defining the image bundle must increase.

2.7.2. Spatial Resolution

Consider the telescope, shown in Figure 2.23, that focuses an incoming parallel ray bundle at its back focal plane. The plane-wavefront W_1 is focused by the lens to a point on the optical axis at plane P_2. The ray bundle on the image side of the lens does not, of course, form an infinitesimally small spot at plane P_2 because of diffraction phenomena. In Chapter 3 we show that the intensity of the diffraction pattern for a uniformly illuminated one-dimensional aperture is $\text{sinc}^2(\xi L/\lambda F)$, where ξ is the coordinate in the image plane as shown in Figure 2.24(a). The sinc^2

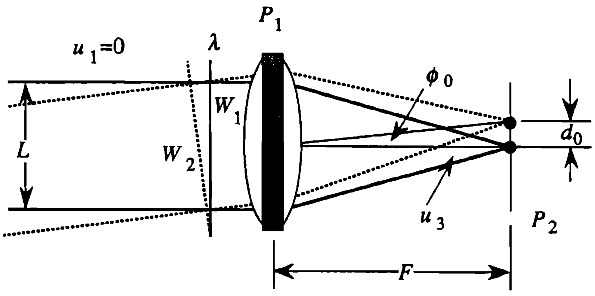

Figure 2.23. Resolution limit of a telescope.

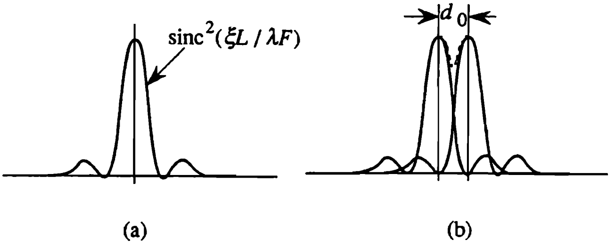

Figure 2.24. Rayleigh resolution criterion.

function is also the impulse response of the system, the impulse in this case being the infinitesimally small star at infinity.

Two samples from an object at infinity are resolved if the wavefront W_2 from the second sample is tilted with respect to W_1 by one wavelength of light over the aperture L of the lens. The *angular resolution* of the telescope is therefore

$$\phi_0 = \frac{\lambda}{L}, \tag{2.89}$$

as shown in Figure 2.23. Thus, the minimum resolvable distance at plane P_2, equivalent to the sampling interval, is

$$d_0 = \left(\frac{\lambda}{L}\right)F = \frac{\lambda}{2\theta_{co}}, \tag{2.90}$$

as shown in Figure 2.24(b), where we use θ_{co} to indicate the maximum value of u_3 as produced by the marginal ray with respect to the central ray. The relationship given by Equation (2.90) establishes the connection between θ_{co} and the interval d_0 between the samples at the image plane, a result that we used in Chapter 1 to describe the optimum sampling interval for a bandlimited analog optical signal.

Consider the spatial resolution of the telescope shown in Figure 2.23. For a lens aperture of $L = 100$ mm and focal length of $F = 1000$ mm, the relative aperture of the telescope is $L/F = 0.1$. A more commonly used measure is the $f/\#$, which is the ratio of the focal length to the aperture; the $f/\#$ for this set of parameters is $f/10$. For $\lambda = 0.5\ \mu$, we use Equation (2.90) to find that the *spatial resolution* of the telescope is $d_0 = 0.5(1000)/100 = 5\ \mu$. From Figure 2.23, we see that the largest angle θ_{co} is equal to $L/2F$ so that $\theta_{co} = 0.5\ \mu/2(5\ \mu) = 0.05 = 2.87°$ This is a surprisingly small angle for a fairly high spatial resolution and supports the notion that most optical systems are accurately analyzed by using paraxial rays.

If we set u_3 to its maximum value of θ_{co}, we have a special case of the optical invariant that we indicate by the symbol J_x. From the optical invariant we find that $J_x = n_3 h_3 \theta_{co}$ or that $J_x = n_3 h_3 \lambda / 2d_0$. We recognize that the height of the image, $2h_3$, divided by the minimum resolvable distance d_0 is a measure of the number of resolvable samples N_x in the image in the x direction. For $n_3 = 1$, we find that

$$\boxed{J_x = \frac{N_x \lambda}{4},} \tag{2.91}$$

so that the optical invariant is equal to the product of the number of samples and a quarter wavelength. Similar comments apply to the optical invariant J_y and the number of samples N_y in the y direction.

2.7.3. Space Bandwidth Product

In Chapter 1 we showed that we need $N = 2TW$ samples to accurately represent a signal that has duration T and highest frequency W. A similar concept applies to optical signals. The *length bandwidth product* of a spatial signal is the product of the object length L and the highest spatial frequency α_{co}: LBP $= \alpha_{co} L$. Thus, $N_x = 2\alpha_{co} L$ is the number of samples necessary to accurately represent the object in the horizontal direction.

To describe a two-dimensional image, we define the *height bandwidth product* as HBP $= \beta_{co} H$. Generally $\beta_{co} = \alpha_{co}$, but sometimes the cutoff frequency is different in the two directions. In a corresponding way, $N_y = 2\beta_{co} H$ is the number of samples necessary to accurately represent the object in the vertical direction. The *space bandwidth product* is simply the product of the length and height bandwidth products with the result that SBP = (LBP)(HBP), and we need $N = N_x N_y$ samples to accurately represent a two-dimensional image.

Finally, as J_x is measured in units of distance, we note that the dimensionless quantities N, TW, LBP, HBP, and SBP are proportional to the optical invariant normalized by the wavelength of light. A typical value of J_x for optical processing systems is of the order of 0.25 mm. As a general rule, lens design starts to get difficult when J_x exceeds 1 mm or so, corresponding to a length bandwidth product of 4000 for green light.

2.7.4. Matching the Information Capacity of System Components

As we showed in Section 2.7.2, the angular resolution of the telescope is dependent only on the aperture of the lens and the wavelength of light. The angular resolution of the telescope, whose parameters are given in Section 2.7.2, is $\phi_0 = \lambda/L = 0.5\ \mu/100(10^3)\ \mu = 5\ \mu\text{rad}$. The angular resolution of the eye is only about 500 μrad; we therefore need an eyepiece which, in combination with the objective lens, provides a 100 × magnification to fully appreciate the resolving capability of the telescope. This magnification is more or less consistent with the idea that the magnification of a telescope is equal to the ratio of the entrance-beam diameter to that of the exit beam, as discussed in Section 2.5.8. The pupil of the eye establishes the exit-beam diameter at 3–5 mm, depending on the illumination level; the overall useful magnification of a small-diameter telescope (80–100 mm) is therefore approximately 20–30 × , although magnifications of about 2–3 × these values seem to produce "sharper" images.

Using a significantly more powerful eyepiece does not provide more resolution. Why not? A principle of system design is that we match the bandwidths of all components of a system. All real-time electronic systems have a fixed metric for the time base. In optical systems, however, the spatial bandwidths may not be equal because the image may have a different size than the object. For optical systems, the *optical invariant plays the same role as does bandwidth in a real-time system*, and it ensures that the number of samples required to represent a signal does not change as the signal progresses through the system. An equivalent statement is that the optical invariant ensures that no signal information is lost.

Increasing the bandwidth of the last component of the system, which is equivalent to using a higher-power eyepiece, does not increase the information content of a signal. The angular resolution has already been set by the primary aperture of the telescope, which is why we generally rate the angular resolution of a telescope by citing its aperture size. Other factors, such as atmospheric turbulence, affect resolution, of course, but the aperture sets the theoretical resolution. The use of a higher-power eyepiece than necessary results in an image that has *empty magnification*.

We further illustrate these points by considering the resolving power of an $f/4$ camera lens, shown in Figure 2.25, whose focal length is $F = 100$ mm and whose diameter is $L = 25$ mm. Suppose that the image

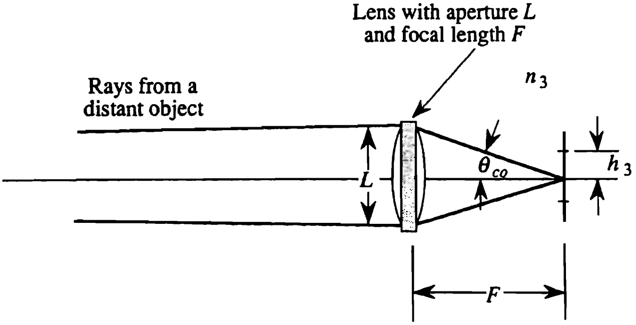
Lens with aperture L and focal length F
Rays from a distant object
n_3
θ_{co}
L
h_3
F

Figure 2.25. Camera with $f/4$ lens.

height is $2h_3 = 25$ mm. At the image plane, we have

$$\theta_{\text{co}} = \frac{L}{2F} = \frac{25\text{ mm}}{200\text{ mm}} = 0.125\text{ rad} = 7.18°,$$

$$J_y = n_3\theta_{\text{co}}h_3 = 1(0.125)(12.5\text{ mm}) = 1.56\text{ mm},$$

$$d_0 = \frac{\lambda}{2\theta_{\text{co}}} = \frac{0.5\,\mu}{0.25} = 2\,\mu,$$

$$N_y = \frac{2h_3}{d_0} = \frac{25{,}000\,\mu}{2\,\mu} = 12{,}500\text{ samples.} \tag{2.92}$$

We see that a fairly simple camera lens produces an image of high quality, as shown by the large value of the optical invariant J_y and the large number of samples as shown by N_y.

If the image length is $L = 35$ mm, the number of samples required is $N_x = 17{,}500$ in that direction and the total number of samples produced is $N = N_xN_y = 2.28(10^8)$. At $f/2$, the image has four times the number of resolvable elements because the sample interval is halved in each direction; at $f/1.4$ the image has two times even more samples. Hence, a high-quality image contains a considerable amount of information.

Suppose that we record the image on photographic film. As the sampling theorem requires two samples per cycle of the highest spatial frequency to accurately represent a signal, the highest spatial frequency that the lens produces is

$$\alpha_{co} = \frac{1}{2d_0}, \tag{2.93}$$

which is called the *cutoff frequency* of the lens system. The units of the spatial frequency α_{co} are cycles/mm when d_0 is expressed in millimeters.

The optics community does not have an equivalent designator, such as Hertz (one cycle per second), to indicate spatial frequencies. We suggest the use of the designator *Abbe*, in honor of Earnst Abbe who did pioneering work in describing the relationship of spatial frequency content to image quality, to mean one cycle per millimeter and to abbreviate it as *Ab*. The reader is cautioned to note that spatial frequencies are often expressed as *lines per millimeter* in the literature and that the television industry tends to describe their systems in terms of *scan lines per inch*. This terminology is potentially confusing because a line sometimes refers to a cycle, but in other instances it may refer to a sample. The use of Ab to represent the spatial frequency of an optical signal may help to eliminate this potentially confusing situation.

We connect the cutoff spatial frequency α_{co} to the scattering angle θ_{co} associated with sample size d_0 through the use of Equations (2.90) and (2.93):

$$\boxed{\alpha_{co} = \frac{1}{2d_0} = \frac{\theta_{co}}{\lambda}.} \tag{2.94}$$

We find that $\alpha_{co} = 250$ Ab for the given parameters of the $f/4$ camera lens. The length bandwidth product of the image is therefore LBP $= 2h_3\alpha_{co} = 6250$. Consistent with normal design rules, photographic film must have a frequency response equal to α_{co} to avoid loss of information in the recording process. As the eye can resolve about 4 Ab at normal viewing distances and pupil sizes, we can magnify the resulting image approximately $M = \alpha_{co}/\alpha_{eye} = 62.5\times$ Additional magnification causes more pronounced film grain noise; less magnification results in loss of detail. Matching the optical invariant J at all image planes and for all components in an optical system therefore provides the maximum information content at the output.

It is important to realize that the cutoff angle θ_{co}, in any given situation, may be determined either by the optical system or by the object itself. For example, in the camera system just analyzed, we assumed that the cutoff angle was limited by the relative aperture of the lens. But in some applications the intrinsic resolution available from the object may be the limit; in this case, the object cannot produce a ray bundle that fills the lens aperture. In other applications the recording film or a CCD photodetector array may set the minimum sampling interval. Ideally, then, we first determine which part of a system imposes the limiting cutoff parameter and then match all the components of the system in terms of the optical invariant. In low-light-level television cameras a lens with an excessive $f/\#$ may be used simply to collect more photons—similar to the use of a larger antenna in a microwave system.

2.8. CLASSIFICATION OF LENSES AND SYSTEMS

Recall that the refraction equation for a lens in air is

$$u_3 = u_1 - hK, \tag{2.95}$$

where $K = (n_2 - 1)(c_1 - c_2)$ is the power of the lens. Because the refractive index of the lens is greater than one, the sign of the power of the lens is determined by the signs and magnitudes of c_1 and c_2. If c_1 is positive and numerically larger than c_2, or if c_1 is positive and c_2 is negative, the power of the lens is positive.

2.8.1. The Coddington Shape Factor

The shape of the lens is also determined by the magnitudes of c_1 and c_2. The *Coddington shape factor* σ is defined as

$$\sigma \equiv \frac{c_1 + c_2}{c_1 - c_2}. \tag{2.96}$$

If we add an incremental curvature Δc to both c_1 and c_2, their difference is constant so that the power of the lens is unchanged. Lens shapes for various values of σ are shown in Figure 2.26. We start with $\Delta c = 0$ and with $c_2 = c_1$ so that the Coddington shape factor is $\sigma = 0$ and the lens is called a *biconvex* lens. If we add an incremental curvature $\Delta c = -|c_1|$ to each surface, we find that $\sigma = -1$; and the lens is called a *plano convex* lens. If $\Delta c > -|c_1|$, we find that $\sigma < -1$; and the lens is called a *positive meniscus* lens. Adding amounts $\Delta c = |c_2|$ and $\Delta c > |c_2|$ results in plano convex and meniscus lenses, as shown in Figure 2.26. The following points

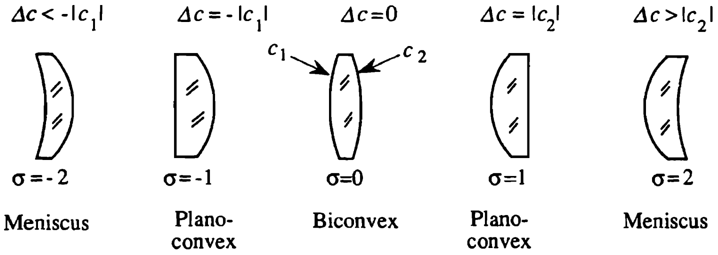

Figure 2.26. Types of positive lenses.

are noted:

- All the lenses have the *same power*.
- All the lenses are *positive* lenses.
- Although not shown in the figure, the principal planes of the lenses are in different places relative to the vertices of the lens surfaces.
- The process of adding a given value to both curvatures of the lens is called *bending the lens*. Bending is easily visualized by keeping the center of the lens fixed and pushing on the rim of the lens in either direction.

A similar set of lens shapes is obtained for lenses with negative power, a condition that arises when c_1 is negative and c_2 is positive, or if c_1 is negative and numerically larger than c_2. These lens shapes, shown in Figure 2.27, are called *biconcave*, *plano concave*, and *negative meniscus*

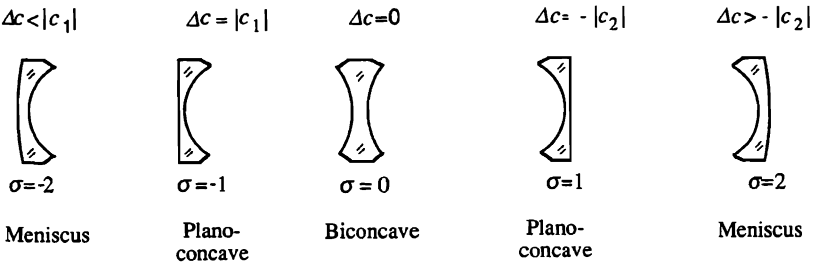

Figure 2.27. Types of negative lenses.

lenses. Comments similar to those made previously apply to these lens shapes.

2.8.2. The Coddington Position Factor

The *Coddington position factor* π is defined as

$$\pi \equiv \frac{u_3 + u_1}{u_3 - u_1}. \tag{2.97}$$

The various imaging geometries are shown in Figure 2.28. The condensing lens configuration shown in Figure 2.28(a) has $\pi = +1$, the unity magnification arrangement shown in Figure 2.28(b) has $\pi = 0$, and the collimating lens configuration shown in Figure 2.28(c) has $\pi = -1$. As $M = u_1/u_3$,

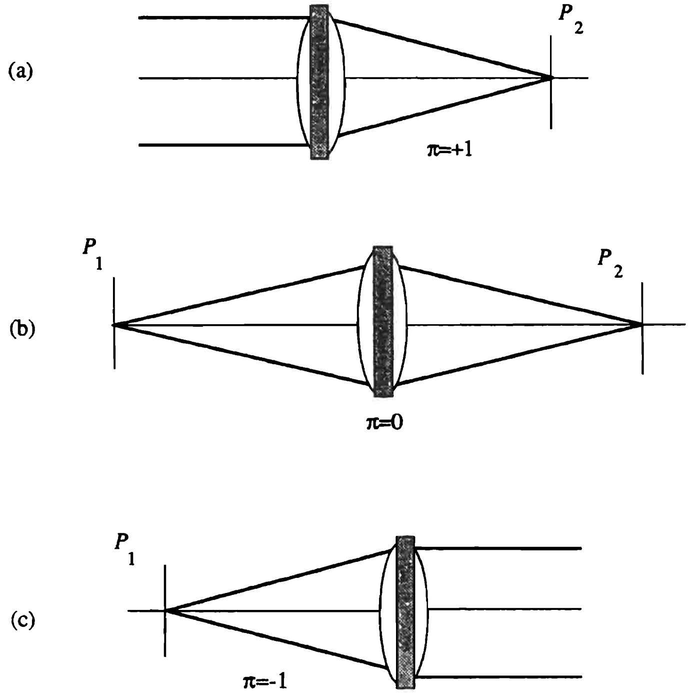

Figure 2.28. Imaging geometries: (a) condensing, $\pi = +1$; (b) unity magnification, $\pi = 0$; and (c) collimating, $\pi = -1$.

we relate the Coddington position factor to the magnification by

$$\pi = \frac{1 + M}{1 - M}, \tag{2.98}$$

so that we easily find the position factor required for any magnification.

2.9. ABERRATIONS

Aberrations result from the imperfect way in which rays are bent as they pass through an optical system. One way to characterize aberrations is to trace rays from selected object samples and to determine where they intersect the image plane. The resulting ray pattern is called the *point spread function*, equivalent to the *impulse response* in linear system theory. Ray tracing is at the heart of geometrical optics design. With present-day computers and lens-design programs, it is relatively easy to arrive at such a well-designed lens that all the rays pass through a region smaller than the diffraction limited resolution of the lens. The ray-tracing program then no longer accurately describes the light distribution near focus because diffraction effects, as we discuss in Chapter 3, dominate.

As an alternative to ray tracing, we calculate the wavefront that is normal to the ray bundle and express the aberrations in terms of a polynomial function. From the wavefront surface, the nature of the aberrations is easier to visualize, and, in conjunction with diffraction theory, the exact form of the light distribution near the focal point is obtained. The aberration polynomial function is equivalent to the *system response* $H(f)$ in linear system theory, except that the system response changes as a function of the position of a sample in the object. The optical system is therefore *space variant* so that a unique system response does not generally exist. Aberration theory recognizes the space-variant property of the system response and accurately predicts the system response to all samples in the object. The intent of this brief discussion of aberrations is to familiarize the reader with the nature of the aberrations, how to recognize them, and how to select a lens shape or the proper system configuration to minimize them in laboratory setups. More extensive treatments of aberrations and methods for correcting them are found in various texts and monographs (10–13). Photographs of the effects of lens aberrations are found in the first three of these references and in a more recent text (14).

Consider the generalized imaging system shown in Figure 2.29, where the curved surface S images an object sample from O_1 at the focal point O_2. Fermat's principle requires that all rays from O_1 to O_2 have the same

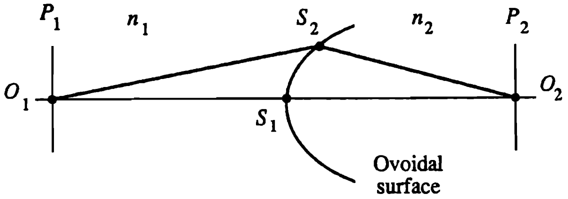

Figure 2.29. Surface to provide aberration-free performance for a single axial point.

optical path length so that the ideal wavefront is the ovoidal surface represented by

$$O_1S_2 + S_2O_2 = O_1S_1 + S_1O_2 = \text{constant}. \tag{2.99}$$

In general we cannot fabricate such surfaces and, even if we could, the imagery is perfect only at one object sample. The lens designer's task, then, is to control aberrations over an extended region, while using surface shapes that are easily manufactured.

We use the coordinate system, shown in Figure 2.30, that defines a sample in the image plane by the distance ρ; the coordinates at the lens plane are r and ϕ. The *monochromatic wavefront aberration polynomial*

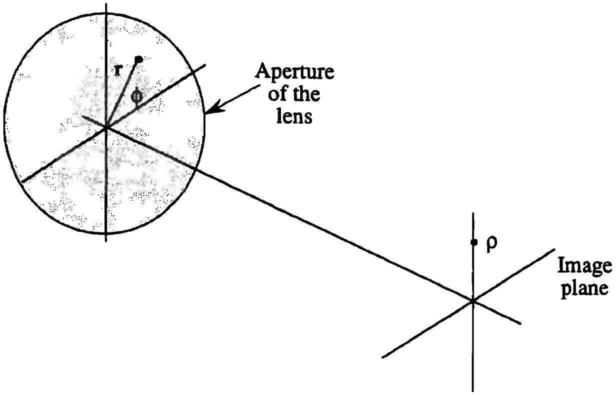

Figure 2.30. Coordinate system for characterizing aberrations.

for third-order aberrations is given by

$$\boxed{W(\rho, r, \phi) = a_1 r^4 + a_2 \rho r^3 \cos\phi + a_3 \rho^2 r^2 \cos^2\phi + a_4 \rho^2 r^2 + a_5 \rho^3 r \cos\phi,} \tag{2.100}$$

where the coefficients determine the magnitude of the aberration. The wavefront aberration $W(\rho, r, \phi)$ is the optical path difference between the actual wavefront and a reference wavefront that is a perfect sphere, with the paraxial focal point as its center. Each of the five primary aberration terms are in the fourth power of combinations of the variables ρ and r.

Because the lateral displacements of the rays at the focal plane are proportional to the derivatives of $W(\rho, r, \phi)$, the aberrations given by Equation (2.100) are called *third-order aberrations*. We have ignored first-order aberrations, such as a defect of focus or a lateral focal shift, which do not affect image quality. We compensate for these "aberrations" by adjusting the axial position of the focal plane or the lateral position of the optical axis. Fifth- and higher-order aberrations are generally not important unless the relative apertures of the lenses are high. This situation does not normally arise in optical signal-processing systems because the optical invariant is held to a reasonably low value by currently available input/output devices. Chromatic aberrations are ignored because the illumination is monochromatic.

2.9.1. Spherical Aberration

In Figure 2.31(a), we show the reference wavefront W_r whose curvature is proportional to r^2 that would produce a perfect image of an object sample located at infinity. The first term of the aberration polynomial is *spherical aberration*, for which the actual wavefront is given by $a_1 r^4$. When spherical aberration is present, the wavefront is curved too much if a_1 is positive, or too little if a_1 is negative. For the case shown, a_1 is positive and we see that the marginal rays are too highly bent so that they cross the optical axis on the object side of the point where the paraxial rays cross. The clue for correcting spherical aberration is to recall that the deviation angle for a prism is a function of the incident ray angle. We consider a lens as a set of prisms, each with a different angle, as shown in Figure 2.31(b); and we attempt to equalize the angles of incidence and refraction by bending the lens.

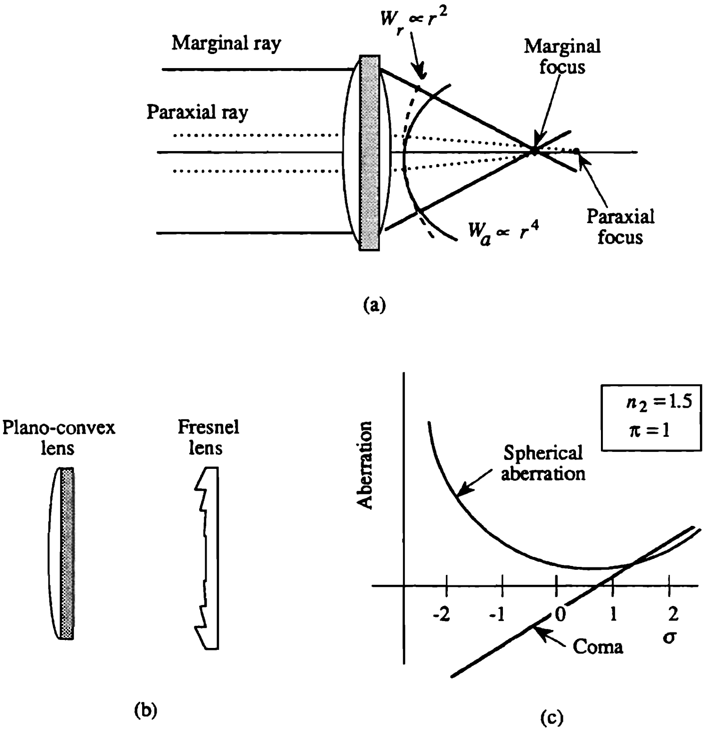

Figure 2.31. Spherical aberration: (a) wavefront representation, (b) equivalent Fresnel lens, and (c) plot of spherical aberration and coma.

A measure of the spherical aberration as a function of the lens shape factor σ is shown in Figure 2.31(c). The proper shape factor to correct spherical aberration is dependent on the object/lens geometry. For a glass lens in air, the optimum shape factor σ for minimizing spherical aberration as a function of the position factor π is (13)

$$\sigma = \frac{2(n_2^2 - 1)}{n_2 + 2}\pi. \tag{2.101}$$

We find that $\sigma = 0.7\pi$ for a typical lens of refractive index $n_2 = 1.5$. When $\pi = 1$, the minimum spherical aberration occurs at $\sigma = 0.7$ as shown in Figure 2.31(c). This σ value is close to that of a plano convex lens, oriented so that its curved surface is toward the plane wavefront produced by the object. With this lens orientation we see that the angle of incidence with respect to the first surface and the angle of refraction with respect to the second surface are nearly equal. When the magnification is unity, the shape factor is zero, independent of n_2; in this case, a biconvex lens minimizes the spherical aberration because the angles of incidence and refraction are then equal. Although spherical aberration is partially corrected by selecting the proper lens shape, it is better controlled by using a cemented doublet. The primary reason for using cemented doublets is to correct chromatic aberrations, but spherical aberration is also significantly reduced.

The *Hartman test* is a simple laboratory test to quickly estimate the amount of spherical aberration and to determine if a lens is overcorrected or undercorrected. As illustrated in Figure 2.32, we construct a mask containing two small apertures, one near the edge of the lens and the second at the center of the lens. We place this mask at the lens plane, and begin by allowing light to pass only through the central aperture to establish the paraxial focal position. This aperture is small enough to produce a well-formed diffraction pattern, sometimes called the *Airy disc*, but large enough to accurately determine the paraxial focus position.

We then cover the central aperture, allow light to pass through the edge aperture, and determine if the second bundle of rays crosses the axis before or after the paraxial focal plane. For example, if the spherical aberration is positive and the edge aperture is above the central aperture, the bundle crosses the axis before the paraxial focal plane and the second Airy disc is below the first Airy disc at the focal plane. Spherical aberration is negative if the relative positions are reversed.

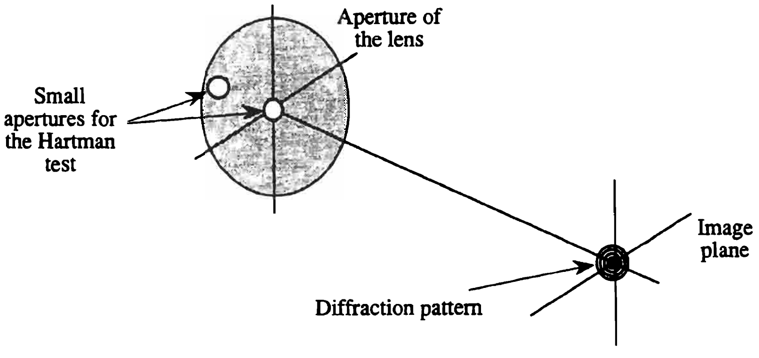

Figure 2.32. Hartman test for spherical aberration.

2.9.2. Coma

From Equation (2.100), we note that spherical aberration is not a function of the position of a sample in the object plane; that is, it is not a function of ρ. It is, therefore, the only primary aberration that produces a space-invariant response. The first aberration that is a function of ρ is *coma*, given by $a_2 \rho r^3 \cos \phi$. Coma arises when the principal planes are curved surfaces, a condition that occurs only in high-performance systems. As a result, the magnification of the system is greater, or less, for marginal rays than for paraxial rays, even in the absence of spherical aberration. When coma is present, the image of a sample has a shape like a comet. Lens designers minimize coma by making the magnification equal for all rays. From the optical invariant, with the sines of the angles retained, we find that $n_3 h_3 \sin u_3 = n_1 h_1 \sin u_1$. For $n_1 = n_3 = 1$ we have

$$M = \frac{\sin u_1}{\sin u_3}, \tag{2.102}$$

known as the *sine condition*, which must hold for all finite angles u_1 and u_3 to ensure that coma is zero.

Coma is also a function of the lens shape and is minimized for a glass lens in air when (13)

$$\sigma = \frac{(2n_2 + 1)(n_2 - 1)}{n_2 + 1}\pi. \tag{2.103}$$

In Figure 2.31(c) we plot the relative value of coma as a function of σ. Coma is minimized when $\sigma = 0.8\pi$ for $n_2 = 1.5$. For $\pi = +1$, both coma and spherical aberration are therefore minimized at nearly the same shape factor. Because the minimum value for spherical aberration is a fairly broad function of σ, we control both aberrations fairly well when we minimize coma.

A simple laboratory test for coma is to construct a set of masks, as illustrated in Figure 2.33, containing two small apertures with various distances between them. We place a mask in the plane of the lens so that the two apertures are at opposite edges of the lens. As the mask is rotated clockwise, the light distribution at the focal plane rotates counterclockwise, tracing out the locus of the extreme tail of the coma which passes through the paraxial focal point. Although the magnification is roughly the same for all rays from either small aperture, it is quite different for the two apertures taken together. As other masks with smaller distances between the apertures are inserted into the system, the light distribution

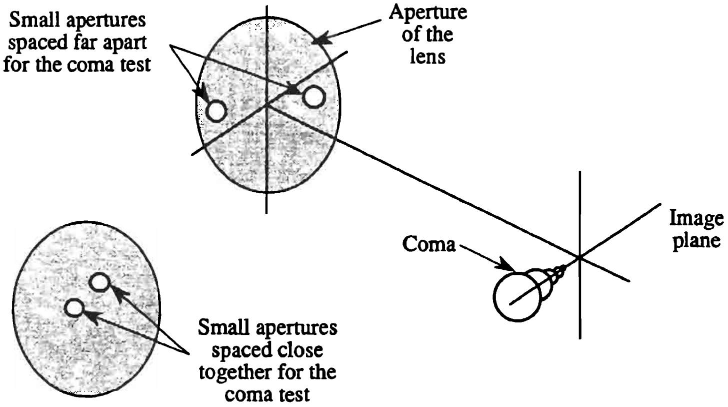
Small apertures spaced far apart for the coma test
Aperture of the lens
Image plane
Coma
Small apertures spaced close together for the coma test

Figure 2.33. Test for coma.

at the focal plane becomes more compact; when only one aperture is present, the head of the comet is produced.

2.9.3. Astigmatism

Astigmatism, the third term in the aberration polynomial (2.100), is given by $a_3\rho^2r^2\cos^2\phi$. Astigmatism results when rays in the tangential plane do not focus at the same point as those from the orthogonal plane, called the *sagittal plane*. Astigmatism is illustrated in Figure 2.34, where we see that the curvature of the wavefront is not the same in the two orthogonal

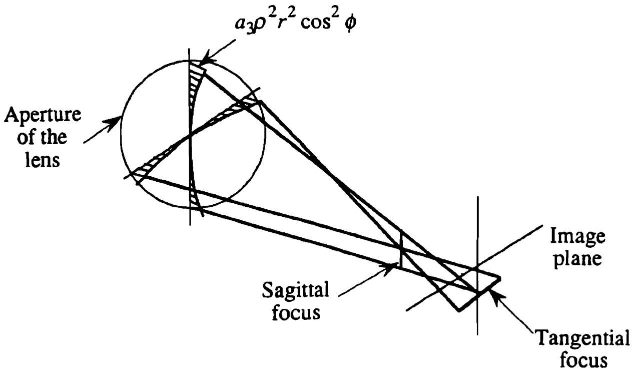

Figure 2.34. Sagittal and tangential focus lines due to astigmatism.

planes, leading to the two focal planes. As astigmatism is not a function of the lens shape, we control it by keeping ρ and r within bounds relative to the lens focal length. A simple laboratory test for astigmatism is to image a test target that looks like a spoked wheel. The rim is in focus at the tangential focal plane, and the spokes are in focus at the sagittal focal plane.

2.9.4. Curvature of Field

A simple lens works best when it focuses an object from a curved surface onto a curved image surface. When a lens is forced to work with flat object and image planes, an aberration called *curvature of field* appears, as illustrated in Figure 2.35. Curvature of field, given by $a_4\rho^2r^2$, is independent of all other aberrations. The coefficient a_4 depends on the ratios of the powers of the lens elements to their refractive indices, summed over all the elements in the system. This value is called the *Petzval sum*:

$$J^2\sum_i \frac{K_i}{n_i}, \tag{2.104}$$

where J is the optical invariant, and K_i and n_i are the powers and the refractive indices of the lens elements. Because a system containing only positive lenses has a large positive Petzval sum, we control curvature of field by introducing negative lenses where they have little effect on image quality. One possibility is to use negative lenses near the object or image planes; in the latter case the lens is called a *field flattener*.

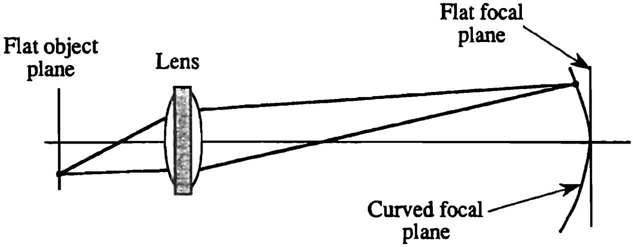

Figure 2.35. Curvature of field.

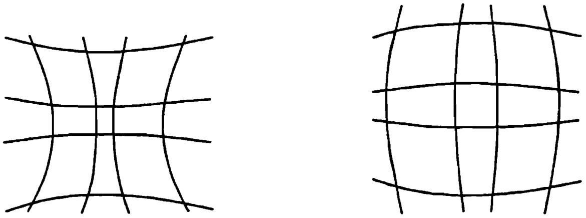

Pincushion distortion

Barrel distortion

Figure 2.36. Distortion.

2.9.5. Distortion

The fifth primary aberration is *distortion*, described by $a_5\rho^3 r\cos\phi$. Distortion affects the shape of an image, not its sharpness. Distortion is due to a variation in the magnification for off-axis object samples. Distortion causes a regular grid of squares to take on a pincushion or barrel shape, as shown in Figure 2.36, according to the sign of a_5. Distortion is zero for longitudinally symmetric systems, whose aperture is in the middle of the system. As optical signal-processing systems are often configured symmetrically, distortion is generally not a problem.

2.9.6. Splitting the Lens

Using more than one lens is a simple method for reducing aberrations in a laboratory setup. Consider the unity magnification imaging system, shown in Figure 2.37(a), in which a lens of power K is placed a distance $2F$ from the object plane. As $M = -1$, we find that $\pi = 0$ and we might be tempted to use a biconvex lens. Suppose, however, that we split the lens into two lenses, each with power $K/2$ as shown in Figure 2.37(b). The object and image planes are still a distance $2F$ from the two lenses, but the position factors are now $\pi = -1$ and $\pi = +1$ for the two lenses.

The major benefit of lens splitting is that the relative apertures of the lenses have been reduced by a factor of 2 so that aberrations such as spherical aberration, coma, astigmatism, and curvature of field are reduced, some rather dramatically. Distortion is identically equal to zero due to symmetry for the special case of unity magnification. Spherical aberration and coma are minimized by using suitable lens shapes, such as a plano convex lens, configured so that the curved surfaces face each other.

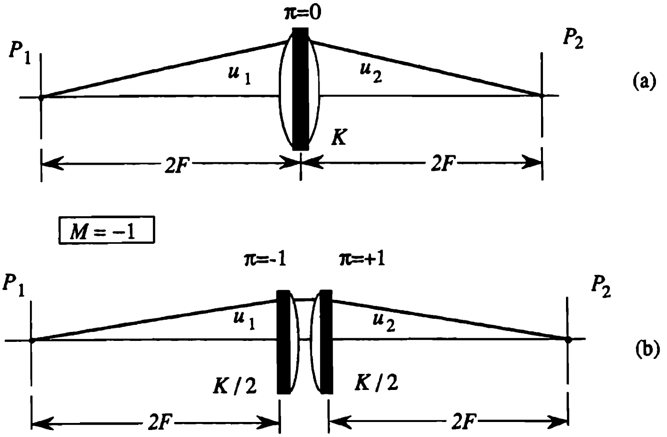

Figure 2.37. Splitting an imaging lens to control aberrations: (a) original system and (b) equivalent system.

Almost any imaging setup benefits from splitting the lens, but the advantages are greatest when the magnification is near unity. To illustrate the more general case, suppose that $M > -1$. The immediate question is how to split the lens of power K into two others. As we would like each of the resulting lenses to operate with $|\pi| = 1$, we find that

$$K_1 = \frac{MK}{M - 1} \tag{2.105}$$

and

$$K_2 = \frac{-K}{M - 1}. \tag{2.106}$$

As a sanity check, we note that $K_{\mathrm{eq}} = K_1 + K_2 = K$. We can therefore split the lens for any system configuration.

For large M, we find that the relative aperture of the first lens is not reduced significantly because the object is already near its front focal plane. The aberrations of the second lens are, however, significantly reduced relative to those of either the original lens or to those of the first lens. Finally, the focal lengths of available lenses in a laboratory may not be what we need to achieve a given magnification. We can then depart slightly from the $\pi = \pm 1$ condition to fine-tune the final magnification without seriously changing the aberrations.

Some final thoughts about aberrations. Be aware of these aberrations—know how to identify them and what causes them. Based on this knowledge, make laboratory setups for preliminary experiments by proper choice of the lens types and the geometric arrangements (the values of σ and π). Consult with a lens designer when you are about to build a system. Learn to specify, but not to overspecify, the operational requirements, and let the lens designer do the rest.

PROBLEMS

2.1. You have a prism for which $n_2 = 1.6$ and $\gamma = 30°$

(a) For an incidence angle of $I_1 = 20°$ (on the base side of the normal of the prism), calculate the deviation angle. Provide a sketch.

(b) What value of I_1 produces total internal reflection? Provide a sketch of the situation.

2.2. A ray is incident at an angle of 10° relative to the normal of a prism whose index of refraction is 1.6. Calculate the apex angle for which the ray is internally reflected by the prism (the critical angle). Plot the angle as a function of the index of refraction of the prism for n_2 ranging from 1.4 to 2.0.

2.3. A parallel beam of light 20 mm high enters a prism normal to its first surface. The prism has an index of refraction of 1.8 and an apex angle of 27 degrees. Calculate:

(a) the magnification of the prism (state clearly the direction in which the light is traveling),

(b) the deviation angle (show clearly by a sketch), and

(c) the smallest apex angle that produces total internal reflection.

2.4. You have a prism whose apex angle is 30° and whose index of refraction is 1.7. Design a second prism (i.e., find its apex angle and index of refraction) if the magnification of the pair must be equal to 0.3. If we were to use two identical prisms whose index of refraction is 1.5, calculate the apex angle needed to produce a magnification of 0.3.

2.5. Derive a general solution for the displacement h of a ray passing through a wobble plate of index n_2 and thickness z_{12} as a function of the angle of incidence I_1. Show that your result reduces to

$$h = \frac{z_{12} I_1 (n_2 - 1)}{n_2},$$

for small I_1. What is the maximum possible displacement? Find the approximate angle at which the exact and approximate solutions differ by 1%.

2.6. Is it possible to image a point object (for simplicity, assume that the object is a star at infinity) on the back surface of a glass sphere whose radius is R? If so, what is the required index of refraction? Hint: Use the refraction equation and remember that it represents the paraxial approximation, i.e., the entering rays should be ones near the optical axis.

2.7. We want to expand and collimate a beam of light from an ideal laser whose beam divergence is zero, using a pair of telescopic lenses whose powers are $K_1 = 0.05$ mm^{-1} and $K_2 = 0.005$ mm^{-1}. The light fills the first lens whose diameter is 5 mm. Upon measurement, we find that we made an error in the spacing between the lenses so that the beam has a convergence angle of 10 mrad. How far, and in what direction, should we move the second lens? Remember that the magnification is negative, i.e., that an entrance ray above the optical axis crosses over and becomes an exit ray below the optical axis. Having found the correct position of the lenses, sketch the system and calculate the magnification.

2.8. Consider a spherical surface that separates media of refractive indices n_1 and n_2. In terms of the power K of the surface, calculate the positions of the front and back focal planes.

2.9. We have an optical system that contains a single lens whose focal length is 100 mm. We want to change its effective focal length to 200 mm by using a second lens. Because of mechanical constraints, we must place the second lens 40 mm beyond the first lens. Find the focal length of the second lens and provide a sketch for the final system.

2.10. You need to image an object with a magnification of $M = -4$. You have been given a blob of glass, whose refractive index is $n = 1.62$, that is just enough to make a single lens element. You want the image to be 100 mm from the lens. Provide a sketch of the general geometry. You melt this glass and give it to a lens maker as a blank circular piece from which he must grind the lens. Calculate (1) the Coddington position factor π, (2) the optimum Coddington shape factor σ that will minimize the spherical aberration, (3) the curvatures c_1 and c_2 necessary to achieve this shape, and (4) the optimum shape factor and the curvatures c_1 and c_2 needed to minimize coma. Hint: Use the refraction equation and the formula for M involving the angles, along with the relationship for π and σ. Please watch the signs and be numerically accurate.

2.11. You have just bought a Camcorder for making home videos. The manufacturer states that the sensor in the camera has 400 resolution elements (equivalent to 400 samples) in the vertical direction, which is 10 mm high. Assume that the wavelength of light is 0.5 μ. Calculate (a) the optical invariant (remember that the optical invariant applies to image planes—use the version involving N), (b) the maximum spatial frequency that can be resolved at the sensor, and (c) the $f/\#$ necessary to match the resolution of the lens to that of the sensor (assume an infinite conjugate imaging condition).

2.12. You want to make a logo for your newest video production, using the Camcorder from Problem 2.11. You identify a useful picture in a magazine that has been printed with a 100 sample/mm halftone screen. If you set the system magnification to record a 250-mm-high logo onto the sensor, what will be the maximum resolvable frequency in cycles/mm (referenced to the plane of the logo) that can be preserved? If you wish to preserve all of the detail (or resolution) available in the logo, how much of its height can you capture?

2.13. You have a TV set with 330 scan lines distributed uniformly over 15 inches in the vertical direction. If the angular resolution of the eye is 500 μrad, at what distance from the set must you be to just resolve the scan lines according to the Rayleigh-resolution criterion? (Consider each scan line to be equivalent to a sample or a smallest resolvable detail.)

2.14. Suppose that we have a CCD detector array with 400 photodetector elements along a 10-mm line. We have an LED array with 250 elements in an 8-mm length that we use as the object. Find the focal lengths of a two-lens system, with each lens operating at infinite conjugates (the π factors are ± 1) such that the resolution is matched, given that the diameter of the lenses must be 5 mm.

2.15. You want to use an injection laser diode having dimensions of 10 μ × 50 μ as a light source. You need a collimated beam of 30 mm in each direction and decide to use a spherical lens, followed by a beam-expanding prism. Calculate the aperture and focal length of the lens, as well as the apex angle for a prism whose index of refraction is 1.55. Do a sketch of the top and side views. Hint: Think of the laser dimensions as the size of a single sample of a generalized signal.

3

Physical Optics

3.1. INTRODUCTION

The basic theory of geometrical optics as given in Chapter 2 describes how optical elements such as lenses, mirrors, and prisms modify the direction of light rays. Physical optics extends the theoretical treatment of optical systems by incorporating the wave nature of light. We take a direct approach and refer the reader to various texts that provide the details of the development from Maxwell's equation (10, 15–18).

We begin with the basic assumption that light waves propagate in an isotropic media with simple harmonic motion and satisfy the scalar wave equation

$$\nabla^2\phi(z,t) = \frac{1}{c^2}\frac{\partial^2\phi(z,t)}{\partial t^2}, \tag{3.1}$$

where t is time and z is distance in the direction that the wave travels. The representation for free-space electromagnetic radiation is a real-valued function of the form $\cos(\omega t - kz)$, where $k = 2\pi/\lambda$ and ω is the radian frequency of light.

The transfer functions for lenses, prisms, and other optical elements are usually represented by complex-valued functions. As an example, Figure 3.1 shows an arbitrary optical element, illuminated by monochromatic light at wavelength λ that propagates parallel to the z axis. The light wave at plane z_0, represented by $\sqrt{2}\,\cos(\omega t - kz_0)$, is spatially modulated by the optical element whose magnitude transmittance is $|a(x)|$ and whose phase is $\phi(x)$. The phase difference between planes z_0 and z_1 is the product of the optical path difference and k:

$$\begin{aligned}\phi(x) &= \frac{2\pi}{\lambda}\left[n_1 d(x) + \{\Delta z - d(x)\}\right]\\ &= \frac{2\pi}{\lambda}\left[(n_1 - 1)d(x) + \Delta z\right],\end{aligned} \tag{3.2}$$

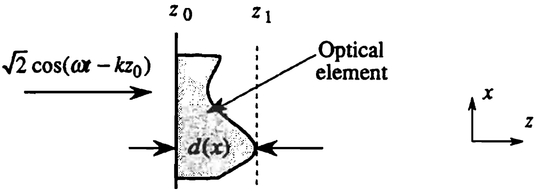

Figure 3.1. A general optical element.

where $\Delta z = z_1 - z_0$. Light at plane z_1 is therefore represented by

$$\sqrt{2}\,|a(x)|\cos[\omega t - kz_0 - \phi(x)], \tag{3.3}$$

which shows that light is modulated in both magnitude and phase.

It is often more convenient to use the phasor notation $\exp[j(\omega t - kz)]$ as a solution of the wave equation. In this sign convention, the wave propagates in the positive spatial z direction and temporal frequencies are positive if, when represented by a phasor diagram, they rotate in a counterclockwise fashion. This time/space sign convention is consistent with those of geometrical optics, physical optics, and electrical engineering. Using this notation, we represent light at plane z_1 of Figure 3.1 as

$$|a(x)|e^{j[\omega t - kz_0 - \phi(x)]}. \tag{3.4}$$

We generally suppress the temporal part of the electromagnetic wave, because no detector has sufficient bandwidth to respond directly to the amplitude fluctuations at light frequencies, and we also generally ignore the relative phase kz_0 at plane z_0. With these conventions, we represent the complex transmittance of the optical element by

$$a(x) = |a(x)|e^{-j\phi(x)}. \tag{3.5}$$

The complex transmittances of several optical elements in series multiply, as we expect. For example, three cascaded elements have an effective transmittance $a_4(x)$:

$$\begin{aligned} a_4(x) &= a_1(x)a_2(x)a_3(x) \\ &= |a_1(x)|\,|a_2(x)|\,|a_3(x)|e^{-j[\phi_1(x)+\phi_2(x)+\phi_3(x)]}, \end{aligned} \tag{3.6}$$

and the associated real-valued representation of the light is

$$\sqrt{2}\,|a_1(x)|\,|a_2(x)|\,|a_3(x)|\cos[\omega t - kz_0 - \phi_1(x) - \phi_2(x) - \phi_3(x)], \tag{3.7}$$

which illustrates that the magnitude transmittances are multiplicative and the phases are additive. Throughout this book we describe optical elements by complex-valued functions of the form given by Equation (3.6), with the understanding that the real-valued representations of propagating light are given by functions represented by Equation (3.7).

Any physical detector senses the *intensity* of light, defined as

$$I(x, y, z) \equiv a(x, y, z, t)a^*(x, y, z, t), \tag{3.8}$$

where * indicates complex conjugate. To illustrate that dropping the time dependence of the wave is valid when the postdetection bandwidth does not extend to the frequency of light, we obtain the intensity of the light at plane z_1 by two different methods. First, we use the real-valued version of the plane wave from Equation (3.3) and find that the intensity at plane z_1 becomes

$$\begin{aligned} I(x,t) &= 2|a(x)|^2\cos^2[\omega t - kz_0 - \phi(x)] \\ &= 2|a(x)|^2\{\tfrac{1}{2} + \tfrac{1}{2}\cos[2\omega t - 2kz_0 - 2\phi(x)]\}. \end{aligned} \tag{3.9}$$

A photodetector responds to the time average of $I(x, t)$ to produce a current $g(x)$ that is a function of only the space variable:

$$g(x) = \langle I(x,t)\rangle = |a(x)|^2 \tag{3.10}$$

The second method is to calculate the current in a direct fashion, as though the temporal component is not present, from Equation (3.5):

$$\begin{aligned} g(x) &= \langle a(x)a^*(x)\rangle \\ &= |a(x)|^2, \end{aligned} \tag{3.11}$$

which confirms that the time average notation is not needed explicitly and that we can ignore the temporal frequency of light in our basic phasor notation.

As an example of phasor notation, consider the complex-valued representation of a plane wave, propagating upward and to the right at an angle

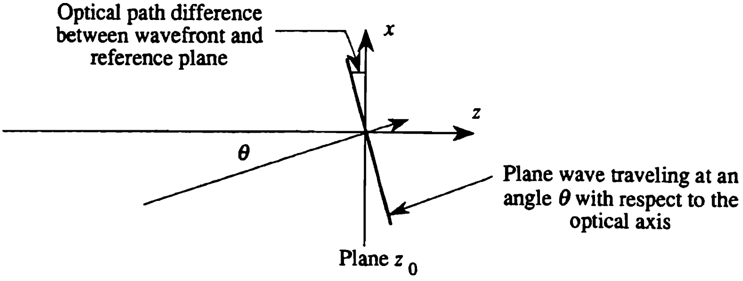
Optical path difference between wavefront and reference plane
x
z
θ
Plane wave traveling at an angle θ with respect to the optical axis
Plane z_0

Figure 3.2. Plane-wave representation.

θ, as shown in Figure 3.2. The wave has magnitude $|a(x)|$ and phase $\exp[-j\phi(x)]$. We measure the phase at any value of the variable x relative to the phase at $x = 0$. As the index of refraction in air is unity, the phase is given by the linear function

$$\phi(x) = \frac{2\pi}{\lambda}\theta x. \tag{3.12}$$

We use the relationship established in Chapter 2 between ray angles and spatial frequencies, namely, that $\alpha = \theta/\lambda$, to find that the plane-wave representation becomes

$$a(x) = e^{-j2\pi\alpha x} \tag{3.13}$$

We see then that we associate a spatial frequency α with a plane wave that propagates at a ray angle θ with respect to the optical axis. The signs of both α and θ are reversed if the wave travels downward and to the right.

The linear phase representation given by Equation (3.13) is also used to represent the complex transmittance of a prism. Recall from Chapter 2 that a prism operates on a plane wave, described there in terms of a set of rays normal to the wavefront, and deflects the wave so that it travels in a new direction. Thus, if θ_1 is the incidence angle of a ray with respect to the optical axis and if θ_2 is the corresponding angle of the refracted ray, the deviation angle is $\theta_3 = \theta_2 - \theta_1$. The prism is therefore represented by $\exp[-j2\pi\alpha_3 x]$, where $\alpha_3 = \pm\theta_3/\lambda$, and the $\pm$ sign indicates whether the wave has an upward or downward component.

From Equations (3.10) and (3.11) we see that the intensity reveals no information regarding either the temporal or the spatial frequency of a plane wave. To strengthen the idea that a plane wave traveling with a ray angle with respect to the optical axis has an associated spatial frequency, we render that frequency visible. Suppose that we add a plane wave $r(x)$, traveling parallel to the optical axis, to the inclined wavefront shown in Figure 3.2. The total amplitude at plane z_0 is then the sum of the two plane waves; the intensity, for $|r(x)| = |a(x)| = 1$, is

$$\begin{aligned} I(x) &= \left|r(x) + a(x)e^{-j2\pi\alpha x}\right|^2 \\ &= \left|1 + e^{-j2\pi\alpha x}\right|^2 \\ &= 2[1 + \cos(2\pi\alpha x)]. \end{aligned} \tag{3.14}$$

From Equation (3.14) it is clear that α is the spatial frequency associated with the light distribution at plane z_0. As the angle θ between the two waves increases, the spatial frequency increases correspondingly. A firm link between spatial frequencies and the angle between two wavefronts is therefore established.

3.2. THE FRESNEL TRANSFORM

Fresnel transforms relate the complex-valued light distributions located at two planes separated by free space. In holography, for example, it is the Fresnel transform of an object that is recorded for subsequent reconstruction. Fresnel transforms are used in synthetic aperture radar processing to determine the appropriate range and azimuth processing operations. In this chapter, we use the Fresnel transform to illustrate interference and diffraction phenomena and to develop the more familiar Fourier transform.

Fresnel extended Young's principle of interference to cases where the light is polarized. His work did much to confirm the transverse nature of light waves. In a key development, Fresnel modified Huygens' principle for relating the complex-valued light distribution at two separated planes in an optical system. Suppose, for example, that we know the light distribution $f(x, y)$ at plane P_1, as shown in Figure 3.3. We want to calculate the light distribution $g(\xi, \eta)$ at plane P_2, a distance D from plane P_1.

Fresnel's idea, stated here in a somewhat revised form, is that the elemental contribution δg at a point (ξ, η) in the observation plane, due to an elemental region $dx\,dy$ near a point (x, y) in the input plane, is proportional to several factors. First, we find that $f(x, y)$ represents the complex-valued amplitude in the neighborhood of a point (x, y) at plane

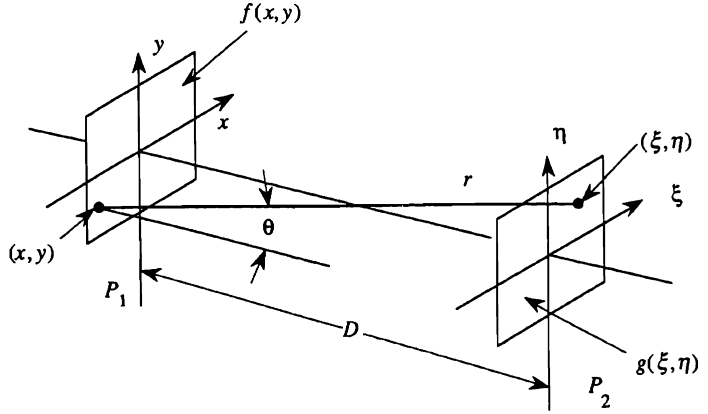

Figure 3.3. Fresnel diffraction.

P_1. Second, the exponential factor $\exp[j(\omega t - kr)]$ represents the phase change in the light as it propagates between planes P_1 and P_2, where r is the length of the ray connecting the points (x, y) and (ξ, η). Third, two factors determine how the magnitude changes as light propagates from plane P_1 to plane P_2. The first factor is $1/r$, which accounts for the fact that intensity is reciprocally related to the square of the propagation distance; the magnitude is therefore inversely proportional to r. The second factor is the *obliquity factor* $(1 + \cos\theta)/2$, where θ is the ray angle with respect to the optical axis. Finally, a fixed phase factor j is needed to obtain the correct results in Fresnel diffraction calculations, as we show in Section 3.2.4, and λ is a scaling factor to account for the wavelength of light. We combine all these factors to find the total contribution at (ξ, η):

$$g(\xi,\eta) = \frac{je^{j\omega t}}{\lambda r} \iint_{-\infty}^{\infty} \left[\frac{1+\cos\theta}{2}\right] f(x,y) e^{-jkr}\, dx\, dy. \qquad (3.15)$$

We begin the solution of Equation (3.15) by considering the obliquity factor $(1 + \cos\theta)/2$. In Chapter 2 we showed that the maximum ray angle $\theta_{co} = \lambda/(2d_0)$, where d_0 is the sample interval required to support a signal bandlimited to the cutoff frequency α_{co}. The distance d_0 is no less than a few wavelengths, even for rather wideband signals. For example, if the sample interval is $d_0 > 3\lambda$, all ray angles are such that $\theta < \frac{1}{6}$ and the minimum value of $(1 + \cos\theta)/2$ is therefore always greater than 0.993. This result, based on a wide-bandwidth signal for which $\alpha_{co} = \theta_{co}/\lambda = 333.3$ Ab, allows us to ignore the obliquity factor and to calculate the Fresnel diffraction integral for arbitrary values of the propagation distance D, including $D \to 0$.

The next step in the solution of Equation (3.15) is to consider the value of r:

$$r^2 = D^2 + (x - \xi)^2 + (y - \eta)^2 \tag{3.16}$$

By use of the binomial expansion, we find that

$$r = D\left[1 + \frac{(x - \xi)^2}{2D^2} + \frac{(y - \eta)^2}{2D^2} + \text{higher-order terms}\right]. \tag{3.17}$$

We neglect the higher-order terms because their effects are dominated by the first-order terms for all practical signal-processing applications. Furthermore, we replace r by D in the denominator of Equation (3.15), with an error in the magnitude that is generally less than 1%; in fact, replacing r by D partially compensates for ignoring the obliquity factor and increases the accuracy of the results. In any event, magnitude weighting has relatively little effect on diffraction; the phase is much more important.

With these factors accounted for, the diffraction integral of Equation (3.15) becomes

$$g(\xi, \eta) = \frac{je^{-jkD}}{\lambda D} \iint_{-\infty}^{\infty} f(x, y) e^{-j(\pi/\lambda D)[(x-\xi)^2 + (y-\eta)^2]}\, dx\, dy. \tag{3.18}$$

We ignore the time exponential factor $e^{-j\omega t}$ because we are mostly concerned with the spatial relationship between $g(\xi, \eta)$ and $f(x, y)$. To further explore the Fresnel transform, we also ignore the exponential phase factor e^{-jkD}, which simply represents the phase accumulation as the light travels from plane P_1 to P_2.

We now switch to a one-dimensional notation and find that free space behaves as an operator that produces a *Fresnel transform* defined by

$$\boxed{g(\xi) \equiv \sqrt{\frac{j}{\lambda D}} \int_{-\infty}^{\infty} f(x) e^{-j(\pi/\lambda D)(x-\xi)^2}\, dx,} \tag{3.19}$$

where the exponential function represents the free-space response to an impulse. The scaling factor in the one-dimensional case is the square root of that for the two-dimensional case because the wave is diverging cylindrically instead of spherically. Because the magnitude does not change in the y direction the magnitude decreases only as $\sqrt{1/D}$

The formulation of the Fresnel transform as given by Equation (3.19) has the following features.

- Shows the convolutional process between the free-space operator and the input signal.
- Explicitly displays the impulse response of free space as the function $\sqrt{j/\lambda D}\, \exp[-j(\pi/\lambda D)x^2]$.
- Produces a continuous transition from the Fresnel, or near-field, diffraction pattern, to the Fraunhofer, or far-field, diffraction pattern as a function of the distance D.
- Retains the necessary phase factors to facilitate the analysis of optical systems, using additional lenses and free-space intervals to achieve other processing operations, as discussed in Section 3.6.

3.2.1. Convolution and Impulse Response

To further illustrate the nature of the Fresnel transform, we define a function

$$\psi(x;d) \equiv e^{j\pi x^2/\lambda D}, \tag{3.20}$$

where $d = 1/D$ is a reciprocal distance. From Equations (3.19) and (3.20), we see that $g(\xi)$ is the convolution of $f(x)$ with the *free-space impulse response* $\sqrt{d}\,\psi^*(x;d)$, where $*$ indicates complex conjugate. We therefore describe the output $g(\xi)$ in terms of the input signal $f(x)$ that has passed through a black box whose impulse response is $\sqrt{d}\,\psi^*(x;d)$, as shown in Figure 3.4. The output of the black box is

$$g(\xi) = \sqrt{d}\int_{-\infty}^{\infty} f(x)\psi^*(\xi - x; d)\, dx, \tag{3.21}$$

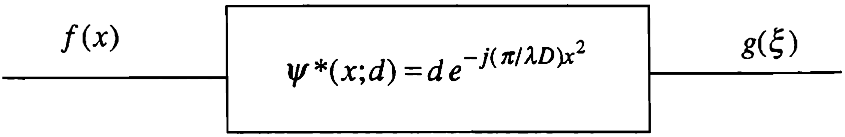

Figure 3.4. Equivalent block diagram for propagation of light through free space.

which is similar to Equation (3.19) in its form. In general, we drop scaling constants when developing major concepts; we restore them when needed to calculate actual light intensities.

To illustrate these concepts, we represent one sample of the input signal by an impulse function so that $f(x) = \delta(x)$. The output of the system, by the sifting property of the delta function, is

$$g(\xi) = \sqrt{d}\,\psi^*(\xi; d) = \frac{1}{\sqrt{D}} e^{-j\pi\xi^2/\lambda D}, \tag{3.22}$$

so that $g(\xi)$ is a cylindrically diverging wave of radius D, as shown in Figure 3.5. Light from the point source is therefore *dispersed* spatially as it propagates through free space. The magnitude of the wave at plane P_2 is uniform, whereas the phase is quadratic in ξ. The phase is proportional to the optical path difference between the wavefront and plane P_2, as a function of the coordinate ξ. As $D \to \infty$, the magnitude of $g(\xi)$ tends to zero while its phase approximates that of a plane wave.

As another example, suppose that the sample is centered at $x = x_0$ so that $f(x) = \delta(x - x_0)$. We again use the sifting property of the delta function to find that

$$g(\xi) = \frac{1}{\sqrt{D}} e^{-j(\pi/\lambda D)(\xi - x_0)^2} \tag{3.23}$$

This result represents a diverging cylindrical wave of radius D, translated

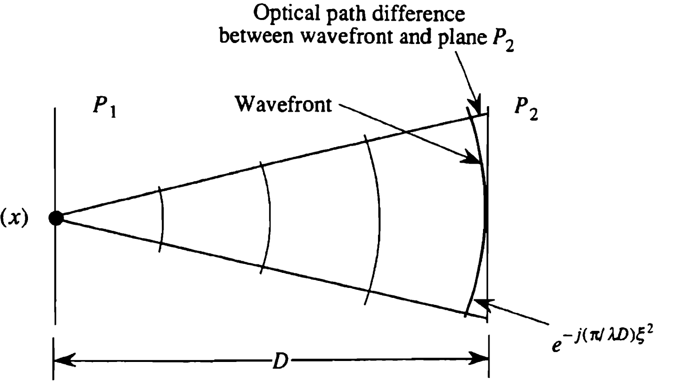
Optical path difference
between wavefront and plane P_2
P_1
Wavefront
P_2
$\delta(x)$
$e^{-j(\pi/\lambda D)\xi^2}$
D

Figure 3.5. Spherical waves propagating from a point source.

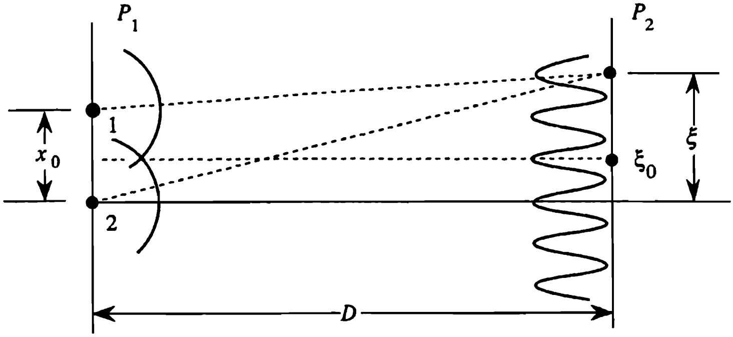

Figure 3.6. One-dimensional representation of the two-source geometry.

a distance x_0 in the x direction throughout the space from P_1 to P_2. Therefore, if an arbitrary signal $f(x)$ is displaced a distance x_0 in plane P_1 of Figure 3.5, so too is its Fresnel transform $g(\xi)$ displaced a distance x_0 in plane P_2.

3.2.2. Diffraction by Two Sources

Figure 3.6 shows two light sources at plane P_1, separated by a distance x_0. The light amplitude at plane P_2, due to the two sources when they are in phase, is given by Equations (3.22) and (3.23):

$$g(\xi) = C_0 e^{-j(\pi/\lambda D)\xi^2} + C_1 e^{-j(\pi/\lambda D)(\xi - x_0)^2}, \tag{3.24}$$

where C_0 and C_1 are the magnitudes of the waves at plane P_2 due to the two sources. The observable quantity at plane P_2 is the intensity of light:

$$\begin{aligned} I(\xi) &= g(\xi)g^*(\xi) = |g(\xi)|^2 \\ &= C_0^2 + C_1^2 + 2\,\mathrm{Re}\left[C_0 C_1 e^{-j(\pi/\lambda D)\xi^2} e^{+j(\pi/\lambda D)(\xi - x_0)^2}\right] \\ &= C_0^2 + C_1^2 + 2C_0C_1 \cos\left[\frac{2\pi}{\lambda D} x_0 \xi - \frac{\pi}{\lambda D} x_0^2\right]. \end{aligned} \tag{3.25}$$

The first two terms of $I(\xi)$ are intensities produced by the individual sources; their sum is a spatially uniform intensity called the *bias*. The third term, a spatially varying cosine distribution called the *fringe pattern*, has a *spatial frequency* α given by the partial derivative of the phase with respect to the spatial variable ξ:

$$\alpha = \frac{1}{2\pi}\frac{\partial}{\partial \xi}\left(\frac{2\pi}{\lambda D}x_0\xi\right) = \frac{x_0}{\lambda D}. \tag{3.26}$$

The spatial frequency of the fringe pattern therefore increases as the separation x_0 between the sources increases and as the observation distance D decreases. Note that the ratio x_0/D is simply the angular size of the entire source as seen from the receiving screen.

The phase of the fringe pattern is also given by Equation (3.25):

$$\varphi = -\frac{\pi x_0^2}{\lambda D}. \tag{3.27}$$

The physical interpretation of the phase is that it specifies the position of the maximum intensity in the observation plane. The *principal maximum* occurs where the argument of the cosine is equal to zero, i.e., where $2\pi\xi x_0/\lambda D - \pi x_0^2/\lambda D = 0$. The principal maximum therefore occurs at $\xi_0 = x_0/2$, which is directly opposite the midpoint between the two sources, as shown in Figure 3.6. Other intensity maxima occur where the phase is an integer multiple of 2π. If the light from the two sources have arbitrary phases ϕ_0 and ϕ_1, the entire fringe pattern at plane P_2 is shifted according to the phase difference, $\phi_1 - \phi_0$, and the principal maximum moves to

$$\xi_1 = \frac{x_0}{2} - \frac{\phi_1 - \phi_0}{2\pi x_0/\lambda D}. \tag{3.28}$$

The variation of the fringe intensity is measured by the *fringe visibility*:

$$\boxed{V = \frac{I_{\max} - I_{\min}}{I_{\max} + I_{\min}} = \frac{2C_0C_1}{C_0^2 + C_1^2}.} \tag{3.29}$$

We see that visibility is not a function of the phase difference between the two sources and that maximum fringe visibility is achieved when the two sources have equal magnitudes.

3.2.3. Fresnel Zones, Chirp Functions, and Holography

Suppose that we add a plane-wave *reference beam* to a unit magnitude wave produced by a sample function as shown in Figure 3.7(a). The plane wave, which may be thought of as the limiting form of $\exp(-j\pi\xi^2/\lambda D)$ as $D \to \infty$, is also assigned unit magnitude. The intensity at plane P_2 due to the sum of the reference and signal waves is

$$\begin{aligned} I(\xi) = |g(\xi)|^2 &= |1 + e^{-j\pi\xi^2/\lambda D}|^2 \\ &= 2\left[1 + \cos(\pi\xi^2/\lambda D)\right]. \end{aligned} \tag{3.30}$$

This fringe pattern is generally called a *Fresnel zone pattern*, as shown in Figure 3.7(b). The first intensity maximum occurs at $\xi = 0$, a point at plane P_2 directly opposite the source at plane P_1. The first minimum occurs where $\pi\xi^2/\lambda D = \pi$ or at $\xi_0 = \sqrt{\lambda D}$. Successive nulls occur when

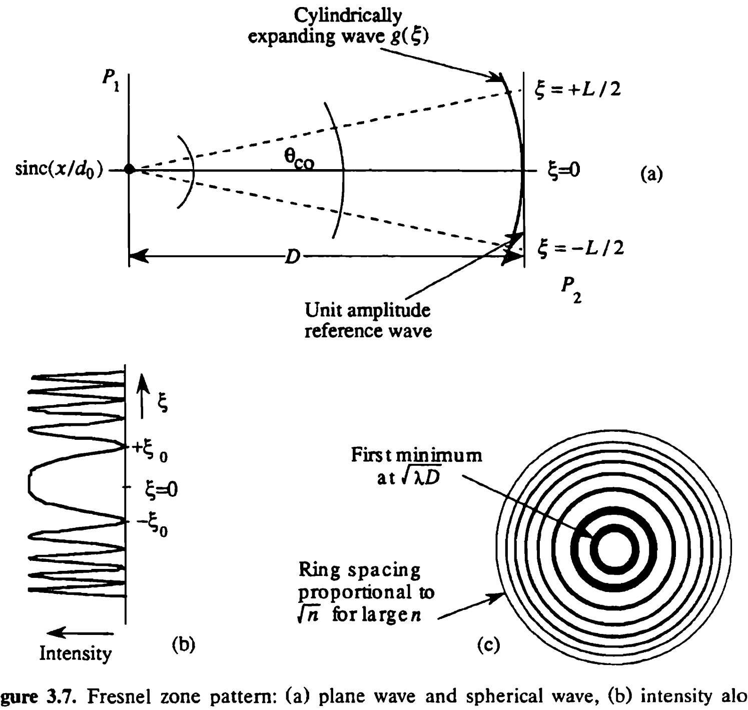
Cylindrically expanding wave $g(\xi)$
P_1
sinc(x/d_0)
θ_{co}
$\xi = +L/2$
$\xi=0$
(a)
$\xi = -L/2$
D
P_2
Unit amplitude reference wave
ξ
$+\xi_0$
$\xi=0$
$-\xi_0$
Intensity
(b)
First minimum at $\sqrt{\lambda D}$
Ring spacing proportional to $\sqrt{n}$ for large n
(c)

Figure 3.7. Fresnel zone pattern: (a) plane wave and spherical wave, (b) intensity along a radial line, and (c) two-dimensional fringes.

$\pi\xi^2/\lambda D = (2n+1)\pi$ or at $\xi = \sqrt{(2n+1)\lambda D}$, where $n = 0, 1, 2, \ldots$ For large values of n, the nulls are spaced according to $\sqrt{n}$ so that the areas of the rings approach a constant as shown in Figure 3.7(c) for the two-dimensional case.

The spatial frequency is low at the center of the pattern, as shown in Figure 3.7(b), and increases at increasing distances from the center. The spatial frequency of the Fresnel zone pattern along a horizontal line is

$$\alpha = \frac{1}{2\pi}\frac{\partial}{\partial\xi}\left[\frac{\pi\xi^2}{\lambda D}\right] = \frac{1}{2\pi}\left[\frac{2\pi\xi}{\lambda D}\right] = \frac{\xi}{\lambda D}, \tag{3.31}$$

from which we see that the spatial frequency is a linear function of the position variable ξ at plane P_2. Because the spatial frequency increases linearly as the distance increases from the origin, the Fresnel zone pattern is called a *chirp function* in signal processing. From Equation (3.31), we see that the slope of the chirp function is $1/\lambda D$, so that a small value of D implies a more rapid change in spatial frequency as a function of spatial position. The slope is called the *chirp rate* and is expressed in Ab/mm.

From Equation (3.31), we see that the highest spatial frequency occurs at the point $\xi_{\text{max}} = L/2$. The maximum spatial frequency is therefore $\alpha_{\text{co}} = L/2\lambda D$, where L is the total length of the chirp at plane P_2. In Chapter 2 we defined the length bandwidth product as LBP $= L\alpha_{\text{co}}$, so that the length bandwidth product of the chirp is

$$\text{LBP} = L\alpha_{\text{co}} = L\left[\frac{\xi_{\text{max}}}{\lambda D}\right] = \frac{L^2}{2\lambda D}. \tag{3.32}$$

From the Nyquist sampling theorem, we know that the number of samples needed to accurately represent the chirp function is equal to twice the length bandwidth product:

$$\boxed{N = 2\text{LBP} = \frac{L^2}{\lambda D}.} \tag{3.33}$$

This important relationship relates the values of LBP and N to the purely geometrical properties of the chirp; we use this result frequently in subsequent developments.

We also relate the chirp function to θ_{co}, the maximum ray angle produced by diffraction from the sample function whose form is $\text{sinc}(x/d_0)$. Again, we use the important fact that a spatial frequency is associated with every ray angle; in particular, the highest spatial frequency α_{co} associated with the cutoff ray angle θ_{co} does not change as the wave propagates. From Equation (3.31), we find that $\alpha_{co} = L/2\lambda D$ and, from Figure 3.7(a), that $\theta_{co} = L/2D$, so that

$$\boxed{\alpha_{co} = \frac{\theta_{co}}{\lambda} = \frac{1}{2d_0},} \tag{3.34}$$

as we established in Chapter 2 by appealing to purely geometric arguments. This curious result shows that the maximum spatial frequency of a chirp at *all* planes from P_1 to P_2 is α_{co}. As a direct consequence, the sample spacing d_0 is also constant for all planes.

The number of samples needed to describe the chirp is $N = L/d_0$, where L is the length of the chirp waveform at an arbitrary plane. The value of N is therefore a function of the propagation distance D, a result that is easily seen by noting that $L = 2\theta_{co}D$. Only one sample is needed to characterize the chirp at plane P_1, whereas many samples are required when D is large. This result seems to conflict, at first, with the notion that the value of N and the optical invariant are connected by $N = 4J/\lambda$. But the optical invariant applies only to *conjugate image planes*, a condition not satisfied here.

The Fresnel zone pattern is fundamental to holography in which the magnitudes of diverging wavefronts caused by secondary scattering samples from a signal are added together and combined with a reference beam. Gabor originally conceived holography as a way to correct the aberrations of an electron beam microscope (19). He recognized that a two-dimensional interference pattern represented by the Fresnel zone, as shown in Figure 3.7(c), contains information about the position of the object sample in three-dimensional space. Because an arbitrary signal consists of many such samples, it should be possible to record the information on film so that the image could be reconstructed at visible wavelengths after the aberrations were corrected. The basic problem with the Gabor hologram, however, is that using a reference beam colinear with the signal beam does not allow the signal beam to be cleanly reconstructed because the desired information spatially overlaps other terms, such as the bias.

In the early 1960's, Leith and Upatnieks demonstrated the benefits of using an off-axis reference wavefront (20). Figure 3.8 shows an arrange-

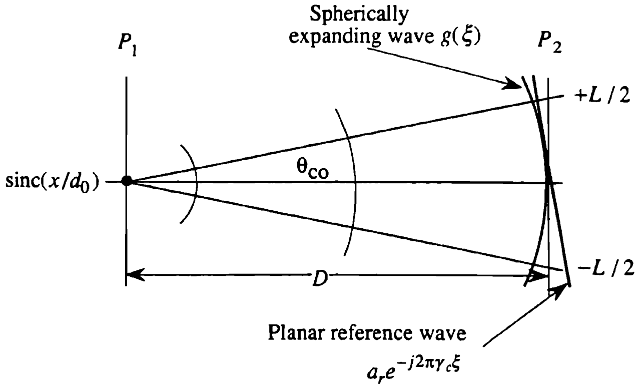

Figure 3.8. Setup for constructing an off-axis hologram.

ment for recording the simplest possible off-axis hologram, a one-dimensional sample of the form sinc(x/d_0). This arrangement is similar to that shown in Figure 3.7, except that the reference wave, represented by $r(\xi) = a_r \exp(-j2\pi\gamma_c\xi)$, now propagates upward and to the right. The signal waveform is represented by $g(\xi) = a_s \exp[-j\pi\xi^2/\lambda D]$ so that the intensity at plane P_2 is

$$\begin{aligned} I(\xi) &= \left| a_r e^{-j2\pi\gamma_c\xi} + a_s e^{-j(\pi/\lambda D)\xi^2} \right|^2 \\ &= a_r^2 + a_s^2 + 2a_r a_s \operatorname{Re}\left[e^{-j2\pi\gamma_c\xi} e^{+j(\pi/\lambda D)\xi^2} \right] \\ &= a_r^2 + a_s^2 + 2a_r a_s \cos\left[2\pi\gamma_c\xi - \frac{\pi}{\lambda D}\xi^2 \right]. \end{aligned} \tag{3.35}$$

The hologram is recorded by illuminating a photosensitive medium, such as photographic film, for a time t_0; the *exposure* is defined as $E(\xi) \equiv t_0 I(\xi)$.

The hologram is reconstructed by illuminating it with a replica of the reference beam; this beam is now called the *reconstruction beam*, as shown in Figure 3.9. If the hologram is recorded so that its amplitude transmittance is linearly proportional to $E(\xi)$, the total amplitude to the right of the hologram is $h(\xi) = t_0 r(\xi) I(\xi)$. The nature of the three wavefronts released from the hologram becomes evident when we expand the cosine

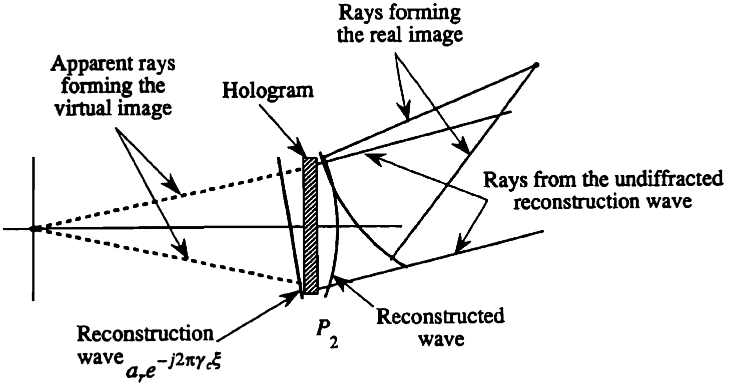
Rays forming the real image
Apparent rays forming the virtual image
Hologram
Rays from the undiffracted reconstruction wave
Reconstruction wave $a_r e^{-j2\pi\gamma_c\xi}$
P_2
Reconstructed wave

Figure 3.9. Setup for reconstructing an off-axis hologram.

in Equation (3.35) using the Euler formula:

$$\begin{aligned} h(\xi) &= t_0 a_r e^{-j2\pi\gamma_c\xi}\Big[a_r^2 + a_s^2 + a_r a_s e^{j2\pi\gamma_c\xi} e^{-j(\pi/\lambda D)\xi^2} \\ &\qquad + a_r a_s e^{-j2\pi\gamma_c\xi} e^{+j(\pi/\lambda D)\xi^2}\Big] \\ &= t_0 a_r\left(a_r^2 + a_s^2\right) e^{-j2\pi\gamma_c\xi} + t_0 a_r^2 a_s e^{-j(\pi/\lambda D)\xi^2} \\ &\quad + t_0 a_r^2 a_s e^{-j4\pi\gamma_c\xi} e^{+j(\pi/\lambda D)\xi^2} \end{aligned} \tag{3.36}$$

The first term of Equation (3.36) is simply the reconstruction beam which continues to propagate upward and to the right, with some attenuation as introduced by the hologram. The second term of Equation (3.36) has the same form as the original signal beam and it propagates to the right of the hologram as though it had never been intercepted. This wavefront produces a *virtual image* whose apparent position, as seen from the right of the hologram, is that of the original signal; the rays associated with this image are shown dashed in Figure 3.9. The last term of Equation (3.36) represents a wave, propagating toward the right at twice the reconstruction beam angle, whose spherical phase factor has a positive sign produced by the conjugation operation. This *conjugate* wavefront represents a convergent wave that forms a *real image* of the original signal as shown by the solid rays. At some distance to the right of the hologram, the three beams no longer overlap, thus producing a clean reconstruction of the signal.

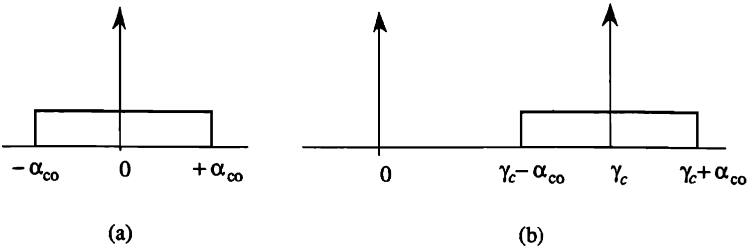

Figure 3.10. Spatial frequencies of (a) a Gabor hologram and (b) a Leith-Upatnieks hologram.

An off-axis hologram requires more spatial frequency response from the recorded hologram. In Figure 3.10(a), we see that the frequency response of a Gabor hologram ranges from zero to α_{co}. In a Leith-Upatnieks hologram, the off-axis reference beam shifts the frequency range from baseband to a bandpass region, as shown in Figure 3.10(b), with γ_c as the center frequency. The frequency range is therefore from $\gamma_c - \alpha_{co}$ to $\gamma_c + \alpha_{co}$. If the signal subtends a large angle, the center frequency required of the hologram is correspondingly large because γ_c must be proportional to the angle subtended by the object.

From Equation (3.35) we see that all the information about the point signal is encoded in the hologram by using a combination of magnitude, frequency, and phase modulation. If the signal contains several samples, each sample produces its own Fresnel zone pattern at the hologram plane. The amplitude responses of each sample are added at the plane of the hologram by the principle of superposition. The hologram reconstruction distinguishes each sample *position* because its associated spatial frequency shifts upward or downward, within the passband, according to whether the sample produces a larger or smaller angle with respect to the reference beam. Three-dimensional signals are recorded by encoding the *distance* of the samples from the hologram through phase modulation of the type shown in Equation (3.35). Finally, we do not require a planar reference wave; holograms can be recorded under a wide range of geometrical conditions. The interested reader can consult one of several books on holography for more details (21–23).

The values of the spatial frequencies associated with the exact Fresnel transform, when the higher-order terms in the expansion of the radius vector r are retained, differ somewhat with the approximate result obtained so far. The difference arises because of the approximations in the expansion for the ray length r as given by Equation (3.17); the approximate form is

$$r \cong D\left[1 + \frac{(x-\xi)^2}{2D^2}\right], \tag{3.37}$$

but the exact form is

$$r = \sqrt{D^2 + (x-\xi)^2} \tag{3.38}$$

As the value of the spatial frequency is dependent only on the ray angle and is independent of x, we set x equal to zero for convenience. The exact frequency is therefore

$$\alpha = \frac{1}{2\pi}\frac{\partial}{\partial\xi}\left[\frac{2\pi}{\lambda}\sqrt{D^2+\xi^2}\right] = \frac{\xi}{\lambda D}\left[1 + \frac{\xi^2}{D^2}\right]^{-1/2} \tag{3.39}$$

so that the approximate spatial frequency value $\alpha = \xi/\lambda D$ must be divided by a correction factor $(1 + \xi^2/D^2)^{1/2}$ to obtain the exact spatial frequency value. Recall that $\alpha_{co} = 1/(2d_0) = 1/(6\lambda)$ for the case where $d_0 = 3\lambda$. In this event, the maximum error in frequency is 1.4% at α_{co}. In most signal-processing systems we find that $d_0 \approx 10\lambda$, for which the maximum frequency error is of the order of 0.5%. The difference between the approximate and the exact solution therefore is often of little consequence in most signal processing applications.

In holography, however, the ray angles between the signal and reference beams can sometimes approach 90°. From the exact solution, we find that the maximum spatial frequency, as $\xi \to \infty$, is bounded by $\alpha = 1/\lambda$. In contrast, the approximate solution for r leads to a spatial frequency that goes to infinity as $\xi \to \infty$. This difference between the exact and approximate spatial frequency is important when calculating Fresnel transforms on a digital computer, because the Fresnel kernel as given by Equation (3.20) will produce alias frequencies if the approximate solution is used, no matter how small the sample interval at the input. When using the exact solution, the Fresnel kernel will not alias, provided that the input signal is sampled with $d_0 \leq \lambda/2$.

3.2.4. The Fresnel Transform of a Slit

Consider the Fresnel transform of a slit of length L, shown in Figure 3.11, and represented by $f(x) = \text{rect}(x/L)$. The Fresnel transform at plane

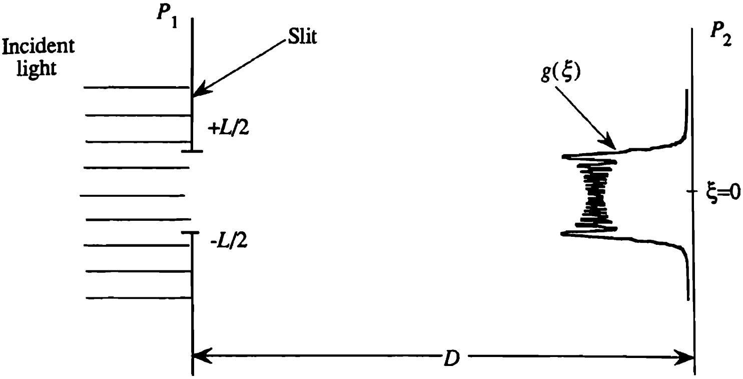

Figure 3.11. Fresnel diffraction by a slit.

P_2 is

$$\begin{aligned} g(\xi) &= \sqrt{\frac{jI_0}{\lambda D}} \int_{-\infty}^{\infty} f(x) e^{-j(\pi/\lambda D)(x-\xi)^2}\,dx \\ &= \sqrt{\frac{jI_0}{\lambda D}} \int_{-\infty}^{\infty} \operatorname{rect}\left(\frac{x}{L}\right) e^{-j(\pi/\lambda D)(x-\xi)^2}\,dx \\ &= \sqrt{\frac{jI_0}{\lambda D}} \int_{-L/2}^{L/2} e^{-j(\pi/\lambda D)(x-\xi)^2}\,dx, \end{aligned} \tag{3.40}$$

where I_0 is the intensity at $x = 0$ at plane P_1. By a change of variables in which $x - \xi = \sqrt{\lambda D/2}\,z$, the differential becomes $dx = \sqrt{\lambda D/2}\,dz$ and the upper and lower limits become

$$\begin{aligned} z_2 &= \sqrt{2/\lambda D}\,(L/2 - \xi), \\ z_1 &= \sqrt{2/\lambda D}\,(-L/2 - \xi). \end{aligned} \tag{3.41}$$

With this change of variables, Equation (3.40) becomes

$$g(\xi) = \sqrt{\frac{jI_0}{2}} \int_{z_1}^{z_2} e^{-j\pi z^2/2}\,dz, \tag{3.42}$$

which is, aside from the scale factor, in the standard form of a Fresnel *integral.*

To examine the Fresnel integral in more detail, we apply the Euler relationship to the exponential to find that

$$g(\xi) = \sqrt{\frac{jI_0}{2}}\left[\int_{z_1}^{z_2}\cos\left(\frac{\pi z^2}{2}\right)dz - j\int_{z_1}^{z_2}\sin\left(\frac{\pi z^2}{2}\right)dz\right], \quad (3.43)$$

which are related to the cosine and sine Fresnel integrals. The definitions of the *Fresnel cosine and sine integrals* are that

$$C(z) \equiv \int_0^z \cos(\pi u^2/2)\,du, \quad (3.44)$$

and

$$S(z) \equiv \int_0^z \sin(\pi u^2/2)\,du. \quad (3.45)$$

Neither $C(z)$ nor $S(z)$ can be solved in closed form. For numerical calculations, the Fresnel sine and cosine integrals are approximated by the relationships that

$$C(z) = \tfrac{1}{2} + f(z)\sin\left(\frac{\pi}{2}z^2\right) - g(z)\cos\left(\frac{\pi}{2}z^2\right) \quad (3.46)$$

and

$$S(z) = \tfrac{1}{2} - f(z)\cos\left(\frac{\pi}{2}z^2\right) - g(z)\sin\left(\frac{\pi}{2}z^2\right), \quad (3.47)$$

where we use the rational approximations that (24)

$$f(z) = \frac{1 + 0.926z}{2 + 1.792z + 3.104z^2} + \varepsilon(z); \qquad |\varepsilon(z)| \le 2(10^{-3}) \quad (3.48)$$

and

$$g(z) = \frac{1}{2 + 4.142z + 3.492z^2 + 6.670z^3} + \varepsilon(z);$$
$$|\varepsilon(z)| \le 2(10^{-3}). \quad (3.49)$$

The error $\varepsilon(z)$ in these approximations is small and the rational approximations are much easier and faster to compute than the integrals given by Equation (3.44) or Equation (3.45). The rational approximations are valid

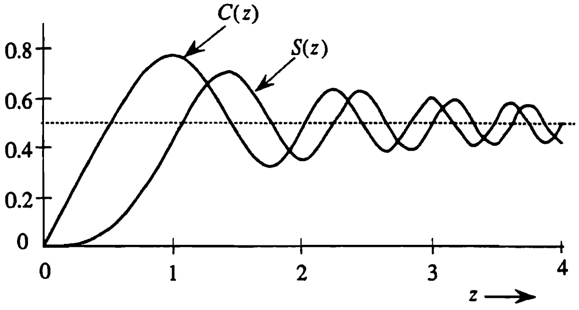

Figure 3.12. Fresnel sine and cosine integrals: $C(z)$ and $S(z)$.

only for positive values of z; and the symmetry relationships for $C(z)$ and $S(z)$ provide the values for all z. The Fresnel sine and cosine integrals are plotted in Figure 3.12. The oscillatory behavior of both functions is obvious and, for large values of z, both functions are asymptotically equal to $\frac{1}{2}$.

One way to better understand the Fresnel integral is through the use of the Cornu spiral, as shown in Figure 3.13. The *Cornu spiral* is a plot of the

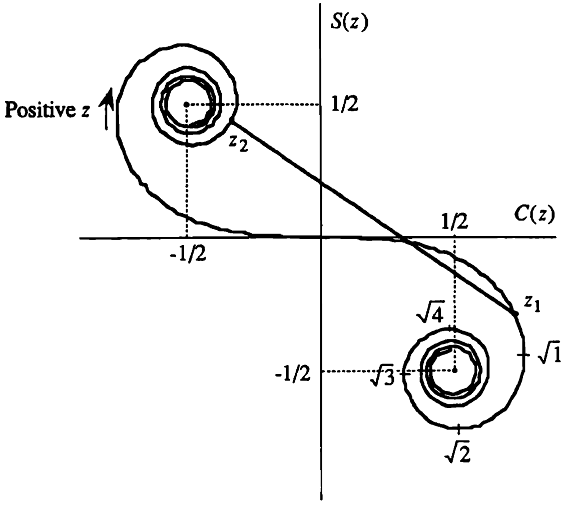

Figure 3.13. Cornu spiral.

real part of the Fresnel integral from Equation (3.43) on the horizontal axis and the imaginary part on the vertical axis; this is equivalent to the parametric plotting of $S(z)$ as a function of $C(z)$. Because the exponential factor in Equation (3.42) is negative as a result of our fundamental sign convention, the Cornu spiral must lie in the second and fourth quadrants. The parameters z_1 and z_2 represent points on the spiral and $z_{12} = z_2 - z_1$ is a measure along the arc of the spiral.

A tangent to the Cornu spiral has zero slope when

$$\frac{\partial}{\partial z}S(z) = \frac{\partial}{\partial z}\left[\int_0^z \sin\left(\frac{\pi u^2}{2}\right) du\right] = \sin\left(\frac{\pi z^2}{2}\right) = 0, \qquad (3.50)$$

from which we conclude that $\pi z^2/2 = n\pi$ so that $z = 0, \sqrt{2}, \sqrt{4}, \ldots$ are the horizontal tangent points. In a similar fashion, the tangent has infinite slope when

$$\frac{\partial}{\partial z}C(z) = \frac{\partial}{\partial z}\left[\int_0^z \cos\left(\frac{\pi u^2}{2}\right) du\right] = \cos\left(\frac{\pi z^2}{2}\right) = 0, \qquad (3.51)$$

so that the vertical tangent points occur when $z = \sqrt{1}, \sqrt{3}, \sqrt{5}, \ldots$ Thus, we see that the quarter turning points on the Cornu spiral occur when the values of the parameter z are the square roots of successive integers.

The parameters z_2 and z_1 represent normalized distances at plane P_1 from a perpendicular line that intersects plane P_2 at the point of observation to the edges of the slit, as shown in Figure 3.14. When the observation point is at a large value of ξ, both z_1 and z_2 are large in magnitude. Depending on the sign of ξ, the line length z_{12} shown in Figure 3.13 is tightly wrapped into one end or the other of the spiral; and the intensity of the Fresnel transform is low.

Suppose that the observation point is initially at $\xi = +\infty$, where the intensity is low. As the observation point moves toward $\xi = 0$, a point is reached when $z_1 = 0$ and $z_2 = -\sqrt{2/\lambda D}\,L$. The intensity in this region increases rapidly because it is the transition region from the geometric shadow to the clear aperture region. As the observation point moves to where $z_2 = 0$, we transition back into the shadow region at the side of the slit where $\xi = -L/2$.

Suppose that the slit is infinitely long so that $L \to \infty$. In this case, $z_1 = \infty$ and $z_2 = -\infty$ and the ends of the vector are located at the centers of each end of the spiral. From the Cornu spiral, we find that the magnitudes of Equations (3.44) and (3.45) are equal to $\sqrt{2}/2$, and the phase of the vector is given by $\exp[-j\pi/4]$. The complex amplitude at

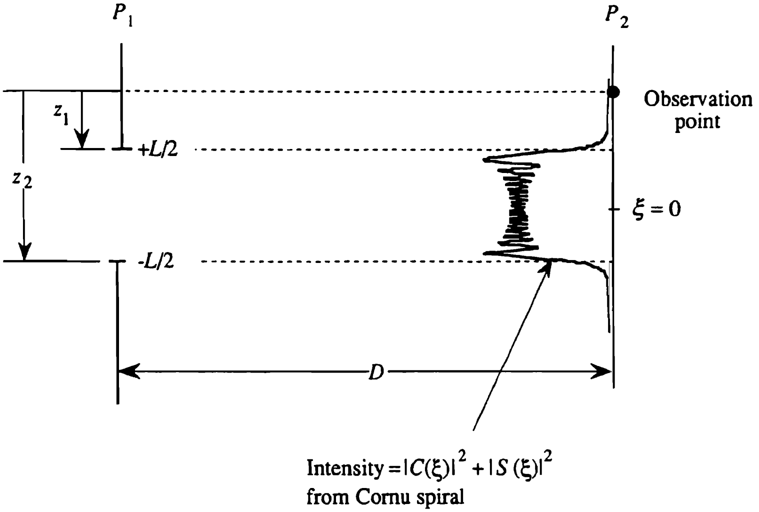

Figure 3.14. Intensity pattern produced by diffraction from a slit.

$\xi = 0$ is therefore

$$g(\xi) = \sqrt{\frac{jI_0}{2}}\left[\sqrt{2}e^{-j\pi/4}\right]$$
$$= \sqrt{\frac{I_0}{2}}\,e^{+j\pi/4}\left[\sqrt{2}e^{-j\pi/4}\right] = \sqrt{I_0}, \qquad (3.52)$$

so that the magnitude is exactly the same at plane P_2 as it is at plane P_1 and intensity is equal to I_0 as expected. From Equation (3.52) we see that the $\exp[-j\pi/4]$ phase factor from the calculation of the Fresnel integral exactly cancels the $\sqrt{j}$ factor from Equation (3.19) that Fresnel included at the onset; the Fresnel transform therefore predicts accurately both the magnitude and the phase of the propagating diffraction pattern.

The key information regarding the behavior of the Fresnel integral is in the limits of integration, because they characterize the transitions into and out of the shadow regions. When $|z_{12}|$ is large, the contributions to the Fresnel integral from the two edges do not interfere and the distance between the half-magnitude points in the Fresnel transform is nearly the same as the slit length. But if $|z_{12}|$ is small so that the slit is narrow, contributions from the two edges interfere with each other. The result is a diffraction pattern that spreads over larger distances at plane P_2.

As an example of using the Cornu spiral to calculate the intensity at a given point in the Fresnel pattern, suppose that z_1 is at $+\infty$. At plane P_2 the intensity is

$$I(\xi) = \frac{I_0}{2}|g(\xi)|^2 = \frac{I_0}{2}|C(\xi) + jS(\xi)|^2$$
$$= \frac{I_0}{2}\left[|C(\xi)|^2 + |S(\xi)|^2\right]. \tag{3.53}$$

The maximum intensity occurs when the vector connecting two points on the Cornu spiral has its largest magnitude. This condition occurs when z_2 is about halfway between the first horizontal and vertical turning points, say at $z_2 = [\sqrt{1} + \sqrt{2}]/2 \approx 1.22$. From tables of the Fresnel transforms (24) we find that $C(1.22) = -0.7021$ and $S(1.22) = 0.6383$. Also, for $z_1 = \infty$, we have $C(\infty) = -0.5$ and $S(\infty) = 0.5$. The maximum intensity is

$$I_{\text{max}} = \frac{I_0}{2}\left[(-0.5 - 0.7021)^2 + (0.5 + 0.6383)^2\right] = \frac{2.74 I_0}{2} = 1.37 I_0. \tag{3.54}$$

The intensity at this point is therefore 37% larger than if the slit were not present. To find the physical coordinate at which the intensity is a maximum, recall that z_2 is measured in units of $\sqrt{2/\lambda D}[L/2 - \xi]$. For the example at hand, the distance from the edge of the half-plane

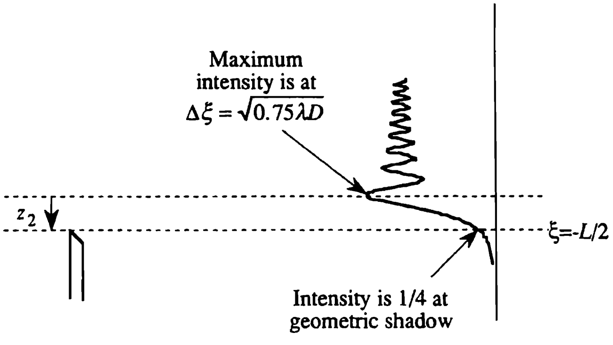
Maximum intensity is at
$\Delta\xi = \sqrt{0.75\lambda D}$
z_2
ξ=-L/2
Intensity is 1/4 at geometric shadow

Figure 3.15. Diffraction produced by a half-plane aperture.

slit to the intensity maximum is $\Delta\xi = [-L/2 - \xi] = z_1\sqrt{\lambda D/2}$. For $z_2 = 1.22$, the maximum intensity is located about $\sqrt{0.75\lambda D}$ units away from the geometric shadow of the edge. The resulting intensity pattern is sketched in Figure 3.15.

3.3. THE FOURIER TRANSFORM

The Fourier transform is a widely used tool in the physical sciences for signal analysis. Its principal value is that it generates a function that displays the frequency content of a signal. As a result, certain signal features are more easily analyzed or detected in the frequency domain than in the spatial domain. For example, the presence of a weak sinusoidal signal may be masked by noise in the spatial domain. In the frequency domain, however, this signal component may be easily detected because all the signal energy is concentrated at one frequency, but the noise energy remains spread over the bandwidth of the total signal. In other applications, signals are characterized by a combination of spectral components —they have a "signature" or a "fingerprint" that is more easily detected in the frequency domain than in the time or space domains.

3.3.1. The Fourier Transform of a Periodic Function

The Fourier transform has its roots in a method used by Fourier to represent a periodic signal by a set of weighted sinusoidal components. The basic idea is that if $f(x)$ is a periodic signal so that $f(x + L) = f(x)$, where L is the period of the signal, the frequency content is revealed if we expand $f(x)$ into a series of the form

$$f(x) = a_0 + \sum_{n=1}^{\infty} [a_n \cos(2\pi nx/L) + b_n \sin(2\pi nx/L)], \quad (3.55)$$

which is known as a *Fourier series*. The coefficients a_n and b_n are obtained by multiplying both sides of Equation (3.55) by $\cos(2\pi nx/L)$ or $\sin(2\pi nx/L)$ and integrating the products over one period of the signal $f(x)$. This method leads directly to expressions for the coefficients because the cosine and sine functions are orthogonal. We find that

$$a_n = \frac{2}{L}\int_c^{c+L} f(x)\cos\left(\frac{2\pi nx}{L}\right) dx \quad (3.56)$$

and

$$b_n = \frac{2}{L}\int_c^{c+L} f(x)\sin\left(\frac{2\pi nx}{L}\right) dx, \tag{3.57}$$

where c is an arbitrary starting point for the integration. The value of a_0 is given by Equation (3.56) with $n = 0$, but the coefficient is halved. From Equation (3.56), it is clear that a_0 gives the average value of $f(x)$. We identify $\alpha_0 = 1/L$ as the fundamental spatial frequency whose dimensions are reciprocal to those of L. As n increases, we obtain the coefficients a_n and b_n associated with the harmonics of α_0.

3.3.2. The Fourier Transform for Nonperiodic Signals

If the period of the signal $f(x)$ becomes large or if $f(x)$ is not periodic, we must develop alternatives to the Fourier-series representation of a signal. One alternative is to induce periodicity by replicating $f(x)$ at regular intervals and to proceed with the frequency decomposition as described above. The other alternative is to extend the basic interval L to infinity so that $\alpha_0 \to 0$ and the discrete coefficients become a continuous function of the spatial variable α. In this case, the summation becomes an integral and the discrete frequency components become the *Fourier transform* of the nonperiodic signal:

$$F(\alpha) = \int_{-\infty}^{\infty} f(x)e^{j2\pi\alpha x}\, dx, \tag{3.58}$$

and the corresponding *inverse Fourier transform* is

$$f(x) = \int_{-\infty}^{\infty} F(\alpha)e^{-j2\pi\alpha x}\, d\alpha. \tag{3.59}$$

The integral relationships of Equations (3.58) and (3.59) are called *Fourier-transform pairs*. We treat the value of the continuous transform $F(\alpha)$ as the limiting form of the weights a_n and b_n at discrete frequencies $2\pi n/L$. That is, if we integrate $|F(\alpha)|^2$ over a small interval $d\alpha$ centered at one of the discrete frequencies $2\pi n/L$, its value is equal to $(a_n^2 + b_n^2)$.

We do not venture into the mathematical subtleties of the Fourier transform nor the conditions for which it exists. As we always consider only those signals that have finite total energy, we can safely say that the Fourier transform $F(\alpha)$ of any spatial signal exists.

3.3.3. The Fourier Transform in Optics

We develop the Fourier transform in optics using the basic system shown in Figure 3.16. To simplify the mathematics, we use a one-dimensional notation to find the light distribution $F(\xi)$ at the back focal plane of the lens. To further simplify the mathematics, we place $f(x)$ at the front focal plane of the lens; the more general conditions under which the Fourier transform exists are treated in Section 3.6. We begin by recognizing that the light distribution $g(u)$ just before the lens is the Fresnel transform of $f(x)$:

$$g(u) = \sqrt{\frac{j}{\lambda F}} \int_{-\infty}^{\infty} f(x) e^{-j(\pi/\lambda F)(u-x)^2}\, dx. \tag{3.60}$$

Next, we find the amplitude $h(u)$ at plane P_3 on the other side of the lens. In Chapter 2 we showed that a lens collimates light from a point source located at its front focal plane. Because collimated light is represented as a plane wave of unit magnitude, the lens must render a cylindrically diverging wavefront, of the form $\exp(-j\pi u^2/\lambda F)$, into a wave of the form $\exp(j0) = 1$:

$$(\text{lens function}) \times e^{-j\pi u^2/\lambda F} = e^{j0} = 1, \tag{3.61}$$

from which we conclude that the lens function must be $\psi(u; K)$, as given by Equation (3.20), where $K = 1/F$ is the power of the lens. The light distribution at plane P_3, just beyond the lens, is therefore

$$h(u) = g(u) e^{j\pi u^2/\lambda F}, \tag{3.62}$$

which is the product of $g(u)$ and the lens function. The light distribution

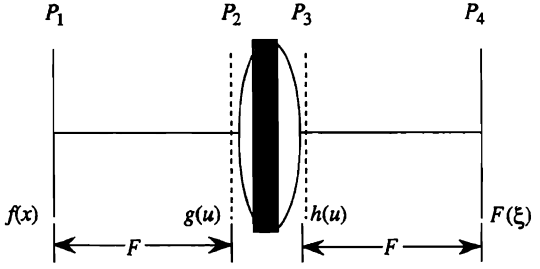

Figure 3.16. Basic Fourier-transform system.

$F(\xi)$ at plane P_4 is obtained by a second application of the Fresnel transform:

$$F(\xi) = \sqrt{\frac{j}{\lambda F}} \int_{P_3} h(u) e^{-j(\pi/\lambda F)(\xi - u)^2} du. \tag{3.63}$$

We use Equations (3.62) and (3.60) in Equation (3.63) to find that

$$F(\xi) = \sqrt{\frac{j}{\lambda F}} \int_{P_3} \left[\sqrt{\frac{j}{\lambda F}} \int_{-\infty}^{\infty} f(x) e^{-j(\pi/\lambda F)(u-x)^2} dx \right] \times e^{j\pi u^2/\lambda F} e^{-j(\pi/\lambda F)(\xi - u)^2} du. \tag{3.64}$$

We collect all the exponential terms and evaluate the resulting kernel function:

$$-j(\pi/\lambda F)\Big[\underbrace{(u-x)^2}_{\substack{\text{first}\\ \text{free space}}} - \underbrace{u^2}_{\text{lens}} + \underbrace{(\xi - u)^2}_{\substack{\text{second}\\ \text{free space}}}\Big]$$
$$= -j(\pi/\lambda F)\left[u^2 - 2u(x + \xi) + x^2 + \xi^2\right]. \tag{3.65}$$

We complete the square in the variable u, and arrange the integral in the form

$$F(\xi) = \frac{j}{\lambda F} \int_{-\infty}^{\infty} f(x) \left\{ \int_{P_3} e^{-j(\pi/\lambda F)(u - x - \xi)^2} du \right\} e^{j2\pi x\xi/\lambda F} dx. \tag{3.66}$$

We almost have the desired Fourier-transform relationship. The final step is to show that the integral in braces is not a function of x or ξ. The integral in question is a Fresnel integral:

$$Q(x, \xi) = \int_{P_3} e^{-j(\pi/\lambda F)(u - x - \xi)^2} du, \tag{3.67}$$

which is put into the standard form, similar to Equation (3.42), by a change of variables to produce

$$Q(x, \xi) = \sqrt{\frac{\lambda F}{2}} \int_{z_1}^{z_2} e^{-j\pi z^2/2} dz, \tag{3.68}$$

where $z_1 = \sqrt{2/\lambda F}[-A/2 - x - \xi]$, $z_2 = \sqrt{2/\lambda F}[A/2 - x - \xi]$ and A is the aperture of the lens. From the results of Section 3.2, we know that the most rapid change in $Q(x, \xi)$ occurs when either z_1 or z_2 approaches zero. Recall from the discussion associated with Equation (3.52) that $Q(x, \xi)$ is approximately equal to $\sqrt{\lambda F/j}$ when the magnitude of either z_1 or z_2 is greater than zero; the value of the integral settles exactly to $\sqrt{\lambda F/j}$ as the magnitudes of z_1 and z_2 become large.

To satisfy the constraint that the integral is constant, we require that $|A/2| > (x + \xi)_{\max}$. The signal $f(x)$ is limited in space to the region $|x|_{\max} < L/2$. To find the maximum value of ξ, we note that light from $f(x)$ is spread over a region equal to $\theta_{co}F$ at plane P_3 so that $\xi_{\max} = \theta_{co}F = \lambda F\alpha_{co}$, because the light is then collimated. Because the sample interval must be d_0 throughout $f(x)$, the condition under which $Q(x, \xi)$ is constant is

$$\left|\frac{A}{2}\right| \geq \left|\frac{L}{2} + \lambda F\alpha_{co}\right|. \qquad (3.69)$$

The required lens aperture is therefore a function of both the object size and its frequency content. In Sections 3.6 and 3.7 we more fully explore how finite lens apertures affect system performance. For now, we assume that Equation (3.69) is satisfied so that we can set $Q(x, \xi) = \sqrt{\lambda F/j}$ in Equation (3.66) to express $F(\xi)$ as

$$\boxed{F(\xi) = \sqrt{\frac{j}{\lambda F}} \int_{-\infty}^{\infty} f(x) e^{j2\pi x\xi/\lambda F}\, dx,} \qquad (3.70)$$

which is a Fourier transform of the signal $f(x)$ in terms of the physical coordinate ξ of the Fourier plane. To satisfy the scalar wave equation, the sign of the kernel in the *spatial* Fourier transform must be opposite to the kernel of the *temporal* Fourier transform. Note that the kernel function has a positive sign, a direct result of the sign convention we have used throughout.

If we want to emphasize that the Fourier transform is a function of the spatial frequency variable α, we express the result as

$$F(\alpha) = \int_{-\infty}^{\infty} f(x) e^{j2\pi\alpha x}\, dx, \qquad (3.71)$$

where $\xi = \lambda F\alpha$, and we generally drop the scaling constant when we use this form of the transform. The two-dimensional version of the Fourier transform, in terms of the orthogonal spatial frequencies α and β, is

$$F(\alpha,\beta) = \iint_{-\infty}^{\infty} f(x,y)e^{j2\pi(\alpha x+\beta y)}\,dx\,dy, \tag{3.72}$$

where β is the spatial frequency in the vertical direction and the vertical coordinate at the frequency plane is $\eta = \lambda F\beta$. The two-dimensional Fourier transform is obtained by a similar line of analysis and is useful in the image-processing applications treated in the following chapters.

3.4. EXAMPLES OF FOURIER TRANSFORMS

In this section we calculate the Fourier transforms of a few functions that illustrate some of the basic principles. Gaskill's book (18) is a thorough and readable discussion of the Fourier transforms of many other functions and their application in optics.

3.4.1. Fourier Transforms of Aperture Functions

Fourier transforms of aperture functions are important in applications such as spectrum analysis, which we discuss in Chapter 4. We use the *aperture function* $a(x)$ to describe the amplitude weighting due to the laser illumination and the truncation effects due to lenses or other elements in an optical system. The effective signal is then the product $a(x)f(x)$ which, by the convolution theorem, produces a Fourier transform that is the convolution of $A(\alpha)$ and $F(\alpha)$.

In the mathematical developments associated with optical signal processing, we can usually calculate integral equations in closed form if we use a uniform aperture function. We therefore examine the form of $A(\alpha)$ when $a(x) = \text{rect}(x/L)$, which represents a clear aperture of length L, centered on the optical axis. From the Fourier transform we find that

$$\begin{aligned} A(\alpha) &= \int_{-\infty}^{\infty} \text{rect}\left(\frac{x}{L}\right)e^{j2\pi\alpha x}\,dx \\ &= \int_{-L/2}^{L/2} e^{j2\pi\alpha x}\,dx \\ &= L\frac{\sin(\pi\alpha L)}{\pi\alpha L} = L\,\text{sinc}(\alpha L). \end{aligned} \tag{3.73}$$

We see that $A(\alpha)$ attains its maximum value when $\alpha = 0$, and that zeros of $A(\alpha)$ occur when the argument of the sinc function is a nonzero integer. The first zeros are at the spatial frequencies $\alpha_0 = \pm 1/L$, or at the physical distances

$$\xi_0 = \pm \frac{\lambda F}{L}. \tag{3.74}$$

From Equation (3.74) we see that the scale of the transform is inversely related to the scale of the aperture; that is, when the aperture length L is large, $A(\alpha)$ is compact because the first zero occurs at a small value of ξ. Conversely, when L is small, $A(\alpha)$ is spread over a large region in the Fourier domain. This relationship satisfies our intuitive notion that a signal with coarse or fine sample intervals has a Fourier transform that contains low or high frequencies as evidenced by the spectral spread in $A(\alpha)$.

In Chapter 1 we showed that the inverse Fourier transform of a rect(α/α_{co}) function in the spatial frequency plane produced a sample function sinc(x/d_0) in the space plane. Here we note the dual relationship: a rect(x/L) function in the space domain produces a sample function of the form sinc(αL) in the frequency plane. We use this sample function in Chapter 4 to characterize the Fourier transforms of arbitrary signals.

A Gaussian-weighted illumination beam is intrinsically produced by gas lasers and injection laser diodes. For our purposes, we define the Gaussian beam as $a(x) = \exp[-2A(x/L)^2]$ so that the intensity response at $x = \pm L/2$ is $1/e^{-A}$. We find that the Fourier transform of a Gaussian beam remains Gaussian:

$$\int_{-\infty}^{\infty} e^{-2A(x/L)^2} e^{j2\pi\alpha x}\, dx = L\sqrt{\frac{\pi}{2A}}\, e^{-(1/2A)(\pi\alpha L)^2} \tag{3.75}$$

The Gaussian function is therefore one of several that retain their functional identity under Fourier transformation. The Fourier transforms of truncated Gaussian beams cannot be calculated in closed form; several computer solutions are given in Chapter 4.

3.4.2. A Partitioned Aperture Function

Suppose that we have a partitioned aperture function of the form

$$f(x) = \begin{cases} 1; & -2.5L \le x \le -1.5L \\ 1; & +1.5L \le x \le +2.5L \\ 0; & \text{elsewhere,} \end{cases} \tag{3.76}$$

as shown in Figure 3.17(a). This function represents an optical system that has a clear aperture with a central occlusion. We can calculate the Fourier transform directly, if we so choose, but a useful trick is to note that $f(x)$ is equal to rect(x/L) convolved with $[\delta(x + 2L) + \delta(x - 2L)]$, as suggested in Figure 3.17(b). By the convolution theorem, we find that $A(\alpha)$ is equal to the product of the individual Fourier transforms of the rect function and of the delta functions. We find that

$$\int_{-\infty}^{\infty} \operatorname{rect}(x/L) e^{j2\pi\alpha x}\, dx = L \operatorname{sinc}(\alpha L), \tag{3.77}$$

and that

$$\int_{-\infty}^{\infty} [\delta(x + 2L) + \delta(x - 2L)] e^{j2\pi\alpha x}\, dx = 2\cos(4\pi\alpha L). \tag{3.78}$$

The Fourier transform of $f(x)$ is then $F(\alpha) = 2L[\operatorname{sinc}(\alpha L)]\cos(4\pi\alpha L)$, the product of a cosine function established by the delta functions and a sinc function established by the rect function. There are exactly four cycles of the cosine function under the main lobe of the sinc function, as shown in Figure 3.17(c). As the distance between the two apertures increases, the

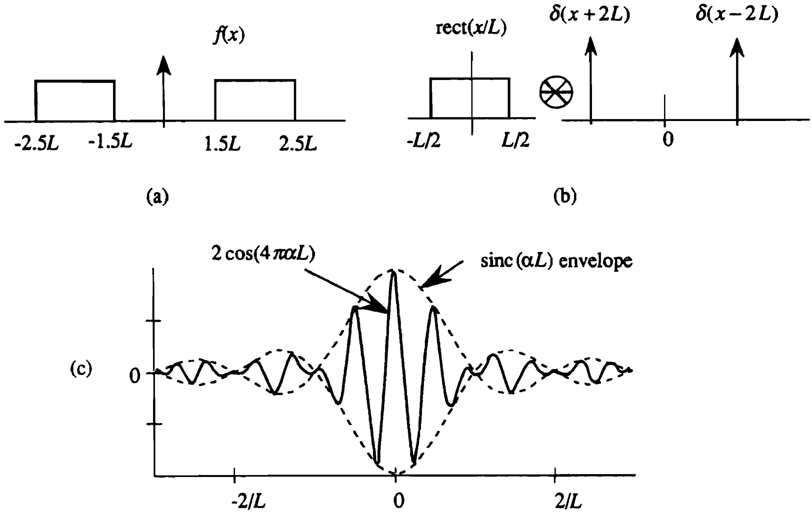

Figure 3.17. Fourier transform of a partitioned aperture: (a) the partitioned aperture, (b) an equivalent representation of the aperture, and (c) the Fourier transform.

frequency of the cosine increases so that more cycles of the cosine appear under the central lobe of the sinc function.

3.4.3. A Periodic Signal

The convolution theorem also helps to calculate Fourier transforms of a train of short pulses represented by

$$f(x) = \mathrm{rect}(x/L) * \sum_{n=-\infty}^{\infty} \delta(x - nx_0), \tag{3.79}$$

where x_0 is the separation between the pulses. The impulse train in Equation (3.79) is called a *comb function*. The Fourier transform of the comb function is

$$\begin{aligned}\int_{-\infty}^{\infty} \sum_{n=-\infty}^{\infty} \delta(x - nx_0) e^{j2\pi\alpha x}\, dx &= \sum_{n=-\infty}^{\infty} e^{j2\pi\alpha n x_0} \\ &= 2\alpha_o \sum_{n=-\infty}^{\infty} \delta(\alpha - 2n\alpha_o), \end{aligned} \tag{3.80}$$

where $\alpha_o = 1/2x_0$. We note that the Fourier transform of the comb function produces many plane waves in the Fourier domain whose phases are arranged so that the spectral distribution is also a comb function. The final result, then, is that

$$F(\alpha) = 2\alpha_o L\, \mathrm{sinc}(\alpha L) \sum_{n=-\infty}^{\infty} \delta(\alpha - 2n\alpha_o), \tag{3.81}$$

which shows that the comb function is weighted by a sinc function which is the Fourier transform of a single short pulse. In this fashion, we see that the Fourier transforms of seemingly complicated signals are found by a combination of the Fourier transforms of their component parts.

3.5. THE INVERSE FOURIER TRANSFORM

Suppose that we cascade two Fourier-transform systems of the type shown in Figure 3.16, with the second following the first, as shown in Figure 3.18. The second system generates the Fourier transform from the output of the

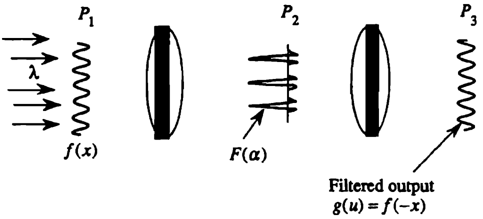

Figure 3.18. Inverse Fourier-transform system.

first system:

$$g(u) = \int_{P_2} F(\alpha) e^{j2\pi\alpha u}\, d\alpha. \tag{3.82}$$

Note that the second spatial Fourier transform also has an exponential whose sign is positive, similar to that of the forward-going transform. We use Equation (3.71) and substitute for $F(\alpha)$:

$$g(u) = \int_{P_2} \left[\int_{-\infty}^{\infty} f(x) e^{j2\pi\alpha x}\, dx \right] e^{j2\pi\alpha u}\, d\alpha. \tag{3.83}$$

If the aperture at plane P_2 does not stop any light rays, we can extend the aperture limits to infinity and perform the integration on α to find that

$$\int_{-\infty}^{\infty} e^{j2\pi\alpha(x+u)}\, d\alpha = \delta(x+u). \tag{3.84}$$

We now use the sifting property of the delta function:

$$\begin{aligned} g(u) &= \int_{-\infty}^{\infty} f(x)\delta(x+u)\, dx \\ &= f(-u), \end{aligned} \tag{3.85}$$

and we see that $g(u)$ is identical to $f(x)$ but with a reversed coordinate, as indicated by the negative sign associated with the space variable.

Space, as contrasted to time, does not have a preferred sense of direction; and geometrical optics requires *two forward-going transforms* to produce the required spatial inversion of the signal. A true "inverse transform" can, in fact, be created by using a negative focal length lens in the second of the two systems shown in Figure 3.18, but the image does not then exist anywhere in the space to the right of the lens. The true inverse transform leads to "virtual" images instead of to "real" images.

3.5.1. Bandlimited Signals

Suppose that $f(x)$ is bandlimited to spatial frequencies less than or equal to α_{co}. Furthermore, suppose that we have a frequency plane weighting function $A(\alpha) = \text{rect}[\alpha/2\alpha_m]$, where $\alpha_m \geq \alpha_{co}$. The light leaving the Fourier plane is then $F(\alpha)A(\alpha)$; and the Fourier transform of this product, by use of the convolution theorem, is

$$\boxed{\begin{aligned} g(x) &= \int_{-\infty}^{\infty} F(\alpha)A(\alpha)e^{j2\pi\alpha x}\,d\alpha \\ &= 2\alpha_m\int_{-\infty}^{\infty} f(u)\text{sinc}[2\alpha_m(x+u)]\,du \\ &= f(-x). \end{aligned}} \tag{3.86}$$

The transition from the second to the third step is made without appeal to complicated mathematical arguments because the function $A(\alpha)$ does not affect, or in any way further limit, the already bandlimited signal $f(x)$ if $\alpha_m \geq \alpha_{co}$. The general rule is this: *if we encounter a convolution between any signal $f(x)$ whose maximum frequency is equal to α_{co} and a function of the form* sinc$(2\alpha_m x)$, *we replace the* sinc *function by a delta function if* $\alpha_m \geq \alpha_{co}$. The sifting theorem is then used with confidence that the spatial frequency content of $f(x)$ has not been altered.

A function of the form $2\alpha_m\text{sinc}(2\alpha_m x)$ is, of course, a suitable form of a delta function, in the limit as $\alpha_m \to \infty$. This development shows that the conditions defining a suitable delta function are relaxed significantly when dealing with signals or systems that are bandlimited. The property of bandlimited functions as given by Equation (3.86) is used frequently in analytical developments throughout this book.

3.5.2. Rayleigh-Resolution Criterion

In our development of the Fresnel transform we ignored the obliquity factor, based on the argument that the angular spreading of light produced by a signal sample is small. We now support this conclusion and

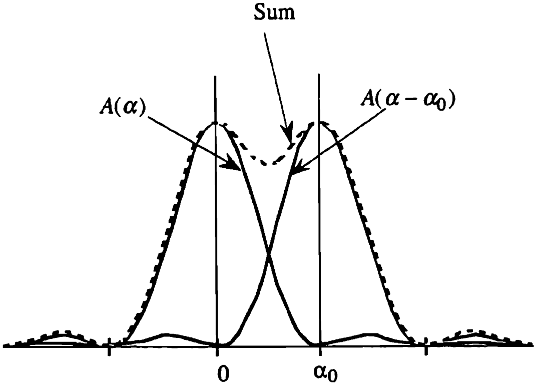

Figure 3.19. Rayleigh-resolution criterion for a sinc^{2}impulse response.

return to the Rayleigh-resolution criterion for a telescope as stated initially in Chapter 2. Suppose, for example, that $f(x) = 1$ so that the product $a(x)f(x)$ is simply $a(x)$. This situation might arise when light from a distant scene, such as an isolated star, enters a lens whose aperture function is $a(x) = \text{rect}(x/L)$. The image of the star appears at the back focal plane of the lens; thus the image is identical to the Fourier transform $A(\alpha)$ of the aperture function $a(x)$ as just derived. The equivalence of $A(\alpha)$ to the image of a star implies that the light distribution at plane P_1 of Figure 3.16 is a plane wave of infinite extent that is rendered to a finite extent by the action of $a(x)$.

The Rayleigh-resolution requirement, based on visually detecting a dip between the peaks of the two stars, is that the peak of the response due to the second star, $A(\alpha - \alpha_0)$, falls at the first zero of $A(\alpha)$, as shown in Figure 3.19. The physical distance between the peaks is $\xi_0 = d_0 = \lambda F/L$, and the angular resolution is therefore $\phi_0 = \lambda/L$, which is just equal to the difference in the angle that the wavefront has as it enters the lens.

3.5.3. Abbe's Resolution Criterion

Abbe showed that, under certain illumination conditions, false details in the image are generated if the frequency components of the signals are altered (25). He showed, by a somewhat different line of analysis from Rayleigh's, that coherently illuminated systems have a resolution limit d_0 which is related to the cutoff spatial frequency: $d_0 = 1/(2\alpha_{\text{co}})$. For example, consider the coherently illuminated optical system shown in

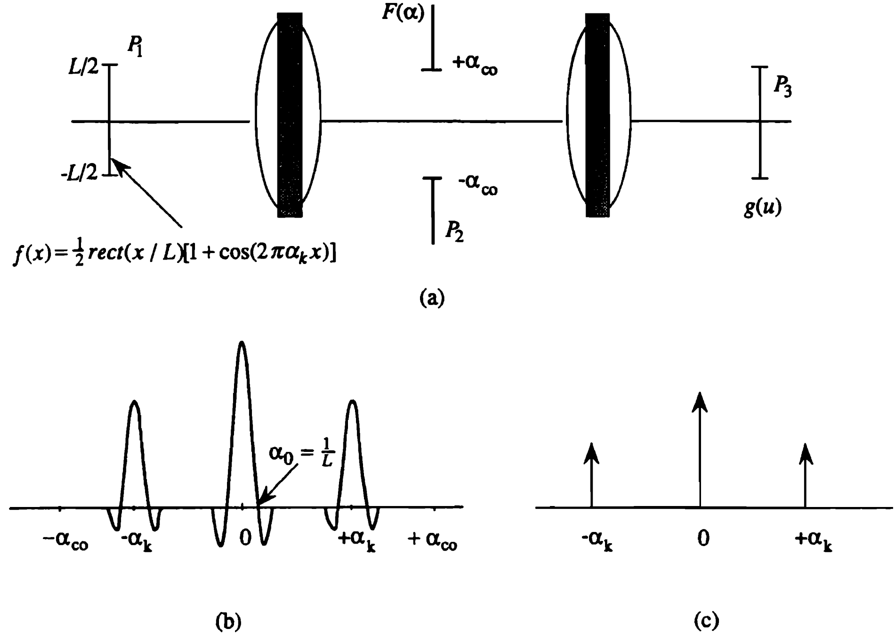

Figure 3.20. Coherently illuminated system to illustrate sharp cutoff: (a) optical system, (b) Fourier transform of a biased cosine, and (c) alternative representation of the Fourier transform.

Figure 3.20(a), in which a sinusoidal function

$$f(x) = 0.5\,\mathrm{rect}(x/L)\left[1 + \cos(2\pi\alpha_k x)\right]$$

is the input signal. The Fourier transform of $f(x)$ is

$$\begin{aligned}
F(\alpha) &= \int_{-\infty}^{\infty} f(x)e^{j2\pi\alpha x}\,dx = \int_{-L/2}^{L/2} \tfrac{1}{2}\left[1 + \cos(2\pi\alpha_k x)\right]e^{j2\pi\alpha x}\,dx \\
&= \int_{-L/2}^{L/2} \tfrac{1}{2}\left[1 + \tfrac{1}{2}e^{j2\pi\alpha_k x} + \tfrac{1}{2}e^{-j2\pi\alpha_k x}\right]e^{j2\pi\alpha x}\,dx \\
&= \int_{-L/2}^{L/2} \tfrac{1}{2}\left[e^{j2\pi\alpha x} + \tfrac{1}{2}e^{j2\pi(\alpha+\alpha_k)x} + \tfrac{1}{2}e^{j2\pi(\alpha-\alpha_k)x}\right]dx \\
&= \frac{L}{2}\left\{\mathrm{sinc}(\alpha L) + \tfrac{1}{4}\,\mathrm{sinc}\left[(\alpha+\alpha_k)L\right] + \tfrac{1}{4}\,\mathrm{sinc}\left[(\alpha-\alpha_k)L\right]\right\}, \quad (3.87)
\end{aligned}$$

where L is the length of the signal at plane P_1. As shown in Figure 3.20(b), $F(\alpha)$ consists of three sinc functions whose first zeros are at $\alpha_0 = \pm 1/L$; one sinc function is centered at $\alpha = 0$, one is centered at $\alpha = \alpha_k$, and one is centered at $\alpha = -\alpha_k$. The sinc functions are typically so much narrower than those shown in the figure that we sometimes represent them by δ functions as shown in Figure 3.20(c).

We place an aperture at plane P_2 whose extent is $\pm\alpha_{\mathrm{co}}$. If the spatial frequency is low so that $|\alpha_k| \ll \alpha_{\mathrm{co}}$, all the energy in $F(\alpha)$ passes through the aperture and the amplitude at image plane P_3 is

$$\begin{aligned} g(u) &= \int_{-\infty}^{\infty} F(\alpha) e^{j2\pi\alpha u}\, d\alpha \\ &= \int_{-\infty}^{\infty} \operatorname{rect}\left[\frac{\alpha}{2\alpha_{\mathrm{co}}}\right]\left\{\frac{L}{2}\operatorname{sinc}(\alpha L) + \frac{L}{4}\operatorname{sinc}[(\alpha+\alpha_k)L]\right. \\ &\qquad \left. + \frac{L}{4}\operatorname{sinc}[(\alpha-\alpha_k)L]\right\} e^{j2\pi\alpha u}\, d\alpha, \qquad (3.88) \end{aligned}$$

where $\operatorname{rect}[\alpha/2\alpha_{\mathrm{co}}]$ represents the frequency response of the system. The output therefore consists of three terms, a typical one being

$$g_1(u) = \int_{-\infty}^{\infty} \operatorname{rect}\left[\frac{\alpha}{2\alpha_{\mathrm{co}}}\right]\frac{L}{2}\operatorname{sinc}(\alpha L) e^{j2\pi\alpha u}\, d\alpha. \qquad (3.89)$$

The easiest way to evaluate Equation (3.89) is to recognize that if we express $\operatorname{sinc}(\alpha L)$ in terms of its Fourier transform, we have

$$g_1(u) = \int_{-\infty}^{\infty} \frac{1}{2}\left\{\operatorname{rect}\left[\frac{\alpha}{2\alpha_{\mathrm{co}}}\right]\int_{-\infty}^{\infty} \operatorname{rect}\left[\frac{x}{L}\right] e^{j2\pi\alpha x}\, dx\right\} e^{j2\pi\alpha u}\, d\alpha. \qquad (3.90)$$

We interchange the order of integration to find that

$$\begin{aligned} g_1(u) &= \int_{-\infty}^{\infty} \frac{1}{2}\operatorname{rect}\left[\frac{x}{L}\right]\left\{\int_{-\infty}^{\infty} \operatorname{rect}\left[\frac{\alpha}{2\alpha_{\mathrm{co}}}\right] e^{j2\pi\alpha(x+u)}\, d\alpha\right\} dx \\ &= \int_{-\infty}^{\infty} \frac{1}{2}\operatorname{rect}\left[\frac{x}{L}\right] 2\alpha_{\mathrm{co}}\operatorname{sinc}[2\alpha_{\mathrm{co}}(x+u)]\, dx. \qquad (3.91) \end{aligned}$$

Because $|\alpha_k| \ll \alpha_{\mathrm{co}}$, the sinc function in the integral on the second line of Equation (3.91) is sufficiently narrow that it behaves as a delta function, as we show in Section 3.5.1. The convolution is therefore easily performed by using the sifting property of the delta function to provide

$$g_1(u) = \frac{1}{2}\,\mathrm{rect}\left[\frac{-u}{L}\right], \tag{3.92}$$

which is simply the image of the average value of the original signal $f(x)$. Each of the other terms of Equation (3.88) is evaluated in a similar fashion and we find that the entire output is

$$g(u) = 0.5\,\mathrm{rect}(-u/L)\left[1 + \cos(-2\pi\alpha_k u)\right] = f(-x),$$

so that the image has exactly the same form as the signal, but with a coordinate reversal.

When we increase α_k so that $|\alpha_k| \approx \alpha_{\mathrm{co}}$, the sinc functions centered at $\alpha = \pm\alpha_k$ are just at the edges of the aperture in the Fourier plane, but the image is still accurately related to the object. A further increase in the frequency, so that $|\alpha_k| > \alpha_{\mathrm{co}}$, results in a sudden change in the structure of the image. Instead of being a sinusoidal function $g(u) = 0.5\,\mathrm{rect}(-u/L)[1 + \cos(-2\pi\alpha_k u)]$, the image becomes a constant $g(u) = 0.5\,\mathrm{rect}(-u/L)$, because all information about the magnitude and frequency of the sinusoid is lost.

As the spatial frequency response is constant for all frequencies below the cutoff frequency and zero thereafter, we represent the normalized *coherent modulation transfer function* of the system as

$$\boxed{H(\alpha) = \mathrm{rect}\left(\frac{\alpha}{2\alpha_{\mathrm{co}}}\right),} \tag{3.93}$$

as shown in Figure 3.21(a). Because the image intensity is the magnitude squared of the image amplitude, the *incoherent modulation transfer func-*

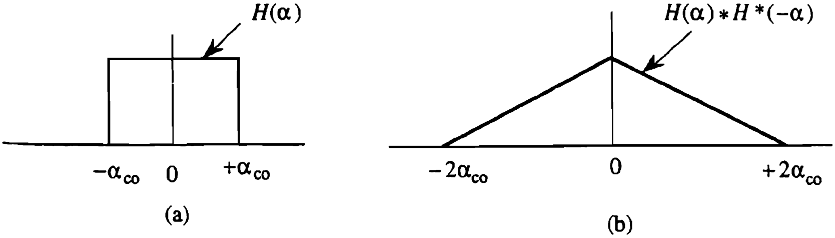

Figure 3.21. Normalized modulation transfer functions: (a) coherently illuminated system and (b) incoherently illuminated system.

tion of an optical system is the normalized autocorrelation of the coherent modulation transfer function:

$$\boxed{\mathcal{H}(\alpha) = \int_{-\infty}^{\infty} H(\gamma)H^*(\gamma + \alpha)\, d\gamma = \operatorname{tri}\left(\frac{\alpha}{2\alpha_{\mathrm{co}}}\right),} \tag{3.94}$$

where $\operatorname{tri}(\alpha/2\alpha_{\mathrm{co}}) = 1 - |\alpha|/2\alpha_{\mathrm{co}}$ for $|\alpha| < 2\alpha_{\mathrm{co}}$ and is equal to zero elsewhere, as shown in Figure 3.21(b). The incoherent and coherent modulation transfer functions are therefore related by the autocorrelation function. As a result, the image contrast in an incoherently illuminated system changes gradually as $|\alpha|$ increases, falling to zero when $|\alpha| = 2\alpha_{\mathrm{co}}$. Although an incoherently illuminated system can resolve spatial frequencies twice as high as its coherently illuminated counterpart, the contrast ratio for the sinusoid is uniformly better, over its bandpass region, for the coherently illuminated system.

Abbe also noticed that the image of a coherently illuminated signal changed its appearance when the angle of the illumination was off axis. We now consider the more general case of *oblique illumination* as shown in Figure 3.22(a). Light leaving plane P_1 is now expressed as

$$f(x) = \tfrac{1}{2}\operatorname{rect}\left(\frac{x}{L}\right)e^{-j2\pi\alpha_i x}[1 + \cos(2\pi\alpha_k x)], \tag{3.95}$$

where $\theta_i = \lambda\alpha_i$ is the oblique illumination angle. The Fourier transform of this signal is found by a procedure similar to that used to derive the result given by Equation (3.87):

$$F(\alpha) = \frac{L}{2}\{\operatorname{sinc}[(\alpha + \alpha_i)L] + \tfrac{1}{2}\operatorname{sinc}[(\alpha + \alpha_i + \alpha_k)L]$$
$$+ \tfrac{1}{2}\operatorname{sinc}[(\alpha + \alpha_i - \alpha_k)L]\}. \tag{3.96}$$

As shown in Figure 3.22(b), $F(\alpha)$ has the same form as before, except that the entire spectrum is shifted in the negative α direction by an amount α_i. We note that oblique illumination provides a nice physical illustration of the shift theorem from Fourier-transform theory.

As α_i increases, we see that eventually some of the spectrum is cut off by the finite aperture at plane P_2. This event occurs when

$$\operatorname{sinc}[(\alpha + \alpha_i + \alpha_k)L]\operatorname{rect}(\alpha/2\alpha_{\mathrm{co}}) = 0. \tag{3.97}$$

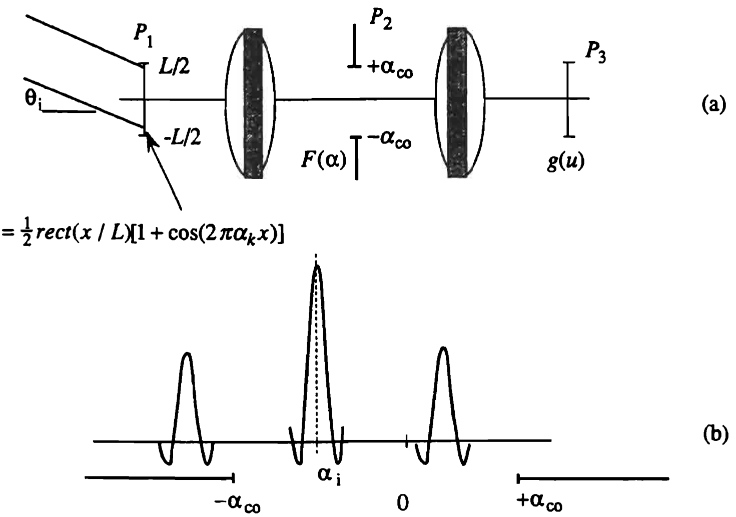

Figure 3.22. Oblique illumination: (a) optical system and (b) shifted spectrum.

From Equation (3.97), we see that the center of the sinc function is within the passband aperture whenever $0 < \alpha_i < (\alpha_{co} - \alpha_k)$. For larger values of the angle of illumination the sinc function is cut off, and the output of the system becomes

$$g(u) = \int_{-\infty}^{\infty} \operatorname{rect}\left[\frac{\alpha}{2\alpha_{co}}\right] \frac{L}{2} \{\operatorname{sinc}[(\alpha + \alpha_i)L) + \tfrac{1}{2} \operatorname{sinc}[(\alpha + \alpha_i - \alpha_k)L]\} e^{j2\pi\alpha u}\, d\alpha, \quad (3.98)$$

so that the complex amplitude at plane P_3 is

$$g(u) = \tfrac{1}{2} e^{-j2\pi\alpha_i u}\left[1 + \tfrac{1}{2} e^{j2\pi\alpha_k u}\right] \operatorname{rect}(u/L). \quad (3.99)$$

This filtering operation generates false information as is seen by examining the intensity of the output signal for these two cases. When $\alpha_i = 0$ and $|\alpha_k| \ll \alpha_{co}$, the intensity is $I_0(u) = |g(u)|^2$:

$$I_0(u) = \tfrac{1}{4}\left[\tfrac{3}{2} + 2\cos(2\pi\alpha_k u) + \tfrac{1}{2}\cos(4\pi\alpha_k u)\right] \operatorname{rect}(u/L), \quad (3.100)$$

whereas when one of the diffracted orders is cut off, the intensity is the squared magnitude of Equation (3.99):

$$I_1(u) = \tfrac{1}{4}\left[\tfrac{5}{4} + \cos(2\pi\alpha_k u)\right]\text{rect}(u/L). \tag{3.101}$$

By comparing Equation (3.101) with Equation (3.100), we conclude that the intensity of the fundamental frequency component has been reduced by a factor of 2 because of the loss of half the energy in the fundamental, and that the harmonic of the fundamental is missing. The output therefore contains false information about the input signal because of filtering the spatial frequencies.

Oblique illumination has the advantage, however, that it increases the bandwidth of a spectrum analyzer. If the input signal is real valued so that the spectrum has polar symmetry, negative spatial frequencies have the same magnitude as positive ones and measuring the spectrum from zero frequency to α_{co} is sufficient to extract all the information. Oblique illumination displays the spatial frequencies from the signal that fall into the range from zero to α_{co} in the interval $(-\alpha_{co}, 0)$ at the Fourier plane, thus making the interval $(0, \alpha_{co})$ at the Fourier plane available for displaying spatial frequencies ranging from α_{co} to $2\alpha_{co}$. The frequency analysis range is therefore doubled. Oblique illumination is also useful in certain special cases of correlation. It is not, however, generally used when accurate imaging is required.

We see that Equation (3.100) reveals a spatial frequency $2\alpha_k$ that was not displayed at the Fourier plane P_2 of the coherent optical system. This apparent discrepancy is explained by noting that the harmonic $2\alpha_k$ arises only when we *observe*, *measure*, or *record* the intensity of an amplitude signal that is a pure sinusoidal waveform. In the example given, the harmonic was, in fact, already present in the intensity stored on the spatial light modulator at the input of the system. The coherently illuminated system produced the Fourier transform of the *amplitude* of the light at plane P_2, and, because the intensity of the input signal was, in fact, $I(x) = |f(x)|^2$, the system properly calculates the Fourier transform of $f(x) = \sqrt{I(x)}$.

3.5.4. The Sample Function, Sampling Theorem, and Decomposition

Both Rayleigh and Abbe studied resolution for optical systems, but from different viewpoints. We now summarize their results and relate them to the sampling theorem and to methods for representing signals. If we follow Rayleigh's resolution criterion, we represent a signal $f(x)$, bandlimited to the frequency range $|\alpha| \leq \alpha_{co}$, by a set of weighted sample

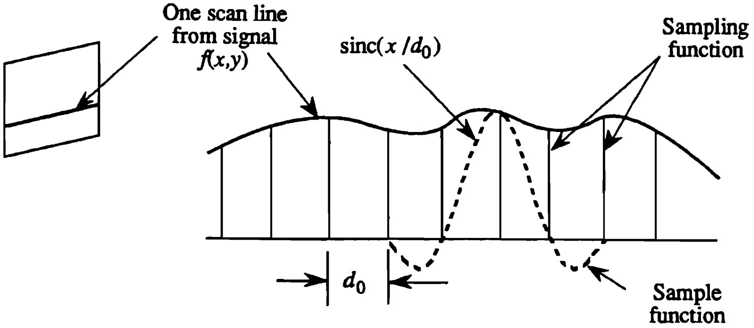

Figure 3.23. The sample (interpolation) function for a sampled bandlimited signal.

functions:

$$f(x) = \underbrace{\mathrm{rect}\left(\frac{x}{L}\right)}_{\substack{\text{sets limit}\\ \text{on signal}\\ \text{length}}} \sum_{n=-\infty}^{\infty} \underbrace{a_n e^{j\phi_n}}_{\substack{\text{weights in}\\ \text{magnitude}\\ \text{and phase}}} \underbrace{\mathrm{sinc}[2\alpha_{\mathrm{co}}(x - nd_0)]}_{\text{sample function}}, \tag{3.102}$$

where the a_n are the sample magnitudes and the ϕ_n are the sample phases at the midpoints of the sinc functions. In general, ϕ_n takes on the value $\pm\pi$ for a real-valued signal, but we also allow for the fact that the signal may become complex-valued after some filtering operations. The sample function $\mathrm{sinc}(2\alpha_{\mathrm{co}}x)$ is wrapped around each element of the sampling function as shown in Figure 3.23. The rect function in Equation (3.102) shows that the number of samples in $f(x)$ is limited to $N = L/d_0$.

The signal representation given by Equation (3.102) is equivalent to the Nyquist criterion for representing a bandlimited signal by a sequence of weighted sample functions. This criterion states that the highest spatial frequency must be sampled at least twice per cycle of the highest frequency to accurately represent the signal; the relationship $\alpha_{\mathrm{co}} = 1/(2d_0)$ fulfills this requirement. By applying the shift theorem to the Fourier transform, we find that all light produced by all samples of $f(x)$ pass through an aperture in the Fourier plane P_2 bounded by $|\alpha| \leq \alpha_{\mathrm{co}}$; the entire signal, as well as each sample, is therefore strictly bandlimited.

If N degrees of freedom completely specify $f(x)$, so too will N degrees of freedom completely specify $F(\alpha)$. As a result of Equation (3.102), we find that the Fourier transform of $f(x)$ is

$$F(\alpha) = \underbrace{\text{rect}\left(\frac{\alpha}{2\alpha_{\text{co}}}\right)}_{\substack{\text{due to the}\\ \text{sample}\\ \text{function}}} \underbrace{\{\text{sinc}(\alpha \text{L}) *}_{\substack{\text{due to}\\ \text{aperture}\\ \text{function}}} \sum_{n=-\infty}^{\infty} \underbrace{a_n e^{j\phi_n}}_{\substack{\text{weights in}\\ \text{magnitude}\\ \text{and phase}}} \underbrace{e^{j2\pi n d_0 \alpha}\}}_{\substack{\text{due to}\\ \text{sample}\\ \text{positions}}}, \tag{3.103}$$

where $*$ indicates convolution. The spectrum therefore consists of a set of weighted plane waves, each wave due to a sample contained in $f(x)$, that interfere to produce the spectrum $F(\alpha)$. The rect function shows that the signal is bandlimited to $|\alpha| \leq \alpha_{\text{co}}$. The convolution of the spectrum with $\text{sinc}(\alpha L)$ is included for completeness; it does not alter the shape of the spectrum by an argument similar to that developed in Section 3.5.1.

Alternatively, we might follow Abbe's approach and represent $f(x)$ as a sequence of weighed sinusoids whose frequencies are separated by $\alpha_0 = 1 / L$. A more convenient representation is to replace the cosines by exponentials, using the Euler expansion, to find that

$$f(x) = \underbrace{\text{rect}\left(\frac{x}{L}\right)}_{\substack{\text{aperture}\\ \text{function}}} \underbrace{\{\text{sinc}(2\alpha_{\text{co}}\text{x}) *}_{\substack{\text{due to the band}\\ \text{limit in the}\\ \text{Fourier plane}}} \sum_{n=-\infty}^{\infty} \underbrace{b_n e^{j\phi_n}}_{\substack{\text{weights in}\\ \text{magnitude}\\ \text{and phase}}} \underbrace{e^{j2\pi n \alpha_0 x}\}}_{\substack{\text{exponential}\\ \text{function}}}, \tag{3.104}$$

where the b_n are the magnitudes and the ϕ_n are the phases of the exponential functions at the signal plane. The sinc function reveals that $2\alpha_{\text{co}}/\alpha_0 = 2L\alpha_{\text{co}} = N$ complex exponentials completely describe $f(x)$. In turn, we express $F(\alpha)$ as

$$F(\alpha) = \underbrace{\text{rect}\left(\frac{\alpha}{2\alpha_{\text{co}}}\right)}_{\substack{\text{frequency}\\ \text{plane cutoff}}} \sum_{n=-\infty}^{\infty} \underbrace{b_n e^{j\phi_n}}_{\substack{\text{weights in}\\ \text{magnitude}\\ \text{and phase}}} \underbrace{\text{sinc}[(\alpha - n\alpha_0)L]}_{\substack{\text{samples in the}\\ \text{Fourier plane}}}, \tag{3.105}$$

where $\alpha_0 = 1/L$ is the minimum resolvable spatial frequency, and the b_n and the ϕ_n provide the weights of the sinc functions in the Fourier plane.

This exercise shows that, since $f(x)$ and $F(\alpha)$ are both functions of space coordinates, we can represent them in either of the two forms listed above. An observer of a sinusoidal spatial signal is hard pressed to know whether they are looking at a space signal, a spatial frequency function, or neither (they may be looking at a Fresnel transform). We can therefore interchange our notions of space and frequency planes as we please, useful for helping to visualize the operation of some signal-processing systems.

Again, we remind the reader that signals cannot, in theory, be both space limited and bandlimited, as we have assumed here. In practice, however, the impact of such an assumption is usually small because the limits of observation are set by noise levels at both the space and spatial frequency planes. In any event, Equations (3.102)–(3.105) are useful to help visualize the general nature of the signals and are accurate, except possibly near the edges of the signals.

3.6. EXTENDED FOURIER-TRANSFORM ANALYSIS

The Fourier-transform result was developed in Section 3.3, under some mild restrictions that simplified the analysis considerably. We assumed that the signal was illuminated by a plane wave of light and was at the front focal plane of the lens. The Fourier-transform relationship exists, however, for a wide range of geometries. To explore these possibilities further, we introduce an operational method of analysis that reveals the richness of the conditions under which the transform exists. In the process, we show that the fundamental results from geometrical optics are obtained from analyses involving only the principles of physical optics. As examples, we generate two key results: the fundamental lens equation and the Fourier-transform relationship.

To facilitate the analysis and to draw analogies to linear system theory, we represent each optical system by a block diagram. By using an operational notation, a basic set of optical elements is synthesized into a system for either imaging or Fourier transforming a signal. Once the basic systems are synthesized, we cascade them to produce more complex ones.

3.6.1. The Basic Elements of an Optical System

Figure 3.24 illustrates that light from the source is represented by $a(x, y) = |a(x, y)|\exp[j\phi(x, y)]$, where $|a(x, y)|$ is the magnitude and $\phi(x, y)$ is the phase of the light. The amplitude transmittance of the spatial light modulator is $f(x, y) = |f(x, y)|\exp[j\theta(x, y)]$ so that the modulated light wave is given by

$$g(x, y) = |a(x, y)||f(x, y)|e^{j[\phi(x, y)+\theta(x, y)]}. \tag{3.106}$$

The block diagram element for a spatial light modulator is therefore a *multiplier*, as shown in Figure 3.24(b).

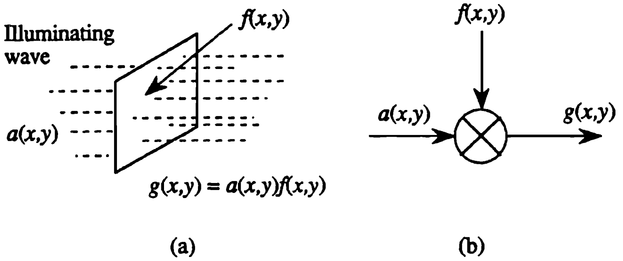

Figure 3.24. Effect of a spatial light modulator: (a) optical system and (b) block diagram.

Lenses are important elements in optical signal-processing systems. In Section 3.3.3 we showed that a spherical lens is represented by the phase function $\exp[j(\pi/\lambda F)(x^2 + y^2)]$, where F is the focal length of the lens. Cylindrical lenses are represented as functions of only one variable: $\exp[j\pi x^2/\lambda F]$ or $\exp[j\pi y^2/\lambda F]$, depending on the direction of the power of the lens. The focal length of cylindrical lenses in the orthogonal direction is infinite. The operation of a lens and its block diagram is shown in Figure 3.25.

The next important step is to represent how light propagates through free space. We showed in Section 3.2 that, if $f(x, y)$ is a light distribution in a given plane, the propagation of light through a distance D produces the Fresnel transform

$$g(\xi, \eta) = \frac{C}{D} \iint_{-\infty}^{\infty} f(x, y) e^{-j(\pi/\lambda D)[(x-\xi)^2+(y-\eta)^2]}\, dx\, dy, \quad (3.107)$$

where ξ, η are coordinates in the new plane and C is a complex-valued constant that is independent of all the variables.

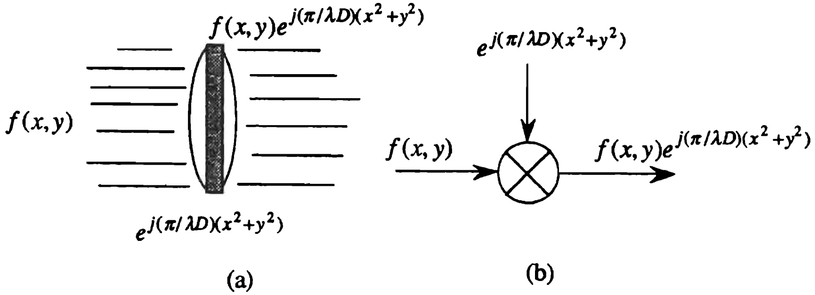
$f(x,y)e^{j(\pi/\lambda D)(x^2+y^2)}$
$f(x,y)$
$e^{j(\pi/\lambda D)(x^2+y^2)}$
$e^{j(\pi/\lambda D)(x^2+y^2)}$
$f(x,y)$
$f(x,y)e^{j(\pi/\lambda D)(x^2+y^2)}$
(a)
(b)

Figure 3.25. Effect of a lens: (a) optical system and (b) block diagram.

3.6.2. Operational Notation

As the lens function and the free-space impulse response have similar forms, we represent both by a ψ function (27):

$$\boxed{\psi(x, y; d) \equiv e^{j(\pi/\lambda D)(x^2+y^2)}.} \tag{3.108}$$

Because the distance between two planes occurs in the denominator of the argument of the exponential function, we use a lower-case letter to represent the reciprocal of the propagation distance as indicated by an upper-case letter. With this notation, we describe the propagation of light through a distance D, shown in Figure 3.26, as though it passed through a black box whose impulse response is $d\psi^*(x, y; d)$, where $*$ indicates complex conjugate and $d = 1/D$. A lens of focal length F is represented by $\psi(x, y; K)$, where K is the power of the lens. A cylindrical lens is represented by $\psi(x; K)$ or $\psi(y; K)$, according to which axis of the cylinder has the focal power.

Some of the more useful properties of the ψ function are

P1 $\quad \psi(x,y;d) = \psi^*(x,y;-d),$

P2 $\quad \psi(-x,-y;d) = \psi(x,y;d),$

P3 $\quad \psi(x,y;d_1)\psi(x,y;d_2) = \psi(x,y;d_1+d_2),$

P4 $\quad \psi(x,y;d) = \psi(x;d)\psi(y;d),$

P5 $\quad \psi(cx,cy;d) = \psi(x,y;c^2d),$

P6 $\quad \psi(x-u,y-v;d) = \psi(x,y;d)\psi(u,v;d)e^{-jkd(ux+vy)},$

P7 $\quad \lim_{K\to 0}\psi(x,y;K) = 1.$

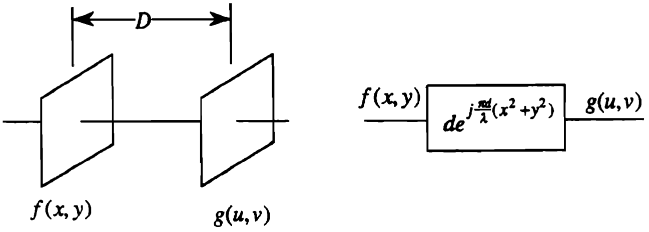

(a) (b)

Figure 3.26. Propagation through free space: (a) optical system and (b) block diagram.

Property P1 shows asymmetry along the optical axis; that is, a spherical wave appears to diverge or converge according to the direction of observation. Property P2 shows symmetry normal to the optical axis; an example is that the power of a spherical lens has polar symmetry. Property P3 gives the rule for multiplication and property P4 shows the separability of the ψ function. Property P5 gives the effect of a scale change, which is useful when we solve certain integral equations; and property P6 is useful in expanding convolution integrals involving the ψ function. Property P7 states that a lens of infinite focal length has no effect on a light distribution.

Another useful property of the ψ function is that the Fourier transform of the function $\psi(x, y; d_1)$ with respect to a parameter d_2 is also a ψ function:

$$\text{P8} \qquad \iint_{-\infty}^{\infty} \psi(x, y; d_1) e^{j(2\pi/\lambda)d_2(ux+vy)}\, dx\, dy = \frac{c}{d_1}\psi*(u, v; d_2^2/d_1), \qquad (3.109)$$

where c is a complex-valued constant that is generally neglected. Property P7 shows that the argument of the integral becomes a constant when $d_1 \to 0$ and P8, in turn, shows that

$$\text{P9} \qquad \lim_{d_1 \to 0} \frac{1}{d_1}\psi^*(x, y; d_2^2/d_1) = \delta(x, y) \qquad (3.110)$$

for any value of d_2. Property P9 is independent of d_2, in the limit, because the Fourier transform of a constant over an infinite interval is a δ function. In Section 3.5.1, we showed that the finite aperture of a lens leads to a sample function in the image plane that is, in an operational sense, equivalent to a δ function, provided that the signal is bandlimited and that the aperture limit does not remove information.

3.6.3. A Basic Optical System

A fundamental combination of the elements described in Section 3.6.1 consists of a spatial light modulator, free space, a spherical lens, and more free space, as shown in Figure 3.27. The spatial light modulator is illuminated by a unit magnitude monochromatic light wave with an arbitrary spherical phase factor. The illumination is represented by $\psi^*(x, y; d_1)$ if the spherical wave is divergent, or by $\psi(x, y; d_1)$ if the wave is convergent; the radius of curvature is $D_1 = 1/d_1$. According to P1 we could also

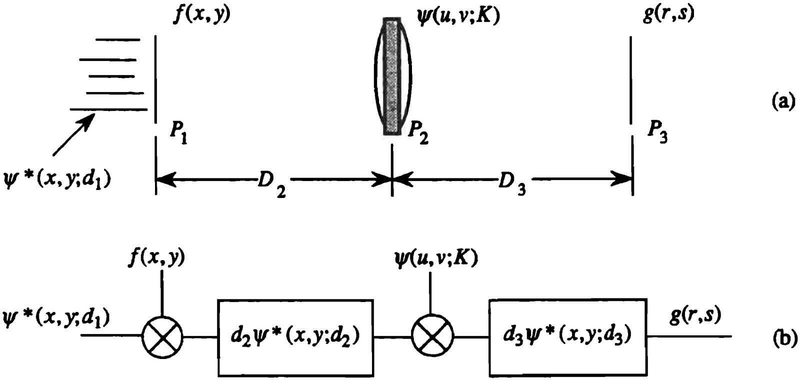

Figure 3.27. General Fourier-transform module: (a) optical system and (b) block diagram.

use $\psi(x, y; -d_1)$ to represent a diverging spherical wave; this notation is consistent with the sign convention adopted in geometrical optics, where we consider D_1 negative when plane P_1 is the origin of the current coordinate system.

From the block diagram we express the output of the system, after using P6, as

$$\begin{aligned} g(r,s) &= d_2 d_3 \iint_{P_1} \iint_{P_2} \psi^*(x,y;d_1) f(x,y) \psi^*(x,y;d_2) \\ &\quad \times \psi^*(u,v;d_2) e^{j(2\pi/\lambda)d_2(ux+vy)} \psi(u,v;K) \psi^*(u,v;d_3) \\ &\quad \times \psi^*(r,s;d_3) e^{j(2\pi/\lambda)d_3(ur+vs)}\, dx\, dy\, du\, dv, \end{aligned} \tag{3.111}$$

where d_2 and d_3 are the reciprocals of the distances D_2 and D_3. Using P3 to collect terms, we have

$$\begin{aligned} g(r,s) &= d_2 d_3 \psi^*(r,s;d_3) \iint_{P_1} \iint_{P_2} \psi^*(x,y;d_1+d_2) f(x,y) \\ &\quad \times \psi^*(u,v;d_2-K+d_3) \\ &\quad \times e^{j(2\pi/\lambda)[u(d_2x+d_3r)+v(d_2y+d_3s)]}\, dx\, dy\, du\, dv. \end{aligned} \tag{3.112}$$

We first carry out the (u, v) integration, with the aid of P8, to obtain

$$\boxed{\begin{aligned} g(r,s) = {} & \frac{d_2 d_3}{d_2 - K + d_3}\psi^*(r,s;d_3)\iint_{P_1}\psi^*(x,y;d_1+d_2)f(x,y)\\ & \times\psi\left(x+\frac{d_3 r}{d_2}, y+\frac{d_3 s}{d_2}; \frac{d_2^2}{d_2 - K + d_3}\right)dx\,dy. \end{aligned}} \tag{3.113}$$

Equation (3.113) is the *central result* in this operational notation. It relates the complex-valued light distribution in the output plane of a basic optical system to the input distribution in terms of the parameters d_1, d_2, d_3, and K.

3.6.3.1. The Imaging Condition. Suppose we wish to synthesize the basic elements shown in Figure 3.27 into an imaging system. First, we note that Equation (3.113) is a convolution operation so that if we find the relationship among d_2, d_3, and K necessary to convert the ψ function into a delta function, the output will be an image of the input. By property P9, we find that

$$\begin{aligned} & \frac{d_2^2}{d_2 - K + d_3}\psi\left(x+\frac{d_3 r}{d_2}, y+\frac{d_3 s}{d_2}; \frac{d_2^2}{d_2 - K + d_3}\right)\\ & = \delta\left(x+\frac{d_3 r}{d_2}, y+\frac{d_3 s}{d_2}\right) \end{aligned} \tag{3.114}$$

when $d_2 - K + d_3 = 0$. We neglect the multiplicative constants and use the sifting property of the delta function so that Equation (3.113) becomes

$$g(r,s) = \psi^*(r,s;d_4)f\left(-\frac{d_3 r}{d_2}, -\frac{d_3 s}{d_2}\right), \tag{3.115}$$

where $d_4 = d_3 + (d_1 + d_2)d_3^2/d_2^2$. Equation (3.115) shows that, aside from a spherical phase factor, $g(r, s)$ is an inverted and scaled image of $f(x, y)$; the scaling factor $-d_3/d_2 = -D_2/D_3$ accurately represents the lateral magnification M of the system. As the imaging condition is valid only when $d_2 + d_3 = K$, we find that $1/D_2 + 1/D_3 = 1/F$. This condition is recognized as the fundamental lens equation or, by suitable modification, as the refraction equation, whose general form is given by $n_2u_2 = n_1u_1 - hK$.

The phase factor that modifies $f(r, s)$ in Equation (3.115) is not important if $g(r, s)$ is recorded or otherwise detected because physical detectors are insensitive to phase. Therefore the intensity $|g(r, s)|^2$ is independent of d_1; i.e., the phase curvature of the illuminating wave does not affect recording of the image. The phase factor provides the information needed to determine where the next image plane occurs if further operations are performed on $g(r, s)$. Thus, all the important features of an imaging system are readily obtained from Equation (3.113).

3.6.3.2. The Fourier-Transform Condition. Suppose that we wish to synthesize the elements of the basic optical system to provide a Fourier-transform relationship between $g(r, s)$ and $f(x, y)$. By using P6 and collecting terms, we rewrite Equation (3.113) as

$$g(r,s) = \psi^*(r,s;d_5) \iint_{P_1} \psi^*\left(x,y;d_1+d_2-\frac{d_2^2}{d_2-K+d_3}\right) f(x,y)$$
$$\times\, e^{j(2\pi/\lambda)[d_2d_3/(d_2-f+d_3)](xr+ys)}\,dx\,dy, \tag{3.116}$$

where $d_5 = d_3 - d_3^2/(d_2 - K + d_3)$. This relationship is almost in the form of a Fourier transform. We apply P7 so that the ψ function in the integral is equal to unity. This condition implies that

$$\boxed{d_1 + d_2 - \frac{d_2^2}{d_2 - K + d_3} = 0} \tag{3.117}$$

must be satisfied. First, suppose that $d_1 = 0$ so that the input signal is illuminated by a plane wave. If Equation (3.117) is satisfied for *any* value of d_2, it is satisfied for *every* value of d_2 so that the distance from the input plane to the lens is of no consequence, aside from ensuring that all the rays pass through the lens. Finally, we find that $d_3 = K$, which implies that the Fourier transform of $f(x, y)$ occurs in the back focal plane of the lens. Under these conditions Equation (3.116) becomes

$$g(r,s) = \psi^*\left(r,s;K-\frac{K^2}{d_2}\right)\iint_{P_1} f(x,y)e^{j(2\pi/\lambda F)(xr+ys)}\,dx\,dy. \tag{3.118}$$

The Fourier-transform relation is made "exact" by setting the ψ function in Equation (3.118) equal to one. To do so, we set $K - K^2/d_2 = 0$ which requires that $d_2 = K$; thus, we place $f(x, y)$ in the front focal plane of the lens. This is the usual result, derived in many texts and papers in the literature. The operational notation used here makes it easy to see what other values of the parameters lead to a useful Fourier-transform relationship—something not easy to do by conventional techniques.

The physical meaning of Equation (3.117) is that the Fourier transform always occurs at the *image plane of the source*. This result is useful in helping us visualize where, for example, the Fourier plane occurs relative to the image plane. The steps necessary to prove this assertion are to observe that Equation (3.117) is rewritten in a sequence of equations as

$$\begin{aligned}
(d_1 + d_2)(d_2 - K + d_3) &= d_2^2, \\
d_1(d_2 - K + d_3) + d_2(d_3 - K) &= 0, \\
d_1 d_2 + d_1(d_3 - K) + d_2(d_3 - K) &= 0, \\
\frac{d_1 d_2}{d_1 + d_2} + d_3 &= K, \\
\frac{1}{D_1 + D_2} + \frac{1}{D_3} &= \frac{1}{F},
\end{aligned} \tag{3.119}$$

which is the condition necessary for imaging the source at plane P_3.

The physical meaning of d_5 in Equation (3.116) is that it represents the phase curvature associated with the Fourier transform. This claim is supported by noting that, if $f(x, y) = \delta(x, y)$ in Equation (3.116),

$$g(r, s) = \psi^*(r, s; d_5), \tag{3.120}$$

which is either a convergent or a divergent spherical wave depending on the sign of d_5. Note that $d_5 = 0$ whenever $d_2 = K$; that is, the Fourier transform has no residual phase curvature whenever the signal is in the front focal plane of the lens, *independently of the curvature of the illuminating wave*. We therefore create an "exact" Fourier transform under a wide range of conditions, contrary to the popular belief that such a transform occurs only when $d_2 = K$ *and* the illumination is a plane wave.

It is not necessary for the Fourier transform to be "exact" in optical signal-processing systems, a point often misunderstood. A residual phase factor in no way affects the spatial filtering operations, to be fully discussed in Chapter 5, other than to determine the position of the output plane.

In a similar fashion, the ψ function associated with the image as given by Equation (3.115) represents a converging or diverging spherical phase function according to the sign of d_4; this result is most easily seen if we set $f(x, y) = 1$. Setting $f(x, y)$ to unity or to $\delta(x, y)$ often provides a quick assessment of how an optical system works. These two functions are a dual pair in the sense that the Fourier transform of a delta function is a constant, and vice versa, as we showed in Section 3.4. These two functions are especially useful for the analysis of anamorphic systems containing cylindrical lenses; often the system is constructed to produce a delta function in one direction while it produces a constant value (in the absence of a signal) in the orthogonal direction.

3.6.3.3. A Variable-Scale Fourier Transform. Equation (3.116) shows that the scale of the Fourier transform is a function of d_2 when $d_1 \neq 0$ and that the transform does not appear in the back focal plane of the lens. From this result we learn that the scale of the Fourier transform is a function of the axial position of the signal if the input signal is placed in nonparallel light. We use this fact to synthesize a variable-scale Fourier transform system, shown in Figure 3.28. From the block diagram we

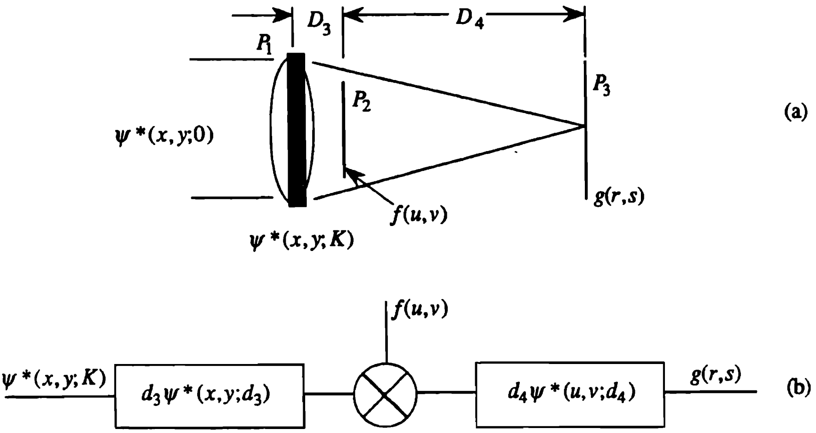

Figure 3.28. Variable-scale Fourier-transform system: (a) optical system and (b) block diagram.

express

$$g(r,s) = d_3 d_4 \psi^*(r,s;d_4) \iint\limits_{P_1} \iint\limits_{P_2} \psi^*(x,y;K)\psi^*(x,y;d_3)\psi^*(u,v;d_3)$$
$$\times f(u,v)e^{j(2\pi/\lambda)d_3(ux+vy)}\psi^*(u,v;d_4)e^{j(2\pi/\lambda)d_4(ur+vs)}\,dx\,dy\,du\,dv. \tag{3.121}$$

Applying the same methods as before, we find that

$$g(r,s) = \psi^*(r,s;d_4) \iint\limits_{P_2} \psi(r,s;d_5)f(u,v)e^{j(2\pi/\lambda)d_4(ur+vs)}\,du\,dv, \tag{3.122}$$

where $d_5 = -d_3 - d_4 + d_3^2/(d_3 - K)$. Again, $g(r,s)$ and $f(u,v)$ are Fourier-transform pairs if the ψ function in the integrand is equal to one. From P7, we find that d_5 must be set equal to zero, which results in the requirement that $d_3^2/(d_3 - K) = d_3 + d_4$ or that

$$\frac{d_3 d_4}{d_3 + d_4} = K. \tag{3.123}$$

This equation is satisfied for *all* values of d_3 and d_4 because $D_3 + D_4 = F$ by the initial constraints imposed on the optical system. Hence, Equation (3.122) becomes

$$\boxed{g(r,s) = \psi^*(r,s;d_4) \iint\limits_{P_2} f(u,v)e^{j(2\pi/\lambda)d_4(ur+vs)}\,du\,dv.} \tag{3.124}$$

The Fourier transform is now carried out using the variable d_4 rather than the parameter K; by varying d_4, we *vary the scale* of the transform of $f(u,v)$. The presence of the ψ function serves to indicate where the inverse transform occurs, as discussed in the next section.

We close this section by noting that the basic optical system shown in Figure 3.27 can either image or Fourier transform a signal, depending on the configuration. We ask whether this system performs both simultaneously. The reader can show, as an exercise, that a Fourier transform must be created somewhere in the system, not necessarily to the right of the lens, if the system produces an image of the input signal $f(x,y)$. The existence of a Fourier transform in an optical system does not, however, guarantee the existence of an image of the signal.

3.6.4. Cascaded Optical Systems

An optical filtering system is most conveniently analyzed by repeated application of the Fourier-transform relationship or, in some cases, by repeated use of the imaging relationship. Hence, the detailed discussion of a basic optical system simplifies the analysis of cascaded optical systems. We often want to perform an operation described by the general linear integral operator

$$g(r,s) = \iint_{-\infty}^{\infty} f(u,v)h(r-u,s-v)\,du\,dv, \tag{3.125}$$

which can also be expressed in the frequency domain as

$$G(\alpha,\beta) = F(\alpha,\beta)H(\alpha,\beta). \tag{3.126}$$

The advantages of being able to perform this operation by realizing the *spatial filter* $H(\alpha,\beta)$ in the frequency plane, where $H(\alpha,\beta)$ is the Fourier transform of $h(x,y)$, will become apparent in Chapter 5.

A typical filtering system consists of a Fourier-transform operation, a mask that introduces $H(\alpha,\beta)$, and a second Fourier-transform operation. Such a system, with a scale searching capability, is shown in Figure 3.29.

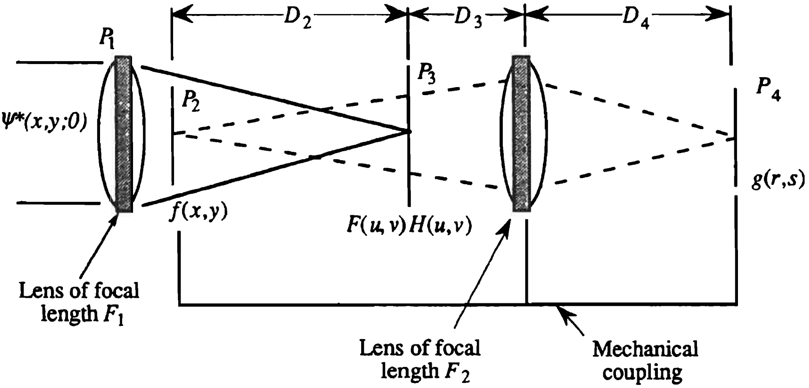

Figure 3.29. Variable-scale correlator.

The input function is illuminated by a converging wave, as before. From the block diagram, we replace the system up to plane P_3 by the equivalent diagram shown in Figure 3.28. Therefore, the distribution at plane P_3 in Figure 3.29 is

$$F(u,v) = \psi^*(u,v;d_2) \iint_{P_1} f(x,y) e^{j(2\pi/\lambda)d_2(ux+vy)}\, dx\, dy. \quad (3.127)$$

The light distribution emerging from P_3 is $F(u,v)H(u,v)$. A second lens, with focal length F_2, takes the Fourier transform of this product and images the filtered signal at the output image plane P_4. This Fourier transform is obtained by applying the general result given in Equation (3.116):

$$g(r,s) = \psi^*(r,s;d_5) \iint_{P_2} \psi^*\left(u,v;d_2 + d_3 - \frac{d_3^2}{d_3 - d_2 + d_4}\right)$$
$$\times F(u,v)H(u,v) e^{j(2\pi/\lambda)[d_3 d_4/(d_3 - K_2 + d_4)](ur+vs)}\, du\, dv, \quad (3.128)$$

where $d_5 = d_4 - d_4^2/(d_3 - K_2 + d_4)$. The condition for making $g(r,s)$ the Fourier transform of $F(u,v)H(u,v)$ is that

$$d_2 + d_3 - d_3^2/(d_3 - K_2 + d_4) = 0$$

or that

$$\frac{1}{D_2 + D_3} + \frac{1}{D_4} = \frac{1}{F_2}. \quad (3.129)$$

Equation (3.129) is the condition for imaging plane P_2 into plane P_4, which satisfies our concept about how the system operates. The variable-scale correlator is implemented by connecting the input plane, the second lens, and the output plane together so that they move as a unit. Hence, $D_2 + D_3$ is constant and Equation (3.129) shows that the output at plane P_3 always represents a focused image of the filtered data.

3.6.5. The Scale of the Fourier Transform

In Section 3.6.3.3, we developed the variable-scale Fourier transform under the condition that the signal $f(x, y)$ is illuminated with convergent light. The scale of the Fourier transform is governed simply by the distance between the signal and the Fourier plane. The signal might,

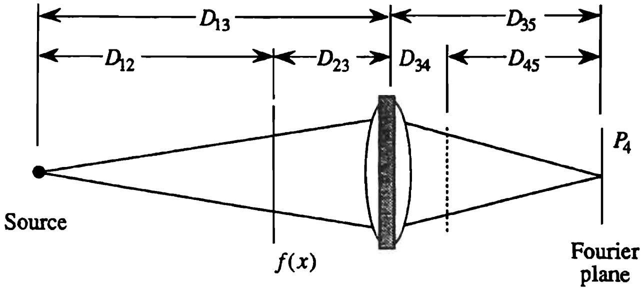

Figure 3.30. Scale of the Fourier transform.

however, by placed in the divergent beam as shown in Figure 3.30, in which case the scaling factor for the Fourier transform seems to be more difficult to find. In this section, we give a simple method for finding this scaling factor. Instead of using the operational notation, we appeal to simple geometrical optics tools and thereby strengthen the relationships between geometrical and physical optics.

The simplest way to find the scale of the Fourier transform of $f(x, y)$ is to temporarily reverse the direction in which the light travels. With light traveling from right to left, we find that the signal is now in *convergent* light. We can therefore calculate the Fourier transform *referenced to the source plane*, using the distance D_{12} as the scaling parameter. The final step is to use the magnification, $M = -D_{35}/D_{13}$, between the source and Fourier planes to get the final scale of the transform.

An alternative technique is to *project* the signal to the lens plane, using the axial point in either the source plane or the Fourier plane as the central projection point. By simple geometrical arguments, we see that the scale of the signal, when projected to the plane of the lens, is $f(Qx, Qy)$, where

$$Q = \frac{D_{12} + D_{23}}{D_{12}}. \tag{3.130}$$

This scaling procedure is equivalent to determining the scale of a signal that would produce the Fourier transform if the signal were illuminated by collimated light and the lens were assigned the focal length D_{35}. Therefore, after the scaling of $f(x, y)$ is done, we can replace the optical system of Figure 3.30 with one in which the signal is illuminated by collimated light at the front focal plane of a lens whose focal length is D_{35}. The usual

Fourier-transform relationships are then applied to find the scale of the transform. A similar procedure can be used when the signal is placed in the convergent beam, replacing D_{12} by D_{45} and D_{23} by D_{34}.

3.7. MAXIMUM INFORMATION CAPACITY AND OPTIMUM PACKING DENSITY

The wide range of configurations, given in Section 3.6, under which a lens produces an image or a Fourier transform, suggests that we seek additional criterion for determining the best configuration of an optical system. A common criterion in communication systems is to maximize the information capacity in terms of bits per unit time. An equivalent criterion in optics is to maximize the packing density in terms of samples per unit length or per unit area. In turn, the size of the optical system determines the total information capacity. We now consider these issues for a coherently illuminated optical system.

Recall that $N = 4(\text{LBP})(\text{HBP})$ is a measure of the number of independent samples required to form a two-dimensional image. The amount of information, on a per-sample basis, is equal to the number of resolvable states, such as magnitudes, polarizations, or wavelengths. The minimum detectable increment in any of these quantities is a function of noise; the noise characteristics therefore set the ultimate rate at which information is transmitted. At this point, we are interested only in the relationship between the geometry of the optical system and the number of samples that is transmitted in a noise-free system. Our results are based on an assumed zero/one state for each sample; we multiply the results by the number of independent states to get the total information capacity.

3.7.1. Maximum Information Capacity

Consider a one-dimensional signal $f(x)$ whose highest frequency is α_{co}, located at the front focal plane of the lens shown in Figure 3.31. The signal has length L and the number of samples necessary to describe the signal is $N = 2LBP = 2L\alpha_{co}$. A sample function $\text{sinc}(x/d_0)$ in $f(x)$ diffracts light within the angle $\theta_{co} = \lambda\alpha_{co}$. If the illumination is collimated, the marginal ray from a sample located at $x = 0$ intercepts the lens plane at $h_2 = \lambda\alpha_{co}F$. The lens must also capture all the rays from samples located at the extreme edges of the signals.

The *relative aperture* R of the lens is the ratio of the clear aperture A to the focal length F of the lens: $R = A/F$. For the conditions shown in Figure 3.31, the aperture is the sum of the aperture $2h_2$ needed to capture

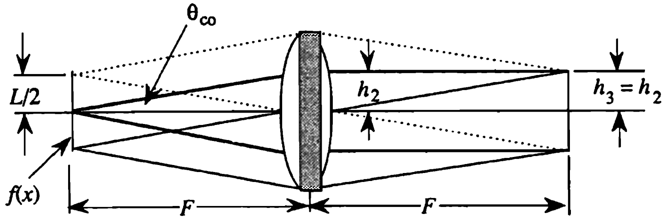

Figure 3.31. Ray diagram for finding the capacity of a lens system.

all the light from an on-axis sample and the aperture L needed to capture all the light diffracted by extreme off-axis samples. The relative aperture therefore is

$$R = \frac{|L| + |2h_2|}{F} = \frac{|L| + |2\lambda a_{co}F|}{F}. \tag{3.131}$$

Because L and h_2 have the same sign at the lens plane, whether we deal with the upper or the lower half of the aperture, we remove the absolute-value signs to obtain

$$R = \frac{L + 2\lambda\alpha_{co}F}{F} = R_0 + R_t, \tag{3.132}$$

where R_0 is the relative aperture of the signal and R_t is the relative aperture of the Fourier-transform plane. This relationship suggests that, for a lens of given relative aperture, we could use a small signal with high resolution or a large signal with low resolution. Which is best? The answer is provided by multiplying R by L/λ and solving for N = 2LBP = $2L\alpha_{co}$:

$$N = \frac{RL}{\lambda} - \frac{L^2}{\lambda F}. \tag{3.133}$$

We now find the signal length that maximizes the system capacity by differentiating N with respect to the signal length L. We find that

$$\frac{\partial N}{\partial L} = \frac{R}{\lambda} - \frac{2L}{\lambda F} = 0, \tag{3.134}$$

from which we conclude that $L = RF/2$ maximizes the number of samples that the system can transmit. We substitute this value of L into Equation (3.132) and conclude that $R = 2R_0 = R_0 + R_t$, which implies that $R_t = R_0$. *Thus, the signal and Fourier planes must have the same size to maximize the system capacity.* The optimum condition is therefore one that strikes a compromise between signal size and signal cutoff frequency so that the number of samples, which is the product of the two quantities, is maximized.

The maximum capacity is found by substituting the value of L into Equation (3.133) to find that

$$\boxed{N_{\max} = \frac{R^2F}{4\lambda} = \frac{RA}{4\lambda}.} \tag{3.135}$$

This result shows a lens with a high relative aperture R and a large clear aperture A yields a system with a high capacity. As $N = 2L\alpha_{\text{co}}$, we also see that

$$\alpha_{\text{co}} = \frac{R}{2\lambda} \tag{3.136}$$

is the maximum frequency that passes through a lens of relative aperture R. These results show that α_{co} is not dependent on the focal length of the lens. Since $\lambda \approx 0.5\ \mu$, a rule of thumb is that $\alpha_{\text{co}} \approx 1000R$ so that an f/2 lens, which has a relative aperture of 0.5, has a coherent cutoff frequency of 500 Ab.

The maximum information capacity was derived under the condition that the lens is operating at infinite conjugates. An image of the signal is easily created by using a second lens, also working at infinite conjugates. If we use finite conjugates, the distance from the signal to the lens is greater than F and the lens aperture would have to increase somewhat to accommodate the diffracted light, thereby lowering the capacity of the system. The results given in this section have application to the design of holographic memories (28) and show that the system capacity is generally set by the optical invariant, not by the capacity of the recording material.

3.7.2. Optimum Packing Density

In applications such as optical storage and retrieval of information, we want to maximize the *packing density*, defined as (29)

$$\rho = \frac{N}{Q}\ \text{samples/mm}, \tag{3.137}$$

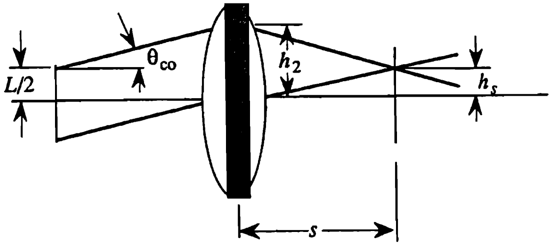

Figure 3.32. Ray diagram for finding the maximum packing density.

where Q is the length of the aperture. We examine all planes in the system shown in Figure 3.32 to find the smallest one through which all information passes. For collimated illumination, the smallest aperture to the left of the lens must be $Q = L$ because no additional aperture is needed to accept diffraction caused by the signal. On the,signal side of the lens, we therefore find that the packing density is

$$\rho = \frac{N}{Q} = \frac{2L\alpha_{co}}{L} = 2\alpha_{co} = \frac{1}{d_0}. \qquad (3.138)$$

This result shows that the maximum packing density ρ is *independent of the size of the signal when we are on the signal side of the lens.*

Consider the rays to the right of the lens, in which the distance from the lens to a candidate plane is s. The smallest aperture that contains all rays occurs where the marginal ray from a sample at the upper edge of the signal and the parallel ray from the lower edge of $f(x)$ intersect. Because these parallel rays intersect at the back focal plane of the lens, $s = F$. Note that the same result is obtained by summing the heights of these two rays at an arbitrary plane to form a relative aperture; we then calculate the partial derivative of ρ with respect to s, following the same procedure as in handling Equation (3.131).

The minimum value of Q on the image side of the lens occurs at the Fourier plane, or when $s = F$ (29). *The highest packing density on the image side of the lens is therefore at the Fourier plane.* As $\theta_{co} = \lambda\alpha_{co}$, we find that $Q = 2\lambda F\alpha_{co}$ so that the packing density at the Fourier plane is

$$\rho = \frac{2L\alpha_{co}}{2\lambda\alpha_{co}F} = \frac{L}{\lambda F} = \frac{R_0}{\lambda}, \qquad (3.139)$$

which is independent of the frequency content of the signal.

The *gain* in packing density is given by the ratio of the maximum density on the image side of the lens to that on the signal side:

$$\boxed{G = \frac{R_0/\lambda}{1/d_0} = \frac{R_0 d_0}{\lambda} = \frac{R_0}{2\lambda\alpha_{co}}.} \tag{3.140}$$

As an example, suppose that the lens has a relative aperture $R_0 \approx 0.5$ and that $\lambda = 0.5\ \mu$ so that $G = 500/\alpha_{co}$. If $\alpha_{co} = 5$ Ab, which is typical for textual material at normal reading distances, $G = 100$. Thus, we store information in an area 10^4 smaller than that occupied by the signal itself; that is, we store an 8 × 11-in page in an area of about 0.1 × 0.1-in. When α_{co} is greater than 500 Ab, the gain is less than unity; there is no advantage to storing information at the Fourier plane when the spatial frequencies of the signal are higher than 500 Ab.

3.7.3. Convergent Illumination

We briefly show how to improve the results from Section 3.7.2 by using convergent illumination and a two-lens solution as shown in Figure 3.33. The first lens serves as a field lens and focuses parallel bundles of rays through an aperture of length L that contains the signal $f(x)$. The signal is placed just to the right of the first lens whose aperture is just large enough to fully illuminate the signal with a convergent wave. The aperture of this lens is clearly *independent of the frequency content* of the signal and is dependent only on the signal length.

The aperture required of the second lens is *independent of the length* of the signal and is dependent only on the frequency content of the signal. Each of these lens apertures are therefore smaller than those of lenses operating at infinite conjugates. If G is fairly large, the aperture of the second lens is much smaller than that of the first lens; for example, if

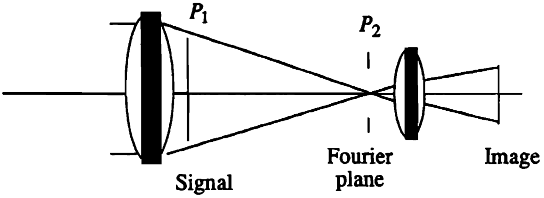

Figure 3.33. Two-lens solution for maximizing the system capacity.

$G = 100$, the aperture of the second lens is 100 times smaller than that of the first lens. Note that the aberrations of the first lens do not affect the imagery; because the second lens has a low relative aperture, it produces high-quality imagery because its aberrations tend to be small.

3.7.4. The Chirp-Z Transform

The configuration shown in Figure 3.33 is suggestive of the configuration needed to create the chirp-Z transform. This transform is sometimes used in electronic systems to convert a time coordinate to a frequency coordinate. Recall that the one-dimensional Fourier transform is

$$F(\xi) = \int_{-\infty}^{\infty} f(x) e^{j(2\pi/\lambda F)\xi x}\, dx. \qquad (3.141)$$

The basic idea of the chirp-Z transform is that

$$2\pi\xi x/\lambda F = (2\pi/\lambda F)\left[(\xi + x)^2 - (\xi - x)^2\right]$$

so that we can also express the Fourier transform as

$$F(\xi) = e^{j(\pi\xi^2/\lambda F)} \int_{-\infty}^{\infty} \left[f(x) e^{j(\pi x^2/\lambda F)}\right] e^{-j(\pi/\lambda F)(\xi - x)^2}\, dx. \quad (3.142)$$

This result shows that we obtain the Fourier transform if we premultiply the signal $f(x)$ by a chirp function, perform a Fresnel transform on the resultant product, and postmultiply the integral by a chirp. The optical equivalent of these operations is shown in Figure 3.34. The first lens

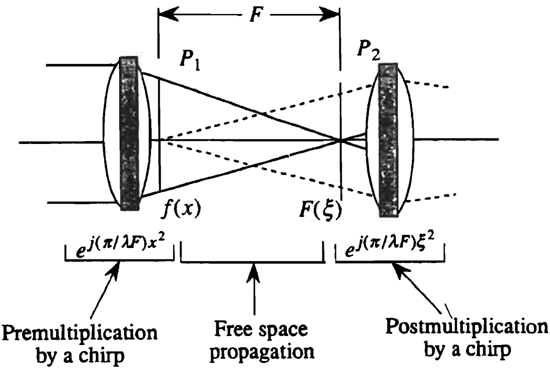

F
P_1
P_2
$f(x)$
$F(\xi)$
$e^{j(\pi/\lambda F)x^2}$
$e^{j(\pi/\lambda F)\xi^2}$
Premultiplication by a chirp
Free space propagation
Postmultiplication by a chirp

Figure 3.34. Chirp-Z transform in optics.

provides the premultiplication by illuminating $f(x)$ with a converging spherical wave, equivalent to a chirp function. Propagation through free space provides the required Fresnel transform between the signals at planes P_1 and P_2. The second lens provides the postmultiplication of the Fourier transform $F(\xi)$ by a chirp. The similarity of the optical layout in Figure 3.34 to that of Figure 3.33 is obvious and we see that the chirp-Z configuration is useful for minimizing the apertures of the lenses and their aberrations.

3.8. SYSTEM COHERENCE

Coherence theory, which deals with the statistical fluctuations of light, is important in physical optics. For our purposes, we want to establish a few working rules that help us understand some of the phenomena we observe and to settle some issues relating to system linearity.

Any system with transfer function T is linear if

$$T[af_1(x) + bf_2(x)] = ag_1(x) + bg_1(x), \tag{3.143}$$

where $g_1(x) = T[f_1(x)]$ and $g_2(x) = T[f_2(x)]$. In optical systems we are faced with some choices that tend to blur the usual concepts of linearity. Optical systems may be linear in terms of amplitude (equivalent to voltage), in terms of intensity (equivalent to power), or in terms of neither. The subject of linearity cannot be resolved until we assess the role of coherence in optics.

Coherence is a measure of how well light from a source is correlated over space and time. If light is nearly monochromatic, which represents the situation of greatest interest to us, we visualize that wave trains of light arrive at an observation screen with the same average frequency but with slowly varying magnitudes and phases. When the source is strictly monochromatic, the amplitude modulation disappears and the fringes are stable in time. In general, an optical system has both spatial and temporal coherence properties.

3.8.1. Spatial Coherence

We quantify spatial coherence by considering the intensity pattern created at plane P_3 from two elemental apertures Q_1 and Q_2 located at plane P_2, as shown in Figure 3.35. At the secondary source plane P_2 the intensities are proportional to the elemental source area $d\sigma$ so that the magnitude is proportional to the square root of the primary source area at plane P_1.

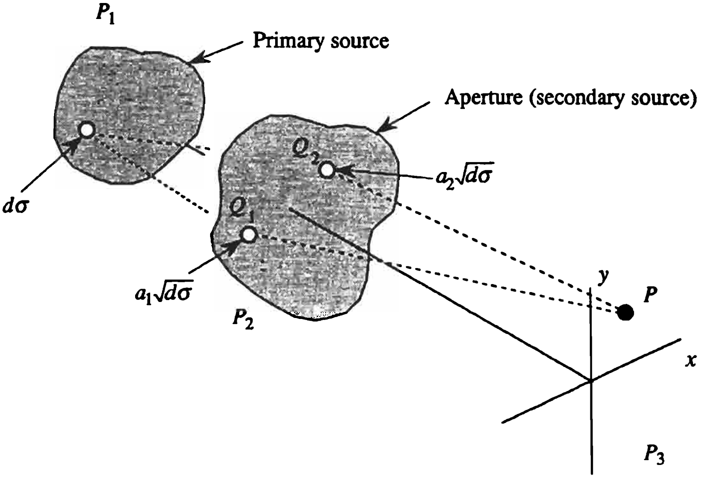

Figure 3.35. Geometry for calculating the spatial coherence function.

Thus, the complex amplitudes $a_1\sqrt{d\sigma}$ and $a_2\sqrt{d\sigma}$ define the secondary sources. If unit value sources at Q_1 and Q_2 produce complex amplitudes u_1 and u_2 at an observation point P at plane P_3, the elemental intensity at P is

$$\delta I_p = |a_1 u_1 \sqrt{d\sigma} + a_2 u_2 \sqrt{d\sigma}|^2 \tag{3.144}$$

The total intensity at P due to the entire primary source is given by the integral of δI_p over the primary source. We define the integral of $|a_1 u_1|^2\, d\sigma$ as I_1 and that of $|a_2 u_2|^2\, d\sigma$ as I_2 to obtain

$$\begin{aligned} I_p &= \int_{-\infty}^{\infty} |a_1 u_1|^2\, d\sigma + \int_{-\infty}^{\infty} |a_2 u_2|^2\, d\sigma + 2\,\mathrm{Re}\left\{\int_{-\infty}^{\infty} a_1 u_1 a_2^* u_2^*\, d\sigma\right\} \\ &= I_1 + I_2 + I_{12}, \end{aligned} \tag{3.145}$$

where

$$I_{12} = 2\,\mathrm{Re}\left\{\int_{-\infty}^{\infty} a_1 u_1 a_2^* u_2^*\, d\sigma\right\} \tag{3.146}$$

is the *mutual intensity* due to the two sources at plane P_2. As the first integral of Equation (3.145) is proportional to I_1 and the second integral is proportional to I_2, we can express the mutual intensity as

$$I_{12} = 2\sqrt{I_1 I_2}\,\gamma_{12}, \tag{3.147}$$

where the function γ_{12} is called the *complex degree of coherence*. Note that γ_{12} is a function of the primary source geometry, the secondary source geometry, and the paths traversed by the light from P_2 to P_3. We express γ_{12} as

$$\gamma_{12} = |\gamma_{12}| e^{j(\phi_1 - \phi_2 + \phi_{12})}, \tag{3.148}$$

where ϕ_1 and ϕ_2 are the phases associated with the path lengths from the sources at Q_1 and Q_2 to the point P and ϕ_{12} is the phase difference between points Q_1 and Q_2.

Finally, we find that the intensity at P is

$$\boxed{I_p = I_1 + I_2 + 2\sqrt{I_1 I_2}|\gamma_{12}|\cos(\phi_1 - \phi_2 + \phi_{12}).} \tag{3.149}$$

Generally the argument of the cosine function is unimportant because it simply establishes the principal maximum of the interference fringes. Of greater importance is the factor $|\gamma_{12}|$, which is called the *degree of spatial coherence*. The degree of coherence is bounded to the interval between zero and one because the mutual intensity has been normalized according to Equation (3.147). We see that when $|\gamma_{12}| = 0$, the intensity $I_p = I_1 + I_2$ is simply the sum of the individual intensities of the two sources. As a result, the optical system is *incoherent* and is linear in *intensity*.

We connect the fringe visibility from Equation (3.29) with the degree of coherence by using Equation (3.149) in Equation (3.29):

$$\begin{aligned} V &= \frac{I_{\max} - I_{\min}}{I_{\max} + I_{\min}} \\ &= \frac{I_1 + I_2 + 2\sqrt{I_1 I_2}|\gamma_{12}| - \left[I_1 + I_2 - 2\sqrt{I_1 I_2}|\gamma_{12}|\right]}{I_1 + I_2 + 2\sqrt{I_1 I_2}|\gamma_{12}| + \left[I_1 + I_2 - 2\sqrt{I_1 I_2}|\gamma_{12}|\right]} \\ &= \frac{2\sqrt{I_1 I_2}|\gamma_{12}|}{I_1 + I_2}. \end{aligned} \tag{3.150}$$

When $I_1 = I_2$, we find that $V = |\gamma_{12}|$ so that the visibility of the fringes is a direct measure of the degree of coherence. When $I_1 \neq I_2$, of course, we must measure I_1 and I_2 independently and use Equation (3.150) to calculate $|\gamma_{12}|$.

When $|\gamma_{12}| = 1$, the intensity at the observation point ranges from $(I_p)_{\max} = I_1 + I_2 + 2\sqrt{I_1 I_2}$ to $(I_p)_{\min} = I_1 + I_2 - 2\sqrt{I_1 I_2}$. When $I_1 = I_2$, the fringe visibility in a region about the point I_p is unity. When $I_1 \neq I_2$, there is an intensity bias and the fringe visibility is not unity. In either case, if $|\gamma_{12}| = 1$, the system is *coherent* and is linear in *amplitude*.

When $0 < |\gamma_{12}| < 1$, the source is *partially coherent*. There is some evidence of fringes over small areas but the fringe visibility is never unity, even if $I_1 = I_2$. Such systems are linear in neither amplitude nor intensity. Although they can be analyzed using linear systems theory, the analysis is complex and rarely offers much physical insight into the performance of the system. We avoid them like the plague.

3.8.2. Temporal Coherence

In an interferometer, light from a single source is divided into two beams and recombined after traversing different paths. If the light is monochromatic, a wave train has an infinitely long duration so that the *coherence distance* ΔD and the *coherence time* $\Delta t = \Delta D/c$ are infinite. As the source becomes increasingly polychromatic, the average length of the wave train shortens, as do coherence time and distance.

Temporal coherence is the property of light that allows interference between a wave train from a source and a delayed wave train from the same source. Consider the Michelson interferometer shown in Figure 3.36, in which we represent the signal from the light source by $s(t)$ at some

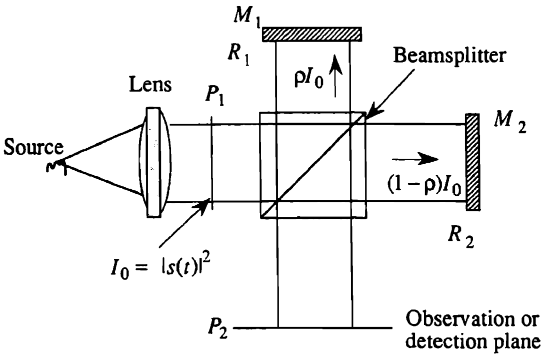

Figure 3.36. Geometry for calculating the temporal coherence function.

arbitrary plane P_1 before the beamsplitter. The intensity at this plane is $I_0 = |s(t)|^2$. Suppose that a fraction ρ of the light intensity is reflected by the beamsplitter and directed toward mirror M_1. If the reflectivity of the mirror is R_1, the light intensity reflected back toward the beamsplitter is ρR_1. If the beamsplitter is nonabsorbing, a fraction $(1 - \rho)$ of the intensity reflected from mirror M_1 reaches the observation plane. The total light intensity reaching plane P_2 due to the first branch of the interferometer is therefore $I_1 = \rho(1 - \rho)R_1 I_0$.

A similar argument is applied to the second branch of the interferometer, in which light is transmitted by the beamsplitter, reflected by mirror M_2, and then reflected by the beamsplitter to reach plane P_2. The total light intensity reaching plane P_2 due to the second branch of the interferometer is therefore $I_2 = \rho(1 - \rho)R_2 I_0$. At the observation plane P_2, the signal is

$$f(t) = \sqrt{\rho(1-\rho)R_1}\, s(t - z_1/c) + \sqrt{\rho(1-\rho)R_2}\, s(t - z_2/c), \quad (3.151)$$

where $z_1/2$ and $z_2/2$ are the distances measured along the optical axis from plane P_1 to plane P_2. The bandwidths of all physical detectors are too low to detect the frequency of light directly. Such detectors have low-pass characteristics, equivalent to integrating the intensity over a time period T. The *effective* intensity, aside from a scaling factor, is therefore given by the time average of the square of the resultant amplitude signal:

$$\begin{aligned} I_d &= \langle f(t) f^*(t) \rangle \\ &= \left\langle \left| \sqrt{\rho(1-\rho)R_1}\, s\left(t - \frac{z_1}{c}\right) \right|^2 \right\rangle + \left\langle \left| \sqrt{\rho(1-\rho)R_2}\, s\left(t - \frac{z_2}{c}\right) \right|^2 \right\rangle \\ &\quad + 2\,\mathrm{Re}\left\{ \left\langle \rho(1-\rho)\, s\left(t - \frac{z_1}{c}\right) s^*\left(t - \frac{z_2}{c}\right) \right\rangle \right\} \\ &= I_1 + I_2 + 2\rho(1-\rho)\sqrt{R_1 R_2} \\ &\quad \times \mathrm{Re}\left\{ \lim_{T\to\infty} \frac{1}{2T} \int_{-T}^{T} s\left(t - \frac{z_1}{c}\right) s^*\left(t - \frac{z_2}{c}\right) dt \right\}. \end{aligned} \quad (3.152)$$

We now change variables so that $t - z_1/c = q$ and find that the third term of Equation (3.152) becomes

$$\begin{aligned} r_{ss}(\tau) &= 2\rho(1-\rho)\sqrt{R_1 R_2} \\ &\quad \times \mathrm{Re}\left\{ \lim_{T\to\infty} \frac{1}{2T} \int_{-T-z_1/c}^{T-z_1/c} s(q)\, s^*\left(q + \frac{z_1}{c} - \frac{z_2}{c}\right) dq \right\}. \end{aligned} \quad (3.153)$$

If $s(t)$ is a stationary process, the integral is a function only of the time difference $(z_1 - z_2)/c = \tau$ so that the time origin is immaterial. We therefore write the integral as

$$r_{ss}(\tau) = 2\rho(1-\rho)\sqrt{R_1 R_2}\,\mathrm{Re}\left\{\lim_{T\to\infty}\frac{1}{2T}\int_{-T}^{T} s(q)s^*(q+\tau)\,dq\right\}, \tag{3.154}$$

which we recognize as the autocorrelation function of $s(t)$.

In the optics literature, $r_{ss}(\tau)$ is normally indicated by $\Gamma_{12}(\tau)$ and is called the *mutual intensity*. If we normalize $\Gamma_{12}(\tau)$ by $\Gamma_{11}(0)$, we find that the intensity at plane P_2 is

$$\boxed{I_d = I_1 + I_2 + 2\sqrt{I_1 I_2}\,\gamma_{12}(\tau),} \tag{3.155}$$

where $\gamma_{12}(\tau)$ is called the *temporal coherence function*. As $s(t)$ must be real valued, $\gamma_{12}(\tau)$ is also real valued and we normally speak of the magnitude $|\gamma_{12}(\tau)|$ as the *degree of temporal coherence*.

The source is completely incoherent when we use white light and $\gamma_{12}(\tau) = \delta(\tau)$. In this case we see that, for $\tau \neq 0$, the intensity at plane P_2 is $I_d = I_1 + I_2$, which is the ordinary splitting case which would result from two independent sources. When the two paths of the interferometer are exactly balanced so that $\tau = 0$, the intensity at the output increases to $I_d = I_1 + I_2 + 2\sqrt{I_1 I_2}$.

To further illustrate the concept of temporal coherence and to relate it to communication theory, suppose that $s(t) = a(t)\cos(2\pi f_l t)$, where $a(t)$ is a baseband modulation signal and f_l is the frequency of an assumed monochromatic light source. Equation (3.154) then becomes

$$\begin{aligned} r_{ss}(\tau) &= 2\rho(1-\rho)R_1 R_2 \\ &\quad \times \mathrm{Re}\left\{\lim_{T\to\infty}\frac{1}{2T}\int_{-T}^{T} a(q)\cos(2\pi f_l q)a^*(q+\tau)\cos[2\pi f_l(q+\tau)]\,dq\right\}. \end{aligned} \tag{3.156}$$

We expand the cosine product to form sum and difference frequencies. The sum frequency, when integrated over a long period of time, does not contribute to the integral so that we have

$$\begin{aligned} r_{ss}(\tau) &= 2\rho(1-\rho)R_1 R_2 \cos(2\pi f_l \tau)\mathrm{Re}\left\{\lim_{T\to\infty}\frac{1}{2T}\int_{-T}^{T} a(q)a^*(q+\tau)\,dq\right\} \\ &= 2\sqrt{I_1 I_2}\, r_{aa}(\tau)\cos(2\pi f_l \tau), \end{aligned} \tag{3.157}$$

where we have noted that the integral is the autocorrelation function of the modulation function $a(t)$. The total intensity at plane P_2 for this example is

$$I_d = I_1 + I_2 + 2\sqrt{I_1 I_2}\, r_{aa}(\tau)\cos(2\pi f_l \tau), \tag{3.158}$$

and the temporal degree of coherence is

$$\gamma_{12}(\tau) = r_{aa}(\tau)\cos(2\pi f_l \tau), \tag{3.159}$$

so that, although the light is monochromatic, the degree of temporal coherence is determined by the baseband signal $a(t)$. When $r_{aa}(\tau) = 1$, Equation (3.158) shows that $I_d = I_1 + I_2 + 2\sqrt{I_1 I_2}$ when the cosine function is at its maximum value. When the cosine term has its minimum value, we have that $I_d = I_1 + I_2 - 2\sqrt{I_1 I_2}$. In general, Equation (3.158) shows that the output of the interferometer, as one of the mirrors is moved to change the value of τ, follows the shape of the autocorrelation function of the baseband signal $a(t)$, but with rapid fluctuations due to the cosine function of τ. The autocorrelation function $r_{aa}(\tau)$ is the envelope of the cosine because it is a slowly varying function.

3.8.3. Spatial and Temporal Coherence

In some systems the temporal coherence may further modify spatial coherence. For example, in Figure 3.35 any point on the observation plane that is equally distant from the two sources will show fringes, even in white light, because $\tau = 0$ and $\gamma_{12}(\tau) = \delta(\tau) = 1$. As we move to a position away from the bisector, the degree of temporal coherence decreases because the path lengths become unequal. The fringe visibility in the observation plane is, to the first order, the product of the degree of spatial coherence and the temporal coherence function.

The coherence length $\Delta L = z_2 - z_1$ is the physical path difference corresponding to the coherence time duration of the source. The coherence length indicates how accurately the two path lengths in an interferometer must be balanced. The coherence length is related to the frequency spread in the source in the following way:

$$\begin{gathered} f = \frac{c}{\lambda}, \\ |\Delta f| = \frac{c\Delta\lambda}{\lambda^2} = \frac{f\Delta\lambda}{\lambda}, \\ \frac{\Delta f}{f} = \frac{\Delta\lambda}{\lambda}, \end{gathered} \tag{3.160}$$

so that the wavelength spread is proportional to the frequency spread. Furthermore, since $\Delta L = c\Delta t$, we have

$$\Delta L = c\Delta t = \frac{c}{\Delta f} = \frac{\lambda^2}{\Delta\lambda}. \tag{3.161}$$

PROBLEMS

3.1. Calculate the observed spatial frequency of the fringe pattern generated in a plane P_2 by applying the Fresnel transform to two sample functions of the form $\mathrm{sinc}(x/d_0)$, spaced 4 mm apart in plane P_1. Let the distance D between the planes be 1000 mm. Assume completely coherent light and a wavelength of 0.5 μ. If the sources each have dimensions of $d_0 = 0.05$ mm, what is the approximate extent of the fringe pattern? Hint: First calculate the diffraction angle produced by each source; then calculate the width (or extent) of the beam in plane P_2; then calculate the extent of the overlap. Recall that interference fringes can occur only when two or more beams of light overlap.

3.2. Suppose that the signal now consists of three sample functions of the form $\mathrm{sinc}(x/d_0)$ in the (x, y) plane: one at $(0, 0)$, one at $(4, 0)$, and one at $(0, 3)$. Sketch the input signal as it would appear if you looked at the x-y plane from the positive z direction. If the other parameters are as in Problem 3.1, provide a two-dimensional sketch of the spatial frequency fringe pattern in the Fresnel plane, calculate the values of the spatial frequencies, and show the regions of overlap. Hint: Treat the sample functions in a pairwise fashion and use the principle of superposition.

3.3. You observe a Fresnel zone present on a viewing screen. You measure the diameter of the first dark ring as 2 mm. If the wavelength is 0.5 μ how far away from the screen is the point source? Assume that the reference beam is collimated and that the intensity of the zone is a maximum in the center. What is the *diameter* of the seventh dark ring?

3.4. Calculate the observed spatial frequency of the fringe pattern at the Fourier-transform plane when the input is the set of two sources given in Problem 3.1; the focal length of the lens is 1000 mm. Is the value of the spatial frequency different from that of Problem 3.1? How about the extent of the fringes; i.e., is the amount of overlap in the Fourier plane less than, the same as, or greater than that of the Fresnel plane? Support your answer with calculations and sketches.

3.5. A source of the form sinc(x/d_0), where $d_0 = 5\ \mu$, is located a distance of 700 mm from a screen. Another source is located 900 mm from the screen and displaced laterally from the first source by 20 mm. Calculate the size that the second source must have so that it completely overlaps light from the first source at the screen and calculate the highest spatial frequency in the interference pattern.

3.6. A plane-wave reference beam is added to the wave produced by a point source of the form sinc(x/d_0). The maximum frequency measured in the interference pattern is 25 Ab. The source is 275 mm from the observation screen. Calculate (a) the chirp rate, (b) the length of the chirp, (c) the number of samples needed to accurately represent the chirp function, and (d) the source size d_0.

3.7. A one-dimensional Fresnel zone is recorded on a strip of film 220 mm long. The spatial frequency at one end is zero and the spatial frequency at the other end is 430 Ab. The strip of film is illuminated by collimated light and is moved through an aperture that is 30 mm long. Calculate where the light is focused when the lowest-frequency portion of the strip is in the aperture. Repeat the calculation for when the highest-frequency portion is in the aperture. Describe what happens to the size and location of the focused spot when the film is moved through the aperture at a constant velocity v_0. Illustrate your results with a sketch. Assume the wavelength to be 500 nm.

3.8. You have a prism whose index of refraction is 1.55 and whose apex angle is 24° The prism is 14 mm high and is illuminated, normal to one of its faces, by a plane wave of collimated light whose extent is infinite in the plane of the prism. Calculate the distance from this plane to the plane where the refracted light completely overlaps the undisturbed light. Calculate the form of the resultant intensity pattern if the prism absorbs a fraction 0.4 of the light (do not forget to calculate the effect of the prism magnification on the amplitude of the transmitted light). Calculate the spatial frequency. Assume the wavelength to be 500 nm. Do a sketch.

3.9. Calculate the two-dimensional Fourier transform of a rectangular aperture that is 4 mm long in the x direction and 6 mm high in the y direction; the focal length of the lens is 200 mm and the wavelength of light is 0.5 μ. Provide labeled sketches of both the object and transform plane light distributions. If the object plane were stretched by a factor of 2 in the x direction, how would the transform change in shape and amplitude?

3.10. The amplitude of a simple one-dimensional signal is given by $f(x) = [1 + \cos(2\pi\alpha_1 x)]\mathrm{rect}(x/L)$. Suppose that the magnitude response of a spatial filter in the region of $\pm\alpha_1$ in the Fourier plane is 0.4, and that its phase response is $e^{j\beta}$; let the transmittance be 1.0 in the region where the undiffracted light is located ($\alpha = 0$). Sketch the magnitude and phase of the filter. Calculate the intensity $|g(u)|^2$ at the output of the filtering system and compare it with the intensity of the object $|f(x)|^2$. Hint: It may be useful to let $L \to \infty$ to solve for the inverse transform. Comment on the effect that the phase β has on the intensity of the output. Make a similar comparison if the magnitudes are as given but the phase response is $e^{j\beta}$ at $+\alpha_1$ and $e^{-j\beta}$ at $-\alpha_1$?

3.11. A function $f(x) = 1 + \cos(2\pi\alpha_1 x) + \cos(2\pi\alpha_2 x)$ is placed in a Fourier-transforming system for which $\lambda = 0.5\ \mu$, the focal length is $F = 200$ mm, and the input aperture is $L = 50$ mm. Assume normal incidence illumination and let $\alpha_1 = 10$ Ab and $\alpha_2 = 15$ Ab. Suppose that the function is moving with velocity $v = 2$ mm/sec in the positive x direction. Part (a): Write the general form of $f(x, t)$ that incorporates $f(x)$ and the velocity v. Part (b): Derive the Fourier transform $F(\alpha, t)$ of $f(x, t)$ in terms of the general variables and parameters. Part (c): Using the specified values of α_1, α_2, λ, F, and v, calculate the locations and the temporal frequencies in the Fourier plane associated with each spectral component of the input signal.

3.12. Consider the convolution in the space domain:

$$g(u) = \int_{-\infty}^{\infty} \mathrm{sinc}(ax)\mathrm{sinc}[b(u - x)]\,dx.$$

Find $g(u)$ for (1) $a > b$, (2) $a = b$, and (3) $a < b$. Hint: There is no need to solve the convolution directly; the solution is apparent when you consider what happens in the Fourier domain.

3.13. You place a lens whose focal length is 100 mm a distance of 400 mm from a source of the form $\mathrm{sinc}(x/d_0)$, where $d_0 = 5\ \mu$. You place an aperture whose diameter is 36 mm a distance of 300 mm from the source; the signal is $f(x) = 1 + \cos(2\pi\alpha_1 x)$, where $\alpha_1 = 50$ Ab. Calculate (a) the position of the Fourier-transform plane, (b) the function $F(\xi)$, (c) the function $F(\xi)$ if the signal and aperture are placed in the plane of the lens, and (d) the distance between the undiffracted light and the diffracted light in the Fourier domain if the signal is placed 10 mm away from the lens on the Fourier-transform side of the lens.

3.14. We enter a laboratory and discover that someone has set up an interferometric system that causes a time delay between two beams of light derived from a common source. We block one of the beams and find that a power meter reads 3 mW/mm^2 at the output plane. We block the other beam and find that the meter reads 1 mW/mm^2. With both beams falling on the power meter, we read 6 mW/mm^2. What is the magnitude of the degree of coherence for this particular set up? Hint: This problem deals with temporal coherence.

3.15. In an adjacent laboratory, we notice a different interferometric arrangement in which two small apertures in a plane appear to be illuminated by a common light source. We notice that a set of spatial fringes exists at an output plane. When we block one of the apertures, we measure the intensity as 2 mW/mm^2. When we block the other aperture, we measure the intensity as 9 mW/mm^2. When both apertures are open, we note that the maximum intensity in the fringes is 12.7 mW/mm^2. Calculate (1) the magnitude of the complex degree of coherence, (2) the minimum intensity in the fringe pattern, and (3) the fringe visibility. Hint: This problem deals with spatial coherence.

3.16. We observe fringes from two apertures located at $x = \pm 4$ mm in plane P_1 at a screen located 100 mm away from plane P_1. The intensities of the two sources are $I_1 = 10$ mW/mm^2 and $\mathrm{I}_2 = 5$ mW/mm^2. The visibility of the fringes is measured as $V = 0.72$ at the observation screen opposite the midpoint between the two sources. For this setup, the visibility drops linearly, being zero at ± 20 mm from the center: (a) Calculate the degree of spatial coherence $|\gamma_{12}|$ and (b) the degree of temporal coherence $\gamma_{12}(\tau)$ at $\tau = 2$ picoseconds (i.e., for a path difference of 0.6 mm).

3.17. Part (a): In a spatial interferometer the intensity due to one beam is 16 times that due to the other (when each is measured separately). In terms of one of the unknown intensities, calculate $I_{\max}$, $I_{\min}$, and the fringe visibility when (1) $\gamma_{12} = 0.4$ and (2) when $\gamma_{12} = 0$. Part (b): Under what general conditions could you adjust the path-length difference of a temporal interferometer and find that the maximum and minimum intensities are periodic? Give at least one specific example to support your claim.

4

Spectrum Analysis

4.1. INTRODUCTION

Spectrum analysis is the most widely used signal-processing technique in the physical sciences for gaining information about unknown signals. It is used in applications such as pattern recognition, cloud-cover analysis, inspection of manufactured items, particle-size analysis, measurements of turbulence, sea state analysis, characterization of the electromagnetic spectrum, determining direction of arrival of emitters, and structural analysis. The Fourier transform, as developed in Chapter 3, plays a central role in optical spectrum analysis. Signal features, such as periodic structures, are more easily detected in the Fourier domain than in the space domain because the energy from each frequency in the signal is concentrated at a particular point in the Fourier plane.

In the optical system shown in Figure 4.1, a signal stored on a spatial light modulator at plane P_1 is illuminated by coherent light. In Chapter 3 we discussed the range of geometrical conditions for which the Fourier transform occurs; for convenience, we use a system in which the signal and Fourier planes are at the front and back focal planes of the lens. The complex-valued light at plane P_2, the image plane of the primary source, is the Fourier transform of the light at plane P_1:

$$S(\alpha, \beta) = \iint\limits_{-\infty}^{\infty} a(x, y) s(x, y) e^{j2\pi(\alpha x + \beta y)}\, dx\, dy, \tag{4.1}$$

where $s(x, y)$ is the amplitude of the signal, $a(x, y)$ is an aperture function, x and y are the spatial coordinates of plane P_1, and α and β are spatial frequencies. The spatial coordinates ξ and η at plane P_2 are related to the spatial frequencies α and β by

$$\begin{aligned} \xi &= \lambda F \alpha, \\ \eta &= \lambda F \beta, \end{aligned} \tag{4.2}$$

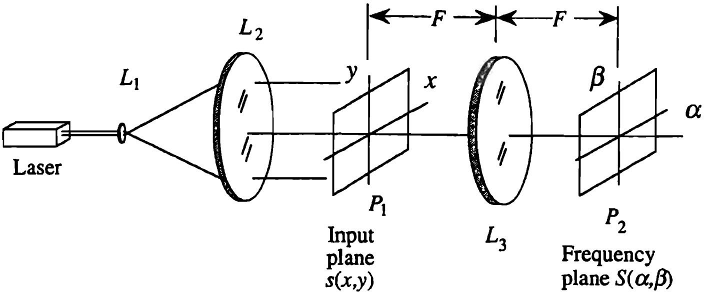

Figure 4.1. The Fourier transform is basic to spectrum analysis.

where F is the focal length of the lens and λ is the wavelength of light. A photodetector array, placed in the Fourier plane, measures the spectral content of the signal.

In this chapter we discuss the key active elements of a typical spectrum analyzer: the light source, the spatial light modulator, and the photodetector array. We then discuss the key performance parameters and develop some design guidelines for maximizing the dynamic range of the analyzer. We conclude this chapter with a discussion of a two-dimensional spectrum analyzer that provides excellent frequency resolution over an extremely wide signal bandwidth.

4.2. LIGHT SOURCES

The usual source of coherent light in optical signal processing is a laser. Water-cooled argon-ion lasers have strong spectral lines at 488.0 and 514.5 nm and power outputs in the 0.2–20-W range. Helium-neon lasers, emitting light at 632.8 nm, are more often used because they are air cooled, compact, and reliable. They are generally less powerful, however, with outputs in the 1–50 mW range.

Semiconductor lasers are the most useful lasers for signal-processing applications because they provide high optical power levels, help to significantly reduce the size of the processing system, and efficiently convert electrical power into optical power. Laser diodes provide output powers comparable to those of much bulkier gas lasers; single-element lasers have been developed, with both spatial and temporal single-mode operation, at powers of greater than 50 mW at 830 nm (using GaAlAs layers of various fractional compositions) and at 1300 nm (using InGaAsP layers). Large arrays of laser diodes have been developed that produce watts of cw optical power (30).

4.3. SPATIAL LIGHT MODULATORS

To create the spectrum of a signal, we structure the input data in an optical format. *Spatial light modulators* are devices that format electronic or incoherent optical information so that it can be processed using coherent light. Historically, the most common spatial light modulator was photographic film as used in pattern recognition and radar processing applications. Photographic film has the attractive feature that its space bandwidth product most nearly matches that of both optical sensors and optical processing systems. In an interesting study, Kardar has shown that film also has a high information channel capacity, even when we account for the relatively long exposure times (31).

For modern signal-processing applications, we need spatial light modulators that have several distinctive features.

- A large space band-width product to provide a high level of performance.
- Adequate bandwidth and response time for use in computationally intensive applications.
- Wide dynamic range for applications such as spectrum analysis and radar processing.
- Good linearity so that intermodulation products are controlled.
- Good efficiency so that optical sources with high power outputs are not required.
- Good phase control so that aberrations do not limit system performance.
- Good geometric fidelity so that the processed signals are not distorted spatially.

We briefly review the current state of two-dimensional spatial light modulators and assess which are most useful for real-time signal processing (32–34). One-dimensional acousto-optic spatial light modulators needed for real-time signal processing, as discussed in the later chapters of this book, are treated separately in Chapter 7.

4.3.1. Light Valve Spatial Light Modulators

An early real-time modulator was a modified *light valve* developed for theater projection television. An electron beam gun is used to deposit charge onto a viscous fluid supported on a rotating disc substrate as shown in Figure 4.2(a). Electrostatic forces deform the fluid to produce a path-length variation that phase modulates light passing through the fluid film. The thickness variation is represented by $f(x, y, t) = s(x, y, t)\cos(2\pi\alpha_c x)$, where $s(x, y, t)$ is the TV baseband signal and α_c is a spatial carrier frequency introduced in the x direction so that we can separate diffracted light, containing the information, from undiffracted light.

The complex-valued amplitude transmittance is a pure phase function $\exp[jmf(x, y, t)]$, where m is a scaling constant, that can be expanded into a power series. If the argument of the exponential is small, we retain just the first two terms and express the transmittance as $1 + jmf(x, y, t)$. To use the light valve in a coherently illuminated system, we want the amplitude transmittance of the device to be proportional to the amplitude of the applied signal. We use the *Schlieren imaging technique* shown in Figure 4.2(b) in which we coherently illuminate the light valve to produce

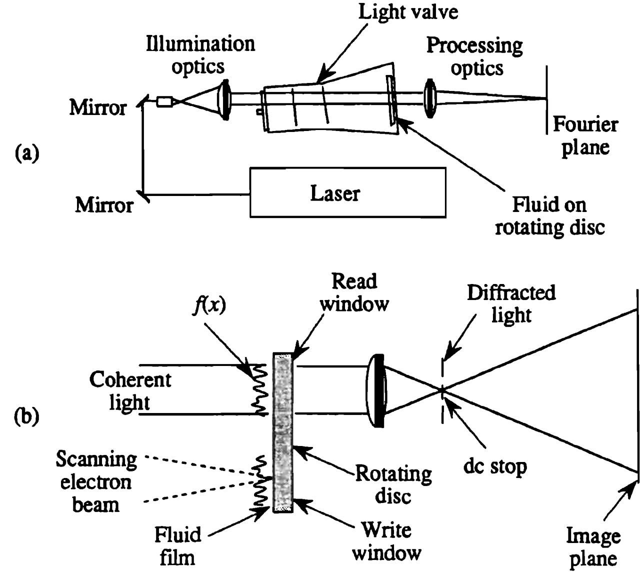

Figure 4.2. Light valve as a spatial light modulator: (a) optical system and (b) details of the recording and reading functions.

the Fourier transform of the input signal and use a stop in the Fourier plane to remove the undiffracted light and one diffracted order. The effective amplitude of the transmitted light is therefore proportional to $jmf(x, y, t)$ so that the light amplitude is now proportional to the applied signal voltage.

The light valve operates at TV frame rates, has a bandwidth in the 30-MHz range, and has a space bandwidth product of approximately 10^6. The maximum diffraction efficiency is 33.8% as dictated by the diffraction theory associated with thin phase modulating media. The light valve is a good real-time display for raster-scanning spectrum analysis, which we discuss in Section 4.7. Its major disadvantages are its large size and the use of high-voltage electron beam tubes.

4.3.2. Optically Addressed Electro-Optic Spatial Light Modulators

One of the first electro-optic spatial light modulators was the Pockels effect Readout Optical Modulator (PROM). The basic concept is that a voltage, applied across a sandwich device as shown in Figure 4.3, produces an electrostatic charge pattern that changes the transmittance of the electro-optic crystal. Incoherent light, striking the device from the left, activates a bismuth silicon oxide photosensitive layer to produce a spatially varying charge pattern that controls the transmittance. Readout light, at a different wavelength from the readin light, reflects from the dichroic mirror and makes two passes through the electro-optic material. By changing the voltage across the device, we can perform useful operations such as contrast reversal or subtraction of two successive images. The

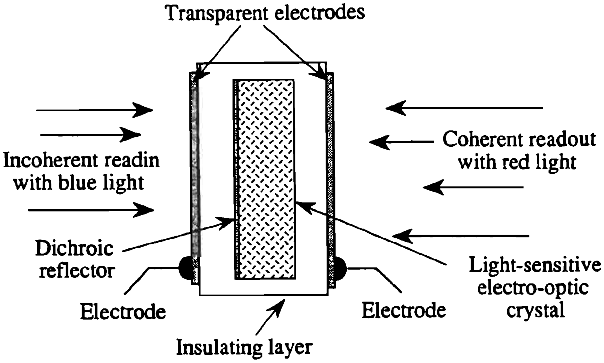
Transparent electrodes
Incoherent readin with blue light
Coherent readout with red light
Dichroic reflector
Electrode
Insulating layer
Electrode
Light-sensitive electro-optic crystal

Figure 4.3. Bismuth silicon oxide spatial light modulator.

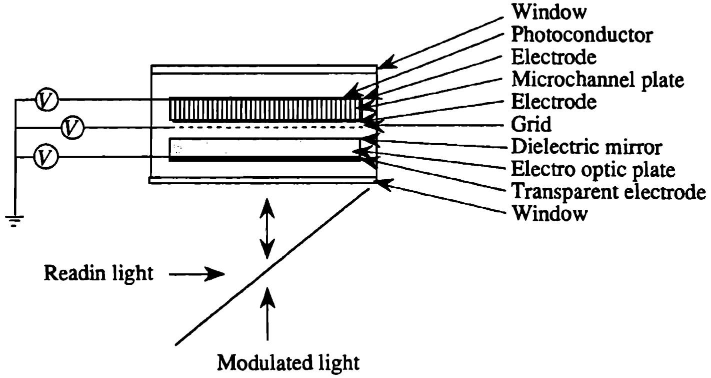

Figure 4.4. A microchannel plate signal light modulator.

space bandwidth products of these devices are of the order of 10^7, with $\alpha_{co} \approx$ 150–500 Ab and contrast ratios of 5000 : 1 or so. The major problem is the uniformity of response across the aperture of the device.

A *microchannel plate* is similar to the PROM. The key difference is that the electro-optic material is replaced by one consisting of several small hollow cylinders, as shown in Figure 4.4. The surfaces of the cylinders are coated with a material that has an electron secondary emission coefficient greater than one. Light strikes a photocathode, which releases electrons into the microchannel tubes. The electrons are amplified and strike an electro-optic plate, as with the electron beam addressed devices, or they strike a fluorescent screen to provide a brighter optical image. These devices have 40–200-Hz frame rates and about 10-Ab resolution. They are sometimes used in nighttime spotting scopes and binoculars; extremely low light level scenes are readily observed with these devices. They can also be addressed by a scanning laser beam to process real-time one-dimensional signals.

4.3.3. Liquid-Crystal Spatial Light Modulators

Liquid-crystal display devices come in many versions. In one version the active material is a *nematic* liquid crystal that changes the polarization of the transmitted light according to the applied voltage. The field is applied by means of a matrix of electrodes or by light falling onto a photoconductive surface. Readout is by means of a single or a double pass, as shown in Figure 4.5. Another version operates in the *variable grating modulation*

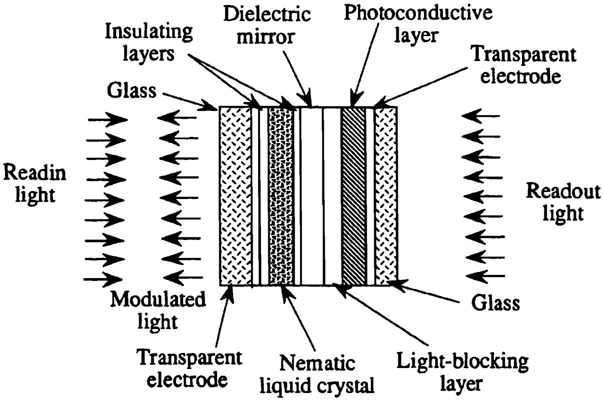

Figure 4.5. Nematic liquid crystal display spatial light modulator.

mode, wherein the application of a dc voltage causes the liquid-crystal display to assume a grating structure. Light is thereby diffracted according to the amplitude of the applied voltage. Typical liquid-crystal displays have frame rates of 10–20 frames per second, contrast ratios of 10 : 1, resolutions in the 8–12-Ab range, and fairly poor throughput efficiencies. Their performance parameters are improving rapidly and they are finding increasing use as flat panel television and computer displays.

4.3.4. Magneto-Optic Spatial Light Modulators

Magneto-optic devices are based on an epitaxial garnet film grown on a nonmagnetic substrate and are addressed by a matrix conductor array. The Faraday effect causes a rotation of the plane of polarization. The time required to switch one element is about 10 μsec so that frame rates range from 3 msec for 48 × 48-element arrays to 20 ms for 128 × 128-element arrays. Efficiency is poor, of the order of 0.1%. Other magneto-optic phenomena include optically writing on a magnetic medium and then heating it to the Curie point at which the magnetic flux rotates appreciably. After cooling, the magnetic domains are rotated such that the amplitude from an analyzer changes according to the exposure; again, the amount of rotation is small, yielding low diffraction efficiencies.

Two-dimensional spatial light modulators have been under development for many years but progress has been relatively slow. The issue is finding a magic material that records analog signals and can be repeatedly erased and recorded without memory of past activity. The material must also have high resolution and a high dynamic range. As materials with these properties are also useful for optical memories to implement a read/write capability, that field may develop alterable materials also suitable for optical processing. A review of two-dimensional light modulators, including deformable mirror technology, has recently been given (34).

4.4. THE DETECTION PROCESS IN THE FOURIER DOMAIN

The outputs of optical processing systems were initially detected, recorded, and displayed using photographic film; we might say that the first two-dimensional "photodetector array" was photographic film. In common with other photodetector devices, film requires a certain number of photons per unit time, is sensitive to light in certain spectral ranges, and has a dynamic transfer function, a modulation transfer function, and a noise floor (often expressed in terms of granularity, grain size, or Selwyn's number). Although the terminology is different, the concepts are similar to those associated with modern photodetector arrays.

A key advantage of photographic film is that its high spatial resolution matches that of the optical system. The major disadvantage is the time delay in developing the film; as a result, it cannot support real-time operations. Electron beam tubes, such as vidicons or image orthicons, have limitations such as inadequate dynamic range and geometric fidelity. One- and two-dimensional photodetector arrays, based on photosensitive charge-coupled device (CCD) structures, provide a new flexibility of operation and have many desirable features.

4.4.1. A Special Photodetector Array

If a signal $s(x, y)$ contains regular features, such as the street pattern of a city, the spacing and width of the sidelobe structure in the spectrum $S(\alpha, \beta)$ indicate the period of the street spacings. In contrast, the spectrum associated with natural terrain is generally more uniformly distributed over all spatial frequencies with no predominant peaks. As an illustration of two-dimensional spectrum analysis, we show, in Figure 4.6, a photograph that contains a variety of ground textures. From the spectra shown in the inserts, we note that strong diffraction occurs in directions normal to the ground texture; this is most notable in the spectra of the bridge and of the streets. Images of the surface of the ocean produce spectra that give information about wave direction and ocean depth. Regions containing clouds and natural terrain have more uniform angular spectra but still show variations in the spatial frequency distribution. If we

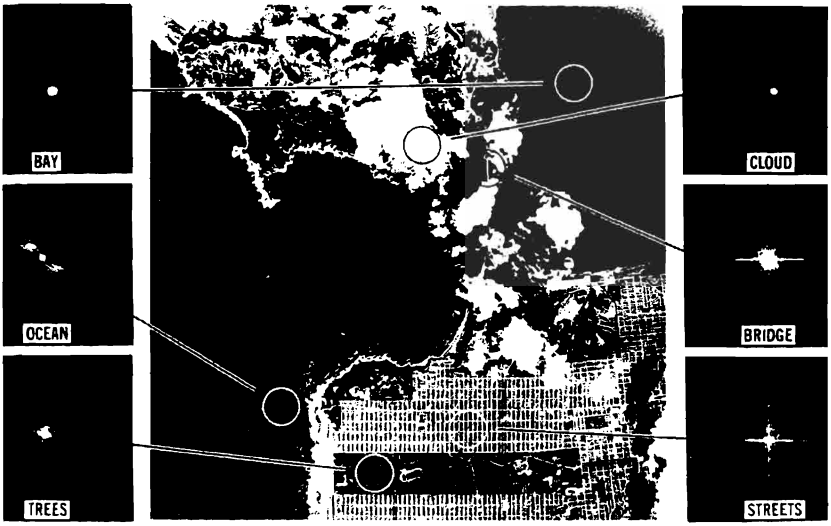

Figure 4.6. Examples of two-dimensional spectrum analyses (courtesy of Robert Leighty, U.S. Army Engineering Topographic Laboratory).

sequentially scan small portions of the input, the spectra of these subregions can be detected in the Fourier plane to give an indication of texture and its variation from one region to another.

To properly characterize the spectral information in a signal, we generally need to illuminate a subregion of the signal with a light beam that is the right size. If the light beam is too large, the spectral characteristics of the region are not well defined; if the light beam is too small, there is insufficient information on which to form a spectral estimate. A typical illumination subsystem is shown in Figure 4.7, in which the laser beam of diameter A_1 is expanded to a diameter A_2 by means of the beam-

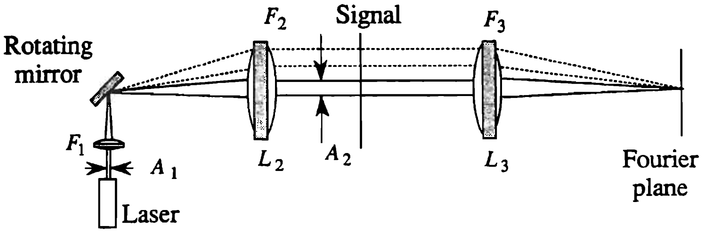

Figure 4.7. Telecentric scanning system.

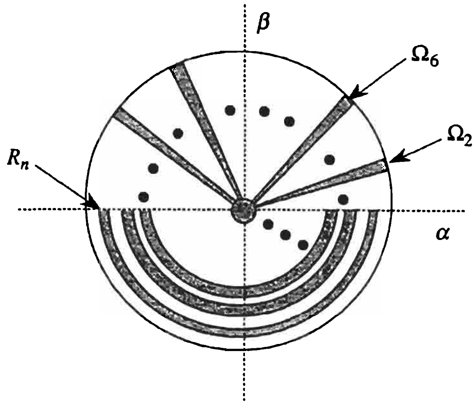

Figure 4.8. Special ring/wedge photodetector.

expanding telescope. The beam size ratio A_1/A_2 is the same as the focal length ratio F_1/F_2. At the common focal plane, we place a rotating mirror to provide the beam-scanning action at the signal plane.

It is important that the light strike the signal normal to its surface so that the Fourier transform, as produced by lens L_3, is always centered on the optical axis in the Fourier plane. At each position of the telecentric illuminating beam, the photodetector array is read out to produce the spectral content of the region being illuminated. Scanning in the orthogonal direction can be provided by a second scanning stage, similar to the one described. Sometimes the first stage is a fast scanning subsystem, using an acousto-optic scanner (see Chapter 7), combined with a slow scanning stage provided by a galvanometer mirror. Multifaceted rotating mirrors may also be used when the scanning velocity is high.

A useful array for detecting these spectral features consists of a set of wedge and annular photosensitive areas (35, 36), as shown in Figure 4.8. In this device, called a *ring/wedge detector*, one half of the area contains N photoconductive surfaces in the shape of wedges. The output signals $\Omega_1, \Omega_2, \ldots, \Omega_N$ are proportional to the amount of light that falls on each of the wedge-shaped photodetector elements to indicate the degree to which the signal $s(x, y)$ has spectral content at specific angles. The other half of the detector consists of N photodetector areas in the shape of narrow annular rings. The ring output signals $R_1, R_2, \ldots, R_N$ indicate the relative energy present in $s(x, y)$ at various spatial frequencies. The output from R_1, due to the circular photodetector element located in the center of the array, is proportional to the integrated amplitude of the signal and is used to normalize the spectrum.

As the spectrum $S(\alpha, \beta)$ is symmetric about the origin when the signal $s(x, y)$ is real valued, no information is lost in the detection process other than that which falls between the active areas. The signal is classified by postprocessing the Ω_i and R_i values according to algorithms developed for specific applications. Details of the postprocessing are not important here; requirements on the photodetector are. We now consider some of these requirements.

4.4.2. Spectral Responsivity and Typical Power Levels

The operating wavelength is dictated by factors such as the diffraction efficiency of the spatial light modulator, scattering in the optical system, and the availability of compact, efficient sources. We need photodetector elements whose *spectral responsivity* is in the 450–850-nm range to operate effectively with commonly available light sources. The photodetector must have a high responsivity at the wavelength generated by the laser but need not have a broad spectral response.

Photometry is a science whose terminology is strange. In the photometry literature we find quantities such as lumens, lux, phots, stilbs, apostilbs, and candelas, which are divided by feet, square feet, steradians, centimeters, and the like, to get even stranger quantities such as a nit (a candela per square meter). Because we deal largely with systems that use monochromatic light, photometry is considerably simplified. We use watts as the measure of optical power and millimeters as the unit of distance. The responsivity S of a discrete photodetector element is the ratio of the photocurrent to the incident light power, expressed in units of amps/watt.

The amount of optical power at the output of a spectrum analyzer is dependent on the efficiency of various components in the system and the collection efficiency of the photodetector. In Section 4.6, we discuss the optical power budget in detail; here we summarize just the main points. In a spectrum analyzer, we generally operate the spatial light modulator at a diffraction efficiency of no more than 1% per frequency to contain intermodulation products at an acceptable level. The rest of the system is typically about 10% efficient, primarily due to beam-shaping losses. The photodetector element collects about 30% of the light power associated with any given frequency because we generally use three detectors per frequency to achieve the required system performance. The maximum power that a photodetector intercepts for a laser with output power in the 10–30-mW range is of the order of 3–9 μW. The weakest signal is often 60–70 dB below this level.

4.4.3. The Number of Photodetector Elements

The ring/wedge photodetector, while useful for feature analysis, does not preserve all the information available in the Fourier plane because it does not have enough elements. The space bandwidth product of the input signal establishes the number of elements required of the photodetector array. The sampling theorem, as stated in Chapter 1, requires that we have $N \geq 4\text{SBP}$ elements in a two-dimensional photodetector array to avoid loss of information.

The number of photodetector elements required is large when processing high-quality signals. For example, if the highest frequency in a two-dimensional signal is 100 Ab and if the signal is 100 mm on a side, we require a 20,000 × 20,000-element array; this is at least an order of magnitude larger, in each dimension, than existing photodetector arrays. Therefore either bandwidth or frequency resolution must be sacrificed until larger photodetector arrays become available.

The situation is more favorable when processing two-dimensional signals with low information content, such as those produced by two-dimensional collection systems that also use CCD technology. Low-resolution video cameras may produce images in a 300 × 400-sample array, requiring a fairly simple photodetector array. The photodetector-array requirements are also more easily achieved in some one-dimensional signal-processing applications. For example, we often use acousto-optic cells to convert a wideband time signal to one that is a function of both space and time. (See Chapter 7 for more details.) Typical values for the time bandwidth product of acousto-optic cells are of the order of TW = 1000, which is almost independent of the interaction material used. Linear photodetector arrays, with up to 4096 elements on a single chip and coupled to a CCD readout structure, are available to satisfy these sampling requirements.

4.4.4. Array Geometry

The appropriate photodetector array for a one-dimensional spectrum analyzer is a linear array as shown in Figure 4.9. The array consists of M active elements shown shaded, each of width d' and height h. Each

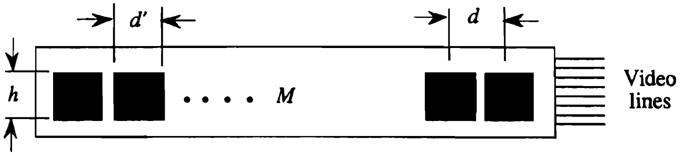

Figure 4.9. One-dimensional linear photodetector array.

element behaves as a photocapacitor on which electric charge accumulates in proportion to the incident light intensity and to the integration time. The array is read out serially by transferring the charge to a CCD structure and shifting the information onto multiple video lines, whose readout rates are each in the 1–10-MHz range.

The center-to-center spacing between photodetector elements is d and $c = d'/d$ is the spatial duty cycle of the array elements. The angular separation between adjacent frequencies and the focal length of the transform lens must be related to the dimensions of the array. For a uniformly illuminated signal of length L, the angular separation $\delta\theta$ between minimum resolvable frequencies $\delta\alpha$ is simply $\delta\theta = \lambda/L$ so that the frequencies are separated by a distance $\lambda F/L$, at plane P_2.

We need at least two detector elements per frequency to satisfy the sampling theorem in the Fourier domain; we therefore conclude that

$$2d \leq \frac{\lambda F}{L}. \tag{4.3}$$

In Section 4.5, we refine these calculations to account for signals that have weighted illumination to control sidelobe levels in spectral analysis applications.

Aberrations in an optical system are most easily kept under control if the relative aperture, which is approximately equal to $2L/F$, is less than $\frac{1}{10}$. Thus, an ideal center-to-center spacing for the photodetector elements is $d \approx 10\lambda$, which is of the order of 6–8 μ. The center-to-center spacing on currently available linear arrays is typically 12 μ or more; as a result, the focal length of the Fourier-transform lens and, therefore, the overall length of the optical system is somewhat greater than the optimum length. The size of the optical system is not a concern for ground-based systems because the volume of the optical system is generally a small fraction of that of the electronics. In airborne systems, however, the electronics are often packaged using very large scale integration (VLSI) techniques so that the volume and weight of the optical spectrum analyzer becomes relatively more important.

For one-dimensional applications, the height h of the photodetector is set by the signal height H in a fashion similar to Equation 4.3. If $H \neq L$, we use cylindrical lenses to match the vertical height of the spectrum to that of the array. For a two-dimensional application the photodetector center spacing and duty cycle are generally the same in both directions.

The required geometric accuracy for most spectrum analysis and correlation applications is that center spacings are within $\pm 1\%$ of their nominal positions, with a cumulative error of less than $\pm d/10$ at any position in the array. Semiconductor fabrication precision is usually better than the optical distortion in the system.

4.4.5. Readout Rate

In two-dimensional applications, the frame rate is a function of how rapidly the signal information changes. The spatial light modulator frame rate, in turn, determines how rapidly the spectrum changes; the photodetector array is typically read out once per frame. Integration on the array may range from a few milliseconds to a few seconds, provided that the detector does not saturate so that a linear response is maintained. The contents of the array are read out just before saturation, digitized, stored, and accumulated in postdetection memory. The accumulated values represent the desired spectrum and are available for further postprocessing operations.

In other applications, such as those involving real-time processing of one-dimensional signals as discussed more fully in Chapters 8 and 10, the spectrum may change rapidly so that we must read the array once every T seconds, where T is of the order of several microseconds. Unfortunately, the resultant temporal sampling rates are often not sustained by CCD transfer rates or by the digital postprocessing system, even when multiple video lines are used.

In both one-dimensional and two-dimensional spectrum analysis, we would benefit from the development of *smart arrays*, in which some postprocessing functions are included on the photodetector chip. Implementing logic functions at the array element level reduces the transfer data rates and the complexity of the subsequent electronics drastically. For example, suppose that we transfer information only if a photodetector element exceeds some preselected threshold. Or, suppose that we transfer information only if the instantaneous intensity exceeds some preset value. These operations require built-in circuitry for each element or groups of elements in the array. The implications of developing such a capability are enormous because the transfer rates associated with processing a wideband received signal may then be reduced by factors of 10^2–10^3 or more.

4.4.6. Blooming and Electrical Crosstalk

When we use long integration times to detect weak signals, we must ensure that the excess charge produced by strong signals is properly drained away so that spillover into adjacent elements does not mask weak signals. The spillover is sometimes optical in origin, with photons migrating from one photodetector element to another through the substrate of the array; this spillover is called *blooming*. Blooming is a more severe problem at longer wavelengths because of increased penetration distances in the substrate.

If the spillover is electrical in origin it is called *crosstalk*. We typically want the effects of crosstalk and blooming to decrease at a rate of at least 10 dB per element, referenced to the saturated element, to a level of at least -70 dB for all elements farther away than the seventh element.

4.4.7. Linearity and Uniformity of Response

At low intensity levels, most discrete photodetector elements have a linear response. At higher intensities the response of the element becomes nonlinear and saturation eventually sets in. Because the dynamic range at the output of a spectrum analyzer is large, we often introduce a compression scheme to facilitate the readout and display of the information. If the response of the photodetector is monotonic, a high degree of linearity is not required, provided that we can establish an inverse mapping that allows us to measure the spectrum to the required accuracy.

The saturation phenomenon is abrupt for some CCD arrays. The charge accumulates until the well is full; additional charge does not accumulate so that there is a discontinuity in the derivative of the transfer curve. As a unique inverse mapping of the signal intensities is not available for this case, we must avoid saturating these CCD arrays. Other CCD arrays offer a more gradual approach to saturation in an effort to gain more dynamic range. Again, an inverse mapping can be used to determine the true magnitude of the spectrum.

The *uniformity of response* of an array is defined as the variation in the output voltage or current due to manufacturing imperfections. A uniformity of response of ±10% is generally adequate; this degree of uniformity is easily met with current technology or can be corrected by using lookup tables. Differences in odd/even channel output levels may be corrected by postdetection gain compensation.

4.5. SYSTEM PERFORMANCE PARAMETERS

The key parameters that affect performance of spectrum analyzers at the system level are summarized as

- Total spatial frequency bandwidth (Section 4.5.1)
- Sidelobe levels/crosstalk (Section 4.5.2)

- Frequency resolution/dip between photodetector elements (Section 4.5.3)
- Array spacing and number of photodetector elements (Section 4.5.4)
- Dynamic range (Section 4.6)
- Intermodulation products (Section 4.6.1)
- Signal-to-noise/minimum signal level (Section 4.6.2)
- Integration time/bandwidth (Section 4.6.3)

We discuss the relationships among these performance parameters in the following paragraphs. Because the relationships are coupled in some cases, an iterative procedure may be needed to satisfy all the specifications simultaneously.

4.5.1. Total Spatial Frequency Bandwidth

The spatial frequency bandwidth for a baseband signal is simply equal to the highest spatial frequency α_{co} contained in the signal. If the signal is real valued, the spectrum is redundant about zero frequency and the photodetector need cover only half the Fourier plane, from 0 to α_{co}, as explained in Section 4.4.1. For a bandpass signal, centered on a carrier frequency α_c, the bandwidth extends from $\alpha_c - \alpha_{co}$ to $\alpha_c + \alpha_{co}$. The spectrum is redundant about α_c if the signal represents a baseband signal modulating a carrier frequency. In the more general case, the spectrum is nonredundant and the total spectral range is $2\alpha_{co}$.

4.5.2. Sidelobe Control and Crosstalk

In Section 4.4.2, we calculated the photodetector element spacing on the assumption that the signal is uniformly illuminated. We now consider the more typical situation in which an *aperture weighting function* is used to control the sidelobe levels of a cw frequency response in the Fourier plane. Aperture functions, a subset of the general class of apodization functions used in optics, are also used in digital signal processing, where they are generally called *window functions*. Candidate aperture functions are the rectangular, Bartlett, Hamming, Hanning, Chebyshev, Dolph-Chebyshev, Gaussian, Kaiser-Bessel, and Blackman window functions. Figure 4.10 shows four representative aperture functions defined over an aperture of length L. We indicate aperture functions by $a(x)$; the specific

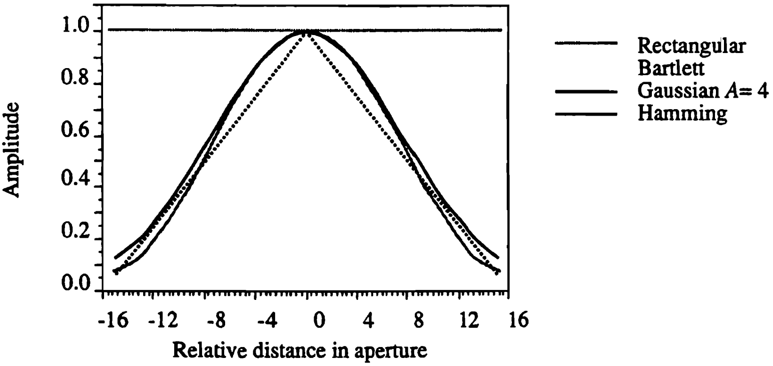

Figure 4.10. Four aperture functions.

functions we consider are

1. *Rectangular*

$$a(x) = \text{rect}(x/L) \equiv \begin{cases} 1, & |x| \le L/2 \\ 0, & \text{elsewhere.} \end{cases} \tag{4.4}$$

2. *Bartlett*

$$a(x) \equiv \text{rect}\left(\frac{x}{L}\right)\left[1 - \frac{2|x|}{L}\right]. \tag{4.5}$$

3. *Gaussian*

$$a(x) \equiv \text{rect}(x/L)e^{-(A/2)(2x/L)^2} \tag{4.6}$$

4. *Hamming*

$$a(x) \equiv \text{rect}(x/L)[0.54 + 0.46\cos(2\pi x/L)]. \tag{4.7}$$

The response in the Fourier plane to an aperture function is

$$A(\xi) = \int_{-\infty}^{\infty} a(x)e^{j(2\pi/\lambda F)\xi x}\,dx. \tag{4.8}$$

Figure 4.10 shows that, aside from the rect function, which has a uniform

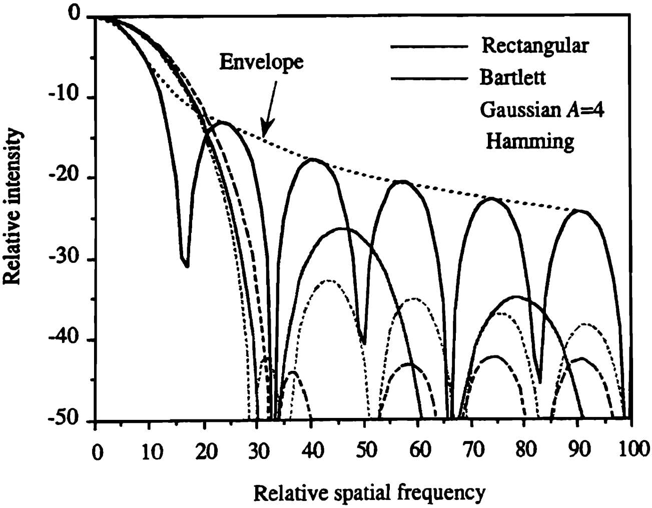

Figure 4.11. Frequency response (in decibels) of aperture functions.

magnitude over the entire aperture, the aperture functions have remarkably similar magnitude responses. Figure 4.11, however, shows that the sidelobe response levels in the Fourier plane are distinctly different for these four aperture functions; all responses have been normalized to unity at zero spatial frequency.

The first aperture function is the rect function for which

$$
\begin{aligned}
A(\xi) &= \int_{-\infty}^{\infty} \operatorname{rect}\left(\frac{x}{L}\right) e^{j(2\pi/\lambda F)\xi x}\, dx \\
&= L \operatorname{sinc}\left(\frac{\xi L}{\lambda F}\right).
\end{aligned}
\tag{4.9}
$$

The sinc function provides good frequency resolution because its *mainlobe* is narrow, but it has high *sidelobes* that decrease slowly as a function of distance from the mainlobe. The first sidelobe of $|A(\xi)|^2$ is only 13 dB down from the mainlobe, and the sidelobe intensity falls off as $1/\xi^2$. High sidelobe levels may obscure weak signals that we want to detect and contribute energy to adjacent photodetector elements as optical crosstalk. Because the sidelobes originate from large, sharp discontinuities in the signal, we can reduce them by using other aperture functions.

The Bartlett aperture function is a triangular function that we can view as the autocorrelation of two rect functions whose widths are just half that of the full aperture. As the Fourier transform of the convolution of two functions is the product of the Fourier transforms of the individual functions, the magnitude response in the Fourier plane is a sinc^2 function whose nulls are spaced twice as far apart as those in the sinc function produced by $\text{rect}[x/L]$. The first sidelobe due to the Bartlett aperture function is therefore located at about the same spatial frequency as the second sidelobe due to the rect function. Although the magnitude of the sidelobes falls off at twice the rate of those due to the rect function, they are still too high for most applications. Note that the rect function has a discontinuity in its magnitude and in all its derivatives; the Bartlett aperture function does not have a discontinuity in its magnitude, but it does have discontinuities in its derivatives.

The Gaussian aperture function produces lower sidelobe levels than either the rect or the Bartlett aperture functions; its sidelobe level is controlled by selecting the value of the parameter A, which determines the magnitude of the illumination at the aperture edges. The rate at which the sidelobe magnitudes decrease depends on the value of A.

The Hamming aperture function has the interesting property that all its sidelobes are about 45 dB down relative to the mainlobe, even though it has discontinuities in both its magnitude and its derivatives.

A typical specification for a spectrum analyzer is that the sidelobe levels are no higher than -50 dB relative to the peak mainlobe level at a position equivalent to five resolvable frequencies away from the centroid of the mainlobe. The measurement is always made to the *envelope* of the sidelobes, shown in Figure 4.11, to avoid any pathological cases where the required measurement position might fall in a null between two sidelobes. The trick is to determine what is meant by "five resolvable frequencies away." To do so, we discuss frequency resolution in greater detail.

4.5.3. Frequency Resolution / Photodetector Spacing

The price to pay for using an aperture function that produces lower sidelobes is a wider mainlobe width, as measured at the -3-dB intensity response point, which leads to a lower frequency resolution. Figure 4.12 shows, on a linear scale, the mainlobes of $|A(\xi)|^2$ for the four aperture functions under consideration. We see that the rect function provides the most narrow mainlobe and that the Hamming function produces the widest mainlobe. The Gaussian aperture function has the

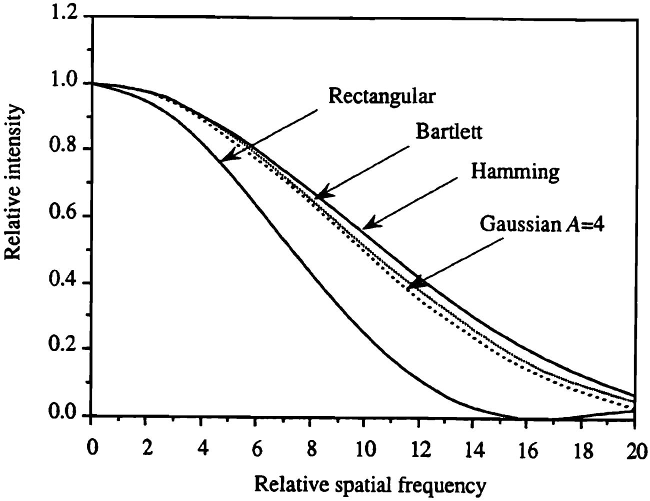

Figure 4.12. Mainlobes plotted on a linear scale.

second-narrowest mainlobe of this set of aperture functions, representing a reasonable compromise between sidelobe control and frequency resolution.

In Figure 4.13 we capture these two key features of the aperture response function by plotting the mainlobe width, relative to that provided by the rect function, on the vertical axis and the highest sidelobe level on the horizontal axis. The performance of the rectangular, Bartlett, and Hamming functions are represented by single points, but the performance of the Gaussian function is given for several values of the parameter A. We also include three other aperture functions for comparison: the Hanning, the Kaiser, and the Chebyshev. These functions are defined as

5. *Hanning*

$$a(x) \equiv \operatorname{rect}(x/L)[0.5 + 0.5\cos(2\pi x/L)] \tag{4.10}$$

and

6. *Kaiser*

$$a(x) \equiv \operatorname{rect}\left(\frac{x}{L}\right)\frac{I_0\left[\beta L\sqrt{1-(2|x|/L)^2}\right]}{I_0(\beta L)}, \tag{4.11}$$

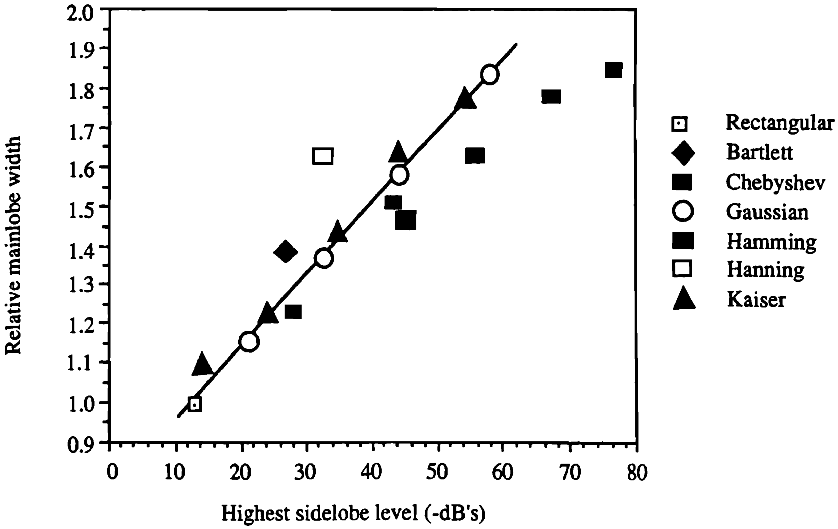

Figure 4.13. Mainlobe width vs. highest sidelobe level.

where $I_0(\cdot)$ is a modified Bessel function and β is a scaling parameter that determines the sidelobe levels.

The last aperture weighting function, the *Chebyshev* function, is described in terms of integrals of the product of polynomials and orthogonal functions. As both the Kaiser and Chebyshev aperture functions are difficult to generate optically, we do not seriously consider them for use in signal-processing systems. Their responses are included here for comparison.

The main conclusion drawn from the data in Figure 4.13 is that the Gaussian aperture function, while not providing the ultimate in performance in terms of sidelobe levels, is the aperture function of choice because it occurs naturally as the intensity profile of illumination from lasers. Attempts to improve on its performance, using additional masks or apertures, generally add noise to the system. We therefore use the Gaussian aperture function as our baseline for optical spectrum analyzers.

Having settled on the Gaussian aperture function as the most practical, we use the parameter A to control the truncation points needed to get the desired sidelobe suppression. Figure 4.14 shows the response in the Fourier plane for $A = 2, 4, 6,$ and 8; the Gaussian function degenerates to the rectangular function when $A = 0$. By referring to Equation (4.6), we see that the illumination is truncated at the $1/e^{-A}$ *intensity* points at the

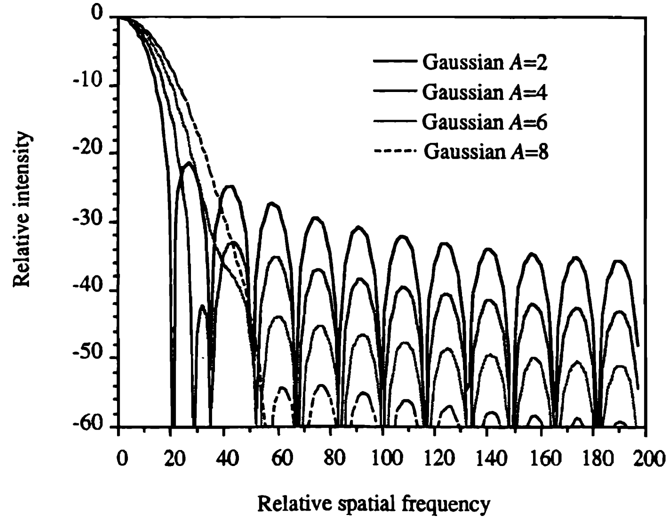

Figure 4.14. Frequency response of four Gaussian aperture functions.

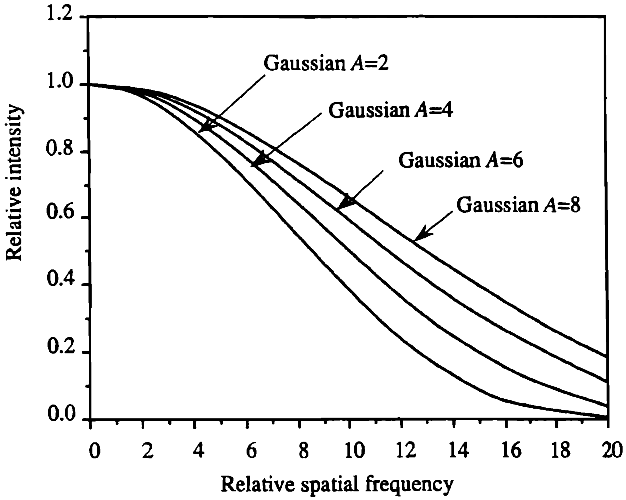

Figure 4.15. Mainlobes for four Gaussian aperture functions.

edges of the signal, where $|x| = L/2$. Figure 4.15 gives the relative mainlobe widths of these aperture functions; we use Figures 4.14 and 4.15 to balance the loss of resolution due to the increased mainlobe width, as a function of a given sidelobe reduction level.

The amount of available laser power used is also a function of the parameter A. The collected power is obtained by integrating the *intensity* of the light over the input plane:

$$\text{fraction of power collected} = \frac{\int_0^{L/2} e^{-A(2x/L)^2}\, dx}{\int_0^{\infty} e^{-A(2x/L)^2}\, dx} = \operatorname{erf}(\sqrt{A}), \quad (4.12)$$

where erf(·) is the error function. For $A > 3$, at least 98.5% of the laser power is used. The Gaussian aperture function, in addition to providing reasonable frequency resolution and sidelobe control, is efficient in terms of the amount of optical power used.

With the sidelobe level under control, we turn our attention to a more complete discussion of frequency resolution. *Frequency resolution* is generally defined in terms of the dip in the intensity response in the Fourier plane produced by two cw signals; the measurement is taken midway between the peak response of the frequencies. A typical specification is that the dip must be 2–3 dB down from the peak response. Figure 4.16(a) shows the response in the Fourier-transform plane to a frequency at ξ_0 and to a frequency spaced $\delta\xi$ away; these frequencies produce the intensity responses $|A(\xi - \xi_0)|^2$ and $|A(\xi - \xi_0 - \delta\xi)|^2$ We sum the intensities from these two functions and find the dip between them relative to the peak response, as shown in Figure 4.16(a).

We cannot, however, simply read the dip value from Figure 4.16(a) because the width of the photodetector element affects the intensity measurements at the Fourier plane. If the photodetector elements were infinitesimally small and the spacing between them were nearly zero, the measured dip would be accurately measured. A photodetector element of finite size d', however, tends to smooth the detected spectrum somewhat, thereby reducing the dip between frequencies.

A few of the elements from the photodetector array are shown in Figure 4.16(a). One way to account for the finite size of the photodetector elements is to integrate the light intensity over the photodetector elements and to then measure the dip relative to the maximum value. Unfortunately, we would need to do this for all possible input frequencies because we do not know *a priori* where the frequencies occur relative to the

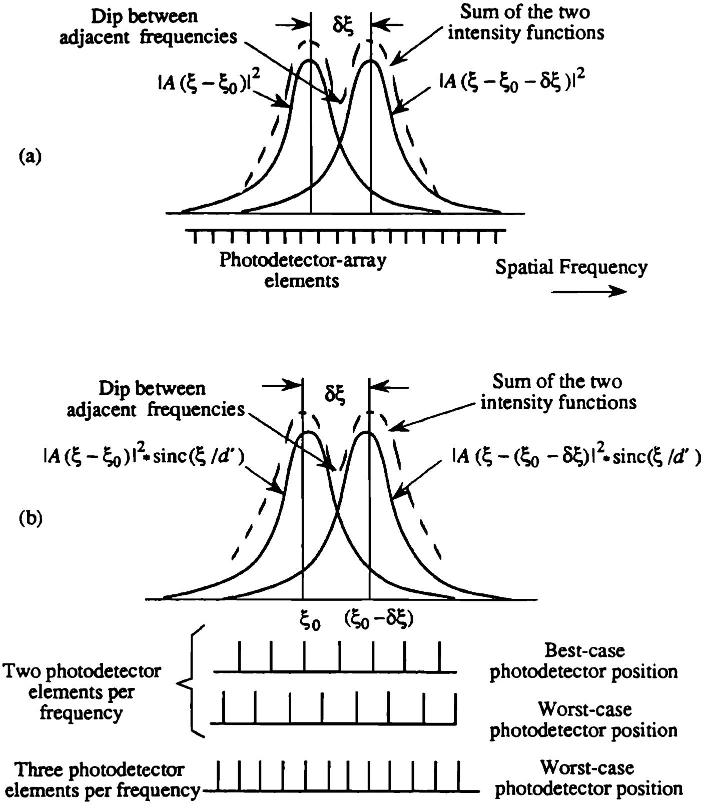
Dip between adjacent frequencies
$\delta\xi$
Sum of the two intensity functions
$|A(\xi-\xi_0)|^2$
$|A(\xi-\xi_0-\delta\xi)|^2$
(a)
Photodetector-array elements
Spatial Frequency
Dip between adjacent frequencies
$\delta\xi$
Sum of the two intensity functions
$|A(\xi-\xi_0)|^2 * \mathrm{sinc}(\xi/d')$
$|A(\xi-(\xi_0-\delta\xi)|^2 * \mathrm{sinc}(\xi/d')$
(b)
ξ_0 $(\xi_0-\delta\xi)$
Two photodetector elements per frequency
Best-case photodetector position
Worst-case photodetector position
Three photodetector elements per frequency
Worst-case photodetector position

Figure 4.16. Frequency resolution and number of photodetectors: (a) sum of intensity of two frequencies after convolution with a photodetector element and (b) method for determining the dip response.

photodetector elements. An easier way to determine the effect of finite photodetector elements is to start by convolving $|A(\xi)|^2$ with a photodetector element of size d'. The question is "what value do I initially assign to d'?". We now describe an iterative procedure that produces a photodetector-element separation that satisfies all the constraints.

4.5.4. Array Spacing and Number of Photodetector Elements

The first issue in determining the array spacing is to find the required number of photodetector elements per frequency. One might argue, of course, for using as many photodetector elements as possible to provide for the best possible frequency resolution under all conditions. But an unnecessarily large number of photodetector elements leads to excessive output data rates from the array, as discussed in Section 4.4.5. The trick is to use the smallest number of elements in the photodetector array that meets the frequency-resolution specification for an aperture function that meets, in turn, the sidelobe level specification. An iterative calculation may be needed in which we increase the value of $\delta\xi$ until all the specifications are met simultaneously. When this process is finished, we must ensure that the length L of signal history is sufficient to provide the frequency resolution and that the sidelobe level still meets specification for that condition.

In Section 3.5.4, we argued that the number of samples in the spatial and Fourier domains are equal. It might appear, therefore, that one detector per resolvable frequency satisfies the sampling theorem. In a spectrum analyzer application, however, we generally need to resolve closely spaced frequencies. To handle the worst-case frequency-resolution specification, we need about three photodetector elements per frequency, as we show shortly.

A starting point is to use the specification for $\delta\alpha$ and the selected $|A(\xi)|^2$ to provide the required sidelobe control to make an estimate of the photodetector size d'. Here is where some judgment is exercised; experience helps, too. As the physical distance in the Fourier plane between resolvable frequencies is $\delta\xi = \delta\alpha\lambda F$, a reasonable starting point is to require three photodetectors per frequency so that $d' \approx (\delta\xi)/3$. We then convolve the photodetector element, represented by $\mathrm{rect}(\xi/d')$, with $|A(\xi)|^2$ to get the responses for the two frequencies as shown in Figure 4.16(b). As we have now accounted for the finite photodetector size, we can replace the $\mathrm{rect}(\xi/d')$ photodetectors by delta functions as shown in the lower part of Figure 4.16(b). The advantage of this method is that we can now simply slide the delta-function representation of the photodetector array along the spatial frequency axis and read the relative detected values from the dotted function representing the sum of the two intensities. This can be done for any position of the frequencies relative to the photodetector array to find the worst-case response.

The danger of using only two photodetector elements per frequency is illustrated in Figure 4.16(b) in which the delta functions sample the sum of the two intensity responses from the two frequencies. In the best-case condition, one of the photodetector elements is located exactly on the minimum value between frequencies and the dip specification is met. But if the two frequencies shift, relative to the photodetector array, as shown for the worst-case condition, the dip may completely disappear so that the frequencies are not resolved at all. Using three photodetector elements per frequency corrects this situation because at least one photodetector element is always near the maximum dip position.

To illustrate this iterative process, suppose that we use three photodetector elements per frequency and initially estimate that a spacing of 18 units between the frequencies will provide a dip of 3 dB. The spacing between photodetector elements is therefore 6 units. We assign the photodetectors a length of 5 units so that the duty cycle is $c = \frac{5}{6}$. The next step is to convolve the photodetector, represented by rect($\xi/5$), with the response $|A(\xi)|^2$; the result is shown in Figure 4.17(a). We then shift the convolved response 18 units and add it to itself to simulate two frequencies, spaced by 18 units, detected by a photodetector array in which the elements are 5 units wide on 6 unit spacings. The sum of the two responses is shown in Figure 4.17(b).

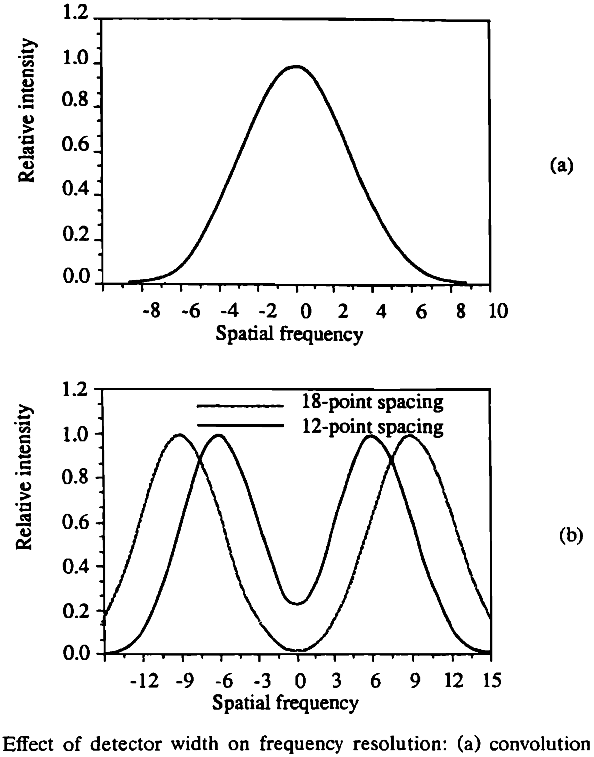

Figure 4.17. Effect of detector width on frequency resolution: (a) convolution of detector with Gaussian response ($A = 4$) and (b) sum of intensities from two frequencies.

We are interested primarily in the region between the two peaks. The worst-case condition for resolving two frequencies occurs when two elements of the photodetector array straddle the null between the frequencies. For this case, the photodetector elements are at the points -9, -3, 3, and 9. We see that the responses at -9 and 9 are equal to one and the responses at -3 and 3 are equal to 0.15. The dip is therefore about 8 dB, which is too high because of our overly conservative decision to space the two frequencies by 18 units.

The next iteration is to space the frequencies by 12 units; the photodetector elements are then chosen as 3 units wide, on 4 unit spacings for a duty cycle of $c = 3/4$. The result of summing the responses from two frequencies is also shown in Figure 4.17(b) for this case. Note that the photodetector elements are located at -6, -2, 2, and 6 for the worst-case situation. The responses at -6 and 6 are equal to one and the responses at -2 and 2 are equal to 0.4, which yields a dip of about 4 dB. This spacing is still slightly too large, but convergence to the desired dip of 3 dB will probably take only one more iteration.

All these calculations are performed without regard to the actual physical size of the photodetector element or the focal length of the Fourier-transform lens. The final step is to calculate the focal length of the lens so that the interval between two resolvable frequencies is equal to three photodetector intervals on the chosen array.

At first glance, it seems that the source size affects the mainlobe width and, therefore, the frequency resolution. Since $a(x)$ is the Fourier transform of the source, the required aperture function $a(x)$ is provided only if the source has the correct size at the onset. Spectral purity of the source may also spread the mainlobe, thereby reducing the frequency resolution. This spreading is rarely a problem with gas lasers where the fractional spectral spread is on the order of $\Delta\lambda/\lambda \approx 10^{-7}$. A high-pressure source has a $\Delta\lambda/\lambda \approx 10^{-3}$, and a typical injection laser diode has $\Delta\lambda/\lambda \approx 10^{-2}$. In all cases, the increased spreading of the mainlobe due to the source wavelength spread is small. Spectral spreading in the source also causes the sidelobes to smear somewhat, filling in the nulls, but this does not significantly change the calculations because we always use the envelope of the sidelobes to determine the required aperture function.

4.6. DYNAMIC RANGE

Dynamic range is the most important performance parameter of a spectrum analyzer. We may require a dynamic range of 60–80 dB in many applications. Dynamic range is defined as the ratio of the largest to the smallest signal supported by the system, ***referenced to the input of the system***. The smallest signal is generally determined when the signal-to-noise ratio is unity, although some users prefer to establish a signal-to-noise ratio of 3–6 dB as the minimum signal level that is meaningful. The maximum signal level is set by intermodulation products, caused by nonlinearities in the response of the spatial light modulator.

4.6.1. Intermodulation Products

All spatial light modulators have nonlinearities that distort the amplitude of the input signal. The input/output curve is generally linear at small input signal levels; at higher signal levels all spatial light modulators eventually saturate and distort the signal amplitudes. This distortion results in intermodulation products that produce false signals in the Fourier plane. For example, suppose that the input/output relationship, shown in Figure 4.18(a), is a sinusoidal function, defined between 0 and

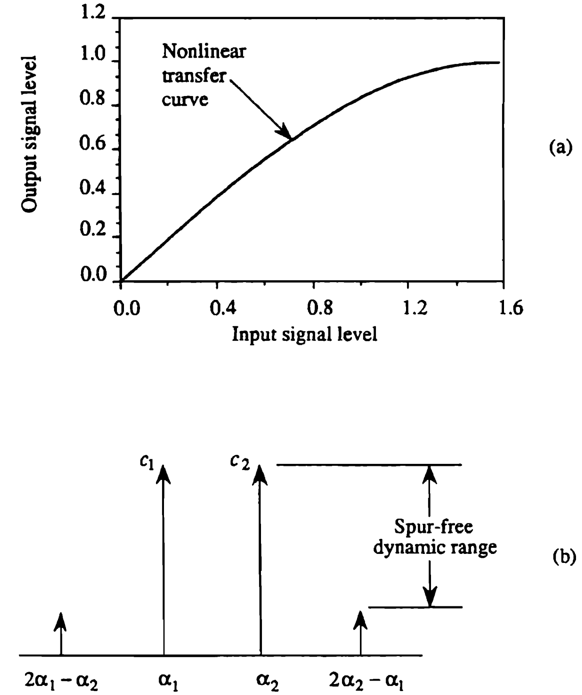

Figure 4.18. Effects of nonlinearities: (a) dynamic transfer curve and (b) spurious frequencies.

$\pi/2$, so that the two leading terms of the power-series expansion are

$$O(x, y) = I(x, y) + \tfrac{1}{6}I^3(x, y), \tag{4.13}$$

where $I(x, y)$ is the input signal and $O(x, y)$ is the output signal from the spatial light modulator. Suppose that the input is the sum of a bias and two cosine waves of the form

$$I(x, y) = \tfrac{1}{3}[1 + \cos(2\pi\alpha_1 x) + \cos(2\pi\alpha_2 x)]. \tag{4.14}$$

After substituting Equation (4.14) into Equation (4.13), we find frequency components at α_1 and α_2, due to the linear part of the input/output curve, and several new frequency components, including those at $2\alpha_1 - \alpha_2$ and at $2\alpha_2 - \alpha_1$, generated by the cubic nonlinearity term in the expansion of the input/output curve.

The new frequencies are *spurious signals*, generally shortened to spurs. A sketch of the frequency components in the Fourier plane is shown in Figure 4.18(b). We cannot, in general, distinguish the spurs from true signal frequencies. An important system specification, therefore, is one that requires a certain *spur-free dynamic range* so that weak signals can be distinguished from the spurs produced by strong signals. The spur-free dynamic range is defined as the ratio of the signal power at α_1 or α_2 to that at $2\alpha_1 - \alpha_2$ or $2\alpha_2 - \alpha_1$. It is met only by keeping the amplitudes of the sine waves below some maximum value by controlling the efficiency ε_m of the spatial light modulator; this efficiency level is stated as the *diffraction efficiency per frequency*.

Another factor in the detection of small signals is the amount of light scattered by various optical elements in the system. Multiple reflections before the spatial light modulator are particularly bad because they produce replicas of the spectrum, displaced from the primary spectrum according to the angles of reflection. Scratches and digs in optical elements, particularly those near the Fourier plane, may also cause scattered light to mask weak signals. Finally, regular structures such as the sample interval in a liquid-crystal display produce spurious noise patterns in the Fourier plane that may obscure signals. The solution to these problems is to ensure that the optical design does not contain flat surfaces which produce multiple reflections and to use antireflecting coatings on all surfaces. Specify minimum scratch and dig tolerances on all optical components and keep the components clean to reduce scattering.

4.6.2. Signal-to-Noise Ratio and the Minimum Signal Level

The minimum detectable signal level is determined by the signal-to-noise ratio available at the output of the system. In a well-designed spectrum

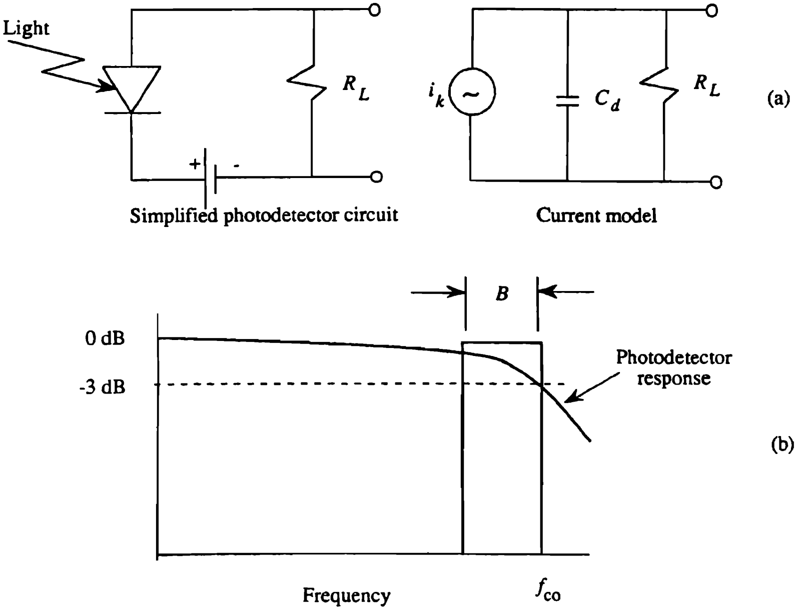

Figure 4.19. Photodetector model for signal-to-noise calculations: (a) photodetector circuit model and (b) frequency response of photodetector.

analyzer, the principal source of noise at the output is from the photodetector and its associated circuitry. A photodetector is modeled by the circuit shown in Figure 4.19(a), in which light falls on a semiconductor junction to generate electrons. The responsivity of the detector is a function of the nature of the material (e.g., silicon or gallium arsenide) and of the wavelength of light. The output current i_k from the kth frequency is the product of the responsivity of the photodetector and the incident optical power: $i_k = SP_k$, where S is the responsivity and P_k is the optical power collected by the photodetector element. In terms of the light intensity I_k, we find that $P_k = I_k\, dA$, where dA is the area of the photodetector. Thus the photocurrent is

$$i_k = SI_k\, dA. \tag{4.15}$$

The *signal-to-noise ratio* is calculated as

$$\text{SNR} = \frac{\text{signal power}}{\text{sum of the noise sources}}. \tag{4.16}$$

For the kth photodetector in the array, the signal-to-noise ratio is

$$\mathrm{SNR} = \frac{\langle i_k^2 \rangle R_L}{2eB\left(i_d + \bar{i}_k\right)R_L + 4kTB}, \tag{4.17}$$

where i_k is the signal current, $e = 1.6(10)^{-19}$ Coulomb is the charge on an electron, B is the postdetection bandwidth, i_d is the dark current of the photodetector, $\bar{i}_k$ is the average signal current, $k = 1.38(10)^{-23}$ J/K is Boltzmann's constant, and T is the temperature in degrees Kelvin. The first term in the denominator of Equation (4.17) is the *shot noise*, sometimes called quantum noise, and the second term is the *thermal noise*, sometimes called Johnson noise.

Equation (4.17) shows that we can increase the signal-to-noise ratio arbitrarily by increasing the load resistance until we are shot-noise limited. This procedure, however, may lead to an insufficient photodetector bandwidth. The relationship between the load resistance, capacitance, and cutoff frequency f_{co} is obtained from basic circuit theory as

$$f_{\mathrm{co}} = \frac{1}{2\pi c_d R_L}. \tag{4.18}$$

We solve Equation (4.18) for R_L and use it in Equation (4.17) to generate a more useful form of the signal-to-noise ratio equation:

$$\boxed{\mathrm{SNR} = \frac{\langle i_k^2 \rangle}{2eB\left(i_d + \bar{i}_k\right) + 8\pi kTBf_{\mathrm{co}}c_d}.} \tag{4.19}$$

In subsequent discussions we still refer to the terms in the denominator of Equation (4.19) as "shot" and "thermal" noise even though they represent the square of the noise *current* instead of the noise *power*, as they normally do.

The signals we detect may be either baseband signals, whose frequency content ranges from 0 to f_{co}, or a bandpass signal whose frequencies range from $f_{\mathrm{co}} - B$ to f_{co}. In either case, the maximum frequency response required of the photodetector circuit is f_{co}. For bandpass signals, we can improve the postdetection signal-to-noise ratio by using a bandpass filter of width $B < f_{\mathrm{co}}$, as shown in Figure 4.19(b).

To find the signal-to-noise ratio we relate the current to the input signal amplitudes. Consider a cw input signal $s(x) = 0.5[1 + c_k \cos(2\pi\alpha_k x)]$. The Fourier transform of the positive diffracted order is

$$\begin{aligned} S(\xi) &= \sqrt{\frac{P_0\varepsilon\varepsilon_m}{\lambda FL}} \int_{-\infty}^{\infty} \tfrac{1}{2}a(x)\left[\tfrac{1}{2}c_k e^{-j(2\pi/\lambda F)\xi_k x}\right] e^{j(2\pi/\lambda F)\xi x}\, dx \\ &= \tfrac{1}{4}\sqrt{\frac{P_0\varepsilon\varepsilon_m}{\lambda FL}}\, c_k \int_{-\infty}^{\infty} a(x) e^{j(2\pi/\lambda F)(\xi-\xi_k)x}\, dx \\ &= 0.25\sqrt{\frac{P_0\varepsilon\varepsilon_m}{\lambda FL}}\, c_k A(\xi - \xi_k), \end{aligned} \tag{4.20}$$

where $A(\xi)$ is the Fourier transform of the aperture function $a(x)$. For the spectrum analyzer shown in Figure 4.1, P_0 is the laser power, L is the length of the line illumination of the signal, ε_m is the efficiency of the spatial light modulator on a per-frequency basis, and ε is the efficiency of the remainder of the optical system, including the effects of the aperture function as discussed in Section 4.5.3. Recall from Chapter 3 that the Fourier transform has a scaling factor of $\sqrt{j/\lambda F}$ for the one-dimensional transform; this term appears in the scaling factor of Equation (4.20) but we ignore the $\sqrt{j}$ factor.

A photodetector element in the Fourier plane integrates the intensity $I(\xi) = |S(\xi)|^2$ of the light over the area of the photodetector element. The total optical power collected is therefore

$$P_k = \int_{-\infty}^{\infty} 0.0625 \frac{P_0\varepsilon\varepsilon_m}{\lambda FL} c_k^2 |A(\xi - \xi_k)|^2\, d\xi. \tag{4.21}$$

Although we use a Gaussian function to control the sidelobe levels, a rectangular aperture function provides closed-form solutions that illustrate details of the integration process. We therefore consider the case where $a(x) = \mathrm{rect}(x/L)$, for which $|A(\xi - \xi_k)|^2 = L^2 \mathrm{sinc}^2[(\xi - \xi_k)L/\lambda F]$, so that Equation (4.21) becomes

$$P_k = 0.0625 \frac{P_0\varepsilon\varepsilon_m}{\lambda FL} c_k^2 L^2 \int_{-\infty}^{\infty} \mathrm{sinc}^2\left[\frac{(\xi - \xi_k)L}{\lambda F}\right] \mathrm{rect}\left[\frac{\xi - \xi_k}{d'}\right] d\xi, \tag{4.22}$$

where $\mathrm{rect}[(\xi - \xi_k)/d')$ represents the size of the photodetector element centered at ξ_k. Figure 4.20(a) shows the geometry in the Fourier plane for

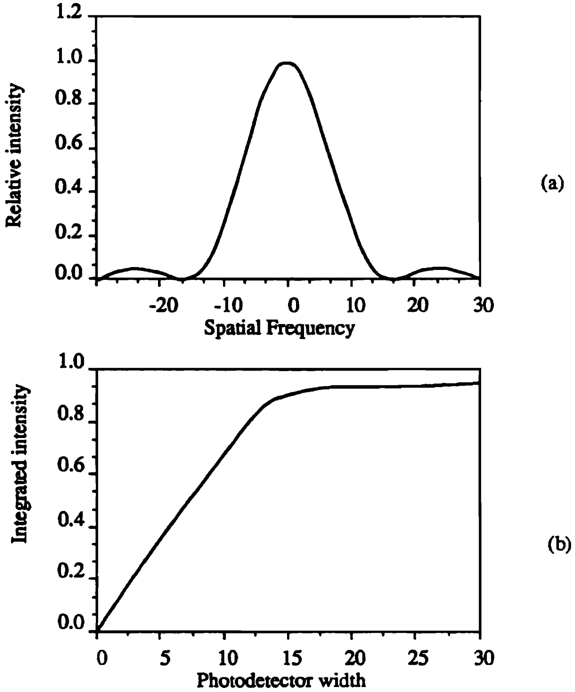

Figure 4.20. Spatially integrating detectors at the Fourier plane: (a) frequency response of a rect function and (b) intensity vs. detector width.

a sinc^2 function produced by the signal. To relate the arbitrary horizontal scale to ξ, we note that the first zero of the sinc^2 function occurs at $\xi = \lambda F/L = 15$ units. When we use three photodetector elements per frequency, the photodetectors are spaced $\Delta\xi = \lambda F/3L = 5$ units apart. The question is how much power the photodetector collects.

Figure 4.20(b) shows the integrated intensity for the sinc^2 function and we note that the integral is nearly a linear function of the photodetector width, for small widths. For a photodetector whose width is 5 units, we find that the value of the integral in Equation (4.22) is equal to $\lambda F/3L$. The total collected power is therefore

$$P_k = 0.0625 \frac{P_0 \varepsilon \varepsilon_m}{\lambda F L} c_k^2 L^2 \left[\frac{\lambda F}{3L} \right] = 0.02 P_0 \varepsilon \varepsilon_m c_k^2, \qquad (4.23)$$

and the photocurrent is

$$i_k = SP_k = 0.02SP_0\varepsilon\varepsilon_m c_k^2. \tag{4.24}$$

This result is interesting from three viewpoints: (1) it gives the connection between the electrical current and the optical signal power, (2) it shows that the detected optical power is not a function of parameters such as λ, L, and F, and (3) it shows that the photocurrent i_k is proportional to the *power* c_k^2 of the input signal.

Having found the optical power collected by the photodetector, we substitute Equation (4.24) into Equation (4.19) and set the signal-to-noise ratio equal to unity (or some other agreed upon value). We then solve for the minimum value of c_k which determines the dynamic range of the spectrum analyzer. The *dynamic range*, for a single tone, given in decibels is

$$\boxed{DR = 10\log\left[\frac{c_{k\,\max}^2}{c_{k\,\min}^2}\right],} \tag{4.25}$$

where $c_{k\,\max}^2 = 1$, by definition, is the maximum signal power that, together with the diffraction efficiency per frequency, establishes the maximum intermodulation product level; $c_{k\,\min}^2$ is the minimum signal power obtained from the signal-to-noise ratio calculation.

From Equations (4.19) and (4.24), we find that

$$1 = \frac{\left(0.02SP_0\varepsilon\varepsilon_m c_{k\,\min}^2\right)^2}{2eB\left(i_d + \bar{i}_k\right) + 8\pi kTBf_{\mathrm{co}}c_d}. \tag{4.26}$$

As all the parameters except c_k are specified, we can solve Equation (4.26) for $c_{k\,\min}^2$:

$$c_{k\,\min}^2 = \frac{\sqrt{2eB\left(i_d + \bar{i}_k\right) + 8\pi kTBf_{\mathrm{co}}c_d}}{0.02SP_0\varepsilon\varepsilon_m}. \tag{4.27}$$

It seems, at first, that we need to solve a quadratic equation in $c_{k\,\min}^2$ because $\bar{i}_k$ is also dependent on $c_{k\,\min}^2$. We find, however, that as c_k^2 becomes small, the value of $\bar{i}_k$ becomes much less than i_d so that we replace $(i_d + \bar{i}_k)$ by i_d.

From Equations (4.25) and (4.27) we find that

$$\boxed{DR = 10\log\left[\frac{0.02SP_0\varepsilon\varepsilon_m}{\sqrt{2eBi_d + 8\pi kTBf_{co}c_d}}\right].} \tag{4.28}$$

From Equation (4.28) we see that the dynamic range increases according to the available laser power and decreases according to the square root of the signal bandwidth.

4.6.3. Integration Time / Bandwidth

Equation (4.19) shows that the signal-to-noise ratio and, therefore, the dynamic range is maximized when the bandwidth B is minimized. The bandwidth is the reciprocal of the integration time of light on the photodetector array. The integration time, in turn, is determined primarily by how often the photodetector array must be read to avoid missing important information.

In some applications, the integration time is the same as the frame cycle time of the input spatial light modulator because each frame may contain a completely new signal. In other applications, such as those where photographic film is moving through the aperture, the integration time is on the order of the amount of time that any given sample stays within the aperture. In yet other applications, the integration time is determined by the rate at which the underlying information content is expected to change. As noted above, the cutoff frequency f_{co} is always dictated by the highest frequency that is passed by the system; the bandwidth B is dependent on whether the input is a baseband or a bandpass signal.

4.6.4. Example

Suppose that a spectrum analyzer has these parameters: $P_0 = 10$ mW, $i_d = 10$ nA, $c_d = 4$ pF, $S = 0.4$ A/W, and $T = 300$ K. Suppose that the maximum diffraction efficiency per frequency to meet a −40-dB intermodulation product specification requires that $\varepsilon_m = 0.05$ and that the rest of the system efficiency is $\varepsilon = 0.25$. If the spectrum analyzer processes information at a frame rate of 1000 frames per second, we have the baseband case for which the cutoff frequency and the bandwidth are $f_{co} = B = 1000$ Hz.

The first step is to find the minimum value of c_k^2 when the signal-to-noise ratio is equal to unity. The solution for $c_{k\,\min}^2$ is therefore found from Equation (4.27):

$$c_{K\,\min}^2 = \frac{\sqrt{2(1.6)(10^{-19})1000(10^{-8}) + 8\pi(1.38)(10^{-23})300(1000)1000(3)(10^{-12})}}{0.02(0.4)(10^{-2})0.25(0.05)}. \tag{4.29}$$

We carry out the calculations to find that

$$c_{k\,\min}^2 = \frac{\sqrt{3.2(10^{-24}) + 3.12(10^{-25})}}{10^{-6}} = 2(10^{-6}), \tag{4.30}$$

and because $c_{k\,\max}^2 = 1$, the dynamic range is easily calculated from Equation (4.25) as 57 dB.

4.6.5. Quantum Noise Limit

In the example of Section 4.6.4, the dominant noise source is shot noise so that the system is quantum noise limited. For low-bandwidth applications where shot noise dominates thermal noise, we can simplify the signal-to-noise ratio expression to

$$\text{SNR} = \frac{\langle i_k^2 \rangle}{2eB\left(i_d + \bar{i}_k\right)}. \tag{4.31}$$

The minimum noise occurs when $\bar{i}_k \approx i_d$.

As the required bandwidth increases, we reach a point at which thermal noise dominates shot noise. By comparing the two noise terms in the denominator of Equation (4.19), we find that the system remains shot-noise limited provided that

$$\boxed{f_{\text{co}} \leq \frac{ei_d}{4\pi kTc_d},} \tag{4.32}$$

which is dependent only on the key parameters of the photodetector. Note, in particular, that Equation (4.32) does not contain the bandwidth explicitly so that it is valid for both baseband and passband applications.

Many photodetector manufacturers quote the performance of their products in terms of *noise equivalent power*, which gives an indication of the amount of optical power needed to just overcome the noise in the detector. The quoted noise equivalent power is usually normalized and expressed as $\mathrm{W}/\sqrt{\mathrm{Hz}}$ so that we simply multiply noise equivalent power by the square root of the predetection bandwidth (f_{co} in this case) to get the required optical power at the photodetector. But this procedure is valid only when the photodetector is shot-noise limited. The noise equivalent power has no provision to include the effects of thermal noise, so be careful when using noise equivalent power in performance calculations.

4.6.5.1. Avalanche Photodiode. When the system is thermal-noise limited, we can improve the system performance by using an avalanche photodiode to provide internal gain. An avalanche photodiode is a normal photodetector element that is operated near its breakdown voltage. When light is collected and current begins to flow, breakdown action is initiated so that additional electrons are generated. This results in amplification, or gain, within the device. The signal is increased by the gain factor G, while the modified shot-noise term becomes (37)

$$SN = 2eB\left(i_d + \bar{i}_k\right)G^m, \tag{4.33}$$

where G^m is a gain factor characteristic of avalanche photodiodes. Typical values for m are 2.3–2.5 for silicon devices and 2.7–3.0 for III-V alloy devices. The thermal noise is not affected by operating the photodiode in the avalanche mode. The signal-to-noise ratio then becomes

$$\mathrm{SNR} = \frac{\langle i_k^2 \rangle G^2}{2eB\left(i_d + \bar{i}_k\right)G^m + 8\pi kTBf_{\mathrm{co}}c_d}, \tag{4.34}$$

and we note that the signal power is increased by the factor G^2.

We want to select the photodetector gain that maximizes dynamic range, using the minimum laser power. As noted before, this maximization occurs when shot noise and thermal noise are approximately equal so that the optimum gain is

$$G^m \approx \frac{4\pi kTf_{\mathrm{co}}c_d}{e\left(i_d + \bar{i}_k\right)}, \tag{4.35}$$

which reveals that avalanche diodes are most useful when the detection bandwidth is large. As the value of m must be greater than 2, any gain larger than that governed by Equation (4.35) results in a deterioration of the dynamic range, although the loss in performance is not a rapid function of the excess gain. The chief disadvantage of using avalanche photodiodes is that breakdown voltage and gain are sensitive functions of temperature so that they are more difficult and costly to regulate than conventional detectors.

4.6.5.2. Relationship between Signal-to-Noise Ratio and Dynamic Range. The relationship between signal-to-noise ratio and dynamic range is illustrated in Figure 4.21, in which we plot the shot noise, thermal noise, and output signal power as a function of input signal power. The maximum input signal power is $c_k^2 = 1$, which yields a signal level of 0 dB, as shown on the horizontal axis. The signal part of the output, as given by the numerator of Equation (4.19), is then at its maximum value. As the input level decreases, the signal part of the output also decreases with a slope of -2 because the output signal power is proportional to c_k^4.

As thermal noise is not a function of the input signal level, it is shown as a constant in Figure 4.21. Shot noise, on the other hand, is determined mainly by the value of the dark current when $\bar{i}_k \leq i_d$. As c_k increases, we reach the point where $\bar{i}_k > i_d$, after which the shot noise increases linearly with a slope of -1. The dynamic range is determined by the point where the straight line representing the output signal power intercepts the sum of the shot and thermal-noise powers. Note that the dynamic range is

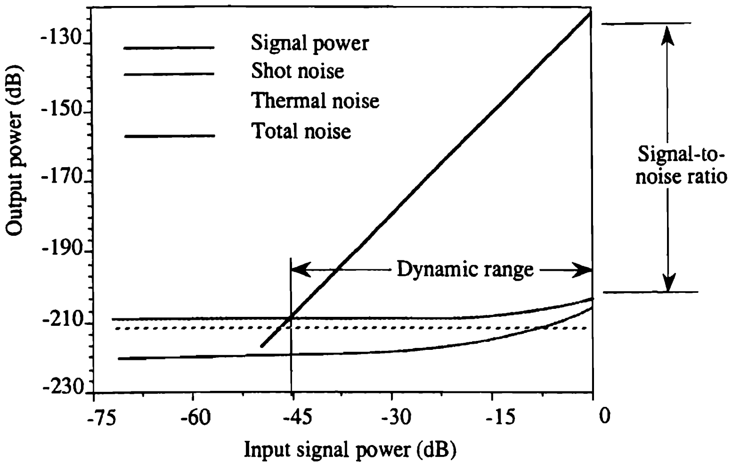

Figure 4.21. Relationship between signal-to-noise ratio and dynamic range.

referenced to the input of the system and is read form the *horizontal* scale in Figure 4.21. The signal-to-noise ratio, on the other hand, is referenced to the output of the system and is read from the *vertical* scale.

4.7. RASTER-FORMAT SPECTRUM ANALYZER

We close this chapter by discussing an important application of two-dimensional optical spectrum analysis, as applied to obtaining high frequency resolution for a wideband one-dimensional time signal. If we want to spectrum analyze a 20-MHz bandwidth signal to a frequency resolution of 20 Hz, we must resolve 10^6 frequencies. The high frequency resolution is obtained only by using a long time history of the signal (at least 50 ms for this example). Given the available resolution capabilities of one-dimensional spatial light modulators, however, we may not be able to process the required signal history.

To overcome this difficulty, we use the full two-dimensional nature of the optical system to process a one-dimensional time signal. The basic idea, according to Thomas (38), is to record a wideband signal of bandwidth W onto photographic film in a raster-scanned format. The raster format is similar to that used for television, in which a wideband time signal of long duration is written onto a cathode-ray tube. Raster-scanning methods are also used in the transmission of images in facsimile systems and in laser printers used as computer peripherals. In all applications, we segment long-duration signals into many shorter ones and record them as a serial set of data lines in the vertical dimension.

4.7.1. The Recording Format

In the raster-scanning format, the wideband time signal modulates a laser beam in magnitude according to the magnitude of the signal $f(t)$, while the laser beam is scanned horizontally across the film by an acousto-optical device as shown in Figure 4.22; these devices are discussed in Chapter 7. For a signal of bandwidth W, the cutoff frequency is $f_{\mathrm{co}} = W$ and the sampling rate R_s, expressed in samples/sec, is

$$R_s = 2f_{\mathrm{co}}. \tag{4.36}$$

Suppose that the required frequency resolution is f_0 so that we need to resolve a total of $M = f_{\mathrm{co}}/f_0$ frequencies in a two-dimensional format. Based on the discussion in Chapter 1, we recognize M_x as the length bandwidth product and M_y as the height bandwidth product for the

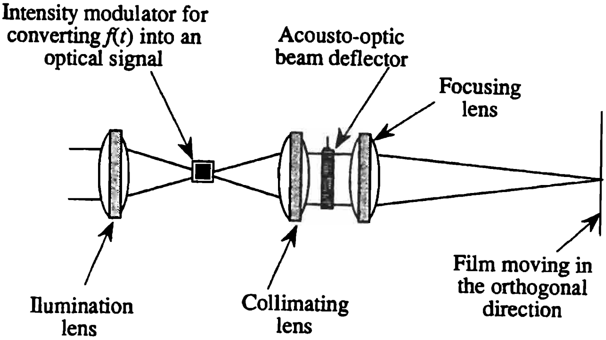
Intensity modulator for converting $f(t)$ into an optical signal
Acousto-optic beam deflector
Focusing lens
Film moving in the orthogonal direction
Illumination lens
Collimating lens

Figure 4.22. Optical wideband recorder.

system, so that $M = M_x M_y$ is the total number of resolvable frequencies. Suitable window functions, needed to control sidelobe levels as discussed in Section 4.5.2, can be introduced later as a refinement to this analysis.

Suppose that the film supports a sample interval of d_0, which means that the cutoff spatial frequency in the horizontal direction is $\alpha_{co} = 1/(2d_0)$ so that the sampling rate at the film is $R_f = 1/d_0$. To record the signal in real time, the laser-beam scanning velocity V_x must be

$$V_x = \frac{R_s}{R_f} = \frac{2f_{co}}{1/d_0} = 2d_0 f_{co}. \tag{4.37}$$

The time duration of a scan line is therefore

$$T_x = \frac{L}{V_x}. \tag{4.38}$$

The minimum resolvable spatial frequency α_0 in the horizontal direction corresponds to a temporal frequency

$$\boxed{f_x = \frac{1}{T_x} = \frac{f_{co}}{M_x},} \tag{4.39}$$

which is generally called the *coarse frequency resolution*.

The film is continuously moving through the scanner, resulting in the scanned line format shown in Figure 4.23. We record the next scan line a

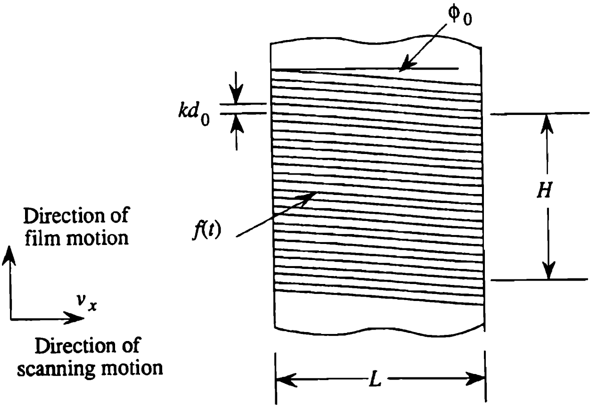

Figure 4.23. Recorded raster format: (a) fine frequencies and (b) full display format.

distance kd_0 from the previous line, where $k \geq 1$ is a parameter whose importance becomes apparent later. The film velocity, based on a zero flyback time for the scanning beam, is

$$V_y = \frac{kd_0}{T_x} = \frac{kd_0 V_x}{L}. \tag{4.40}$$

The height of the processing aperture is given by the product of the film velocity and the recording time T required to provide the frequency resolution f_0. Hence, we find that

$$H = V_y T \tag{4.41}$$

is the height of the processing aperture.

It is tempting to assume that the length and height of the processing aperture should be equal, but this assumption can lead to incompatibilities among other system parameters. We therefore set $L = cH$, where c is a parameter whose value is to be found after other important relationships are developed. From Equations (4.40) and (4.41) we find that

$$L = \frac{kd_0 V_x}{V_y} = cH = cV_y T, \tag{4.42}$$

from which we deduce that

$$V_y = \sqrt{\frac{kd_0V_x}{cT}} \tag{4.43}$$

We now use Equation (4.37) in Equation (4.43) to yield

$$V_y = \sqrt{\frac{2d_0^2kf_{\rm co}}{cT}} \tag{4.44}$$

We use Equation (4.44) in Equation (4.41) to find the size of the processing aperture:

$$\begin{aligned} H &= T\sqrt{\frac{2d_0^2kf_{\rm co}}{cT}} = \sqrt{\frac{2d_0^2kf_{\rm co}T}{c}} = \sqrt{\frac{2d_0^2kf_{\rm co}}{cf_0}} = \sqrt{\frac{2d_0^2kM}{c}}, \\ L &= cH = \sqrt{2d_0^2kcM} \end{aligned} \tag{4.45}$$

We use the values of H and L in Equations (4.38) and (4.39) to find that the coarse frequency f_x is

$$f_x = \frac{1}{T_x} = \frac{V_x}{L} = \frac{f_{\rm co}}{\sqrt{kcM/2}}. \tag{4.46}$$

We are now in a position to calculate the number of frequencies in the horizontal and vertical directions:

$$\boxed{\begin{aligned} M_x &= \frac{f_{\rm co}}{f_x} = \frac{\sqrt{2d_0^2kcM}}{2d_0} = \sqrt{kcM/2}\,; \\ M_y &= \frac{f_x}{f_0} = \frac{2d_0M}{\sqrt{2d_0^2kcM}} = \sqrt{2M/kc} \end{aligned}} \tag{4.47}$$

From Equation (4.47) we see that the number of frequencies in the two directions are not equal, in general, but that the product M_xM_y is always equal to M, independent of the values of the parameters k and c.

From the relationships developed so far, we deduce some interesting features about the system that are not intuitively obvious. For example, suppose that we set $k = 1$ to make the most efficient use of the capacity of the film. We might then expect that a square processing aperture, for which $L = H$, leads to an equal number of frequencies in the two directions so that $M_x = M_y$ which, in turn, leads to a square format in the frequency plane. This condition cannot be obtained for $k = 1$, however, as we note by setting $M_x = M_y$ and using the result from Equation (4.47):

$$M_x = \sqrt{kcM/2} = M_y = \sqrt{2M/kc}, \tag{4.48}$$

which implies that $kc = 2$. Therefore, to obtain a consistent solution, we find that $c = 2$ when $k = 1$ so that the length of the processing aperture is exactly twice that of the height: $L = 2H$. Furthermore, the minimum resolvable spatial frequency β_0 in the vertical direction, which corresponds to the temporal frequency f_0, and the minimum resolvable spatial frequency α_0 in the horizontal direction, which corresponds to the temporal frequency f_x, are given by

$$\begin{aligned} \alpha_0 &= \frac{\xi_0}{\lambda F} = \frac{1}{L}, \\ \beta_0 &= \frac{\eta_0}{\lambda F} = \frac{1}{H} = \frac{2}{L}. \end{aligned} \tag{4.49}$$

The spot spacings ξ_0 and η_0 in the frequency plane therefore have a two-to-one relationship, as noted in Equation (4.49). The format in the Fourier plane is therefore such that

$$\begin{aligned} \xi_{\max} &= M_x \xi_0 = \frac{M_x \lambda F}{L}, \\ \eta_{\max} &= M_y \eta_0 = \frac{2M_y \lambda F}{L}, \end{aligned} \tag{4.50}$$

so that the required photodetector array format is rectangular, being twice as high as it is wide. Furthermore, Equation (4.49) reveals that the resolution requirements of the photodetector array are different in the two directions.

Most photodetector arrays are made with equal sampling in the two directions. If we use such a detector, we waste half of its intrinsic bandwidth. Suppose, then, that we set $c = 1$ so that the photodetector array is square. From Equation (4.47) we then find, again with $k = 1$, that $M_y = 2M_x$. In this case we find that $\xi_0 = \eta_0$, which is desirable; but $\xi_{\max}$ is still equal to $2\eta_{\max}$ because $M_y = 2M_x$. The requirements on the overall size of the photodetector array are therefore the same as before.

To avoid wasting photodetector-array capabilities, we remove the constraint that $k = 1$. We want to find a condition, if possible, for which $L = H$ and $M_y = M_x$ so that the photodetector-array format is square. We return to Equation (4.48) and find that $M_y = M_x$ under the general condition that $kc = 2$. As we want to set $c = 1$ so that $L = H$, we find that we must set $k = 2$. This means that successive scan lines are recorded twice as far apart in the vertical direction. Although this procedure wastes half of the film's recording capacity, it is typically a good tradeoff relative to the other options.

A by-product of setting $k = 2$ is that the aperture of the Fourier-transform lens is $\sqrt{2}$ larger than the suboptimum case when $k = 1$ and the film velocity is doubled. Some judgment is therefore needed to find a solution that can be implemented using current technology in the various areas. In the discussions to follow, we assume that the $k = 2$ and $c = 1$ solution is used; appropriate compensations can be made for other conditions as needed.

4.7.2. The Two-Dimensional Spectrum Analyzer

After the recording is finished and the film is developed, it is placed at plane P_1 of the spectrum analyzer as shown in Figure 4.24. One way to understand the spatial frequency display is to follow the locus of the spectrum while we imagine the input temporal frequency to start at zero and finish at f_{co}. First, suppose that the only frequency component present is zero frequency. The recording will therefore consist of $N_y = 2M_y$ scan lines, spaced a distance $2d_0$ apart, with no amplitude modulation. The Fourier transform of the scan lines consists of functions of the form

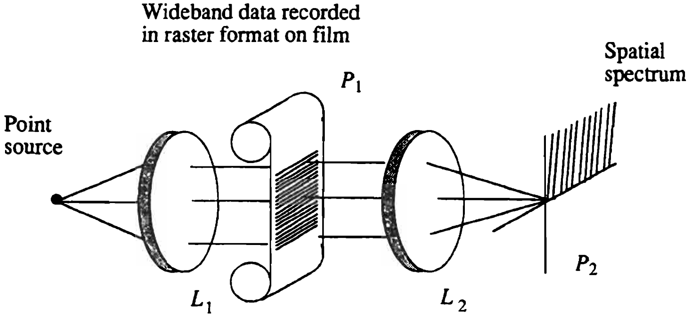

Figure 4.24. Optical spectrum analyzer for raster-scanning applications.

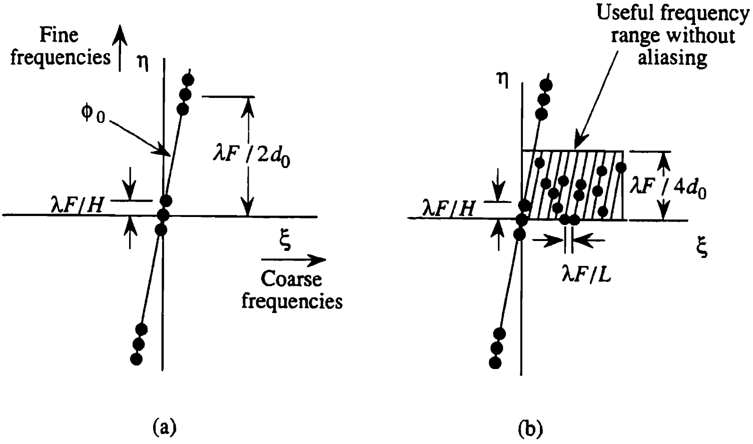

Figure 4.25. Fourier plane.

$\mathrm{sinc}(\xi L/\lambda F)\mathrm{sinc}(\eta H/\lambda F)$, located at $\eta = \pm n\lambda F/2d_0$, as shown in Figure 4.25(a), where F is the focal length of the Fourier-transform lens and n is a positive integer. The spectral components of the scanning pattern do not lie exactly on the $\xi = 0$ axis; instead they lie along a line that is tilted at an angle $\phi_0 = 2d_0/L$. This angle is of the order of $2/N_x$, which is generally small.

The lowest resolvable temporal frequency produces exactly one spatial cycle over the aperture of height H in the vertical direction, as depicted in Figure 4.26. A sinusoidal spatial frequency that has just one full cycle over the aperture produces $\mathrm{sinc}(\xi L/\lambda F)\mathrm{sinc}(\eta H/\lambda F)$ functions, located at $\eta_0 = \pm\lambda F/H$ relative to the sampling spectral points at $\eta = \pm n\lambda F/2d_0$, as shown in Figure 4.25(a). Replicas of the spectrum of the lowest spatial frequency are therefore formed around each of the spectral components, because of the scanning function. We refer to this resolution as the *fine frequency* resolution of the system. The next highest frequency has exactly two cycles over the aperture in the vertical direction, which causes the sinc functions to move a distance $\pm 2\lambda F/H$ with respect to each of the sampling spectral points. This process continues, as the temporal frequency increases, with the spectral components in the Fourier plane moving along the line making an angle ϕ_0 with respect to the vertical axis.

The highest frequency displayed on the first locus is one half the sampling frequency in the vertical direction; the spectrum of this frequency is located at $\eta = \pm\lambda F/4d_0$, as shown in Figure 4.25(b). At this

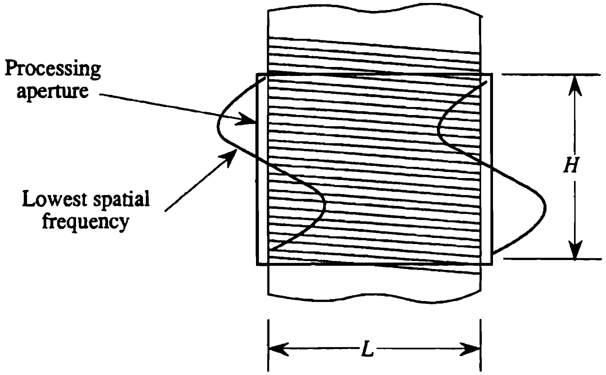

Figure 4.26. Lowest spatial frequency corresponding to lowest temporal frequency.

temporal frequency there is exactly one spatial cycle over the aperture length L in the horizontal direction, in addition to the M_y cycles in the vertical direction. Hence, the spectrum of this frequency has moved a distance $\xi = \lambda F/L$ in the horizontal direction shown in Figure 4.25(b). This coarse frequency resolution, from Equation (4.39), is equal to the cutoff frequency in the vertical direction. As the temporal frequency increases still further, the horizontal spatial frequency remains at one cycle over the aperture, while the vertical spatial frequencies vary from one to M_y cycles; this process forms the second raster scan line in the Fourier plane. At this point, there are two complete spatial cycles in the horizontal direction and this raster movement of the frequency component continues as the temporal frequency increases until we reach f_{co}. This spectral component is located at the upper right-hand corner of the Fourier plane display.

The spectrum at plane P_2 of the optical spectrum analyzer has symmetry about both the ξ and η axes. We generally mask all but one quadrant because the remainder of the information in the Fourier plane is redundant. To completely avoid aliasing, we would like the raster-scanning function on the film to have a sinc-function distribution in the vertical direction so that the spectrum can be cleanly masked. As the film cannot record negative values, we generally shape the raster lines to minimize the overlapping of the spectrum due to aliasing.

To illustrate the performance of a raster-scanning spectrum analyzer, we consider a wideband signal for which $f_{co} = 15$ MHz and want to obtain frequency resolution to 15 Hz. For this example we find that we need

$M = (15 \text{ MHz})/15 \text{ Hz} = (10^6)$ resolvable frequencies. Suppose that we set $M_x = M_y = \sqrt{M} = 1000$, and use a film for which $d_0 = 5\ \mu$. We begin by using Equation (4.37) to find that the scanning velocity is

$$V_x = 2d_0 f_{\text{co}} = 2(5\ \mu)15(10^6) \text{ Hz} = 150 \text{ m/sec}. \qquad (4.51)$$

The coarse frequency resolution in the horizontal direction is obtained from Equation (4.39):

$$f_x = \frac{15(10^6)}{1000} \text{ Hz} = 15 \text{ kHz}, \qquad (4.52)$$

and the scan time in the horizontal direction is $T_x = 1/f_x = 66.7$ msec. The film velocity is given by Equation (4.44):

$$V_y = \sqrt{\frac{2d_0^2 k f_{\text{co}}}{cT}} = \sqrt{\frac{2(0.005)^2 2(15)(10^6)}{1/15}} = 150 \text{ mm/sec}, \quad (4.53)$$

which is reasonable. The aperture size is $L = H = 2d_0\sqrt{M} = 10$ mm.

Suppose that we want to find the location of a cw signal whose frequency is 9,873,705 Hz. We begin by dividing this frequency by 15 kHz to determine the coarse frequency position of the signal; we find that 9,873,705/15,000 = 658.247. The integer part of this result shows that the frequency response for this signal falls on the 658th coarse frequency locus. We then multiply the fractional part of the result by 15 kHz to find the residual frequency and to find its position on the stated coarse loci: 0.247 × 15,000/15 = 247. Hence the frequency response occurs at the 247th fine frequency position on the 658th coarse frequency line.

It is interesting to note that the input recording process maps a long-duration, one-dimensional time signal into a raster format. In a similar fashion, the output raster format can be mapped into a continuous one-dimensional spectrum of the input time signal. This process is illustrated in Figure 4.27. A time signal of duration T is subdivided into segments of duration T_x, recorded in the raster format and spectrum analyzed to produce a raster-format spectrum. The spectrum of the signal is reconstructed by taking the spectral segments of bandwidth W_y and assembling them into the one-dimensional spectrum of bandwidth W.

This spectrum analyzer produces a result equivalent to implementing 10^6 narrowband filters, each with a bandwidth of 15 Hz, with their center frequencies ranging from 0 to 15 MHz. Designing and implementing that many filters using discrete electronic elements or by using digital signal

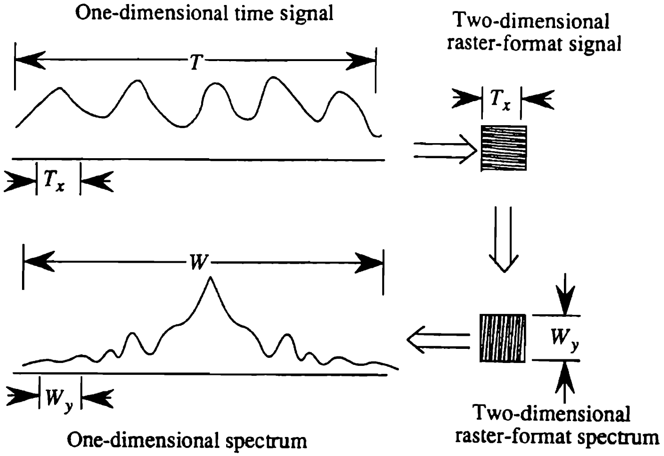
One-dimensional time signal
T
T_x
W
W_y
One-dimensional spectrum
Two-dimensional raster-format signal
T_x
W_y
Two-dimensional raster-format spectrum

Figure 4.27. Conversion from one-dimensional/two-dimensional functions.

processing is difficult. Furthermore, depending on the beam apodization used, the equivalent optical filters have steep transitions from the passband to the stopband, small inband ripple, and small inband phase variations. None of the performance parameters given here are difficult to achieve optically, even with a relatively modest optical system. It is possible to increase the input signal bandwidth to as high as 1 GHz and to obtain a frequency resolution of about 100 Hz over the entire band.

4.7.3. Illustration of Raster-Format Spectra

In Figure 4.28 we show experimental results for the spectra of several signals displayed in different formats (39). One display format is a two-dimensional format obtained by directly viewing the spectra or by recording the spectra on photographic film. The other display format is a three-dimensional format obtained by plotting the magnitude of the spectrum as a function of the scanned coordinates ξ and η in the Fourier plane. The signal characteristics are given in Table 4.1. The first signal is a sine wave whose time bandwidth product, by definition, is $TW = 1$. The parameter f_c/B gives the ratio of the carrier frequency to the bandwidth of the signal. The number of repeats shows how many times a given signal waveform is repeated within the time interval covered by the Fourier transform; for the sine wave, the value shows that 100 cycles are analyzed.

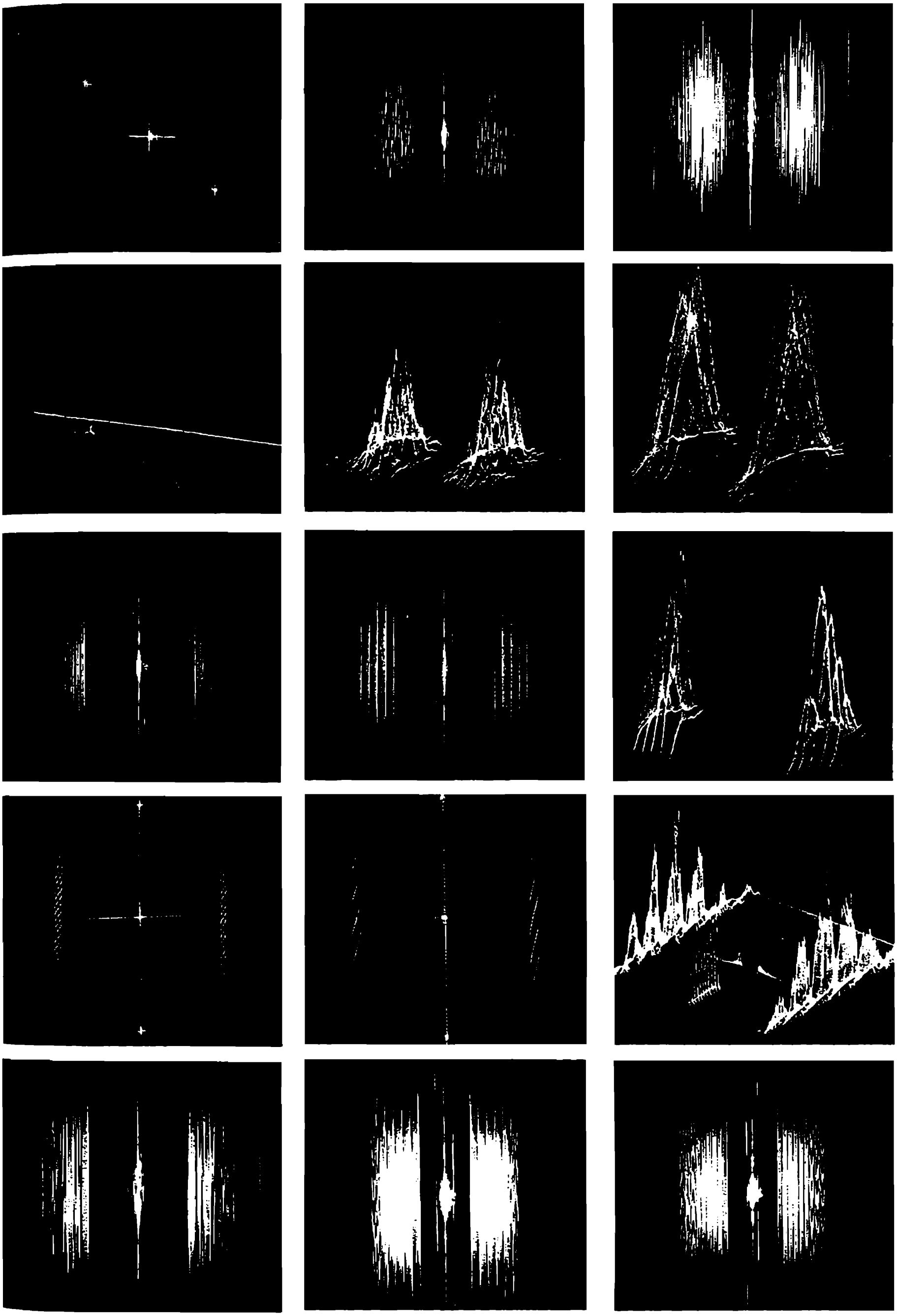

Figure 4.28. Experimental results of raster-scanned data (courtesy G. Lebreton) (39). Top row: two-diinensional spectra of s_1, s_2 and s_3; second row: analog three-dimensional display of spectra s_1, s_2 and s_3; third row: two-dimensional spectra of s_4 and s_5; three-dimensional display for s_5; fourth row: two-dimensional spectra of s_6 and s_7; three-dimensional display for s_7; fifth row: two-dimensional spectra of s_8, s_9 and s_{10}.

Table 4.1

Signal	Modulation	TW	f_c/B	Number of repeats
s_1	Sine wave	1	—	100
s_2	Random	1000	1	9
s_3	Random	1000	1	3
s_4	Linear FM	1000	3/2	9
s_5	Linear FM	1000	3/2	6
s_6	Linear FM	288	17	68
s_7	Linear FM	288	17	34
s_8	V-FM	2 × 500	1	2 × 2
s_9	Linear FM	1000	1	6
s_{10}	Linear FM	1000	1	9

The two-dimensional display of this spectrum is shown on the left panel in the top row of Figure 4.28. The other two panels in the top row are for the random signals for which $TW = 1000$; we see that the fine detail in the spectrum is more visible as the number of repeats increases. The second row shows the same information in the three-dimensional format. The remaining signals are linear FM or chirp signals with various combinations of parameters as shown in Table 4.1. The V-FM signal consists of a downchirp FM followed by an upchirp FM, giving the characteristic V shape to the waveform in frequency space. The effects of different time bandwidth products, number of repeats, and carrier-to-bandwidth ratios are apparent.

4.8. SUMMARY OF THE MAIN DESIGN CONCEPTS

The major steps in the design of a spectrum analyzer are summarized in the following notes, using a one-dimensional notation:

1. From the required frequency resolution $\delta\alpha$ and total bandwidth α_{co} to be covered, calculate the required space bandwidth product $M = \alpha_{co}/\delta\alpha = L\alpha_{co}$. This number gives a quick assessment of the difficulty of the design task and a preliminary estimate of the required length L of the input signal.
2. From the specification on the sidelobe level needed to detect weak signals in the presence of strong ones, determine the required value

of A for the Gaussian illumination and calculate the Fourier transform $A(\alpha)$ for the chosen truncated Gaussian function.

3. For the chosen Gaussian aperture weighting, calculate the relative loss in resolution and increase the required time bandwidth product by this factor. Since the bandwidth is fixed, we must increase the length of the signal that is processed.
4. From the required dynamic range considerations, determine what type of photodetector subsystem is needed (discrete detectors, a photodetector array, etc).
5. Based on the criterion of using three photodetector elements per resolved frequency, calculate the convolution of the aperture response $A(\alpha)$ and a single detector width.
6. Using the convolved aperture response, determine the value of $\delta\alpha$ needed to satisfy the dip criterion for frequency resolution. Several iterations may be required to achieve the desired result for the worst-case conditions.
7. From the value of $\delta\alpha$ and the photodetector array spacing, calculate the focal length of the Fourier transform lens so that the scale of the displayed spectrum matches that of the detector array.
8. From the required dynamic range, determine the required laser power, select the appropriate laser, and find its Gaussian-beam illumination parameter.
9. Design an illumination subsystem to magnify the laser beam to the plane of the signal so that the required truncation takes place at the edges of the revised signal length.
10. From the spur-free dynamic range specification, determine the maximum value of the input signal level.

PROBLEMS

4.1. The lowest spatial frequency component expected of a signal is 10 Ab and the highest is 200 Ab. Provide an optical layout for a spectrum analyzing system to display the highest and lowest spectral components with a separation of 80 mm in the frequency plane, under the constraint that you have no lenses available whose focal lengths are longer than 100 mm. As an added challenge, see if you can solve this problem using a single 100-mm lens. Sketch and dimension your resulting system.

4.2. Suppose that you have a collection of aerial images. Given a coherently illuminated optical system and a ring/wedge detector, how would you propose to use the outputs of these photodetector elements to classify

(a) wheatfields,

(b) cornfields (or any crop planted in rows),

(c) urban areas, and

(d) an oil tank field (lots of circular objects)?

Provide a rough algorithm for using the outputs to separate these four classes of objects.

4.3. In your laboratory you demonstrate the Fourier transform, using a system similar to the variable-scale correlator shown in Figure 3.29 of the text. You use a 4-μ source that is placed 55 mm in front of a 50-mm focal length lens. You then place a second lens whose focal length is 80 mm a distance of 500 mm behind the first lens. A signal $f(x) = 1 + \cos(2\pi\alpha_1 x)$ is located in contact with the first lens. Part (a): where is the Fourier transform plane located relative to the first and second lenses? Part (b): where is the *image* of the signal located relative to the second lens? Part (c): if $\alpha_1 = 60$ Ab, how far from the optical axis are the centroids of the diffracted light located in the Fourier plane? Solve this problem purely by using ray-tracing methods from geometrical optics, along with the basic connections between physical angles and spatial frequencies.

4.4. Suppose that the aperture of the first lens in Problem 4.3 is 25 mm. We want to create a variable-scale Fourier transform by moving the signal axially, closer to or farther from the first lens. If we need a 20% change in the scale of the transform, over what axial distance must the signal be moved? Can this range of scales be achieved if the object has a diameter of 20 mm? If not, what is the maximum object size that can be illuminated at the extreme end of the scaling range?

4.5. Suppose that the illumination beam in a spectrum analyzer has a Gaussian form $\exp[-(A/2)(2x/L)^2]$. Also, suppose that we want to truncate the beam so that the highest sidelobe is about 30 dB down relative to the peak of the main lobe. Find, from the curves in the text, the value of A required to achieve this performance. What is the penalty in loss of resolution as compared to uniform illumination (use the linear curves for accuracy). Calculate the fraction of laser power available for use.

4.6. From the data in the figures, calculate the relative loss in mainlobe resolution when using a Gaussian illumination beam for which $A = 6$ with that for which $A = 2$. Use the response at the -3-dB level as the criterion for resolution. If the half-width of the mainlobe is r_0 at the -3-dB point, what are the corresponding sidelobe levels at $7r_0$ for each of the same two Gaussian beams?

4.7. Suppose that you have a light source containing a spectral line at 500 nm and a line of equal strength at 550 nm. Sketch the Fourier transform of an aperture function $a(x) = \text{rect}(x/L)$ when using this source. Will you observe any complete nulls? If so, where? If not, why not? Do not forget about the $\cos(2\pi f_1 t)$ and $\cos(2\pi f_2 t)$ terms that denote the frequency of light for these two spectral lines.

4.8. Compare the mainlobe half-power widths and the sidelobe levels when the aperture weighting function $a(x)$ is

$$a(x) = \text{rect}(x/L)$$

with that when

$$a(x) = \text{tri}(x/L)$$

where

$$\begin{aligned} \text{tri}(x/L) &= 1 - |2x/L|, && |x| \leq L/2 \\ &= 0, && \text{otherwise}. \end{aligned}$$

Quantify how rapidly the intensity envelope of the sidelobes falls off in each case. Compute the frequency resolution based on the half-power point for the two cases. Hint: the second weighting function can be obtained from the first through the use of the convolution theorem. But be careful with the scaling! A sketch for both $a(x)$ and $|A(\alpha)|^2$ in each case should keep you out of trouble. Label the half-power points of $|A(\alpha)|^2$ and the positions of the first few nulls of $|A(\alpha)|^2$ in each case.

4.9. We design a power spectrum analyzer using direct detection of the light in the Fourier domain. Assume a signal of the form $f(x) = 0.5[1 + c_k \cos(2\pi\alpha_k x)]$. Assume that the optical system produces a current $i_k = 0.02\varepsilon\varepsilon_m SP_0 c_k^2$. The photodetector parameters are

$$\begin{aligned} i_d &= 10 \text{ nA}, \\ c_d &= 3 \text{ pF}, \\ \varepsilon &= 0.5, \\ \varepsilon_m &= 0.2, \\ S &= 0.4 \text{ A/W} \\ T &= 300 \text{ K, and} \\ f_c = B &= 12 \text{ kHz}. \end{aligned}$$

Calculate the amount of laser power that will make the system shot-noise limited when the signal is such that $c_k = 0.002$. Calculate the minimum signal level. Calculate the dynamic range on the assumption that $c_k = 1$ is the maximum value of the input signal.

4.10. (Double credit) We design a power spectrum analyzer using direct detection of the light in the Fourier domain. To make a first cut, we assume a signal of the form $f(x) = 0.5[1 + c_k \cos(2\pi\alpha_k x)]$. We want the dynamic range to be 40 dB (i.e., we have a SNR = 1 when $c_k^2 = 10^{-4}$). Assume that the optical system produces a current $i_k = 0.02\varepsilon\varepsilon_m SP_0 c_k^2$. The photodetector parameters are

$$\begin{aligned} i_d &= 12 \text{ nA}, \\ c_d &= 5 \text{ pF}, \\ \varepsilon &= 0.5, \\ \varepsilon_m &= 0.2, \\ S &= 0.4 \text{ A/W}, \\ T &= 300 \text{ K, and} \\ B &= 500 \text{ kHz}. \end{aligned}$$

If you follow the questions in the order in which they are posed, you should have no trouble getting some reasonable answers. Calculate:

(a) The cutoff frequency (f_{co}) that makes the shot-noise and thermal-noise terms equal when the signal current $i_k \ll i_d$.

(b) Calculate the required load resistor (assume $f_{\text{co}} = 500$ kHz).

(c) Is the system as it stands shot-noise or thermal-noise limited? (Assume that dark current dominates the signal current when the signal is small.) Calculate both $2eBi_d$ and $8\pi kTBf_{co}c_d$ to support your answer and for use later on.

(d) Calculate the laser power P_0 required to achieve the necessary dynamic range.

(e) For this amount of laser power, calculate the minimum signal current and compare it to the dark current as a sanity check. Does this change your mind about whether dark current really does dominate when the signal is at its minimum value?

(f) Calculate the amount of laser power required to make the system shot-noise limited at the minimum signal level. This will be a fairly large value relative to the value calculated in (e).

(g) As an alternative to using lots of laser power, calculate the gain required of an avalanche photodetector (APD) to make the system shot-noise limited. Assume that $m = 2.3$ when you use G_m in the calculation.

(h) Recalculate the laser power required to achieve the necessary dynamic range when using the APD. Compare this value to that obtained in part (d), which uses a PIN detector (an APD whose gain is 1), and to that obtained in part (f), which achieves shot-noise performance by brute force. Of the three, which do you think is the best engineering solution?

4.11. We want to spectrum analyze a 200-MHz bandwidth signal using a falling raster recording format. We have available a spectrum analyzer for which $L = 2H$. The film has a cutoff frequency of $\alpha_{co} = 200$ Ab, and the width of the film is 20 mm. Calculate:

(a) the horizontal velocity V_x,

(b) the number of samples in the horizontal direction N_x,

(c) the minimum resolvable frequency in the horizontal direction (the coarse frequency resolution) f_x,

(d) the film velocity V_y, and

(e) the minimum frequency resolution of the system (the fine frequency resolution) f_0.

4.12. For the spectrum analyzer of Problem 4.11, find the position of a cw signal at 126,290 Hz.

7

Acousto-Optic Devices

7.1. INTRODUCTION

Spatial light modulators form the interfaces between electrical and optical systems. In Chapter 4 we described several two-dimensional spatial light modulators whose inputs are either incoherently illuminated objects or raster-scanned electrical signals. None of those modulators, however, are able to accept signals with hundreds-of-megahertz bandwidths. We therefore concentrate in this chapter on acousto-optic spatial light modulators that help to implement a wide range of processing operations on wide-bandwidth signals. These devices are key to the signal-processing architectures discussed in the remainder of this book.

7.2. ACOUSTO-OPTIC CELL SPATIAL LIGHT MODULATORS

The advantages of optical systems, based on the use of acousto-optic cells for processing either analog or digital signals, may be summarized as a combination of high throughput, a small volume relative to competing rf systems, and low power consumption. Optical systems offer the potential for a large number of parallel channels with complete connectivity, and the high carrier frequencies ($\approx 10^{14}$ Hz) allow very high channel bandwidths with little crosstalk of the type present in electronic processors. Also, optical channels have comparatively smaller power requirements, as the dissipative losses associated with electrical transmission are not present; the losses in typical optical transmission media, such as air and glass, are low.

Brillouin (75) predicted in 1922 how light and sound would interact, and early experimental results were obtained by Debye and Sears (76) and Lucas and Biquard (77). Raman and Nath (78) put the interaction phenomena on a solid mathematical foundation in 1935. It was not until the 1960's, however, that devices with large bandwidths and good optical quality were developed. Acousto-optic cells have bandwidths up to 2 GHz,

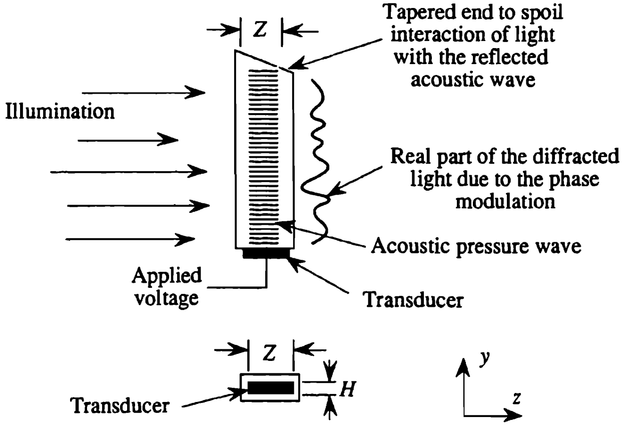
Z
Tapered end to spoil interaction of light with the reflected acoustic wave
Illumination
Real part of the diffracted light due to the phase modulation
Acoustic pressure wave
Applied voltage
Transducer
Z
Transducer
H
y
z

Figure 7.1. Acousto-optic cell spatial light modulator.

frame times of about 1 μsec, diffraction efficiencies of up to 90%, time bandwidth products of 1000–3000, good phase responses, and reasonable dynamic ranges.

An acousto-optic cell consists of an *interaction material*, such as water, glass, or an exotic crystal, to which a piezoelectric *transducer* is bonded, as shown in Figure 7.1. These one-dimensional devices are driven by an electrical signal connected to the transducer. The transducer launches either a compression or a shear acoustic wave into the x direction of the material which, in turn, creates strain waves. The strain waves lead to density changes in the interaction medium and, consequently, to index of refraction changes. The net result is that light passing through the acousto-optic cell in the z direction is modulated in phase according to changes in the optical path. The end of the acousto-optic cell is generally angled so that the reflected acoustic wave does not interact with the incident illumination.

As most signal-processing operations require many acoustic cycles in the cell to support sophisticated signals, the signal to be processed is translated to a center frequency f_c. Suppose that $s(t)$ is a baseband signal with highest frequency $W/2$. We mix this signal with $\cos(2\pi f_c t)$, as shown in Figure 7.2(a), to produce a double sideband modulated signal $f(t)$ whose spectral bandwidth is $W = f_2 - f_1$, centered at $\pm f_c$, as shown in Figure 7.2(b). In those applications where the rf signal spectrum falls naturally between f_1 and f_2, the signal can be fed directly into the acousto-optic cell without further preprocessing.

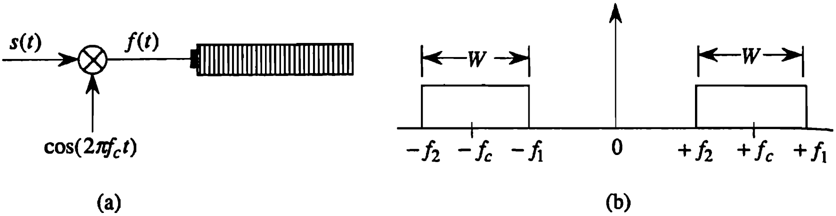

Figure 7.2. Acousto-optic cell: (a) electrical connection and (b) spectrum of drive signal.

When the interaction width Z of the acousto-optic cell is short relative to an acoustic wavelength, the device behaves as a thin diffracting material, as studied extensively by Raman and Nath in their 1935 papers (78). At the other extreme, the axial width of the cell may be large relative to the acoustic wavelength. We then speak of the device as operating in the Bragg mode, resulting in effects similar to those produced by x-ray diffraction in three-dimensional crystals.

7.2.1. Raman-Nath Mode

In Chapter 3, Section 3.1 we showed that a light wave is phase and amplitude modulated as it passes through an element whose response is $|a(x)|\exp[j\phi(x)]$; the wave then has the form $|a(x)|\cos[2\pi f_l t + \phi(x)]$, where f_l is the frequency of light. In a similar fashion, light passing through the acousto-optic cell, when driven by a pure sinusoidal frequency f_j, is phase modulated so that

$$A(x,t) = A_0 \cos\left[2\pi f_l t + \frac{2\pi Z}{\lambda}\left\{n_0 + \Delta n \cos\left[2\pi f_j\left(t - \frac{T}{2} - \frac{x}{v}\right)\right]\right\}\right], \tag{7.1}$$

where $A(x,t)$ is the amplitude of the output wave in space and time, A_0 is the amplitude of the incident light wave, and Δn is the change in the index of refraction within the interaction medium induced by the traveling strain wave. In Equation (7.1), the argument $t - T/2 - x/v$ shows that $A(x,t)$ is a wave traveling in the positive x direction with velocity v and that the cell has a transit time of $T = L/v$, where L is the length of the acousto-optic cell and v is the velocity of sound in the interaction medium.

The strain wave within the cell is proportional to the amplitude of the acoustic wave. As the modulated optical wave given by Equation (7.1) is a function of both space and time, a sinusoidal input signal causes the cell to

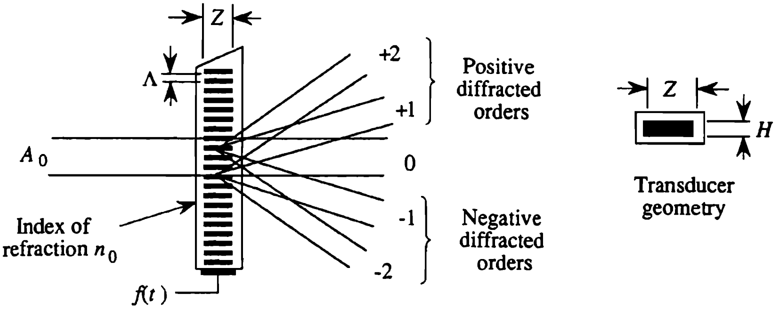
Z
Λ
A_0
Index of refraction n_0
$f(t)$
+2
+1
0
-1
-2
Positive diffracted orders
Negative diffracted orders
Z
H
Transducer geometry

Figure 7.3. Diffracted orders in the Raman-Nath mode.

behave as a phase diffraction grating traveling in the x direction. Light is diffracted by the phase grating to produce several positive and negative diffracted orders. Figure 7.3 shows the rays associated with the incident illumination on the acousto-optic cell, as well as the first two of many diffracted waves. A rigorous analysis of the operation of an acousto-optic cell yields the Raman-Nath equation for the amplitude of the ith diffracted order (79):

$$|A_i| = |A_0 J_i(\gamma)|, \tag{7.2}$$

where A_0 is the amplitude of the incident light, J_i is the ith-order Bessel function, and γ is the phase shift of the light induced by the refractive index change. The normalized diffracted amplitude of the ith wave is indicated by m_i (79):

$$m_i = \frac{A_i}{A_0} = (-j)^i J_i\left[\frac{2\pi Z \Delta n}{\lambda}\right], \tag{7.3}$$

where $J_i(\cdot)$ is an ith-order Bessel function of the first kind. We define m_i as the *modulation index* for the ith order; it is defined as the ratio of the diffracted light amplitude to the incident light amplitude. The amplitude of the diffracted light, as a function of the phase shift of the Bessel function, is shown in Figure 7.4 for the undiffracted light and for the first two diffracted orders. The phase of each order, relative to its neighbors, is shifted by 90° as indicated by the $(-j)^i$ factor in Equation (7.3). For example, we find that the positive and negative orders are 180° out of phase. This result is also found from the fact that $J_{-n}(x) = (-1)^n J_n(x)$

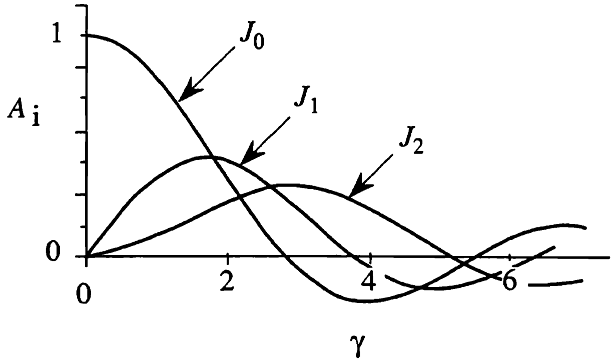

Figure 7.4. Bessel functions of order 0, 1, and 2.

and that

$$J_1(x) = \left(\tfrac{1}{2}x\right)\left[1 - \frac{\tfrac{1}{4}x^2}{2!} + \frac{\left(\tfrac{1}{4}x^2\right)^2}{2!3!} - \frac{\left(\tfrac{1}{4}x^2\right)^3}{3!4!} + \qquad\right]. \tag{7.4}$$

As $J_1(x)$ is odd, the sign reversal between the two orders is apparent.

7.2.2. The Bragg Mode

From Equation (7.3) we see that large values of Δn and Z lead to high diffraction efficiencies. As light is wasted when multiple orders are generated, we generally increase the interaction width Z until the Bragg mode of operation is reached. We characterize the transition from the Raman-Nath mode to the Bragg mode by defining a Q factor:

$$Q \equiv \frac{2\pi}{n_0}\frac{\lambda Z}{\Lambda^2}, \tag{7.5}$$

where n_0 is the index of refraction of the interaction material and Λ is the acoustic wavelength. The acoustic wavelength is related to the applied drive frequency f by $\Lambda = v/f$, where v is the velocity of the acoustic wave. A $Q \approx 2\pi$ establishes a boundary between the two modes. If $Q < 2\pi$, the acousto-optic cell is operating in the *Raman-Nath mode*; if $Q > 2\pi$, it is operating in the *Bragg mode*. In optical signal processing, the acousto-optic cell is primarily used in the Bragg mode because more of

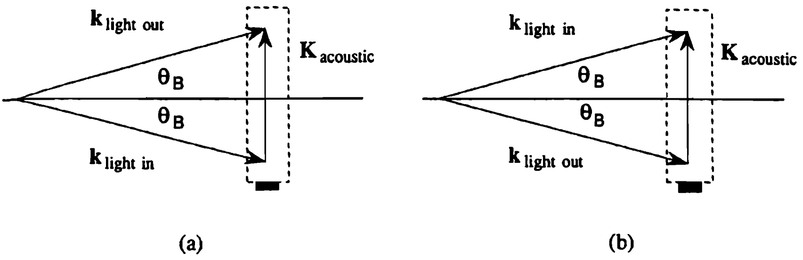

Figure 7.5. Bragg diffraction: (a) upshift mode and (b) downshift mode.

the optical power is coupled into a single diffracted order. In the strong Bragg region, only two diffracted orders are present, either the zero and one positive diffracted order or the zero and one negative diffracted order.

The essential properties of acousto-optic diffraction are explained with the aid of a model showing the collision between photons and phonons. The momenta of the interacting particles are given by $\hbar\mathbf{k}$ and $\hbar\mathbf{K}$, where $\hbar$ is Planck's constant and $\mathbf{k}$ and $\mathbf{K}$ are the wave vectors of light and sound. From Figure 7.5(a), we see that the optimum illumination angle for wave matching occurs when $\mathbf{k}_{\text{out}} = \mathbf{k}_{\text{in}} + \mathbf{K}$ so that

$$\sin\theta_B = \frac{|\mathbf{K}|}{2|\mathbf{k}|}. \tag{7.6}$$

The magnitude of the wave vectors are inversely proportional to the wavelengths (e.g., $|\mathbf{k}| = 2\pi/\lambda$), so that

$$\boxed{\sin\theta_B = \frac{\lambda}{2\Lambda},} \tag{7.7}$$

where Λ is the wavelength of the acoustic signal in the medium. In general, $\Lambda \gg \lambda$, so that

$$\theta_B \approx \sin\theta_B = \frac{\lambda}{2\Lambda}. \tag{7.8}$$

The optimum illumination for the Bragg mode is therefore at the off-axis *Bragg angle* θ_B, whereas the illumination is normal to the surface of the acousto-optic cell in the Raman-Nath mode.

In addition to the geometrical matching of the wave directions, conservation of energy requires that the frequency of light is shifted when it interacts with the traveling acoustic wave. We therefore find that

$$\left.\begin{aligned}\omega_+ &= \omega + \Omega\\ \omega_- &= \omega - \Omega\end{aligned}\right\}, \tag{7.9}$$

where ω_+ and ω_- refer to the radian frequency of the diffracted light in the positive and negative orders and where ω and Ω refer to the frequencies of the incident light and the sound wave. These relationships predict a frequency shift in the light, visualized by considering the motion of the sound wave. If the sound wave is moving toward the incident light, as shown in Figure 7.5(a), it shortens the wavelength of the diffracted light; the diffracted light is Doppler shifted upward by an amount equal to the frequency of the sound wave, as shown by ω_+ in Equation (7.9). The frequency ω_+ refers to the *upshifted* condition associated with the *positive diffracted order*. If we reverse the angle of the incident light on the acousto-optic cell, as shown in Figure 7.5(b), we see that $\mathbf{k}_{\text{out}}$ and $\mathbf{k}_{\text{in}}$ exchange positions to produce the negative diffracted order; the frequency of light is then downshifted. In this case, ω_- refers to the *downshifted* condition associated with the *negative diffracted order*.

Although we almost always use the Bragg mode in practice to produce the highest diffraction efficiency, there are compelling reasons to use the Raman-Nath mode in explaining basic optical signal-processing technology. In the Raman-Nath mode there is a nice degree of symmetry in the results and having the choice of which diffracted order to use is often convenient for developing the proper processing architectures, as we see in subsequent chapters. We generally confine our attention to the undiffracted light and the first positive and negative diffracted orders. The physical angles between the diffracted orders are typically of the order of milliradians; we exaggerate them in our diagrams for clarity.

7.2.3. Diffraction Angles, Spatial Frequencies, and Temporal Frequencies

Figure 7.6 shows the connections among diffraction angles, spatial frequencies, temporal frequencies, and acoustic wavelengths. For a given drive frequency f, we find that the acoustic wavelength is $\Lambda = v/f$. By definition, the spatial frequency is therefore $\alpha = 1/\Lambda$, which gives an

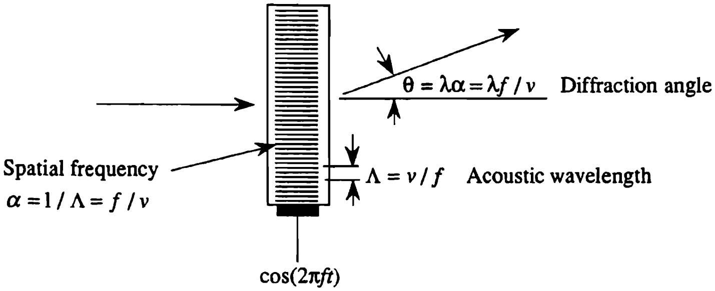
θ = λα = λf / v Diffraction angle
Spatial frequency
α = 1 / Λ = f / v
Λ = v / f Acoustic wavelength
cos(2πft)

Figure 7.6. Relationships among wavelength, spatial frequency, and diffraction angle.

important relationship between spatial frequencies and temporal frequencies:

$$\boxed{\alpha \equiv \frac{1}{\Lambda} = \frac{f}{v}.} \tag{7.10}$$

Thus, there is a unique spatial frequency associated with every temporal frequency present in the acousto-optic cell. Furthermore, the diffracted ray angle is connected to the spatial and temporal frequencies by

$$\boxed{\theta = \lambda\alpha = \frac{\lambda f}{v},} \tag{7.11}$$

which nicely ties together all the important parameters.

When the drive signal is an arbitrary sum of cw components, light is diffracted over a large set of angles simultaneously, with angles and amplitudes determined by the frequencies and amplitudes of the cw components. In particular, suppose that the drive signal is

$$f(t) = \sum_{n=-\infty}^{\infty} a_n e^{j2\pi n f_0 t} \operatorname{rect}\left[\frac{nf_0 - f_c}{W}\right], \tag{7.12}$$

where f_0 is the smallest resolvable frequency. The rect function shows that the spectrum of $f(t)$ is centered at f_c and that it has bandwidth $W = f_2 - f_1 = K_2 f_0 - K_1 f_0$. This signal contains $M = K_2 - K_1 + 1$ discrete frequency components, each a multiple of f_0, beginning at frequency f_1 and ending at f_2. The signal $f(t)$ may be generated directly by an rf signal or by a baseband signal

$$s(t) = \sum_{n=0}^{\infty} a_n \cos(2\pi n f_0 t) \operatorname{rect}\left[\frac{nf_0}{W}\right], \tag{7.13}$$

that is multiplied by $\cos(2\pi f_c t)$, where $f_c = (f_2 + f_1)/2$, to put its spectrum at the center of the passband of the acousto-optic cell. Thus, the signal within the acousto-optic cell can be represented by M discrete temporal/spatial frequencies, leading to M discrete diffraction angles.

7.2.4. The Time Bandwidth Product

An important parameter in signal processing is the *time bandwidth product*, which is the product of the bandwidth and the time duration of the processed signal. The time bandwidth product tells us, in general, the degree of complexity of the signal or of an optical system. We begin the derivation of the time bandwidth product for an acousto-optic cell by relating the total angular deflection range $\Delta\theta$ to the bandwidth Δf:

$$\Delta\theta = \frac{\lambda}{v}\Delta f, \tag{7.14}$$

so that the deflection angle is linear in applied frequency. The number M of resolvable angles produced by the cell is

$$M = \frac{\text{angular range}}{\text{angular resolution}} = \frac{\Delta\theta}{\lambda/L}, \tag{7.15}$$

where L is the length of the acousto-optic cell and λ/L is the intrinsic angular resolution of any physical system, as discussed in Chapter 3, Section 3.5.2. We use Equation (7.14) in Equation (7.15) to find that

$$\boxed{M = \frac{\lambda\Delta f/v}{\lambda/L} = \frac{L}{v}\Delta f = T\Delta f = TW,} \tag{7.16}$$

where we made use of the fact that $L = vT$ and that the total bandwidth of the cell is $\Delta f = W$. Depending on the application, T is called the *transit time* of the cell, the *time delay* of the cell, the *access time* of the cell, or the *time duration* of the signal within the cell.

Equation (7.16) shows that the number of resolvable angles M is equal to the time bandwidth product of the cell. The angular resolution λ/L is predicated on illuminating the cell with a uniform-magnitude plane wave of light. If the incident wave is amplitude weighted in the x direction, as in most spectrum analysis applications, the angular resolution decreases; the value of M is therefore reduced accordingly. Time bandwidth products for acousto-optic cells are generally in the 1000–3000 range. The time bandwidth product is limited by the basic tradeoff between time and bandwidth and involves the physical limitations of important material properties such as attenuation and available crystal sizes. The reader is referred to the literature for more detailed discussions of the design relationships that govern acousto-optic cells (80, 81).

7.3. DYNAMIC TRANSFER RELATIONSHIPS

In Chapter 3, Section 3.8, we noted that the input/output relationship for an optical system is linear in amplitude when the system is coherently illuminated, is linear in intensity when the system is incoherently illuminated, or is linear in neither amplitude nor intensity when the system is partially coherently illuminated. Acousto-optic systems also provide linearity in any of these quantities depending on how they are illuminated and on the nature of the drive signal.

7.3.1. Diffraction Efficiency

A key performance parameter associated with acousto-optic cells is the amount of light diffracted into the first order. Suppose that the input electrical signal has voltage V_s and that the incident light has intensity I_0. The *diffraction efficiency* of the acousto-optic cell is defined as (80)

$$\eta \equiv m^2 \equiv \frac{I_d}{I_0} = \sin^2\left[\frac{\pi^2 P_s}{2\lambda^2}\frac{Z}{H}M_2\right]^{1/2} \tag{7.17}$$

where I_d is the intensity of the diffracted light, I_0 is the intensity of the incident light, P_s is the acoustic power within the material, Z and H are the transducer dimensions as shown in Figure 7.3, and M_2 is a figure of merit used to evaluate acousto-optic configurations. The *figure of merit* is defined as

$$M_2 = \frac{n_0^6 p^2}{\rho v^3}, \qquad (7.18)$$

where n_0 is the refractive index of the material, p is a strain-optic coefficient, ρ is the density of the material, and v is the sound velocity. From Equation (7.17) we note that the diffraction efficiency increases for large values of M_2; from Equation (7.18) we see that the diffraction efficiency, in turn, increases for high indices of refraction and low acoustic-wave velocities. Equation (7.17) shows that a large value for the interaction width Z and a small transducer height help to achieve high diffraction efficiencies.

A high diffraction efficiency must be balanced against increased attenuation as the sound propagates through the cell and against a reduction in the cell bandwidth. As the drive frequency f_j changes, a mismatch of the wave vectors occurs within the acousto-optic cell and the diffraction efficiency suffers. We express the 3 dB bandwidth Δf as (80)

$$\Delta f = \frac{2v^2}{\lambda f_c Z}, \qquad (7.19)$$

where f_c is the center frequency of the cell. From Equations (7.17) and (7.19) we note a conflict among bandwidth, velocity, and interaction width. For example, acousto-optic cells that have low acoustic velocities have high diffraction efficiencies, as we see from Equation (7.17), but also tend to have narrow bandwidths, as we see from Equation (7.19).

An important parameter of acoustic devices is the attenuation of the acoustic wave as it propagates in the acousto-optic cell. Attenuation reduces the effective diffraction efficiency, reduces the effective time aperture of the cell, and reduces the frequency response. High attenuation also results in heating of the acoustic material, which can lead to effects such as a change in the acoustic velocity and defocusing of the optical beam. Some work has been done to obtain higher frequency responses and better time bandwidth products by cooling the acoustic material (82), taking advantage of the decrease in attenuation with temperature below 30 K (83).

The material must also have a high homogeneous optical transmission and low defect levels to minimize optical loss and scatter. Relatively few materials are sufficiently developed to provide high quality routinely. Single-crystal $LiNbO_3$ and TeO_2 are popular largely due to their availability, in spite of their less than optimum values for M_2 and attenuation; GaP is particularly well suited for operation at the wavelengths available from injection laser diodes.

7.3.2. Input / Output Relationships

From Equation (7.17) we see that the diffraction efficiency of the acousto-optic cell is given by

$$\eta = \sin^2\left(\sqrt{BP_s}\right), \tag{7.20}$$

where the input acoustic power P_s is proportional to the square of the input signal voltage V_s and B is a constant that accounts for the parameters associated with the interaction medium. The value of B is

$$B = \frac{\pi^2}{2\lambda^2}\frac{Z}{H}M_2, \tag{7.21}$$

where Z is the interaction width and H is the height of the transducer. The ratio of the amplitude of the diffracted light to the amplitude of the incident light is the *modulation index* as given by Equation (7.3) so that

$$m = \sqrt{\eta} = \sin\left(\sqrt{BP_s}\right). \tag{7.22}$$

For $\sqrt{BP_s} \ll \pi/2$, we can replace the sine function by its argument so that

$$m = \sqrt{BP_s} = B'V_s, \tag{7.23}$$

where B' is a new constant. As the modulation index is linearly proportional to the input voltage, we find that *the amplitude of the diffracted light is linearly proportional to the input voltage*. Figure 7.7(a) shows the operating condition for achieving linearity in amplitude; the signal is double-sideband modulated with a low modulation level so that the signal envelope stays on the linear part of the sine function.

We sometimes make the diffraction efficiency η proportional to the signal voltage V_s to operate the system so that it is linear in intensity. We first add a bias voltage V_b to V_s, so that the new drive signal $V_b + V_s$ is nonnegative. The diffraction efficiency is then

$$\eta = \sin^2\{B''[V_b + V_s]\}, \tag{7.24}$$

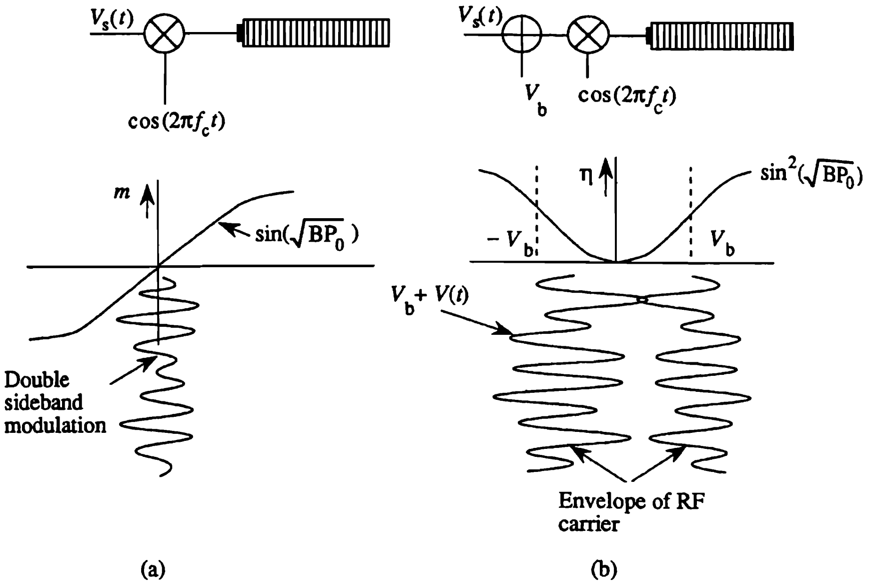

Figure 7.7. Operating conditions: (a) linearity in amplitude or (b) linearity in intensity.

where B'' is a constant. We use the fact that $\sin^2 x = (1 - \cos 2x)/2$ and that $\cos(x + y) = [\cos x \cos y - \sin x \sin y]$ to find that

$$\eta = \tfrac{1}{2}[1 - \cos(2B''V_b)\cos(2B''V_s) + \sin(2B''V_b)\sin(2B''V_s)]. \quad (7.25)$$

When we choose the bias so that $B''V_b = \pi/4$, the second term of Equation (7.25) vanishes and we achieve the highest degree of linearity. The diffraction efficiency then becomes

$$\eta = \tfrac{1}{2}\{1 + \sin[2B''V_s]\}. \quad (7.26)$$

If the value of the input voltage is small, we find that

$$\eta = \tfrac{1}{2}\{1 + 2B''V_s\}. \quad (7.27)$$

From Equation (7.27) we see that, for biased signals, *the intensity of the diffracted light is linearly proportional to the input signal voltage.* Figure 7.7(b) shows the operating conditions required for achieving linearity in intensity. Here we arrange for the signal envelope to be centered on the most linear region of the square of the sine function.

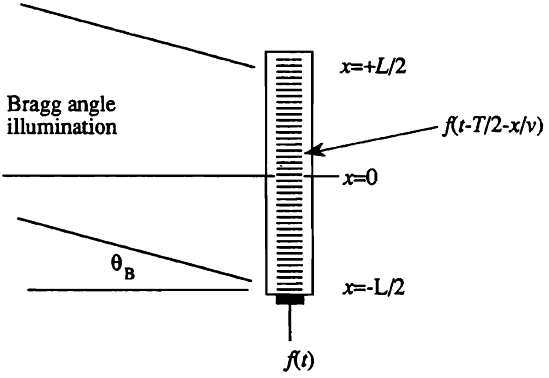

Figure 7.8. Traveling wave geometry.

Finally, the input voltage generally varies as a function of time. To represent the time dependence, we let $V_s \rightarrow f(t)$ represent the input signal, we let $m \rightarrow A(x, t)$ represent the output amplitude signal, and we let $\eta \rightarrow I(x, t)$ represent the output intensity signal.

7.4. TIME DELAYS AND NOTATION

We regard the acousto-optic cell as a delay line that is tapped optically, or as a device that stores a certain time history of the signal. The time signal propagates through the cell with velocity v so that it has characteristics of a traveling wave of the form $f(t - x/v)$, as shown in Figure 7.8, where x is a coordinate along the acousto-optic cell. As $x = 0$ represents the midpoint of the acousto-optic cell, we introduce a delay $T/2$ so that the signal becomes $f(t - T/2 - x/v)$. We use this notation so that when we evaluate the space/time function at the transducer, for which $x = -L/2$, we obtain $f(t)$ as expected. At the midpoint of the acousto-optic cell where $x = 0$, we obtain $f(t - T/2)$, which is the input signal delayed $T/2$ seconds. Finally, at the far end of the cell, where $x = L/2$, we obtain $f(t - T)$, which represents the eldest signal value and the maximum time delay.

7.5. PHASE-MODULATION NOTATION

For mathematical convenience, we want to represent complex-valued functions in phasor form instead of in trigonometric form. The transition from Equation (7.1) to the phasor form is not obvious unless the intermediate steps are spelled out. We begin with the assumption that Δn is small so that the cosine terms involving Δn are set equal to one and the sine of terms involving Δn are replaced by their arguments. With these conventions in place, Equation (7.1) becomes

$$A(x,t) = A_0\left\{\cos\left(2\pi f_l t + \frac{2\pi Z n_0}{\lambda}\right) - \frac{2\pi Z\Delta n}{\lambda}\right.$$
$$\left.\times\cos\left[2\pi f_c\left(t - \frac{T}{2} - \frac{x}{v}\right)\right]\sin\left(2\pi f_l t + \frac{2\pi Z n_0}{\lambda}\right)\right\}, \quad (7.28)$$

where $2\pi Z n_0/\lambda$ is the phase associated with the optical path through the acousto-optic cell and f_c is the carrier frequency of the baseband signal that produces the index variations Δn. By some straightforward expansions using the relationships that $\sin\gamma = \cos(\gamma - \pi/2)$ and that $j = \exp(j\pi/2)$, we find

$$A(x,t) = A_0 \operatorname{Re}\left[e^{j(2\pi f_l t + 2\pi Z n_0/\lambda)}\left\{1 + jms\left(t - \frac{T}{2} - \frac{x}{v}\right)\right.\right.$$
$$\left.\left.\times\cos\left[2\pi f_c\left(t - \frac{T}{2} - \frac{x}{v}\right)\right]\right\}\right], \quad (7.29)$$

where we have replaced the change in refractive index Δn by the corresponding time signal $ms(t - T/2 - x/v)$.

In earlier chapters we generally ignored the frequency of light in deriving the results because the light distributions with which we dealt were generally functions of space only. When we treat optical signal-processing systems using acousto-optic cells, the light distributions are functions of both space and time. It is therefore important to recognize that the light amplitude leaving the acousto-optic cell is given by Equation (7.29). For mathematical convenience, however, we often ignore the exponential terms in derivations and express the light distribution leaving the acousto-optic cell as

$$A(x,t) = A_0\left[1 + jms\left(t - \frac{T}{2} - \frac{x}{v}\right)\cos\left\{2\pi f_c\left(t - \frac{T}{2} - \frac{x}{v}\right)\right\}\right], \quad (7.30)$$

with the understanding that Equation (7.29) provides the complete result.

7.6. SIGN NOTATION

In optical signal-processing applications we generally use only one of the diffracted orders. We therefore further refine our description of the transmitted signal as just the positive or just the negative diffracted order. When we propagate the acoustic wave in the positive x direction, the light leaving the acousto-optic cell in the first positive diffracted order is expressed in phasor form by the equivalent function

$$f_+(x,t) = jma(x)s\left(t - \frac{T}{2} - \frac{x}{v}\right)e^{j2\pi f_c(t - T/2 - x/v)}. \tag{7.31}$$

In this expression, $f_+(x,t)$ indicates the amplitude of the light for the positive order just outside the acousto-optic cell. The *amplitude weighting function* $a(x)$ includes the illumination function, attenuation factors, the laser power level, and truncation effects due to the acousto-optic cell itself or other optical elements. The next term is the real-valued baseband signal $s(t)$, traveling in the positive x direction and time delayed by $T/2$. The final term implies that $s(t)$ has been multiplied by $\cos(2\pi f_c t)$ to translate it to the center frequency f_c of the acousto-optic cell. The positive sign associated with the overall argument of the exponential shows that the positive diffracted order is selected.

There are other combinations of illumination direction, acoustic-wave direction, and choice of diffracted order. The most general way to express the equivalent amplitude function of the acousto-optic cell at its exit face is

$$\boxed{f_\pm(x,t) = jma(x)s\left(t - \frac{T}{2} \pm \frac{x}{v}\right)e^{\pm j2\pi f_c(t - T/2 \pm x/v)}.} \tag{7.32}$$

In Equation (7.32) the ± signs combine to produce four possibilities. We first determine which diffracted order we need to use; this decision determines the $f_+(x,t)$ or $f_-(x,t)$ notation for the positive and negative orders, respectively. The sign of the exponential is the same as that of the diffracted order when the acoustic wave is propagating in the positive x direction. The frequency of light is therefore upshifted in the positive order and downshifted in the negative order. If the acoustic wave is propagating in the negative x direction, the sign associated with the exponential is opposite to that of the diffracted order; the sign associated with x/v in the argument of the signal envelope is then positive.

Recall that a basic assumption in the development of diffraction theory was that $\exp[j(\omega t - kr)]$ is a satisfactory eigenfunction for the wave equation. As the term that led to a positive kernel function for the spatial Fourier transform is $\exp(-jkr)$, we associate a positive exponential $\exp(j2\pi f_l t)$ with the temporal frequency of light. The last term in $f_{\pm}(x, t)$ is of the form $\exp(j2\pi f_c t)$ which shows that, relative to $\exp(j2\pi f_l t)$, the frequency of light is upshifted or downshifted because f_c is added to or subtracted from f_l.

The four possible configurations of the acousto-optic cell are shown schematically in Figure 7.9. These schematics are easy to construct and remember, plus they tell us pictorially the spatial direction of the diffracted light as well as its temporal shift. Note that both of these characteristics come from the last term of $f_{\pm}(x, t)$:

$$e^{\pm j2\pi f_c(t - T/2 \pm x/v)} = e^{\pm j2\pi f_c(t-T/2)} e^{\pm j2\pi f_c x/v}. \tag{7.33}$$

After the direction of the acoustic wave is chosen, we know whether the + or − sign is used for the x/v term; we then choose the + or − sign in the temporal frequency exponential to shift the frequency in the correct direction.

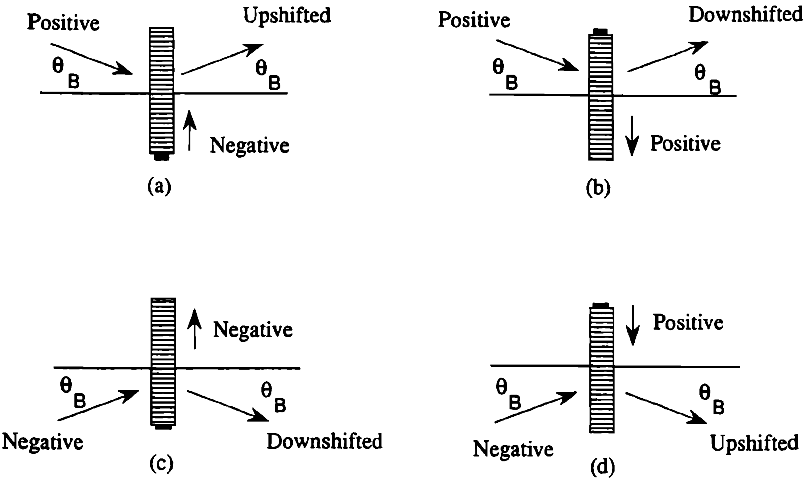

Figure 7.9. Various combinations of illumination and propagation directions.

7.7. CONJUGATE RELATIONSHIPS

The conjugate relationships between the positive and negative orders are obtained if we begin with the representation of the real-valued drive signal:

$$\begin{aligned}\text{Drive signal} &= |s(t)|\cos[2\pi f_c t + \phi(t)]\\ &= |s(t)|\mathrm{Re}[e^{j[2\pi f_c t + \phi(t)]}],\end{aligned} \tag{7.34}$$

where $\phi(t)$ is the phase of the complex-valued signal $s(t)$. From Equation (7.33) we see that the terms in x/v have the same sign, as they are due solely to the direction of acoustic-wave propagation. Suppose that we propagate the acoustic wave into the positive x direction so that this sign is negative. If we arrange the illumination direction so that the light is downshifted in frequency, the signal becomes

$$\begin{aligned}&jma(x)\left|s\left(t - \frac{T}{2} - \frac{x}{v}\right)\right|e^{-j[2\pi f_c(t - T/2 - x/v) - \phi(t - T/2 - x/v)]}\\ &\qquad = jma(x)s^*\left(t - \frac{T}{2} - \frac{x}{v}\right)e^{-j2\pi f_c(t - T/2 - x/v)}.\end{aligned} \tag{7.35}$$

Thus we see that the *downshifted signal is the conjugate of the upshifted signal.* When we want to obtain a "true" signal spectrum, we use the upshift mode of operation; when we want to obtain the conjugate of the spectrum of a signal, we simply use the downshifted mode of operation. Nice, and useful, too.

7.8. VISUALIZATION OF THE ACOUSTO-OPTIC INTERACTION

The observed light intensity leaving an acousto-optic cell operating in the Raman-Nath mode is the same as the illuminating beam because the effect of the acoustic interaction is pure phase modulation. In Figure 7.10(a) we use a Schlieren method (see Chapter 4, Section 4.3.1) to help visualize the interaction of light and sound for a single-channel acousto-optic cell driven by a pure rf signal at 400 MHz (84). The acoustic waves spread in the vertical direction as they propagate away from the transducer, which is at the left end of the cell. In the region near the transducer, we see some detailed structure caused by acoustic interference; this structure is equivalent to the near-field diffraction pattern or the Fresnel diffraction of a slit,

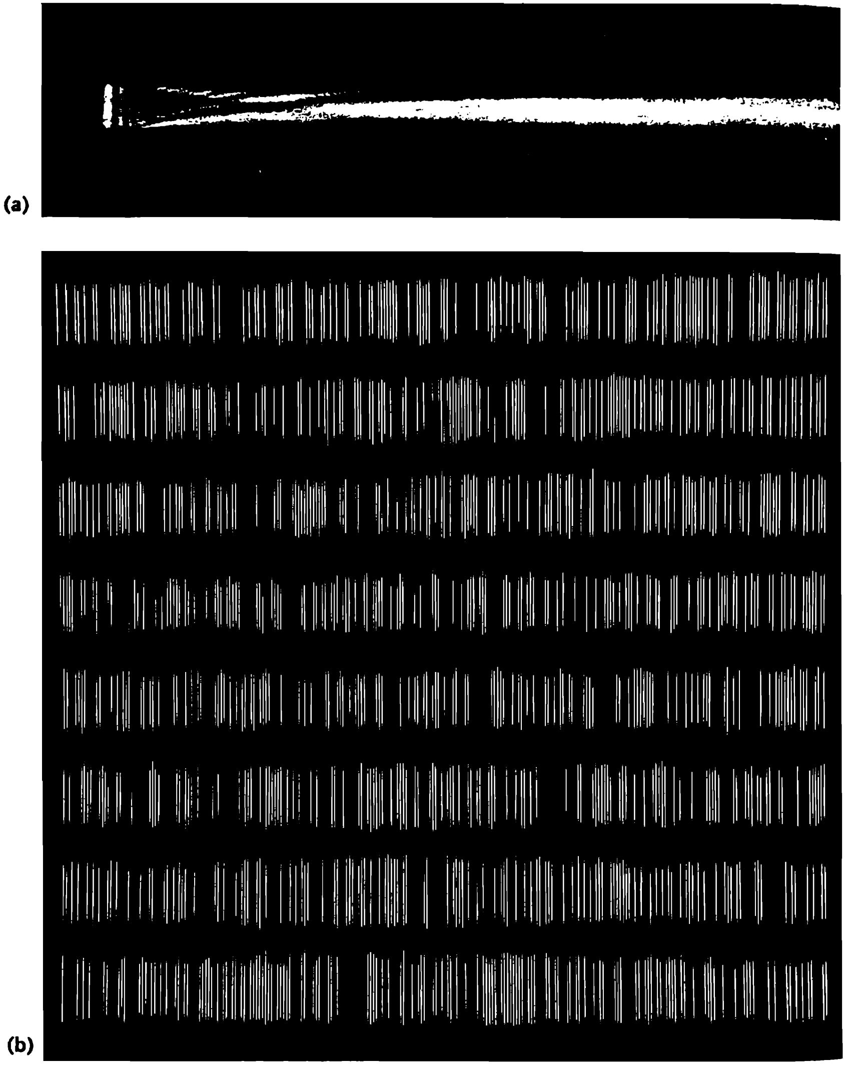

Figure 7.10. Schlieren images of acoustic waves within Bragg cells: (a) single channel cell and (b) multichannel cell (courtesy H. N. Roberts et al.) (85).

as we showed in Chapter 3, Section 3.2.5. In fact, the acoustic diffraction pattern is a scaled version of the diffraction patterns that occur at light wavelengths; the scaling factor is Λ/λ.

Figure 7.10(b) shows a Schlieren image of an eight-channel acousto-optic cell, wherein the center frequency f_c is modulated by eight different pseudorandom sequences (85). The acoustic spreading is not as pronounced in this example because the time bandwidth product of the cell is lower. Multichannel acousto-optic cells with up to 128 active channels have been built, although 32 channel cells are more commonly available.

7.9. APPLICATIONS OF ACOUSTO-OPTIC DEVICES

Acousto-optic cells are configured in different ways, such as with single-channel or multichannel transducers. They perform different functions, such as modulating light temporally, deflecting light, or serving as a delay line. In this section we review some of these functions.

7.9.1. Acousto-Optic Modulation

For optical signal processing we are primarily interested in using acousto-optic cells as delay lines or as short-term memories. They are sometimes useful, however, as *modulators* to impart a temporal variation onto the entire optical beam. In our model of these applications, we reduce the length of acousto-optic cell by letting $L \rightarrow 0$ so that the space/time signal $f(t - T/2 - x/v)$ degenerates to the purely temporal signal $f(t)$, as illustrated in Figure 7.11. The illumination must be a focused beam because the rise time associated with the modulation bandwidth is proportional to the time τ required for the acoustic beam to travel across the optical beam. As the acoustic transit time decreases, the rise time decreases so that the corresponding bandwidth increases.

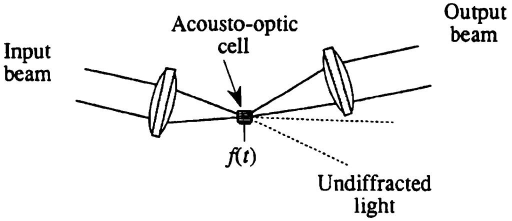

Figure 7.11. Acousto-optic temporal modulator.

As the bandwidth of the acousto-optic cell increases, however, the output cone of light becomes elliptical because the optical and acoustic waves do not match over the full range of input ray angles (80). The momentum-conservation law is given by $\mathbf{k}_{\text{out}} = \mathbf{k}_{\text{in}} + \mathbf{K}$, as shown in Section 7.2.2. In a modulator, the incident light beam has a range of $\mathbf{k}_{\text{in}}$ vectors of constant magnitude, distributed over an angular range $\delta\theta_0$ because the light beam is convergent. To satisfy the vector relationship, the acoustic wave must have a corresponding range of angular directions $\delta\theta$. When $\delta\theta < \delta\theta_0$, momentum cannot be conserved for all optical wave components; this loss of momentum produces an elliptical output beam cross section. If $\delta\theta > \delta\theta_0$, the bandwidth is reduced.

The 10–90% rise time t_r for an acousto-optic modulator is a function of the transit time T. For a Gaussian input beam profile, truncated at the $1/e^2$ points in intensity, we find that $t_r \approx T/1.5$ and that the frequency response rolloff β, defined in decibels, is (80)

$$\beta = 10\log\left[e^{-\pi^2 f^2 T^2/8}\right], \tag{7.36}$$

where f is the frequency. We solve for the cutoff frequency f_{co} at which the response has rolled off to the value β:

$$f_{\text{co}} = \frac{c\sqrt{\beta}}{\pi T}, \tag{7.37}$$

where $c = \sqrt{0.8 \ln 10} \approx 1.4$. The relationship between rise time and modulation bandwidth is, therefore, that

$$\Delta f = \frac{0.29\sqrt{\beta}}{t_r}. \tag{7.38}$$

Note that Δf is the *modulation bandwidth of a baseband signal*; the rf bandwidth is twice Δf because we retain both the upper and lower sidebands of the signal about the carrier frequency.

Acousto-optic cells also have application as Q switches, mode lockers, cavity dumpers, and other devices associated with lasers for controlling light (79–81). Table 7.1 gives the properties of selected interaction materials as used in specific acousto-optic configurations (80). The attenuation of these devices is indicated by Γ and is stated as the number of decibels of attenuation per μsec of cell length per GHz^2 of the applied frequency. For example, a 3-μsec cell made from LiNbO_3 and operating at a frequency of 750 MHz has an attenuation of $0.098 \times 3 \times (0.75)^2 = 0.17$ dB at the end of the cell.

Table 7.1 Properties of Selected Acousto-Optic Interactions

Material	Velocity v (10^3 m/s)	Index n	Attenuation Γ dB/(μsec · Ghz^2)	Figure of Merit M_2 (10^{-15} sec^3/kg)
$LiTaO_2$	6.19	2.18	0.062	1.37
$LiNbO_3$	6.57	2.20	0.098	7.00
TiO_2	8.03	2.584	0.566	3.93
$Sr_{0.75}Ba_{0.25}Nb_2O_6$	5.50	2.299	2.20	38.6
GaP	6.32	3.31	3.80	44.6
TeO_2 (longitudinal)	4.20	2.26	6.30	34.6
TeO_2 (slow shear)	0.617	2.26	17.6	1200

The data given in Table 7.1 is representative of the interaction parameters. The specific values are dependent on factors such as the strain mode (longitudinal or shear), the polarization and direction of the incident light, and the acoustic **K** vector direction with respect to the crystal axes. Furthermore, the acoustic attenuation dependence on frequency is sometimes proportional to the 1.5 power instead of the square of the frequency. In a similar fashion, the figure of merit M_2 is not a pure material constant but is dependent on the factors cited above.

7.9.2. Acousto-Optic Beam Deflectors

The acousto-optic cell, when driven by a cw frequency, behaves as a random access beam deflector which addresses a specific position at the focal plane of a lens. Figure 7.12 shows an acousto-optic cell at plane P_1 with an acoustic velocity v and a length $L = vT$. We drive the cell with a signal $f(t) = \cos(2\pi f_k t)$ to access the kth spot position in the scan line. This signal produces a positive diffracted order whose Fourier transform is

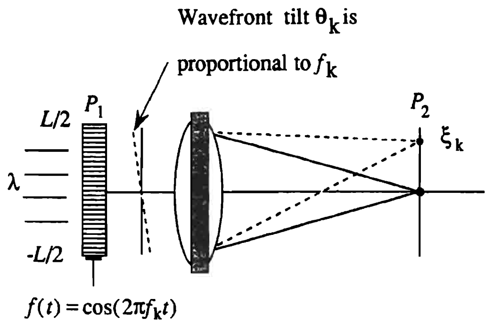

Figure 7.12. Acousto-optic scanner.

generated by a lens with focal length F:

$$F_+(\xi, t) = \int_{-\infty}^{\infty} f_+(x, t) e^{j(2\pi/\lambda F)\xi x}\, dx, \tag{7.39}$$

where $f_+(x, t) = \mathrm{rect}(x/L)\exp[j2\pi f_k(t - T/2 - x/v)]$. The Fourier transform of $f_+(x, t)$ is

$$\begin{aligned} F_+(\xi, t) &= \int_{-L/2}^{L/2} e^{j2\pi f_k(t - T/2 - x/v)} e^{j(2\pi/\lambda F)\xi x}\, dx \\ &= e^{j2\pi f_k(t - T/2)} \,\mathrm{sinc}\left[\left(\frac{\xi}{\lambda F} - \frac{f_k}{v}\right)L\right], \end{aligned} \tag{7.40}$$

when we ignore amplitude scaling factors. From Equation (7.40), we find that the lens focuses light at the spatial position

$$\xi_k = \frac{\lambda F}{v} f_k \tag{7.41}$$

at plane P_2. This result shows that the spot position is linearly proportional to the applied frequency. The first zero of the sinc function occurs at

$$\xi_0 = \frac{\lambda F}{L} = d_0, \tag{7.42}$$

in accordance with basic Fourier-transform theory. We use d_0 both as a measure of the spot size as well as the Nyquist sampling interval at plane P_2.

In addition to the random-access mode, we can use cw frequencies to scan a light beam along a line in a stepwise fashion. However, a continuous scanning action provided by a chirp drive signal provides higher line scan rates. Figure 7.13 shows an acousto-optic cell driven by a signal whose frequency increases linearly from f_1 to f_2 in a time duration T_c. Such a frequency-modulation signal is called a *chirp signal* as characterized by

$$c(t) = \cos(2\pi f_1 t + \pi a t^2); \qquad 0 \le t \le T_c, \tag{7.43}$$

where a is the *chirp rate*, expressed in Hz/sec and T_c is the *chirp*

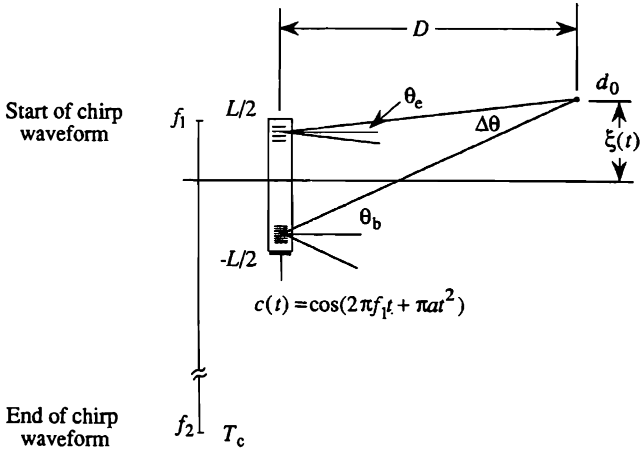

Figure 7.13. Linear scanning with chirp waveform.

duration. From Equation (7.43), we see that the *instantaneous frequency* f_i is

$$\begin{aligned} f_i &= \frac{1}{2\pi}\frac{\partial}{\partial t}\left(2\pi f_1 t + \pi a t^2\right) \\ &= f_1 + at; \qquad 0 \le t \le T_c. \end{aligned} \tag{7.44}$$

The instantaneous frequency of the chirp sweeps over the bandwidth $W = f_2 - f_1$ of the acousto-optic cell in the chirp duration T_c so that the chirp rate a is

$$\boxed{a = \frac{W}{T_c}.} \tag{7.45}$$

Because the instantaneous frequency at the end of the acousto-optic cell is f_e, the frequency at the beginning of the cell must be

$$f_b = f_e + aT = f_e + \frac{WT}{T_c}. \tag{7.46}$$

In the example shown, the chirp frequency is increasing in time, generally called the *upchirp* condition; the chirp frequency may also decrease in time, called the *downchirp* condition.

The behavior of the scanning action produced by the cell can be explained by using elementary diffraction theory and geometrical ray tracing or by using a diffraction integral. Each method provides useful insights into the scanning phenomena; we begin with the ray tracing approach.

7.9.2.1. Linear Scanning with Chirp Waveforms: The Ray-Tracing Approach. Consider a ray trace for a stationary chirp segment that has just filled the acousto-optic cell, as shown in Figure 7.13. Basic diffraction theory shows that the instantaneous frequency in the small region near the end of the cell produces an undiffracted waveform, indicated by a ray traveling parallel to the optical axis, along with positive and negative diffracted waveforms, indicated by rays that each make an angle θ_e with respect to the undiffracted light. The diffraction angle is related to the spatial frequency α_e and the temporal frequency f_e by

$$\theta_e = \lambda \alpha_e = \frac{\lambda f_e}{v}. \tag{7.47}$$

A similar relationship holds for the region near the beginning of the cell:

$$\theta_b = \lambda \alpha_b = \frac{\lambda f_b}{v} = \frac{\lambda(f_e + WT/T_c)}{v}. \tag{7.48}$$

When we trace the rays associated with the positive diffracted orders of each subregion within the cell, we find that they intersect a distance D from the cell to form a spot whose size is d_0. For the small diffraction angles produced by the acousto-optic cell, the included angle between the extreme rays is

$$\Delta\theta = \theta_b - \theta_e = \frac{\lambda WT}{vT_c}, \tag{7.49}$$

so that the distance to the plane of focus is

$$D = \frac{L}{\Delta\theta} = \frac{vLT_c}{\lambda WT} = \frac{v^2 T_c}{\lambda W}. \tag{7.50}$$

From Equation (7.50) we find a useful relationship between the chirp rate a and the radiu‿ ˀf curvature D of the chirp wavefront within the cell. By rearranging the factors, we find that

$$\boxed{\frac{v^2}{\lambda D} = \frac{W}{T_c} = a.} \tag{7.51}$$

The key geometrical parameters of the acoustic signal, such as v, λ, and D, are on the left of this relationship while the key drive signal parameters, such as W and T_c, are on the right.

The spot size, following the Rayleigh criterion as given in Chapter 3, Section 3.5.2, is $d_0 = \lambda/\Delta\theta$, where $\Delta\theta$ is the angle between the two rays. For the configuration of Figure 7.13, we find that

$$d_0 = \frac{\lambda}{\Delta\theta} = \frac{vT_c}{TW}. \tag{7.52}$$

For a given chirp duration, the spot size is inversely proportional to the time bandwidth product of the cell.

The scanning velocity is most easily calculated by noting that the spot position, as a function of time, is

$$\begin{aligned} \xi(t) &= -\frac{L}{2} + D\theta_b(t) \\ &= -\frac{L}{2} + D\frac{\lambda(f_e + Wt/T_c)}{v}, \end{aligned} \tag{7.53}$$

where we used the general form of Equation (7.48) to produce Equation (7.53). The scanning velocity v_s is then

$$v_s = \frac{\partial}{\partial t}\xi(t) = D\frac{\lambda W}{vT_c}. \tag{7.54}$$

We now use the value of D from Equation (7.50) in Equation (7.54) to find that

$$v_s = \frac{v^2 T_c}{\lambda W}\frac{\lambda W}{vT_c} = v. \tag{7.55}$$

The scanning velocity is therefore always equal to the acoustic velocity and cannot be controlled by any of the system parameters.

The length of the scan line is equal to the product of the scan velocity and the *active* scanning time. Scanning begins at $t = T$ and continues until $t = T_c$ so that the active scan time interval is $(T_c - T)$. The length of the scan line is therefore

$$L_s = v_s(T_c - T) = v(T_c - T) = \left[\frac{T_c}{T} - 1\right]L, \tag{7.56}$$

so that the scan line is longer than the length of the acousto-optic cell. The number of samples in a scan line is

$$\boxed{M = \frac{L_s}{d_0} = \frac{v(T_c - T)}{vT_c/TW} = \left[1 - \frac{T}{T_c}\right]TW,} \tag{7.57}$$

so that the number of samples in a scan line approaches the time bandwidth product of the cell, if $T_c \gg T$.

7.9.2.2. Linear Scanning with Chirp Waveforms: The Diffraction Approach. To control the scanning velocity, we must introduce a lens to the right of the acousto-optic cell. To analyze this condition, we use the diffraction method exclusively; in the process, we develop some new analytical tools and provide other useful insights. Furthermore, we can now more fully address the effects produced by the temporal characteristics of the chirp waveform.

Figure 7.14 shows a condition for which the acousto-optic cell aperture is small compared to the chirp duration. The chirp duration T_c is the time between the lowest and highest frequencies of the chirp, the difference

Chirp train

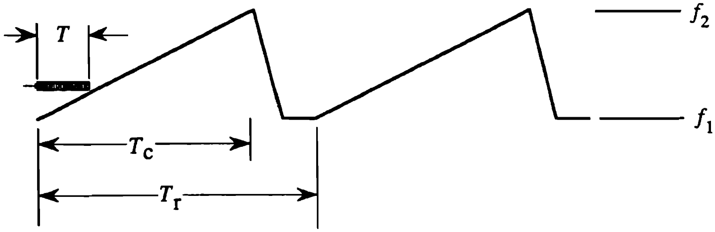

Figure 7.14. ⁻requency/time relationship for a chirp trai

being $W = f_2 - f_1$. The *repetition period* T_r is the time interval between a given point on one chirp segment and a similar point on the next chirp segment, for example, the time between the highest frequencies of two adjacent segments. The repetitive nature of the *chirp train* between the highest frequencies of two adjacent segments. The repetitive nature of the *chirp train*, shown in Figure 7.14, is expressed by a time convolution of the chirp signal with an impulse train:

$$\begin{aligned} f(t) &= c(t) * \sum_{n=-\infty}^{\infty} \delta(t - nT_r) \\ &= \cos\left(2\pi f_1 t + \pi a t^2\right) * \sum_{n=-\infty}^{\infty} \delta(t - nT_r), \end{aligned} \tag{7.58}$$

where T_r is the repetition period of the chirp train.

We consider the general case in which T_c may be larger than, comparable to, or even less than, the aperture time T of the acousto-optic cell. We classify scanners according to two criteria: the active aperture time and the active scan time. If $T_c \geq T$, the active aperture time is governed by the length of the acousto-optic cell; we refer to this condition as the *long-chirp scanner*. If $T_c < T$, the active aperture time is governed by the length of the chirp, we refer to this condition as the *short-chirp scanner*. For the long-chirp scanner, the active scan time is $T_s = T_c - T$, as noted in Section 7.9.2.1. For the short-chirp scanner, the active scan time is $T_s = T - T_c$. These two scan times can be combined to give a single active scan time of $T_s = |T - T_c|$.

When we use a voltage-controlled oscillator to generate the chirp signal, T_r must be greater than T_c because the signal does not return instantaneously from f_2 to f_1. A part of the chirp train is therefore not available for active scanning. We can, however, arrange for the chirp waveforms to overlap to an arbitrary extent by impulsing a surface acoustic wave device that produces a chirp waveform at arbitrary repetition intervals. The active scan time is then either T_s or T_r, whichever is shorter. When the active scan time is T_s, the system is *aperture limited*. When the active scan time is T_r, the system is *repetition rate limited*.

7.9.2.2.1. ***A Long-Chirp, Aperture-Limited Scanner.*** There are four basic scanner configurations: a long or short chirp scanner; each is either aperture or repetition rate limited. We begin our diffraction analysis for a long-chirp scanner that is aperture limited. The optical arrangement is essentially the same as that shown in Figure 7.12, except that the acousto-optic cell is now driven by a chirp signal represented by Equation (7.58).

For this exercise, we select the negative diffracted order, whose amplitude just to the right of the acousto-optic cell is

$$f_-(x,t) = \mathrm{rect}(x/L)e^{-j[2\pi f_1(t-T/2-x/v)+\pi a(t-T/2-x/v)^2]}; \qquad T \le t \le T_c, \tag{7.59}$$

where we have dropped scaling factors and used uniform illumination. The scan time starts at $t = T$ and finishes when the end of the chirp segment arrives at the transducer. For the moment we assume that the lens is in contact with the acousto-optic cell; we show how to handle a finite separation later in this section. A positive lens is represented by the phase response

$$h(x) = e^{j(\pi/\lambda F)x^2}, \tag{7.60}$$

so that the light distribution to the right of the lens is

$$f_-(x,t) = \mathrm{rect}(x/L)e^{-j[2\pi f_1(t-T/2-x/v)+\pi a(t-T/2-x/v)^2]}e^{j(\pi/\lambda F)x^2}; \qquad T \le t \le T_c. \tag{7.61}$$

The light distribution at any plane a distance D_f to the right of the lens is given by the Fresnel transform of $r_-(x,t)$:

$$F(\xi,t) = \int_{-\infty}^{\infty} f_-(x,t)e^{-j(\pi/\lambda D_f)(\xi-x)^2}\,dx. \tag{7.62}$$

We substitute Equation (7.61) into Equation (7.62), to find that

$$F(\xi,t) = \int_{-\infty}^{\infty} \mathrm{rect}(x/L)e^{-j[2\pi f_1(t-T/2-x/v)+\pi a(t-T/2-x/v)^2]} e^{j(\pi/\lambda F)x^2}e^{-j(\pi/\lambda D_f)(\xi-x)^2}\,dx; \qquad T \le t \le T_c. \tag{7.63}$$

We use Equation (7.51) in Equation (7.63) to find that

$$\begin{aligned} F(\xi,t) &= e^{-j2\pi f_1(t-T/2)}\int_{-\infty}^{\infty} \mathrm{rect}(x/L)e^{j2\pi f_1 x/v}e^{-j[(\pi v^2/\lambda D)(t-T/2-x/v)^2]} \\ &\qquad \times e^{j(\pi/\lambda F)x^2}e^{-j(\pi/\lambda D_f)(\xi-x)^2}\,dx \\ &= e^{j\phi}\int_{-L/2}^{L/2} e^{j(\pi x^2/\lambda)[1/F-1/D-1/D_f]} \\ &\qquad \times e^{j(2\pi x/\lambda)[v(t-T/2)/D+\xi/D_f+\lambda f_1/v]}\,dx; \qquad T \le t \le (T_c - T), \end{aligned} \tag{7.64}$$

where we collect all phase factors that are not functions of x into the term ϕ. Note that the chirp rate $a = W/T_c$ is positive when we use the upchirp mode, as we do here, and negative when we use the downchirp mode of modulation.

The focal position occurs when the integral has its maximum value so that the light intensity is highest. The integral in Equation (7.64) has its maximum value when the integrand is set equal to one. Let us begin, however, by setting just the value of the exponential that is quadratic in x equal to one. The first condition necessary to obtain focus is therefore that

$$\frac{1}{F} - \frac{1}{D} - \frac{1}{D_f} = 0, \tag{7.65}$$

or that

$$D_f = \frac{DF}{D - F}. \tag{7.66}$$

When Equation (7.66) is satisfied, Equation (7.64) produces the spatial light distribution at the focal point:

$$\begin{aligned} F(\xi, t) &= \int_{-L/2}^{L/2} e^{j(2\pi x/\lambda)[v(t-T/2)/D + \xi/D_f + \lambda f_1/v]}\, dx \\ &= L \operatorname{sinc}\left[\frac{v(t - T/2)L}{\lambda D} + \frac{\xi(D - F)L}{\lambda FD} + \frac{f_1 L}{v}\right]; \qquad T \le t \le T_c. \end{aligned} \tag{7.67}$$

The position of the scanning spot at any instant in time is found by setting the argument of the sinc function equal to zero, equivalent to setting the value of the exponential in Equation (7.64) that is linear in x equal to 1:

$$\xi = -\frac{\lambda f_1 DF}{v(D - F)} - \frac{v(t - T/2)F}{D - F}, \qquad T \le t \le T_c. \tag{7.68}$$

The spot position at the beginning of scan when $t = T$ is

$$\xi_b = -\frac{\lambda f_1 DF}{v(D - F)} - \frac{v(T/2)F}{D - F}, \tag{7.69}$$

and the spot position at the end of scan when $t = T_c$ is

$$\xi_e = -\frac{\lambda f_1 DF}{v(D-F)} - \frac{v(T_c - T/2)F}{D-F}, \tag{7.70}$$

so that the length of scan is

$$L_s = |\xi_e - \xi_b| = \left|\frac{v(T_c - T)F}{D-F}\right|. \tag{7.71}$$

The scanning velocity is readily obtained from Equation (7.68) as

$$\boxed{v_s = \frac{\partial \xi}{\partial t} = -\frac{vF}{D-F}.} \tag{7.72}$$

The scanning velocity v_s has the same or opposite direction as v depending on the value D of the wavefront radius of curvature. When we use a configuration in which the acoustic wave is traveling in the positive x direction, the rules are that:

1. When D is positive and greater than F, as for the case analyzed here, v_s is negative so that the spot moves in the negative x direction. In this case, the chirp signal in the acousto-optic cell is equivalent to a negative lens whose focal length is longer than that of the positive lens. The light therefore focuses at some plane to the right of the lens because the distance D_f is positive, as we see from Equation (7.66).
2. When D is negative, the scanning spot moves in the positive x direction. In this case, the focal length of the chirp is equivalent to a positive lens and the net result, as confirmed by Equation (7.66), is that of two positive lenses working together.
3. When D is positive and less than F, the scanning velocity is positive so that the spot moves in the same direction as v, but the light does not focus anywhere to the right of the lens. In this case, the focal length of the chirp is equivalent to a negative lens whose focal length is shorter than that of the positive lens, and Equation (7.66) confirms that D_f is negative.

These rules are illustrated in Figure 7.15. The negative diffracted order satisfies the first rule. The value of D is positive, equivalent to stating that

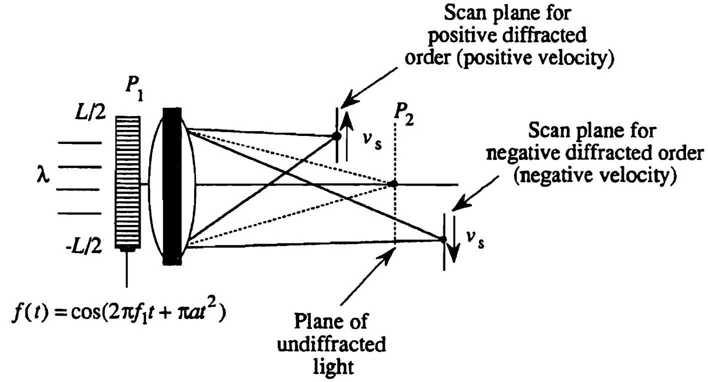
Scan plane for positive diffracted order (positive velocity)
P_1
$L/2$
λ
$-L/2$
P_2
v_s
Scan plane for negative diffracted order (negative velocity)
v_s
$f(t) = \cos(2\pi f_1 t + \pi a t^2)$
Plane of undiffracted light

Figure 7.15. Scanning action diagram.

the focal power of the chirp is negative so that the scan plane lies to the right of the plane at which the undiffracted light is focused. As the chirp signal flows through the acousto-optic cell, the ray angles increase in the negative direction, leading to a negative scan velocity. The start-of-scan position, as seen from Equation (7.69), is negative as is the end-of-scan position, as we see from Equation (7.70).

The positive diffracted order satisfies the second rule. The value of D is negative, equivalent to stating that the focal power of the chirp is positive, so that the scan plane lies to the left of the plane at which the undiffracted light is focused. As the chirp signal flows through the acousto-optic cell, the ray angles increase in the positive direction, leading to a positive scan velocity. The start-of-scan position, as seen from Equation (7.69), is positive; the end-of-scan position, as we see from Equation (7.70), is also positive. The positive diffracted order exists for all values of D because the equivalent focal length of two lenses with positive powers must be positive.

Rule three applies to a special case for the negative diffracted order and states that the light may not focus at any plane to the right of the lens for certain values of D. For example, as the value of D approaches F, the negative power due to the chirp signal subtracts from the positive power of the lens; the focal plane for the negative diffracted order therefore recedes to infinity. When $D = F$, the two focal powers exactly cancel and the focal plane is at infinity. As stated in the third rule, the negative diffracted order does not focus at any plane to the right of the lens if D is positive and less than F; it generates a virtual scan plane.

When we drive the acousto-optic cell with a downchirp signal of the form

$$f(t) = \cos\left(2\pi f_2 t - \pi a t^2\right), \tag{7.73}$$

instead of with the upchirp signal, the same general results apply except that we interchange f_1 and f_2 to account for the different starting frequency and replace D by $-D$ to account for the negative chirp rate. The roles of the two scan planes shown in Figure 7.16 are then interchanged so that the negative diffracted order focuses to the left of the positive diffracted order. As expected, the scan velocities also have opposite signs so that the spots scan toward the optical axis instead of away from the optical axis.

Equation (7.72) shows how to control the scanning velocity by selecting the value of the focal length of the lens. For a desired scan velocity, the required focal length of the lens is

$$F = \frac{D}{1 - v/v_s}. \tag{7.74}$$

The signs of D and v_s can combine, according to the rules, only to cause the focal length of the lens to be positive.

The size of the scanning spot is obtained from Equations (7.52) and (7.66):

$$d_0 = \frac{\lambda}{L/D_f} = \frac{\lambda DF}{(D - F)L}. \tag{7.75}$$

As the chirp radius of curvature $D \to \infty$, the spot size tends to a value of $d_0 = \lambda F/L$, as expected, because then the chirp waveform contributes no power to the system; the lens alone acts on the diffracted light.

The number of samples in the scan line is

$$M = \frac{L_s}{d_0} = \left|\frac{v(T_c - T)L}{\lambda D}\right|. \tag{7.76}$$

We use Equation (7.51) in Equation (7.76) to find that

$$M = \left[1 - \frac{T}{T_c}\right]TW, \tag{7.77}$$

just as we found from the geometrical analysis.

The *scan duty cycle* is defined as the ratio of the active scan time divided by the repetition period:

$$U = \frac{\min(T_s, T_r)}{T_r} = \frac{T_c - T}{T_r}. \tag{7.78}$$

The *sample rate* at which samples are recorded is given by the ratio of the scan velocity to the spot size:

$$R_s = \frac{|v_s|}{d_0} = \frac{T}{T_c} W. \tag{7.79}$$

The throughput rate is the average number of samples recorded per unit time and is the product of the sample rate and the scan duty cycle;

$$R_t = UR_s = \left[1 - \frac{T}{T_c}\right] \frac{T}{T_r} W, \tag{7.80}$$

where we have used Equations (7.78) and (7.79) to produce Equation (7.80).

If the acousto-optic cell and the lens are not in contact, as shown in Figure 7.15, we can use the thin-lens formula to find the equivalent position of the plane at which the light is focused. If the separation between two thin lenses with powers $K_1 = 1/F_1$ and $K_2 = 1/F_2$ is z_{12}, the equivalent power of the combination, as given in Chapter 2, Section 2.5.8, is

$$K_{\text{eq}} = K_1 + K_2 - z_{12} K_1 K_2. \tag{7.81}$$

We associate the power of the chirp signal in the acousto-optic cell with K_1 so that $K_1 = -1/D$ and associate the lens power with K_2. The net power of the combination gives the distance to the scan plane from the acousto-optic cell: $D_f = 1/K_{\text{eq}}$.

7.9.2.2.2. ***A Short-Chirp, Aperture-Limited Scanner.*** In the short-chirp scanner, the active aperture time is limited by the chirp duration T_c. Suppose that one of the chirp segments from the chirp train is completely within the acousto-optic cell, as shown in Figure 7.16. The relationships given from Equation (7.67) onward are modified for application to the short-chirp, aperture-limited scanner. For example, the start-of-scan time is T_c and the end-of-scan time is $T - T_c$, and the integrations are over a

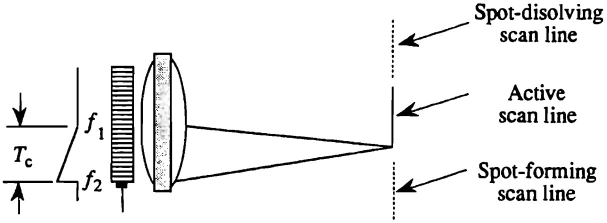

Figure 7.16. Short-chirp scanner.

spatial range $L_c = vT_c$. We study the diffraction phenomenon as the chirp transitions into and out of the cell at the end of this section.

The new form of Equation (7.67) becomes

$$\begin{aligned} F(\xi, t) &= \int_{-L/2}^{(L-L_c)/2} e^{j(2\pi x/\lambda)[v(t-T/2)/D+\xi/D_f+\lambda f_1/v]}\,dx \\ &= L_c \operatorname{sinc}\left[\frac{v(t-T/2)L_c}{\lambda D} + \frac{\xi(D-F)L_c}{\lambda FD} + \frac{f_1 L_c}{v}\right]; \\ &\qquad T_c \le t \le (T - T_c), \end{aligned} \tag{7.82}$$

where we ignore unessential magnitude and phase factors. As before, the position of the scanning spot at any instant in time is found by setting the argument of the sinc function equal to zero, from which we find that

$$\xi = -\frac{\lambda f_1 DF}{v(D-F)} - \frac{v(t-T/2)F}{D-F}, \qquad T_c \le t \le (T - T_c). \tag{7.83}$$

The spot position of the beginning of scan when $t = T_c$ is

$$\xi_b = -\frac{\lambda f_1 DF}{v(D-F)} - \frac{v(T_c/2)F}{D-F}, \tag{7.84}$$

and the spot position at the end of scan when $t = T - T_c$ is

$$\xi_e = -\frac{\lambda f_1 DF}{v(D-F)} - \frac{v(T/2 - T_c)F}{D-F}, \tag{7.85}$$

so that the length of scan is

$$L_s = |\xi_e - \xi_b| = \left|\frac{v(T - T_c)F}{D - F}\right|. \tag{7.86}$$

The scanning velocity is still given by Equation (7.72), but the spot size is slightly different:

$$d_0 = \frac{\lambda}{L_c/D_f} = \frac{\lambda DF}{(D - F)L_c}, \tag{7.87}$$

which is similar to Equation (7.75), except that L is replaced by L_c because the spot size is now determined by the length of the chirp, not by the length of the acousto-optic cell. The number of samples in the scan line is

$$M = \frac{L_s}{d_0} = \left|\frac{vF(T - T_c)}{(D - F)}\right| \frac{(D - F)L_c}{\lambda DF} = \left|\frac{v(T - T_c)L_c}{\lambda D}\right|. \tag{7.88}$$

We now use Equation (7.51) in Equation (7.88) to find that the number of samples in the scan line is

$$M = \left[1 - \frac{T_c}{T}\right]TW. \tag{7.89}$$

Because the chirp duration is less than the cell duration, the time bandwidth product of the acousto-optic cell is not fully utilized.

The scan duty cycle for this configuration is

$$U = \frac{T - T_c}{T_r}, \tag{7.90}$$

and the sample rate is

$$R_s = \frac{|v_s|}{d_0} = W, \tag{7.91}$$

which is the maximum achievable sample rate. The throughput rate is

$$R = U\frac{|v_s|}{d_0} = \frac{T - T_c}{T_r}W, \tag{7.92}$$

obtained in a fashion similar to that used to produce Equation (7.79).

Figure 7.16 shows the situation when at least one period of a chirp signal is fully in the acousto-optic cell and the scanning spots are therefore well formed. We now examine the scanning spot shape and position as the chirp segments enter and leave the cell. The light from these transition times is located in regions just before and just after the scan line. To account for the spot-forming condition, we modify the limits of integration in Equation (7.64):

$$\begin{aligned} F(\xi, t) = \int_{-L/2}^{-L/2+vt} & e^{j(\pi x^2/\lambda)[1/F - 1/D - 1/D_f]} \\ & \times e^{j(2\pi x/\lambda)[v(t-T/2)/D + \xi/D_f + \lambda f_1/v]}\, dx; \qquad 0 \le t \le T_c, \end{aligned} \tag{7.93}$$

which is applicable for a chirp waveform as it just enters the cell. The limits of integration show that the integral is over a small spatial region when t is small and that the region of integration increases linearly for $0 \le t \le T_c$. As before, we set the value of D_f so that the quadratic term in x is equal to unity, leaving the integral

$$\begin{aligned} F(\xi, t) &= \int_{-L/2}^{-L/2+vt} e^{j(2\pi x/\lambda)[v(t-T/2)/D + \xi/D_f + \lambda f_1/v]}\, dx \\ &= vt \operatorname{sinc}\left[\left\{\frac{v(t - T/2)}{D} + \frac{\xi}{D_f} + \frac{\lambda f_1}{v}\right\} vt/\lambda\right]; \qquad 0 \le t \le T_c, \end{aligned} \tag{7.94}$$

where we ignore unimportant scale factors.

The behavior of this sinc function, whose argument is quadratic in the time variable, has some interesting features that are exhibited in the dotted line region of Figure 7.16 where the spot is first formed:

1. The magnitude of the sinc is small for small values of t, as we expect from a consideration of the region of integration, and reaches a limit that is proportional to vT_c when the chirp in the cell is fully illuminated.

2. The centroid of the spot as a function of time is located at

$$\xi = -\frac{\lambda f_1 DF}{v(D-F)} - \frac{v(t - T/2)F}{D-F}, \qquad 0 \le t \le T_c, \quad (7.95)$$

just as in Equation (7.83) but with a slightly different time interval of validity. The spot position when the chirp just enters the cell is

$$\xi_b = -\frac{\lambda f_1 DF}{v(D-F)} - \frac{v(-T/2)F}{D-F}, \qquad (7.96)$$

and its position when it is fully in the cell is

$$\xi_e = -\frac{\lambda f_1 DF}{v(D-F)} - \frac{v(T/2)F}{D-F}. \qquad (7.97)$$

By comparing Equations (7.96) and (7.97) with Equations (7.84) and (7.85), we see that the end positions of the scanning spot produced by the chirp as it enters the cell are displaced a distance L_s below that of the active scan line.

3. The most interesting feature of the sinc function is that the spot changes its size continuously as the chirp enters the cell. The spot size is determined by finding the position of the first zero of the sinc function relative to its centroid. This distance is

$$\Delta\xi = d_0 = \frac{\lambda D_f}{vt}; \qquad 0 \le t \le T_c. \qquad (7.98)$$

From Equation (7.94) we see that the sinc function is infinitely broad when $t = 0$, but its magnitude is zero. As time increases, the spot moves towards the active scanning region and its size decreases while its magnitude increases. The rate at which the spot size decreases, as the centroid moves closer to the beginning of the active scan position, is just sufficient to keep the light from spilling into the active scanning region prematurely. When the chirp has fully entered the cell at $t = T_c$, the spot has full resolution and the active scanning begins as the chirp travels through the remainder of the acousto-optic cell.

As the chirp segment leaves the cell, the spot dissolves in an order that is a reversal of its evolution. The spot gradually loses intensity as it broadens, until it reaches the end of the spot dissolving scan line shown in Figure 7.16.

*7.9.2.2.3. **A Long-Chirp, Repetition-Rate-Limited Scanner.*** To achieve a high throughput rate, we need a high scan duty cycle; Equation (7.78) shows that we want the active scan time to equal the repetition period of the chirp train. Suppose that we use a surface acoustic device to generate a chirp segment whenever it is driven by an impulse function. By controlling the timing of the impulses, we produce chirp segments with any desired repetition period T_r. Depending on the ratio of the repetition period to the chirp duration, one or more overlapping chirp segments may be in the cell at the same time. If the response of the cell is linear, the chirp signals do not interfere and the only effect of the overlapping chirps is to lower the diffraction efficiency. As the chirp signal is on a carrier frequency, a nonlinear response from the cell produces higher-order terms that are easily eliminated by spatial filters.

In this section, we assume that the chirp segments overlap so that $T_r \leq T_c$, and that $T_r > T$. The system parameters that are changed are the scan length which, through a line of analysis similar to that given in Section 7.9.2.2.1, is now

$$L_s = |\xi_e - \xi_b| = \left|\frac{vT_rF}{D - F}\right|. \tag{7.99}$$

The spot size is still determined by the cell aperture because $T_r > T$:

$$d_0 = \frac{\lambda DF}{(D - F)L}, \tag{7.100}$$

so that the number of samples in a scan line is

$$M = \frac{T_r}{T_c}TW. \tag{7.101}$$

The scan duty cycle for this scanner configuration is

$$U = \frac{\min(T_s, T_r)}{T_r} = \frac{T_r}{T_r} = 1, \tag{7.102}$$

as expected. The sample rate and the throughput rate are equal in this configuration at

$$R_t = UR_s = \frac{|v_s|}{d_0} = \frac{T}{T_c}W \tag{7.103}$$

As before, we see that the throughput rate is maximized only when $T_c = T$. To achieve this condition, we consider the final of the four basic configurations.

7.9.2.2.4. ***A Short-Chirp, Repetition-Rate-Limited Scanner.*** In this configuration, the chirp segments also overlap so that $T_r \leq T_c$, and we assume that $T_r \leq T$. The scan length, found through a line of analysis similar to that given in Section 7.9.2.2.1, is

$$L_s = |\xi_e - \xi_b| = \left|\frac{vT_rF}{D - F}\right|. \tag{7.104}$$

The spot size is now determined by the active scan aperture because $L_c = vT_c$ so that

$$d_0 = \frac{\lambda DF}{(D - F)L_c}, \tag{7.105}$$

and the number of samples in a scan line is

$$M = T_rW, \tag{7.106}$$

which achieves its maximum value when $T_r = T$. The scan duty cycle for this configuration is

$$U = \frac{\min(T_s, T_r)}{T_r} = \frac{T_r}{T_r} = 1, \tag{7.107}$$

as expected. The sample rate and the throughput rate are equal in this configuration at

$$R_t = UR_s = \frac{|v_s|}{d_0} = W \tag{7.108}$$

In this configuration, the throughput rate is maximized independently of the values of T_r or T_c, provided that the constraints necessary to implement the short-chirp, repetition-rate-limited scanner are observed.

7.9.2.3. Summary of Scanner Performance Criteria. Table 7.2 gives a summary of the important performance parameters of the four basic scanning configurations and serves as a useful aid in beginning a design. For example, some applications require a high throughput rate R_t. The

Table 7.2 Acousto-Optic Scanner Parameters

Type of Chirp	Long Chirp $T_c \geq T$		Short Chirp $T_c < T$	
Scan Time	Aperture Limited $T_c - T \leq T_r$	Repetition-Rate Limited $T_c - T > T_r$	Aperture Limited $T_c + T_r \geq T$	Repetition-Rate Limited $T_c + T_r < T$
Active scan time = $\min(T_s, T_r)$	$T_c - T$	$T_c - T$	$T - T_c$	$T - T_c$
Active aperture time = $\min(T, T_c)$	T	T	T_c	T_c
Scan length = L_s	$\left\lvert \frac{v(T_c - T)F}{D - F} \right\rvert$	$\left\lvert \frac{vT_rF}{D - F} \right\rvert$	$\left\lvert \frac{v(T - T_c)F}{D - F} \right\rvert$	$\left\lvert \frac{vT_rF}{D - F} \right\rvert$
Spot size = d_0	$\frac{\lambda DF}{(D-F)L}$	$\frac{\lambda DF}{(D-F)L}$	$\frac{\lambda DF}{(D-F)L_c}$	$\frac{\lambda DF}{(D-F)L_c}$
Number of samples per line = M	$\left[1 - \frac{T}{T_c}\right]TW$	$\frac{T_r}{T_c}TW$	$\left[1 - \frac{T_c}{T}\right]TW$	$\frac{T_r}{T}TW$
Scan duty cycle = U $\min(T_s, T_r)/T_r$	$\frac{T_c - T}{T_r}$	1	$\frac{T - T_c}{T_r}$	1
Sample rate = R_s	$\frac{T}{T_c}W$	$\frac{T}{T_c}W$	W	W
Throughput rate = R_t	$\left[1 - \frac{T}{T_c}\right]\frac{T}{T_r}W$	$\frac{T}{T_c}W$	$\frac{T - T_c}{T_r}W$	W

maximum rate of W samples per second can be achieved with a short-chirp scanner that is repetition-rate limited. The number of samples per line, however, is always less than TW because the highest useful ratio for T_r/T is $\frac{1}{2}$. On the other hand, we can achieve nearly TW spots per scan line with either of the long-chirp scanners, but only with a reduction in the throughput rate.

To more fully appreciate the relationships among the design parameters, we use two key graphic representations. The first graphic, shown in Figure 7.17(a), illustrates the number of samples M per scan line, normalized to its maximum value of TW, as a function of the ratios T/T_c and T_r/T_c. The vertical line passing through $T/T_c = 1$ is the dividing line between the long- and short-chirp configurations. The horizontal line for which $T_r = T_c$ is the boundary between those configurations in which the chirp segments do or do not overlap. The diagonal lines passing through the points (0, 1), (1, 0), and (2, 1) represent the boundaries between the full scan duty cycle configurations (below the diagonal lines) and the partial scan duty cycles conditions (above the diagonal lines). The loci of constant number of samples per scan line are shown for each of the four basic configurations. We note that the largest number is obtained by using a long-chirp scanner for which the ratio T/T_c is small; the scanner may be either aperture- or repetition-rate limited. When $T/T_c = 1$, the number of samples reaches its minimum value because the active scan time is at its minimum value so that only one spot can be formed in each scan line. For aperture-limited short-chirp scanners, the number of samples per scan line is reciprocally related to the ratio T/T_c, while the lines for repetition-rate-limited short-chirp scanners have slopes whose values are equal to the normalized values themselves.

The second graphic, shown in Figure 7.17(b), illustrates the throughput rate R_t, normalized to its maximum value of W samples per second, as a function of the ratios T/T_c and T_r/T_c. The normalized throughput rate follows parabolic curves when the scanner is aperture limited. Aperture-limited short-chirp scanners have throughput rates that follow straight-line segments, and the normalized throughput rate is fixed at unity for all repetition-rate limited short-chirp scanners. The throughput rate is not a function of the ratio T/T_c for repetition-rate-limited long-chirp scanners.

7.9.2.4. Examples of an Acousto-Optic Recording System. In this section, we provide some brief design guidelines for using the results summarized in Table 7.2 and in Figure 7.17.

Example 1. Suppose that we design a relatively low-performance system, such as a facsimile scanner or recorder. In this case, a large number of

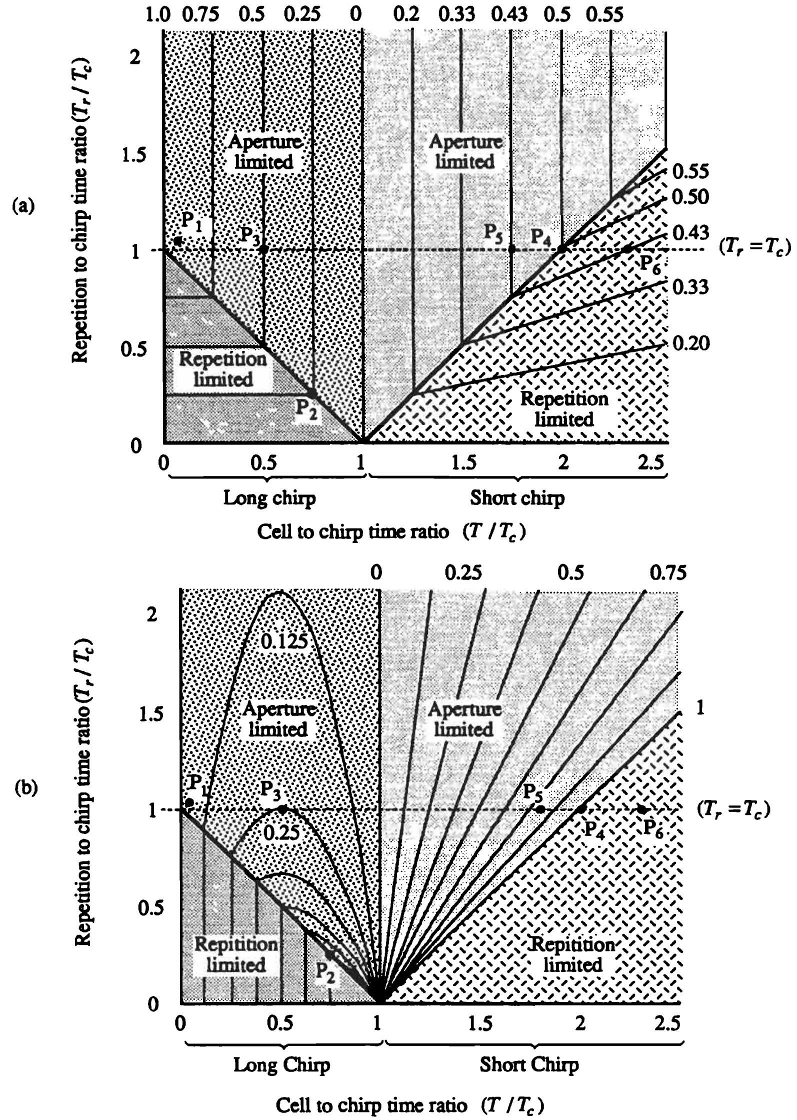

Figure 7.17. Normalized plots: (a) number of samples per scan and (b) throughput rate.

samples per scan line is typically more important than a high throughput rate. We therefore select an acousto-optic cell, such as one made from slow shear-wave tellurium dioxide material with a large time bandwidth product (for example, $T = 50$ μs and $W = 40$ MHz so that $TW = 2000$). Because the required throughput rate for a typical facsimile is well under 1 MHz, the normalized throughput rate is much less than 0.025; as the repetition period is nearly equal to the chirp length ($T_r = T_c$), only a small data buffer is needed. This scanner/recorder configuration is represented by the point P_1 in the graphics of Figure 7.17.

Example 2. Suppose that the requirements are the same as in the first example, but we need to operate at a much higher throughput rate of $30(10^6)$ samples per second. If we use the same acousto-optic cell as before, the normalized throughput rate is 0.75. For a long-chirp scanner, Figure 7.17(b) shows that the operating point is at P_2. Unfortunately, Figure 7.17(a) shows that the normalized number of samples per scan line is only 0.25 for this arrangement and a significant amount of high-speed buffering is needed because the scan duty cycle is low $[(T_c - T)/T_c < 1]$. To achieve better performance, we might consider using an 8.3 μs, 120 MHz acousto-optic cell, operating as an aperture-limited, long-chirp scanner with a normalized throughput rate of 0.25 to provide a normalized number of samples per scan line of 0.5, operating at point P_3. Although the actual number of samples per line are the same in the two alternatives [(0.25)(50 μs)(40 MHz) = 500 as compared to (0.5)(8.3 μs)(120 MHz) = 500], the requirements on the data buffer are not as severe in the second instance. An even better solution for these requirements may be to use just 30 MHz of the 40 MHz bandwidth of the slow shear-wave cell and to operate a short-chirp scanner at point P_4, where the scan duty cycle is 100% and where the normalized number of samples is 0.48, to provide (0.48)(50 μs)(30 MHz) = 720 samples per scan line.

The graphs of Figure 7.17, coupled with the data from Table 7.2, provide the information needed to quickly sort through the possible scanner solutions for a particular problem. For example, the two scanner configurations shown by P_5 and P_6 in Figure 7.17 provide the same number of samples per scan line, but the solution at P_5 has a normalized throughput rate of only 0.8, as compared to a normalized rate of one for the solution at P_6.

7.9.2.5. Other Considerations. In the analyses given so far, we have assumed uniform illumination of the acousto-optic cell so that the design relationships can be clearly stated in closed form. In practice, the

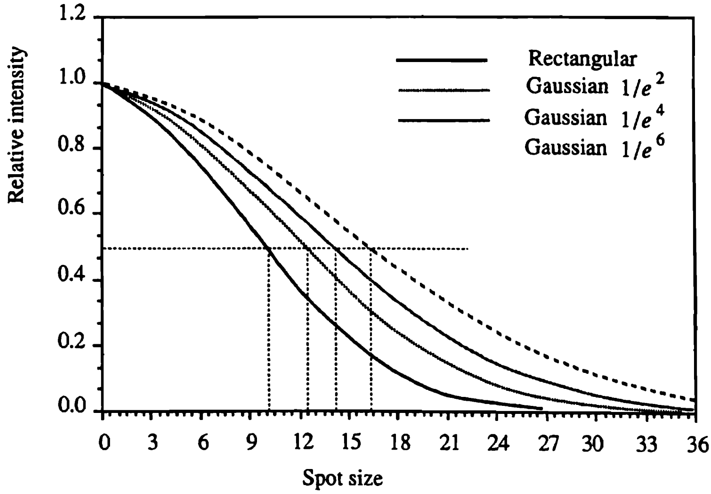

Figure 7.18. Spot sizes for various illumination profiles.

acousto-optic cell is usually illuminated by a laser beam with a Gaussian intensity weighting so that the spot size, for a given aperture, is greater than that for a uniform illuminating beam. Figure 7.18 shows the spot sizes for a uniform illumination and for Gaussian illuminations in which the intensity at the edges of the cell drops to $1/e^2$, $1/e^4$, and $1/e^6$ of the central value. If we use the half-power response of the spot distribution as a convenient measure of the spot size, the spot sizes for these Gaussian illuminations have increased by a factor G, where G is equal to 1.15 for the $1/e^2$ illumination, to 1.36 for the $1/e^4$ illumination, and to 1.58 for the $1/e^6$ illumination. All the relationships developed in previous sections are still valid, except that the spot size d_0 must be multiplied by G, while the number of samples per scan line M, the sample rate R_s, and the throughput rate R_t must all be divided by G.

PROBLEMS

7.1. A spatial signal contains a maximum frequency $\alpha_{co} = 150$ Ab. What is the required sample spacing d_0 to satisfy the Nyquist criterion? If the signal is illuminated with light of wavelength $\lambda = 0.5\ \mu$, calculate the maximum physical angle θ_{co} that the geometric rays can have as the wavefront diverges from any sample point of the signal.

7.2. We have an acousto-optic cell constructed from gallium phosphide material. The index of refraction is 3.31 and the velocity of sound is $v = 6320$ m/sec. The crystal is $L = 12$ mm long and we use light of wavelength $\lambda = 0.5\ \mu$. For a center frequency $f_c = 500$ MHz and a total bandwidth of $W = 200$ MHz, calculate

(a) the acoustic wavelength at the center frequency

(b) the Bragg angle needed for optimum illumination, and

(c) the time bandwidth product.

7.3. For the parameters given in Problem 7.2, calculate

(a) the angular spread $\Delta\theta$, the maximum diffracted angle, and the minimum diffracted angle, and

(b) the distance occupied by the spectrum of the signal in the Fourier plane if we use a 100-mm focal length lens. Sketch and label the regions where the spectrum lies if we operate in the Raman-Nath mode.

7.4. Suppose that you have a scanner of the long-chirp, aperture-limited type, using an acousto-optic cell made of TeO_2 operated in the longitudinal mode. Further, suppose that $W = 1000$ MHz, $T = 1\ \mu$sec, $T_c = 10\ \mu$sec, $\lambda = 0.5\ \mu$, $f_1 = 900$ MHz, and you use a lens having a 50-mm focal length. Calculate

(a) the distance from the lens to the scan plane,

(b) the position for the beginning of scan,

(c) the position of the end of scan,

(d) the length of the scan line,

(e) the spot size,

(f) the scan velocity, and

(g) the number of spots in the scan line.

Be sure to include a sketch of the system that clearly shows where the scan interval lies relative to the focal plane of the lens. Hint: Use a consistent set of relationships to solve this problem and then use an independent set, where possible, as a sanity check.

7.5. A periodic chirp signal has a chirp rate CR = $100(10^{12})$ Hz/sec, with a chirp length of $T_c = 1\ \mu$sec. Suppose that exactly two periods of the chirp can fit within an acousto-optic cell made of GaP material.

(a) What is the scanner type?

(b) What is the required cell bandwidth?

(c) Calculate the distance from the acousto-optic cell to the plane where the chirp is focused.

(d) What is the scanning spot size d_0? Note that T_c sets the time bandwidth product of the signal in this example.

(e) What is the scanning spot velocity?

7.6. We want to scan a focused beam over a distance $L_s = 200$ mm at a rate of 100,000 scans per second. We want a spot size of $d_0 = 0.4$ mm at the plane of focus and we need a 100% duty cycle so that no data buffers are needed. Design an acousto-optic scanning system to achieve these goals. What is the best type of scanner to use? Select a suitable interaction material and determine values for T, W, L, v, chirp rate, center frequency, focal lengths, magnifications, etc. Sketch and label the drive signal with time and frequency. Provide a sketch of all the basic optical elements needed to make the scanner work (use a top and side view sketch). Note: Your design rational should lead you to use a TeO_2 slow shear-wave acousto-optic cell (be sure to support this conclusion).

7.7. From a crumpled and torn spec sheet, you note that a manufacturer has an acousto-optic scanner made of TeO_2, operating in the slow shear mode, with a line scan rate of 40,000 scans/second. They claim that, when used with a 1000-mm focal length lens, the scanning spot velocity is 5,000 m/sec, in a direction opposite to that of the acoustic velocity. Furthermore, they claim that the system has a 100% duty cycle and that the sample rate is equal to the bandwidth when the time duration of the chirp segment is just equal to the repetition period. Unfortunately, the information about the bandwidth of the cell cannot be read from the spec sheet. Calculate it from the data given. Also, calculate the required time bandwidth product. Be careful with the signs!

8

Acousto-Optic Power Spectrum Analyzers

8.1. INTRODUCTION

In Chapters 3 and 4, we showed how coherently illuminated optical systems naturally display the Fourier transform of a signal and how to use this information in spectrum-analysis applications. Optical spectrum analyzers are divided into several major architectural classes based on the variable of integration for the Fourier-transform operation. One architecture, described as *space integrating*, performs a Fourier transform with respect to a space variable. This is the natural mode of operation because lenses collect or integrate light over a given area. The second architecture, described as *time integrating*, performs a Fourier transform with respect to a time variable. The integration is achieved by collecting light on a photodetector array for a given time period. In some cases the two types are combined to form *hybrid* architectures. Both one- and two-dimensional Fourier transforms exist for all types of architectures.

In this chapter we concentrate our attention on one-dimensional power spectrum analyzers of the space integrating type. These systems are often called *instantaneous power spectrum analyzers* because the Fourier transform is computed for the signal history resident in the cell at every instant in time. Because the calculations are completed as soon as light has propagated to the Fourier-transform plane, generally in a few nanoseconds, the computation is essentially instantaneous. A photodetector array in the Fourier-transform plane measures the intensity of the light, which is directly proportional to the rf power of the temporal frequencies contained in the input signal.

It was not until the mid-1950's that the connection between spectrum analysis and diffraction in a coherently illuminated optical system was fully appreciated. The application of acousto-optic cells in spectrum analysis began with the work of Rosenthal (86), Wilmotte (87), and Lambert (88). The interaction medium, in these early systems, was often a liquid such as water. As liquids support only low-frequency signals, the cells were generof the spherical lens between the acousto-optic cell and the detector. Assume that $\lambda = 0.5\ \mu$. If you use all the elements in the array, calculate the length L of the cell and the total bandwidth W of the system.

8.6. The Rayleigh-resolution criterion requires a dip between adjacent frequencies of 0.8 (≈ 1 dB). A more frequently specified dip in spectrum analyzers is 2–3 dB. The corresponding intensity dips are 0.631 and 0.50, and the corresponding increases in separation at the Fourier plane are factors of 1.13 and 1.19 over that established by the Rayleigh limit for a rectangular aperture function. Show, by analysis, that these separation factors are correct.

8.7. For GaP the sound velocity is given as $v = 6.32$ km/sec and $\Gamma = 3.8$ dB/μsec/GHz^2 (from Table 7.1 of Chapter 7). For $f_c = 750$ MHz, $T = 2\ \mu$sec, and $A = 4$, calculate the attenuation of the center frequency at the end of the cell and calculate the amount and direction of the shift. Also calculate the ratio of the peak intensity of the effective illumination to that of the original illumination. Be careful regarding amplitudes vs intensities.

8.8. If five cw signals of different frequencies are injected into an acousto-optic cell at a power level of 100 mW each, what is the diffraction efficiency per frequency if the parameter $B = 0.0156\pi/\text{mW}$? Calculate the compression.

8.9. A radar warning system requires that a spectrum analyzer have a SFDR of 45 dB and that the dynamic range be no less than 10 dB greater than the SFDR. Calculate the minimum laser power required to implement the system for the parameters given in Problem 8.2.

9

Heterodyne Systems

9.1. INTRODUCTION

In Chapter 8 we discussed acousto-optic power spectrum analyzers in which we use *direct detection* of the intensity of the light at the Fourier-transform plane. Detecting light intensities is sometimes restrictive because both the phase and the temporal frequency of the signal are lost. In this chapter we show how the range of signal processing operations can be expanded considerably by using *heterodyne detection* in which we add a reference wave, sometimes called the *local oscillator*, to the light distribution to be detected. The interference between the signal and reference waves produces an output signal that is linearly proportional to the input signal voltage so that magnitude, frequency, and phase information are preserved. More sophisticated signal-processing operations, based on heterodyne detection, are discussed in subsequent chapters.

Heterodyne detection is also used in holography, matched filtering, and synthetic aperture radar processing. In the first two instances the signals are functions of two or three *spatial* dimensions while, in the last instance, we perform heterodyne detection on the *temporal* radar returns, which are then recorded on film as a raster-scanned, two-dimensional spatial function. Leith and Upatnieks recognized that the angle between the interfering waves in the holographic process must be large enough to separate the desired terms from all others upon reconstruction. They applied the principles of communication theory to the problem and recognized that the holographic fringe structure is similar to a temporal carrier frequency that is modulated in both magnitude and phase (93). If the carrier frequency is at least twice the signal bandwidth, the information can be completely recovered. In Chapter 5, we showed how these ideas, suitably modified, are used for constructing matched filters.

Heterodyne detection in either the spatial or frequency domain dates to the early work on spectrum analysis (94) based on even earlier work on correlation (86, 95). The basic ideas were brought together in an interesting series of papers related to probing coherent light fields by means of heterodyne techniques (96–98). In the study of heterodyne systems we sometimes encounter surprising results that do not, at first, seem consistent with our intuition. Further exploration of these concepts, however, reveals a satisfying richness of information and new arrangements for visualizing the fundamentals of optical signal processing.

9.2. THE INTERFERENCE BETWEEN TWO WAVES

As the basic heterodyne process is caused by the interference between two waves of light, we begin with a summary of the key results from Chapter 3 associated with spatially modulated signals. We then introduce a temporal modulation on one of the signals to illustrate the results of both spatial and temporal interference.

9.2.1. Spatial Interference

Consider the spatial interference caused by two plane waves traveling in directions θ_1 and θ_2 with respect to the optical axis and with magnitudes A_1 and A_2 as shown in Figure 9.1. Recall that the relationship between the angles and the spatial frequencies is $\alpha = \theta/\lambda$ so that the amplitude at plane P_2 is

$$A(x) = A_1 e^{-j2\pi\alpha_1 x} + A_2 e^{-j(2\pi\alpha_2 x + \phi_0)}, \tag{9.1}$$

where ϕ_0 is the relative phase between the two waves and where we have suppressed the time-dependent factor due to the frequency of light. The physical meaning of the phase is that one wave has advanced, at some instant in time, a distance $\lambda\phi_0/2\pi$ relative to the other wave.

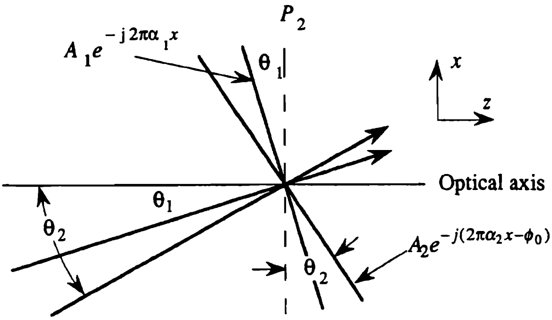

Figure 9.1. Interference between two plane waves.

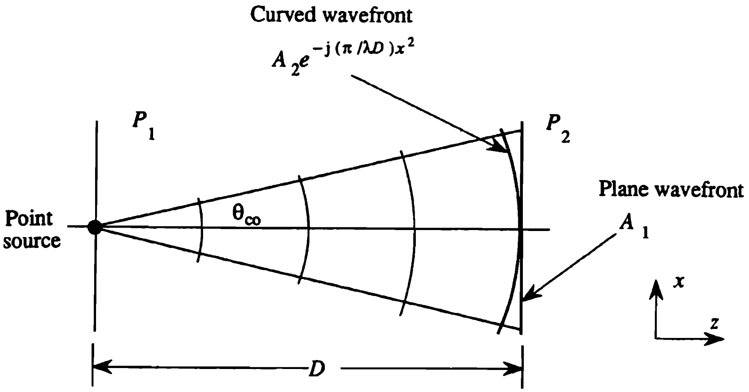

Figure 9.2. Interference between plane and curved wavefronts.

The intensity is the product of the amplitude and its complex conjugate:

$$\begin{aligned} I(x) &= \left|A_1e^{-j2\pi\alpha_1 x} + A_2e^{-j(2\pi\alpha_2 x+\phi_0)}\right|^2 \\ &= A_1^2 + A_2^2 + 2A_1A_2\cos[2\pi(\alpha_1-\alpha_2)x - \phi_0]. \end{aligned} \tag{9.2}$$

From Equation (9.2) we learn that the spatial frequency of the resultant intensity is proportional to the angle between the two waves; that is, $\alpha_1 - \alpha_2 = (\theta_1 - \theta_2)/\lambda$. Because the phase accumulates more rapidly as the included angle increases, the greater the included angle, the higher the spatial frequency. The fringe pattern produced by two plane waves is called a *linear, one-dimensional fringe pattern* because the fringes are equally spaced in the x direction and do not vary in the y direction.

Spatial fringes are also produced by the interference of a plane wave and a cylindrically diverging wave from a point source, as shown in Figure 9.2. The plane wave has amplitude A_1, which is the limiting form of $A_1\exp(-j\pi x^2/\lambda D)$ as $D \to \infty$. The intensity of the Fresnel zone pattern at plane P_2 is

$$I(x) = \left|A_1 + A_2e^{-j(\pi x^2/\lambda D)}\right|^2 = A_1^2 + A_2^2 + 2A_1A_2\cos\left(\frac{\pi x^2}{\lambda D}\right). \tag{9.3}$$

The spatial frequency of the interference pattern, at plane P_2, is

$$\alpha = \frac{1}{2\pi}\frac{\partial}{\partial x}\left[\frac{\pi x^2}{\lambda D}\right] = \frac{x}{\lambda D}, \tag{9.4}$$

so that the spatial frequency is a linear function of the position variable x at plane P_2. We associate the instantaneous spatial frequency of the fringe pattern at any value of x to an associated ray angle; in particular, the cutoff spatial frequency α_{co} is associated with the highest ray angle θ_{co}. Once again, we see that the spatial frequency at any point in plane P_2 is proportional to the angle between the interfering waves at that point. The fringe frequency is *quadratic* in the x direction and is called a *chirp signal.*

As the interference phenomena reviewed so far are due to waves that have the same temporal frequency, we have suppressed the temporal frequency for mathematical simplicity. When we deal with heterodyne detection in acousto-optic signal-processing systems, however, we generally encounter the interference between waves with different temporal frequencies.

9.2.2. Temporal and Spatial Interference

Figure 9.3 shows a Mach-Zehnder interferometer in which the upper branch contains no spatial or temporal modulators, whereas the lower branch contains an acousto-optic cell driven by a cw signal at a frequency f_k. Suppose that the light amplitude at plane P_2 from the upper branch is

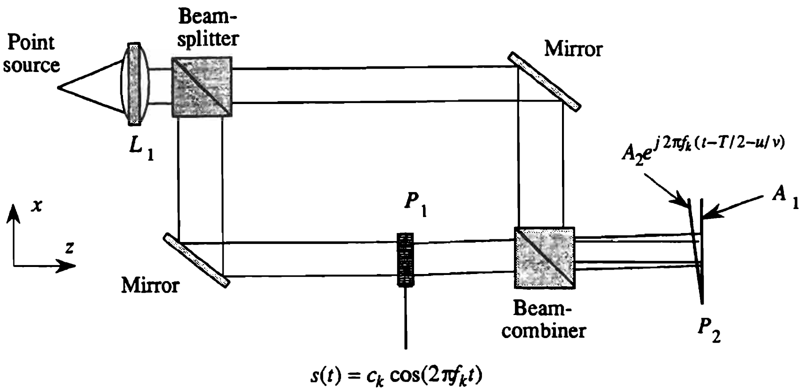

Figure 9.3. Interference between wave of different temporal and spatial frequencies.

represented by $A_1 \exp(j0)$, that is, a plane wave traveling parallel to the optical axis. For the moment, consider only the positive diffracted order from the acousto-optic cell. The intensity at plane P_2, due to these two plane waves, is

$$I(u,t) = \left|A_1 + A_2 e^{j2\pi f_k(t - T/2 - u/v)}\right|^2, \qquad (9.5)$$

where u is the coordinate at plane P_2. As usual, we have dropped the explicit dependence of these two waves on the frequency f_l of light. The intensity from Equation (9.5) is

$$\boxed{I(u,t) = A_0^2 + A_1^2 + 2A_1A_1 \cos[2\pi f_k(t - T/2 - u/v)],} \qquad (9.6)$$

and we see that the linear interference pattern is now a function of both space and time. If we freeze the pattern at some time t_0, the intensity is

$$I(u,t_0) = A_0^2 + A_1^2 + 2A_0A_1 \cos[2\pi\alpha_k - \phi_0], \qquad (9.7)$$

where $\alpha_k = f_k/v$ and $\phi_0 = 2\pi f_k(t_0 - T/2)$ is a fixed phase that is independent of the space variable. This intensity pattern is similar to that given by Equation (9.2) due to two plane waves with the same temporal frequency. On the other hand, if we focus our attention at the point u_0, we find that the intensity, as a function of time, is

$$I(u_0,t) = A_1^2 + A_2^2 + 2A_1A_2 \cos[2\pi f_k t - \phi_1], \qquad (9.8)$$

where $\phi_1 = 2\pi f_k(T/2 + u_0/v)$ is a fixed phase. Here we note that the intensity pattern oscillates in time according to the temporal frequency f_k, which confirms our notion that the temporal frequency content of an applied signal is retained when we invoke heterodyne detection.

We visualize Equation (9.6) as a spatial fringe pattern that is traveling in the positive u direction with velocity v. The connection between the spatial and temporal frequencies then becomes clear: a photodetector, placed at some point u_0, senses a moving fringe structure whose spatial frequency is α_k and generates a temporal frequency $f_k = v\alpha_k$. The contrast, visibility, or modulation of the detected signal is, however, a function of the photodetector size; we now turn our attention to this question of the optimum photodetector size.

9.3. OVERLAPPING WAVES AND PHOTODETECTOR SIZE

In Chapters 4 and 8 we developed the design guidelines for determining the photodetector size required to achieve a specified dip between frequencies in a spectrum analyzer. A similar issue arises with heterodyne detection, but calculating the required photodetector size is more subtle. In a direct detection system, it is more or less a matter of "what you see is what you get." Light falling on the photodetector surface contributes to the induced photocurrent, more or less independently of its direction of arrival or temporal frequency. Light also contributes to the photocurrent in heterodyne detection, but not necessarily to the *cross-product* term, which is the third term of the intensity given, for example, by Equation (9.8). The cross-product term is separated from the bias terms by a bandpass filter centered at f_k. We therefore retain only the temporally oscillating part from Equation (9.8), the bias $A_1^2 + A_2^2$ being rejected by the filter.

Both the signal and reference beams must *overlap* to achieve heterodyne detection. In heterodyne detection we often call the reference beam the *probe* that allows us to detect both the magnitude and phase of a light distribution at some position in the optical system; in this sense, its purpose is similar to that of an oscilloscope probe used to determine the voltage waveform at a particular point in an electronic circuit.

Consider the plane-wave signal beam, represented in Figure 9.4 by solid rays and by a solid plane wavefront, and the reference beam, represented by dotted rays and by a dotted curved wavefront. These waves can be created by the interferometer shown in Figure 9.3 by placing a lens in the upper branch of the system. A photodetector placed anywhere between planes A and C will provide the same total current because the two

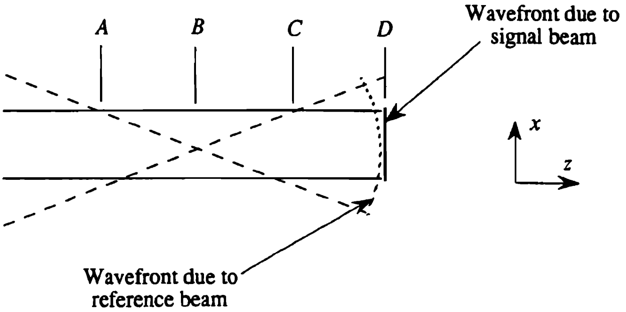

Figure 9.4. Reference- and signal-beam geometries.

beams overlap completely in this region. What is the situation at plane D? Here the reference beam extends beyond the signal beam, and we might expect that the amplitude of the cross-product signal will be reduced because the two beams do not completely overlap. As we show in the next section, a surprising result is that the cross-product output has the same value at all the planes shown in Figure 9.4. This nonintuitive result is due to a second key principle of heterodyne detection; namely, wavefronts must both overlap *and be nearly parallel*. How parallel need they be?

9.3.1. Optimum Photodetector Size for Plane-Wave Interference

To determine the required degree of parallelism, consider the simple case of a photodetector, a plane-wave signal beam, and a plane-wave reference probe as shown in Figure 9.5. The angle between the signal and reference beams is θ_k. The reference beam is represented by a plane wave of magnitude A_1 with zero spatial and temporal frequencies. The signal beam is represented as a plane wave with magnitude A_2 and temporal frequency f_k so that it is a function of both space and time. The photodetector current is the integral over the photodetector surface of the intensity of the sum of the reference and signal beam amplitudes:

$$\begin{aligned} g(t) &= S\int_{-\infty}^{\infty} I(x)\text{rect}(x/h)\,dx \\ &= S\int_{-\infty}^{\infty} \left|A_1 + A_2 e^{j(2\pi f_k t + 2\pi\alpha_k x)}\right|^2 \text{rect}(x/h)\,dx \\ &= S\int_{-h/2}^{h/2} \left[A_1^2 + A_2^2 + 2A_1A_2\,\text{Re}\{e^{j(2\pi f_k t - 2\pi\alpha_k x)}\}\right] dx, \qquad (9.9) \end{aligned}$$

where $\alpha_k = \theta_k/\lambda$, S is the responsivity of the photodetector, and the rect function shows that the photodetector has a total width h. When we expand the integrand, we find three contributions to the photodetector current. We see by inspection that $g_1(t) = A_1^2hS$ and $g_2(t) = A_2^2hS$ are signal components that are not functions of time; their temporal spectra are therefore centered at zero frequency. The third, or cross-product term, is a bandpass signal centered at f_k:

$$\begin{aligned} g_3(t) &= 2\,\text{Re}\left[SA_1A_2e^{j2\pi f_k t}\int_{-h/2}^{h/2} e^{j2\pi\alpha_k x}\,dx\right] \\ &= 2hSA_1A_2\,\text{sinc}(\alpha_k h)\cos(2\pi f_k t). \qquad (9.10) \end{aligned}$$

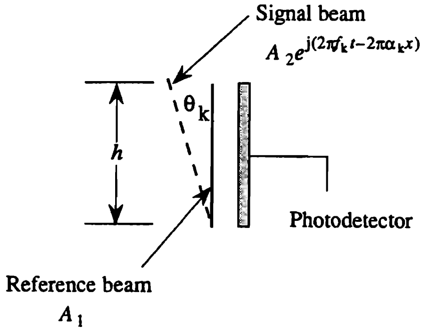

Figure 9.5. Plane-wave and photodetector geometry.

As expected, we find that $g_3(t)$ is proportional to the magnitudes of the signal and reference beams. This result also reveals, however, a new key factor. The magnitude of the output signal is controlled by a sinc function whose argument is a function of $\alpha_k = \theta_k/\lambda$, where θ_k is the angle between the signal and reference beams; the argument is also a function of h, the photodetector size. This sinc function is, in effect, a modulation transfer function that determines the magnitude of the cross-product temporal signal.

The condition for maximizing the output is found by expanding the sinc function:

$$\boxed{\begin{aligned} g_3(t) &= 2hSA_1A_2\,\mathrm{sinc}(\alpha_k h)\cos(2\pi f_k t) \\ &= 2hSA_1A_2\frac{\sin(\pi\alpha_k h)}{(\pi\alpha_k h)}\cos(2\pi f_k t) \\ &= \frac{2SA_1A_2}{\pi\alpha_k}\sin(\pi\alpha_k h)\cos(2\pi f_k t). \end{aligned}} \tag{9.11}$$

From Equation (9.11) we see that the output is small when the photodetector size h is small, as expected. The output increases as h increases, according to the sine function, until it reaches its maximum value when the argument of the sine function is $\pi/2$. This result shows that the optimum photodetector size is

$$h = \frac{1}{2\alpha_k}. \tag{9.12}$$

From Equation (9.12) we discover that the optimum photodetector size is the same as the optimum sample spacing d_0 for a spatial frequency α_k. As $\alpha_k = f_k/\lambda$, we find that the maximum allowable angle between the two waves for a photodetector of size h is

$$\theta_k = \frac{\lambda}{2h}. \tag{9.13}$$

If the photodetector size increases, the heterodyned signal is reduced, as shown by Equation (9.10), and reaches zero when $\theta_k h = \lambda$. This means that, over the physical aperture h of the photodetector, the phase change between the two waves is equal to exactly one-half wavelength of light.

One way to visualize this result is to note that if $\theta_k \gg \lambda/h$, there are several spatial interference fringes over the aperture, as shown in Figure 9.6(a). The spatial integral of the oscillating part of the interference determines the magnitude of the sinc function, and the value of the cross-product term is small in this case. As θ_k decreases, so too does the spatial frequency produced by the cross-product term until $\theta_k = \lambda/2h$ so that we have one-half cycle over the aperture, as shown in Figure 9.6(b).

From Equation (9.10) we also see that if θ_k is large, we need a small photodetector to keep the modulation transfer function at a high level. To keep the signal level within at least 3 dB of the maximum, we require that sinc$(\alpha_k h)$, as contained in Equation (9.10), has a value of 0.5 or greater.

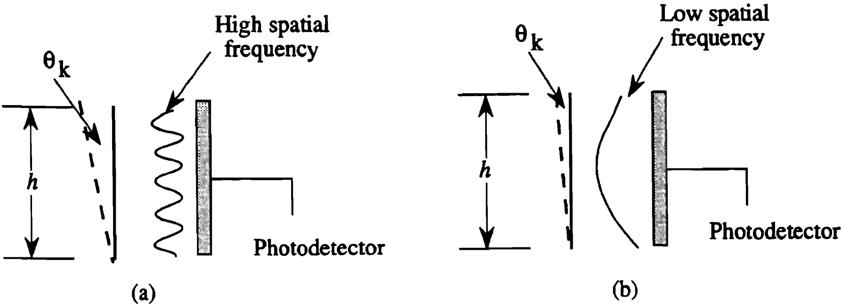

Figure 9.6. Interference fringe period and photodetector geometry. (a) high spatial frequency and (b) low spatial frequency.

This occurs whenever the argument of the sinc function is greater than 0.6 so that we require $\theta_k \leq 0.6\lambda/h$. We have, therefore, established a criterion for how parallel plane waves must be to produce a contribution to the cross-product term at the output of the system.

9.3.2. Optimum Photodetector Size for a Two-Dimensional Chirp

Consider the spatial/temporal interference produced by a spherically diverging wave at frequency f_k and a plane wave. The plane-wave reference beam is represented by A_1 and the spherically diverging signal beam is represented by

$$s(\rho, t) = A_2 e^{j(2\pi f_k t - \pi\rho^2/\lambda D)}, \tag{9.14}$$

where ρ is a polar coordinate at plane P_2. The intensity is the square of the sum of the reference and signal light distributions:

$$\begin{aligned} I(\rho, t) &= \left| A_1 + A_2 e^{j(2\pi f_k t - \pi\rho^2/\lambda D)} \right|^2 \\ &= A_1^2 + A_2^2 + 2\,\mathrm{Re}\left\{ A_1 A_2 e^{j(2\pi f_k t - \pi\rho^2/\lambda D)} \right\}. \end{aligned} \tag{9.15}$$

The general form of the output after ignoring unessential constants is

$$\begin{aligned} g(t) &= \int_0^{2\pi} \int_0^R I(\rho, t)\rho \, d\rho \, d\theta, \\ &= g_1(t) + g_2(t) + g_3(t), \end{aligned} \tag{9.16}$$

where R is the radius of the photodetector. The first two terms are simply the constants $g_1(t) = \pi A_1^2 R^2$ and $g_2(t) = \pi A_2^2 R^2$. The cross-product t rm is

$$\begin{aligned} g_3(t) &= \int_0^{2\pi} \int_0^R 2\,\mathrm{Re}\left\{ A_1 A_2 e^{j(2\pi f_k t - \pi\rho^2/\lambda D)} \right\} \rho \, d\rho \, d\theta, \\ &= 4\pi A_1 A_2 \,\mathrm{Re}\left\{ e^{j(2\pi f_k t)} \int_0^R e^{-j(\pi\rho^2/\lambda D)} \rho \, d\rho \right\}. \end{aligned} \tag{9.17}$$

To integrate this function, we let $\pi\rho^2/\lambda D = z^2$ and supply the factors needed for a perfect differential to produce

$$g_3(t) = 4\pi A_1 A_2 \left[\frac{\lambda D}{-j2\pi} \right] \mathrm{Re}\left\{ e^{j(2\pi f_k t)} \left[e^{-j(\pi R^2/\lambda D)} - 1 \right] \right\}. \tag{9.18}$$

The condition for maximizing the output is found by rearranging the terms in Equation (9.18) to produce

$$\boxed{\begin{aligned} g_3(t) &= 2\pi A_1 A_2 R^2 \operatorname{Re}\left\{ e^{j(2\pi f_k t)} e^{-j(\pi R^2/2\lambda D)} \left[\frac{e^{-j(\pi R^2/2\lambda D)} - e^{+j(\pi R^2/2\lambda D)}}{-j(\pi R^2/\lambda D)} \right] \right\} \\ &= 2\pi A_1 A_2 R^2 \operatorname{sinc}\left[\frac{R^2}{2\lambda D}\right] \cos\left(2\pi f_k t - \frac{\pi R^2}{2\lambda D}\right). \end{aligned}} \tag{9.19}$$

We see that, once again, the magnitude of the output is determined by a sinc function that plays the role of a modulation transfer function with R as a parameter. We maximize Equation (9.19) with respect to the photodetector radius R by noting that

$$\pi R^2 \operatorname{sinc}[R^2/2\lambda D] = 2\lambda D \sin(\pi R^2/2\lambda D), \tag{9.20}$$

which reaches its maximum value, for a given value of D, when

$$R = \sqrt{\lambda D} \tag{9.21}$$

The optimum photodetector size, for this case, is therefore simply a function of its distance from the source and of the wavelength of light.

An unanticipated and interesting result from Equation (9.19) is that the phase of the cosine carrier is a function of both R and D when the output is maximized. What does this mean physically? The phase reveals the shape of the *spatial* chirp pattern at that moment in time when $g_3(t)$ is at its maximum value. If we include the phase term from Equation (9.19) in Equation (9.15), we find that the spatial intensity pattern for the maximum output condition becomes

$$\begin{aligned} I(\rho,t) &= \left| A_1 + A_2 e^{j(2\pi f_k t - \pi\rho^2/\lambda D - \pi R^2/2\lambda D)} \right|^2 \\ &= A_1^2 + A_2^2 + 2A_1A_2 \cos\left(2\pi f_k t - \frac{\pi\rho^2}{\lambda D} - \frac{\pi R^2}{2\lambda D}\right). \end{aligned} \tag{9.22}$$

We can associate the phase with either the spatial or the temporal part of Equation (9.22). If we select the spatial part, the chirp function changes from the cophasal function, shown in Figure 9.7, to the one shifted by 90°.

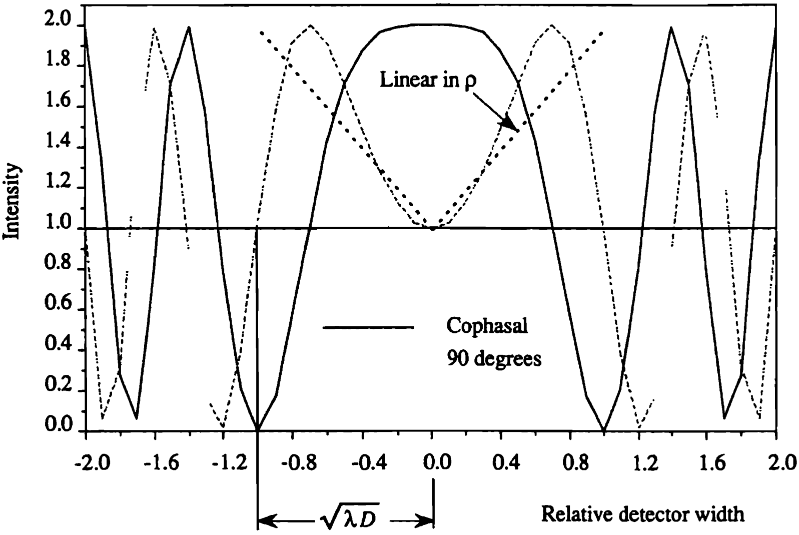

Figure 9.7. Two-dimensional Fresnel zones with different initial phases.

It is clear that there is significantly more positive contribution to the integral from the phase-shifted chirp than from the cophasal chirp for a photodetector radius of $\sqrt{\lambda D}$. The key to this difference is that the integrand in Equation (9.16) contains a term linear in ρ that multiplies the intensity $I(\rho, t)$ before the integration is carried out; this linear term is shown in Figure 9.7 as two straight dotted lines. In effect, the phase tei n serves to push more of the energy toward the larger values of ρ so that the integral is maximized. Also note that when $R = \sqrt{\lambda D}$ the phase-shifted chirp is just crossing the bias level so that any larger photodetector will produce a smaller output for the cross-product term.

9.3.3. Optimum Photodetector Size for a One-Dimensional Chirp

The optimum photodetector size for the one-dimensional chirp case is obtained by an analysis similar to that used in Section 9.3.2. We use the same general definitions for the reference and signal beams to find the intensity

$$I(x,t) = A_1^2 + A_2^2 + 2\,\mathrm{Re}\left\{A_1 A_2 e^{j(2\pi f_k t - \pi x^2/\lambda D)}\right\}, \qquad (9.23)$$

where x is the spatial variable at the detector plane. The cross-product output is

$$g_3(t) = 2A_1A_2 \operatorname{Re}\left\{ e^{j2\pi f_k t} \int_{-h/2}^{h/2} e^{-j\pi x^2/\lambda D}\, dx \right\}, \tag{9.24}$$

where h is the photodetector width. In this case the integral plays the role of the modulation transfer function. We recognize the integral as a Fresnel integral, which we cannot evaluate in closed form. We put the integral into its standard form by a change of variables in which $\pi x^2/\lambda D = \pi z^2/2$

$$g_3(t) = \sqrt{2\lambda D}\, A_1A_2 \operatorname{Re}\left\{ e^{j2\pi f_k t} \int_{-\sqrt{2/\lambda D}\, h/2}^{\sqrt{2/\lambda D}\, h/2} e^{-j\pi z^2/2}\, dz \right\}. \tag{9.25}$$

As we showed in Chapter 3, Section 3.2.5, the maximum value of the Fresnel integral occurs when

$$\sqrt{\frac{2}{\lambda D}}\, \frac{h}{2} = 1.21, \tag{9.26}$$

so that the optimum value of h is $1.72\sqrt{\lambda D}$. At this value of h, the integral is equal to $1.8 \exp(j\phi)$, where $\phi = 42.3°$ so that the maximum value of $g_3(t)$ becomes

$$\boxed{g_3(t) = 1.8\sqrt{2\lambda D}\, A_1A_2 \cos(2\pi f_k t + \phi).} \tag{9.27}$$

As before, we relate the optimum photodetector size to the spatial interference patterns as shown in Figure 9.8. The phase shift of 42.3° maximizes the integral of the function from zero to $1.72\sqrt{\lambda D}$. If the phase shift were greater, the dip near $x = 0$ would become deeper and would more than offset any gain from an increased photodetector size.

9.3.4. Optimum Photodetector Size for a General Signal

Would the optimum detector size change if, in Figure 9.4, we were to place at plane B a signal with length L and high spatial frequency content? From the sketch in Figure 9.9 we have two ways to proceed; each provides additional insights into the detection process.

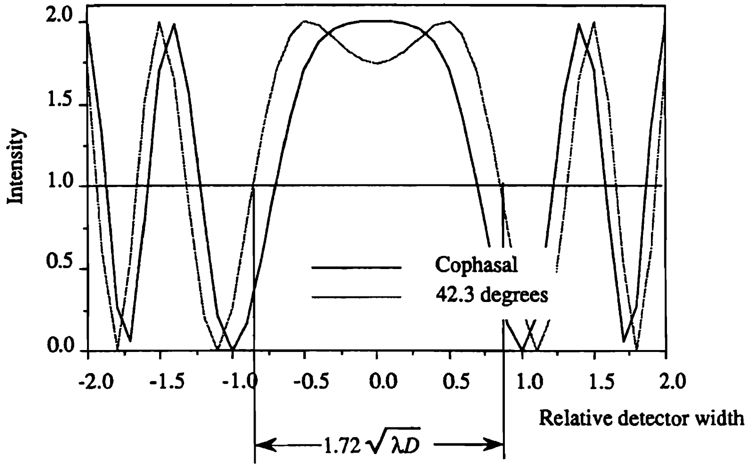

Figure 9.8. One-dimensional Fresnel zones with different initial phases.

The first method is to represent the signal by M plane waves whose incremental angles change by $\theta_0 = \lambda/L$, where L is the total length of the signal at plane B. To capture the undiffracted light from the signal, we must have some photodetector surface available at position $x = 0$, as we just explained. To capture the highest positive frequency, we need some photodetector surface at $+M\theta_0 D$, where D is the distance from plane B to plane D. Note that the latter position is where the Mth plane wave from the signal is *tangent* to the diverging wavefront produced by th : probe. It is only near this point that the signal and probe wavefronts a

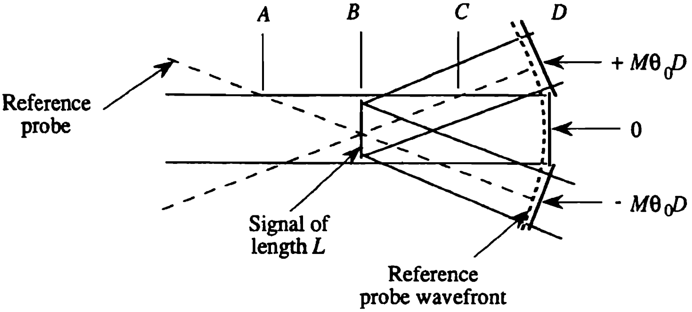

Figure 9.9. Heterodyne action with plane-wave signal decomposition.

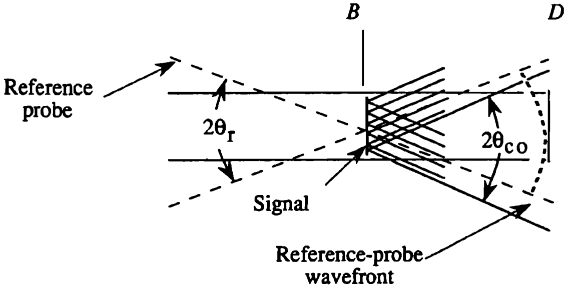

Figure 9.10. Heterodyne action with sinc function signal decomposition.

sufficiently parallel so that photons contribute to the cross-product term. Similarly, we need some photodetector surface at $-M\theta_0 D$ to capture the negative spatial frequencies produced by the signal. A different part of the photodetector therefore collects photons from different spatial frequencies produced by the signal to form the cross-product term. From these considerations, we see that the photodetector must be sufficiently large to capture the overlapping light from both beams, up to the required size of the divergent wavefront representing the probe.

The required size of the probe is clearly determined by the maximum frequency content of the signal. To further explore this relationship, consider a second method for representing the signal, namely, as a set of sinc functions of the form $\text{sinc}(x/d_0)$. In Figure 9.10, we show the reference-beam probe just before the signal at plane B, as a convergent bundle of rays, with $2\theta_r$ as its included angle. The signal, with cutoff frequency α_{co}, is represented by a sequence of sinc functions that propagate as divergent waveforms into the region to the right of plane B, with the marginal rays forming a cone of angle $2\theta_{\text{co}}$. The meaning of "nearly parallel beams" is now at its simplest and clearest form; we require that $\theta_r = \theta_{\text{co}}$ so that the *reference probe contains a ray that is parallel to every ray that is diffracted by the signal.*

From Figure 9.10 we also conclude that only one sample of the signal plane contributes to the output: the one that coincides with the probe! The size of the photodetector at an arbitrary plane is simply $h = 2\theta_r D$; as $D \to 0$, the value of h tends toward its minimum value of d_0 as set by the diffraction limit. The photodetector size at plane B is therefore also equal to d_0. All the other light, at least from a heterodyne detection viewpoint, is irrelevant. Once again, these results emphasize that light contributes to the cross-product term only if the beams overlap and are collinear.

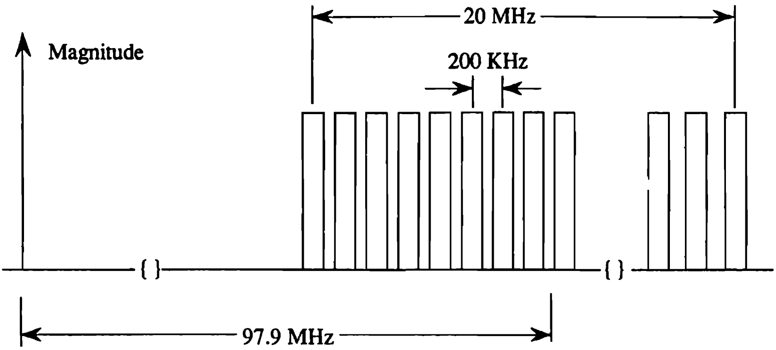

Figure 9.11. Frequency allocation in the FM band.

9.4. THE OPTICAL RADIO

We describe an optical radio to illustrate various techniques for using heterodyne detection in recovering both the magnitude and phase of a time signal. This simple system forms the basis for a discussion of heterodyne spectrum analysis in Chapter 10 because a frequency spectrum analyzer that resolves M frequencies is equivalent to operating M optical radios in parallel. Each radio detects the signal power in an assigned channel.

Consider the FM band of radio frequencies shown in Figure 9.11. In a 20-MHz frequency band, centered at 97.9 MHz, we have 100 possible FM channels, spaced at 200-kHz intervals. We represent the composite signal due to all channels by

$$f(t) = \sum_{n=1}^{N} a_n \cos[2\pi f_n t + \phi_n(t)], \tag{9.28}$$

where a_n is the magnitude of the nth signal and $\phi_n(t)$ is the FM modulation that contains the message signal $m_n(t)$:

$$m_n(t) = \frac{\partial}{\partial t}[\phi_n(t)]. \tag{9.29}$$

If $f(t)$ drives the acousto-optic cell in the interferometer of Figure 9.12, the light distribution at plane P_2 due to the lower branch resembles that shown in Figure 9.11, where the temporal frequencies have been con-

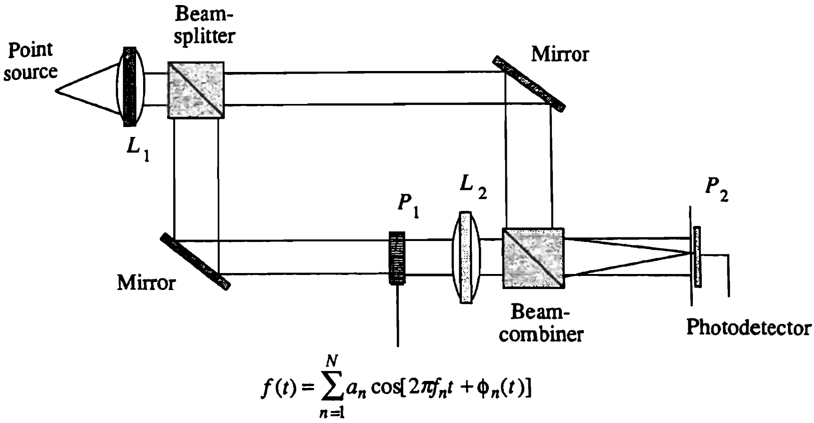

Figure 9.12. An optical radio.

verted to spatial frequencies through the relationship that $\alpha = f/v$. We arrive at this conclusion based on the Fourier-transform properties of coherently illuminated optical systems as described in Chapter 8. In Figure 9.11, we have shown the idealized situation where there are guard bands between the channels and no crosstalk between adjacent channels.

We now consider several potential detection arrangements. Our objective is to produce a signal corresponding to one of the selected channels in the system at the output of a photodetector. Ideally, the signal should occur at an IF frequency so that it can be fed directly to an FM discriminator circuit. The system shown in Figure 9.12 is therefore equivalent to the front end of an FM receiver.

9.4.1. Direct Detection

If we block the reference beam, the lower branch of the interferometer of Figure 9.12 is equivalent to the power spectrum analyzer discussed in Chapter 8. Suppose that a small photodetector element is positioned so that it collects light at the nth channel. The output of the photodetector is then proportional to a_n^2, as suggested by Equation (8.9), because all phase information is lost when light is detected directly. We clearly need heterodyne detection to recover the phase modulation of the input signal; we now consider several possibilities.

9.4.2. Heterodyne Detection

If we unblock the reference beam, interference between the signal and reference beams is restored. At the nth channel the intensity is

$$I(\alpha, t) = |R(\alpha) + S_n(\alpha, t)|^2, \tag{9.30}$$

where $R(\alpha)$ is the response at plane P_2 due to the reference function $r(x)$, and $S_n(\alpha, t)$ is the response due to the signal in the nth channel. When the phase modulation is slowly varying with respect to the cell duration T, we modify Equation (8.9) to find that the positive diffracted order becomes

$$S_n(\alpha, t) = jma_n e^{j[2\pi f_n(t-T/2)+\phi_n(t)]} A(\alpha - \alpha_n), \tag{9.31}$$

so that the resultant intensity produced by the nth channel is represented by

$$I_n(\alpha, t) = \left|R(\alpha) + jma_n e^{j[2\pi f_n(t-T/2)+\phi_n(t)]} A(\alpha - \alpha_n)\right|^2, \tag{9.32}$$

which becomes

$$\boxed{\begin{aligned} I_n(\alpha, t) = {} & |R(\alpha)|^2 + |ma_n A(\alpha - \alpha_n)|^2 + 2ma_n|R(\alpha)| \\ & \times |A(\alpha - \alpha_n)| \cos[2\pi f_n(t - T/2) + \phi_n(t) + \pi/2]. \end{aligned}} \tag{9.33}$$

In Equation (9.33) the reference-beam response $|R(\alpha)|^2$ is a constant in both space and time. The second term of Equation (9.33) is the same as we would obtain for direct detection and shows that the phase information is lost.

The first two terms of Equation (9.33) are at baseband and are easily removed by a bandpass filter whose center frequency is at 97.9 MHz, the midband frequency. The last term of Equation (9.33) has the proper form of an FM modulated signal; it can be fed directly to a discriminator after $I(\alpha, t)$ is detected by the photodetector to produce the output current. The phase factor $\pi/2$ in the argument of the cosine is due to the j factor in Equation (9.31), which reminds us that the diffracted light is in phase quadrature with respect to the undiffracted light. This phase factor merely shifts the phase of the carrier and has no effect on the demodulated signal.

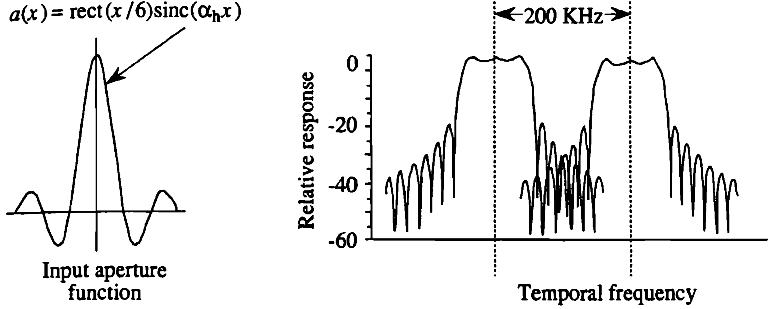

Figure 9.13. Channel response for a sinc aperture function.

To maintain well-formed channels that have steep slopes and low skirt levels, as shown in Figure 9.11, the aperture function $a(x)$ must produce a response in the Fourier plane proportional to $\mathrm{rect}(\alpha/\alpha_h)$, where α_h is the width of the photodetector expressed in terms of a spatial frequency. This means that the aperture weighting function must be $a(x) = \mathrm{sinc}(\alpha_h x)$. At first glance, it seems that this aperture function is difficult to synthesize because we need to generate a mask with negative magnitudes. Recall from Chapter 3, however, that the Fourier transform occurs at an image plane of the source. Therefore, if the primary source in Figure 9.12 is a rect function of the proper dimension, its Fourier transform at plane P_1 must generate the required sinc function and, in turn, the second transform at plane P_2 produces the desired rect function.

The steepness of the channel slopes and the depth of the skirt levels depend on how many sidelobes of the sinc function are passed by the acousto-optic cell. Figure 9.13 shows a candidate aperture function $a(x) = \mathrm{rect}(x/6)\mathrm{sinc}(\alpha_h x)$, which represents a sinc function that has been truncated at the third null on each side of the mainlobe, and its frequency response. The Fourier transform of this truncated function has a reasonably flat bandpass over the channel bandwidth, a region where the response falls rapidly, and a sidelobe level that is at least 20 dB down at the first sidelobe. Crosstalk is about 40 dB down in adjacent channels. Steeper skirts and lower sidelobe levels can be obtained by illuminating the acousto-optic cell with more sidelobes of the sinc function although the rate of gain is not very high.

There are several arrangements of the reference beam that provide the desired signal at the output. Some of these are impractical for various reasons, but it is worthwhile to present them all because we learn some interesting facts about the detection process from each.

Arrangement 1. Given the arrangement of Figure 9.12, we can simply place a small photodetector at the position corresponding to the channel we want to select. The finite size of the photodetector serves to isolate the proper channel and to prevent crosstalk due to neighboring channels. Tuning to a new station is then a matter of moving the photodetector to the new channel position. The disadvantages of this arrangement are the mechanical movement of the photodetector and inefficient use of the reference-beam power because it is spread over the entire FM band. Furthermore, since the output of the photodetector is at the same frequency as the input, we have not brought the output to an IF frequency.

Arrangement 2. We avoid the need to move the photodetector by using an array of photodetector elements at plane P_2. Selecting a channel is then accomplished by switching to the desired photodetector element. The other disadvantages of Arrangement 1 are still present, however.

Arrangement 3. We more efficiently use the reference-beam power and therefore produce a higher signal-to-noise ratio, by modifying the interferometer, as shown in Figure 9.14. Suppose that we move lens L_2 outside the interferometer so that it creates the Fourier transform of the signal and reference beams simultaneously. If we arrange for $r(x) = a(x) = \text{sinc}(\alpha_h x)$, we find that the reference beam is only one channel wide at plane P_2. As a result, the reference beam power is approximately 100 times greater than in the previous two arrangements. Tuning to a new channel is achieved by rotating the beam combiner to an appropriate angle; for a given angle of rotation Ψ, the reflected reference beam is rotated by 2Ψ. The signal from the lower branch is largely unaffected by the rotation; recall from Chapter 2 that when a plane parallel plate is rotated, the rays passing through the plate are simply displaced somewhat. As the angle of rotation is of the order of a few milliradians, the spectrum is not shifted a great deal (see Problem 9.3).

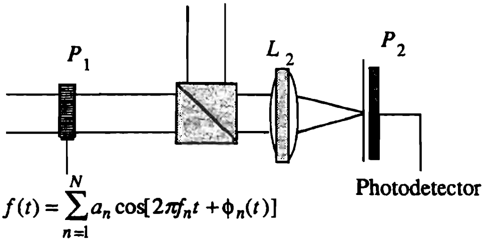

Figure 9.14. Optical radio with the Fourier-transform lens outside the interferometer.

A second advantage of this arrangement is that we can use a large, single photodetector element that covers the entire FM band, as the reference beam is now confined to a single channel. From Section 9.2 we learned that a heterodyne output occurs only if two signals overlap and are collinear. In this case lens L_2 ensures that the beams are sufficiently collinear at the output and the choice of $r(x)$ restricts the region of overlap to the selected channel. Using a single photodetector simplifies the postdetection circuitry at the expense of a somewhat higher shot-noise level because more signal energy than is necessary is falling on the photodetector. As we show in Chapter 10, shot noise is generally dominated by noise introduced by the reference beam so that the additional photodetector size is not a serious drawback. The disadvantages of this arrangement are that the output is still at rf and that we need to mechanically rotate the beam combiner to tune the system.

Arrangement 4. We avoid the mechanical rotation of the beam combiner by further modifying the interferometer as shown in Figure 9.15. Here we use a second acousto-optic cell to provide electronic tuning of the radio. In particular, we drive the second acousto-optic cell with a reference signal $r(t) = \cos(2\pi f_n t)$ to access the nth channel. The channel selection process is fast, limited only by the access time of the reference-beam acousto-optic cell. A new and unfortunate problem has arisen, however; the output, instead of being at rf as in the other arrangements, is now at baseband. This problem becomes apparent when we remember that the reference-beam signal is

$$R(\alpha, t) = jme^{j[2\pi f_n(t-T/2)]}R(\alpha - \alpha_n). \tag{9.34}$$

This reference probe selects just one frequency component from the signal

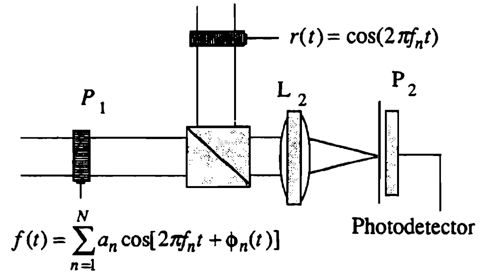
$r(t) = \cos(2\pi f_n t)$
P_1
L_2
P_2
Photodetector
$f(t) = \sum_{n=1}^{N} a_n \cos[2\pi f_n t + \phi_n(t)]$

Figure 9.15. Use of an acousto-optic cell to provide the reference beam.

so that the intensity becomes

$$I_n(\alpha, t) = \left| jme^{j[2\pi f_n(t-T/2)]}R(\alpha - \alpha_n) + jma_n e^{j[2\pi f_n(t-T/2)+\phi_n(t)]}A(\alpha - \alpha_n)\right|^2 \qquad (9.35)$$

When we carry out the expansion, we have

$$I_n(\alpha, t) = |mR(\alpha - \alpha_n)|^2 + |ma_n A(\alpha - \alpha_n)|^2 + 2m^2 a_n R(\alpha - \alpha_n)A^*(\alpha - \alpha_n)\cos[\phi_n(t)], \qquad (9.36)$$

which confirms that the cross-product term has been heterodyne shifted to baseband. The cross-product term therefore cannot be separated from the bias terms, rendering this arrangement useless because the output is not at a convenient intermediate frequency.

Arrangement 5. A final modification is to change the reference frequency to f_m so that the reference beam overlaps the mth channel *and* to then rotate the beam combiner to geometrically move the reference probe back to the nth channel. This fixed rotation is performed only when the system is calibrated. In this fashion, we find that the reference and signal beams have slightly different frequencies so that Equation (9.35) becomes

$$I_n(\alpha, t) = \left| jme^{j[2\pi f_m(t-T/2)]}R(\alpha - \alpha_m) + jma_n e^{j[2\pi f_n(t-T/2)+\phi_n(t)]}A(\alpha - \alpha_n)\right|^2, \qquad (9.37)$$

and the corresponding intensity becomes

$$I_n(\alpha, t) = |mR(\alpha - \alpha_m)|^2 + |ma_n A(\alpha - \alpha_n)|^2 + 2m^2 a_n R(\alpha - \alpha_m) \times A^*(\alpha - \alpha_n)\cos[2\pi f_d t + \phi_n(t) - \pi f_n T], \qquad (9.38)$$

where $f_d = |f_m - f_n|$ is the offset frequency. For FM reception, it is convenient to set f_d at 10.7 MHz, the normal IF frequency. The optical system therefore both tunes to the desired channel and simultaneously brings the output to the desired IF. The tuning procedure is simply to add 10.7 MHz to the desired channel frequency f_n to produce the required reference drive frequency f_m.

Arrangement 6. Although Arrangement 5 provides all the desired features of a heterodyne system, we offer a more general modification, as shown in

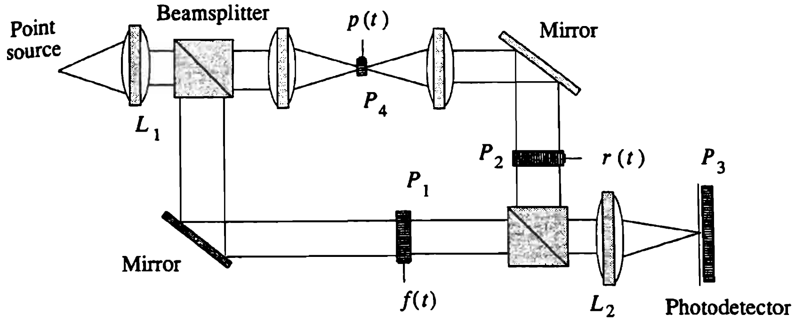

Figure 9.16. A general purpose heterodyne system.

Figure 9.16, in which the lower branch contains an acousto-optic cell driven by a signal $f(t)$. The upper branch contains a similar acousto-optic cell driven by a reference signal $r(t)$. The upper branch may also contain a means for purely time modulating the reference beam at plane P_4 with a signal $p(t)$. The signal $p(t)$ is introduced by means of an acousto-optic point modulator as described in Chapter 7, Section 7.9.1 or by other types of temporal modulators; it is a part of the illumination of the acousto-optic cell in the upper branch that contains $r(t)$.

To illustrate the features of this system, we drive the temporal modulator with the desired offset frequency f_d so that

$$p(t) = \cos(2\pi f_d t). \tag{9.39}$$

Because the offset frequency is provided by the point modulator, the frequency of the reference signal should now be set to that of the channel we want to select. To illustrate the effects of a mistuned radio, we let the reference frequency be f_j:

$$r(t) = \cos(2\pi f_j t). \tag{9.40}$$

The signal at plane P_3 due to the upper branch of the interferometer is

$$R(\alpha, t) = jmR(\alpha - \alpha_j)e^{j2\pi f_j(t-T/2-x/v)}e^{-j2\pi f_d t}, \tag{9.41}$$

where we have retained the downshifted diffracted order from the point modulator for reasons that will become apparent shortly.

The drive signal to the acousto-optic cell in the lower branch of the interferometer is

$$f(t) = \cos(2\pi f_k t + \phi_k), \tag{9.42}$$

and its Fourier transform at plane P_3 is

$$S(\alpha, t) = jma_k A(\alpha - \alpha_k) e^{j[2\pi f_k(t-T/2)+\phi_k]}. \tag{9.43}$$

Suppose that we use a large-area photodetector at plane P_3 to collect all the light produced by the two branches of the system. The output signal is then

$$\begin{aligned} g(t) &= \int_{-\infty}^{\infty} I(\alpha, t)\, d\alpha = \int_{-\infty}^{\infty} |R(\alpha, t) + S(\alpha, t)|^2\, d\alpha \\ &= g_1(t) + g_2(t) + g_3(t). \end{aligned} \tag{9.44}$$

The cross-product term produces an output

$$\begin{aligned} g_3(t) &= 2\,\mathrm{Re}\left\{\int_{-\infty}^{\infty} S(\alpha, t) R^*(\alpha, t)\, d\alpha\right\} \\ &= 2\,\mathrm{Re}\left\{\int_{-\infty}^{\infty} jma_k A(\alpha - \alpha_k) e^{j[2\pi f_k(t-T/2)+\phi_k(t)]}\right. \\ &\qquad \left. \times(-j) mR^*(\alpha - \alpha_j) e^{-j2\pi f_j(t-T/2)} e^{j2\pi f_d t}\, d\alpha\right\} \\ &= 2\,\mathrm{Re}\left\{m^2 a_k e^{j[2\pi(f_k - f_j)(t-T/2)+2\pi f_d t+\phi_k]}\right. \\ &\qquad \left. \times \int_{-\infty}^{\infty} A(\alpha - \alpha_k) R^*(\alpha - \alpha_j)\, d\alpha\right\}. \end{aligned} \tag{9.45}$$

Suppose that we set $a(x) = r(x) = \mathrm{rect}(x/L)$ so that we can evaluate the integral on α. The integral is a function of the difference between α_j and α_k as is seen by making a change of variables in which $\gamma = \alpha - \alpha_j$:

$$\begin{aligned} c(\alpha_k - \alpha_j) &= \int_{-\infty}^{\infty} \mathrm{sinc}[\gamma L]\mathrm{sinc}\big[(\gamma + \alpha_k - \alpha_j)L\big]\, d\gamma \\ &= \mathrm{sinc}\big[(\alpha_k - \alpha_j)L\big]. \end{aligned} \tag{9.46}$$

In Equation (9.46), we recognize that the convolution of two sinc functions produces a sinc function of the delay variable. This result shows that the output is maximized when $\alpha_j = \alpha_k$, as we expected; it also shows the rate at which the output drops as the degree of mistuning increases.

To maximize the output, we set $f_j = f_k$ so that Equation (9.45) becomes

$$g_3(t) = 2m^2 a_k \cos[2\pi f_d t + \phi_k]. \tag{9.47}$$

From Equation (9.47) we see that we have recovered the magnitude and the phase of the input signal. If either the magnitude or phase are a function of time, the carrier frequency will be properly modulated by these time-dependent signals. The reason for selecting the downshifted diffraction order from the point modulator is that we retain the proper sign on the phase term. If we had used the upshifted diffracted order, the output would be the conjugate of the desired signal. This option is useful in some signal-processing applications, as we note in later chapters.

The desired signal is available at the output of a bandpass filter centered at f_d, provided that neither of the other two terms from Equation (9.44) have spectral energy in that band. In this example, both the reference and signal are narrowband functions so that the frequency content of both $g_1(t)$ and $g_2(t)$ is concentrated at $f = 0$. We leave it as an exercise for the reader to calculate the frequency content of the two baseband terms when the signal has a finite bandwidth (see Problem 9.2).

Through this sequence of arrangements, we have developed a practical solution for the optical radio. Both Arrangements 5 and 6 have all the desired features: rapid tuning, efficient use of the reference power, and a phase competent output at IF. This study of the optical radio is useful because it leads to an interesting generalization in Section 9.5 from which we can develop other optical computing architectures. This study also leads directly to the development of a heterodyne spectrum analyzer, as discussed in Chapter 10.

9.5. A GENERALIZED HETERODYNE SYSTEM

The optical radio described in Arrangement 5 is the preferred implementation for recovering the magnitude and phase of an arbitrary signal at the output of the system because it is more cost effective than the system given in Arrangement 6. The general-purpose interferometric system shown in Figure 9.16, however, has a higher degree of flexibility and can be configured to perform a wide range of processing operations.

Suppose, for the moment, that the combined beams are Fourier transformed by lens L_2. The Fourier transform of the signal in the lower branch is

$$F_+(\alpha, t) = \int_{-\infty}^{\infty} a(x) f_+\left(t - \frac{T}{2} - \frac{x}{v}\right) e^{j2\pi\alpha x}\, dx. \tag{9.48}$$

Given that the reference beam contains a point modulator $p(t)$ and a Bragg cell driven by $r(t)$, we express the intensity at plane P_3 as

$$I(\alpha, t) = \left| F_+(\alpha, t) + p(t) R_+(\alpha, t) \right|^2, \tag{9.49}$$

where $R_+(\alpha, t)$ is defined in a similar fashion to that for $F_+(\alpha, t)$. We expand the intensity to obtain

$$I(\alpha, t) = I_1(\alpha, t) + I_2(\alpha, t) + I_3(\alpha, t), \tag{9.50}$$

where

$$\boxed{\begin{aligned} I_1(\alpha, t) &= \left| F_+(\alpha, t) \right|^2, \\ I_2(\alpha, t) &= \left| p(t) R_+(\alpha, t) \right|^2, \\ I_3(\alpha, t) &= 2\,\mathrm{Re}\left[F_+(\alpha, t) p^*(t) R_+^*(\alpha, t) \right]. \end{aligned}} \tag{9.51}$$

This general result suggests several processing possibilities. As one example, suppose that the purely time modulation $p(t)$ is given, in analytic form, by

$$p(t) = e^{-j2\pi f_d t}, \tag{9.52}$$

so that the temporal modulation is a simple cw frequency at f_d. Suppose, too, that

$$F_+(\alpha, t) = \left| F_+(\alpha, t) \right| e^{j\phi(\alpha, t)} \tag{9.53}$$

and

$$R_+(\alpha, t) = \left| R_+(\alpha, t) \right| e^{j\theta(\alpha, t)} \tag{9.54}$$

are completely arbitrary, complex-valued functions, where we explicitly show the magnitude and phase parts of the transforms of the two signals that drive the acousto-optic cells. We express the intensity at plane P_3 as

$$\boxed{\begin{aligned} I(\alpha,t) = {} & |F_+(\alpha,t)|^2 + |R_+(\alpha,t)|^2 \\ & + 2|F_+(\alpha,t)|\,|R_+(\alpha,t)|\cos[2\pi f_d t + \phi(\alpha,t) - \theta(\alpha,t)]. \end{aligned}} \tag{9.55}$$

This is the central result of the analysis of the general-purpose interferometer. The cross-product term of Equation (9.55) reminds us of the general equation, given in many communication texts, that represents phase, magnitude, or frequency-modulated signals:

$$\begin{aligned} v(t) &= A\cos[2\pi f_c t + \phi(t)] \text{ angle modulation} \\ v(t) &= A[1 + m(t)]\cos(2\pi f_c t) \text{ amplitude modulation} \\ v(t) &= Am(t)\cos(2\pi f_c t) \text{ double-sideband modulation} \end{aligned} \tag{9.56}$$

In these representations, f_c is a carrier frequency, $\phi(t)$ is an angle modulation signal, $m(t)$ is a baseband amplitude modulation signal, and A is a constant. By comparing Equation (9.56) with Equation (9.55), we see that the cross-product term from $I(\alpha, t)$ can, with suitable assignment of the reference signals and choice of α, be put into any one of the forms listed for $v(t)$. The main difference between $I(\alpha, t)$ and $v(t)$ is the presence of the two bias terms $|F_+(\alpha, t)|^2$ and $|p(t)R + (\alpha, t)|^2$. This difference disappears when we separate the desired cross-product term from the first two with a bandpass filter. Therefore, a key requirement on the reference functions is that they introduce an offset frequency f_d of suitable value to achieve the separation. In subsequent chapters we consider several applications using this general architecture and signal sources.

PROBLEMS

9.1. The *baseband* signal to an FM optical radio consists of $M = 100$ channels, each one narrowband, so that the input signal can be approximated by

$$s(t) = \sum_{k=1}^{N} b_k(t)\cos(2\pi f_k t),$$

where $b_k(t)$ is a narrow-band modulation. The reference function $r(t) = \cos(2\pi f_j t)$ accesses the jth frequency band of interest and an auxiliary reference function $p(t) = \cos(2\pi f_d t)$ provides the required frequency offset which is the IF frequency (see Figure 9.16). Develop a general relationship for the output $g(t)$ of the system, where

$$g(t) = \int_{-\infty}^{\infty} |R(\alpha, t) + S(\alpha, t)|^2 \, d\alpha$$

and where $R(\alpha, t)$ is the total reference waveform at the output. Calculate the temporal frequency content of the two terms

$$g_1(t) = \int_{-\infty}^{\infty} |R(\alpha, t)|^2 \, d\alpha$$

and

$$g_2(t) = \int_{-\infty}^{\infty} |S(\alpha, t)|^2 \, d\alpha.$$

Calculate the minimum value of f_d to prevent overlap of the spectral terms of the three output signals $g_1(t)$, $g_2(t)$, and $g_3(t)$ if the total *baseband* bandwidth of $s(t)$ is 20 MHz and TW = 1000 for the acousto-optic cell. You are expected to chose a realistic aperture weighting function to support your answer. Sketch the temporal spectrum of all three terms to support your answer.

9.2. Suppose that we use a plane-wave reference probe at the Fourier plane to heterodyne detect the signal produced by the positive diffracted order from an acousto-optic cell. The cell is made of LiNbO_3 and operates at a center frequency of $f_c = 1600$ MHz. Suppose that the photodetector size is 25 μ. What is the input frequency range that can be detected if the magnitude of the cross-product term must be within $\frac{1}{2}$ of its maximum value for the following two cases:

(a) when the reference beam is parallel to the optical axis and

(b) when the reference beam is parallel to the chief ray caused by f_c.

Plot the frequency response of the system, when using this photodetector, for a full 1000-MHz bandwidth centered at $f_c = 1600$ MHz. Also, calculate the photodetector size needed to keep the system response to no more than a 3-dB rolloff over the full bandwidth.

9.3. Suppose the beam combiner in the optical radio of Figure 9.12 is rotated 10 mrad. If the combiner is 15 mm on a side and has a refractive index of 1.5, calculate the amount that the spectrum is shifted when it is transmitted *through* the prism, if the distance from the center of the combiner to the Fourier plane is 100 mm?

10

Heterodyne Spectrum Analysis

10.1. INTRODUCTION

The emphasis in this chapter is on achieving more dynamic range in spectrum analyzers by using heterodyne-detection techniques. Other benefits, such as the ability to measure both the magnitude and phase of a signal, also accrue as a result of heterodyne detection. As we learned in Chapter 8, the photodetector current produced by a power spectrum analyzer is proportional to the input rf signal *power*. In heterodyne detection we combine the signal spectrum with a reference beam, called a local oscillator, the magnitude and phase of which are known, so that the photodetector current is proportional to the signal *voltage* instead of to the signal power. The result is a significant increase in the dynamic range.

King et al. (94) described heterodyne detection techniques for recovering both the magnitude and phase information of a light distribution. In their system, shown in Chapter 9, Figure 9.3, the interference of an unmodulated reference beam with a spectrum $F(\alpha, t)$ produces a temporal frequency proportional to the input signal frequency f. Because the wideband input signal is typically centered on a frequency of several hundred megahertz, the interference term occurs at a high temporal frequency that varies as a function of the spatial frequency. As a result, implementing the postdetection filter design for each discrete photodetector element, each with a different center frequency, is not cost effective.

In this chapter we describe a heterodyne spectrum analyzer in which a spatially modulated reference beam is used to reduce the temporal IF frequency to a fixed value over the entire spectrum (99). Discrete element photodetectors with small bandwidths and low-noise equivalent powers are used in the Fourier domain to detect the time-varying signal in each frequency channel. An additional benefit of discrete detectors is that the postdetection processing operations are more flexible and can be performed in parallel to reduce the output data rate. Other advantages of heterodyne spectrum analysis are improved crosstalk rejection, scatter-noise immunity, and uninterrupted evaluation of the spectrum to achieve a 100% probability of intercept.

Self-scanned photodetector arrays cannot be used with this detection technique because they integrate light over a time period that is large compared to $1/W$, where W is the bandwidth of the signal. As a result of the integration, the temporal information contained in the heterodyne output is lost. Although discrete photodetectors are not the most elegant for use in systems whose time bandwidth products are large, arrays with about 100 elements have been implemented; advanced photodetector fabrication techniques may produce integrated devices with attractive operational features (100, 101). Furthermore, there are several applications, such as radar warning receivers, where a reasonably small number of photodetectors are adequate because the channel frequency intervals are fairly large relative to the bandwidth covered.

We begin with a description of the basic theory of the heterodyne spectrum analyzer and the spatial/temporal frequency content of several signal types, including cw and short-pulse signals. We then establish the required characteristics of the reference beam and determine the photodetector geometry and postdetection bandwidth required to achieve a given frequency resolution. We analyze and compare the performance of various reference waveforms based on both their temporal and spatial frequency content. Finally, we calculate the dynamic range obtained by heterodyne detection and compare it with that of a power spectrum analyzer.

10.2. BASIC THEORY

The basic theory of heterodyne spectrum analysis is developed in connection with the interferometric system shown in Figure 10.1. The signal waveform $f(t)$ is applied to the transducer of the acousto-optic cell located in the lower branch of the interferometer at plane P_1. The drive signal may be a carrier frequency modulated by a baseband signal $s(t)$, or a portion of the rf spectrum that is translated to a center frequency f_c. The acousto-optic cell in the signal branch of the interferometer has length L_S, centered at $x = 0$. The reference signal $r(t)$ is applied to the transducer of the acousto-optic cell located in the upper branch of the interferometer at plane P_2; this acousto-optic cell has length L_r centered at $x = 0$. The two acousto-optic cells are illuminated by a collimated source of monochromatic light.

The complex light amplitude $f_+(x, t)$ leaving the signal cell is

$$f_+(x,t) = jma(x)s\left(t - \frac{T_s}{2} - \frac{x}{v}\right)e^{j2\pi f_c(t - T_s/2 - x/v)}, \qquad (10.1)$$

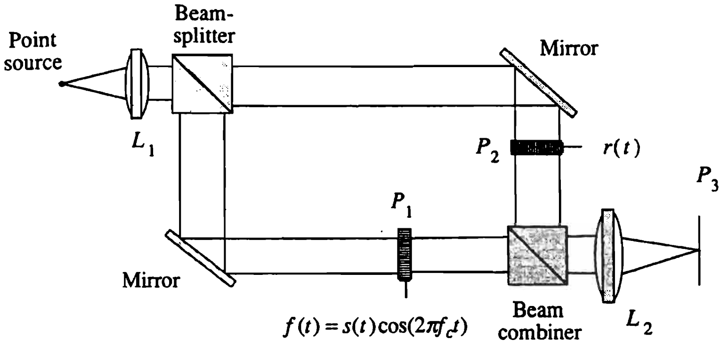

Figure 10.1. Heterodyne spectrum analyzer.

where m is the modulation index, $a(x)$ is the aperture function, T_s is the time duration of the cell, and f_c is the center frequency of the applied rf signal. The spatial Fourier transform of the positive diffracted order is

$$F_+(\alpha, t) = \int_{-\infty}^{\infty} jma(x)s\left(t - \frac{T_s}{2} - \frac{x}{v}\right)e^{j2\pi f_c(t - T_s/2 - x/v)}e^{j2\pi\alpha x}\,dx. \quad (10.2)$$

In a similar fashion, $R_+(\alpha, t)$ is the Fourier transform of the positive diffracted order $r_+(x, t)$. The intensity at plane P_3 is the square of the sum of $F_+(\alpha, t)$ and $R_+(\alpha, t)$:

$$\begin{aligned} I(\alpha, t) &= |F_+(\alpha, t) + R_+(\alpha, t)|^2 \\ &= |F_+(\alpha, t)|^2 + |R_+(\alpha, t)|^2 + 2\,\mathrm{Re}\{F_+(\alpha, t)R_+^*(\alpha, t)\}. \quad (10.3) \end{aligned}$$

After removing the first two bias terms by a bandpass filter centered at f_c, as we discussed in Chapter 9, we detect the cross-product term from Equation (10.3), which contains the desired magnitude, frequency, and phase information.

We relate the spatial Fourier transform given by Equation (10.2) to the temporal transform of $s(t)$ by setting $a(x) = \mathrm{rect}(x/L_s)$ and making a change of variables

$$\begin{aligned} t - T_s/2 - x/v &= u \\ dx &= -v\,du \quad (10.4) \end{aligned}$$

to obtain

$$\boxed{F_+(\alpha, t) = jmve^{j2\pi\alpha v(t-T_s/2)}\int_{t-T_s}^{t} s(u)e^{-j2\pi(f-f_c)u}\,du.} \qquad (10.5)$$

We recognize the integral as the Fourier transform $S(f, t)$ of the baseband signal $s(t)$, evaluated over a time window that extends T_s seconds into the past. This spectrum is centered at f_c to reflect the fact that the signal is on a carrier frequency. The spectrum $S(f, t)$ is called the *instantaneous spectrum* of the signal $s(t)$ for two main reasons. First, and most importantly, the limits of integration include the current time variable t. As the signal flows through the cell, the spectrum is recomputed continuously in time. From a sampling viewpoint, however, we preserve information if we confine our attention to the transform computed at time intervals of T_0, where $T_0 = T_s/N$. As usual, $N = 2T_sW$ is the total number of samples for the signal history in the cell. In this sense, the instantaneous spectrum is clearly different from a batch spectrum analyzer, such as an FFT-based system which might compute the spectrum of successive, nonoverlapping blocks of N samples. Second, the time of flight from the signal plane to the Fourier plane is of the order of a few nanoseconds at most. In this sense the spectrum is calculated nearl instantaneously after the most recent N samples are available. Thus spectrum is also sometimes called the *short-time spectrum* of a signal or the *Gabor transform*.

In a power spectrum analyzer, the intensity of the spatial transform of the signal is sufficient to fully describe the behavior of the system. Heterodyne spectrum analyzers, however, produce temporal signals that can be processed further to extract useful information. It is important, therefore, to examine both the spatial and temporal spectra of the signals to accurately interpret the results and indicate how we can improve the performance of the system.

10.3. SPATIAL AND TEMPORAL FREQUENCIES: THE MIXED TRANSFORM

The temporal frequency content of a signal is an important guideline for designing the postdetection filter that separates the cross-product term from the bias terms in Equation (10.3). Furthermore, after the system has been built, we must verify that its performance meets specifications, using test equipment such as oscilloscopes and electronic spectrum analyzers. The temporal frequency content of the output signal significantly affects our interpretation of the performance of the system. To find both the spatial and temporal frequency content of a signal, we use the *mixed transform*, which is defined as is the simultaneous spatial/temporal Fourier transform of the input space/time signal (102):

$$\boxed{F_+(\alpha, f) = \iint\limits_{-\infty}^{\infty} f_+(x,t) e^{j2\pi(\alpha x - ft)}\, dx\, dt.} \tag{10.6}$$

When displayed as a two-dimensional function, the independent variables represent spatial and temporal frequencies. Another way to view the mixed transform is that it reveals the temporal frequency content at any position α of a probe in the spatial frequency plane. The term *probe* is used here in exactly the same sense as in Chapter 9; it represents a reference beam which, in combination with a photodetector, is used to detect the magnitude, frequency, and phase of light.

We generally first calculate the spatial frequency transform of a signal, as given by Equation (10.2), and then find the mixed transform by completing the temporal part of the transform:

$$F_+(\alpha, f) = \int_{-\infty}^{\infty} F_+(\alpha, t) e^{-j2\pi ft}\, dt. \tag{10.7}$$

The spatial transform part of the mixed transform $F_+(\alpha, t)$ is most useful for visualizing the spectrum detected at the output of the optical system; the mixed transform $F_+(\alpha, f)$ provides additional information about the temporal frequencies and is useful in interpreting the results as displayed on test equipment such as oscilloscopes and spectrum analyzers.

We apply the mixed transform to three signals to demonstrate different relationships between the spatial and temporal frequencies: a cw signal, a short pulse, and a dynamic case of a long pulse that evolves into the system.

10.3.1. The cw Signal

First, suppose that the input waveform is a pure cw signal at frequency f_k with magnitude $c_k = 1$. The spatial part of the mixed transform can be calculated from either Equation (10.2) or Equation (10.5); in this case it is simpler to use Equation (10.2):

$$\begin{aligned} F_{+}(\alpha, t) &= jme^{j2\pi f_k(t - T_s/2)} \int_{-\infty}^{\infty} a(x) e^{j2\pi(\alpha - \alpha_k)x}\, dx, \\ &= jme^{j2\pi f_k(t - T_s/2)} L_s \operatorname{sinc}[(\alpha - \alpha_k) L_s], \qquad (10.8) \end{aligned}$$

where we have set $a(x)$ equal to rect(x/L_s) for convenience. This result indicates that the spatial spectrum is a sinc function, centered at α_k, with magnitude proportional to the length of the acousto-optic cell. In addition, the entire spectrum has temporal frequency f_k, as shown by the phasor in Equation (10.8), independent of which spatial frequency α we probe at plane P_3. An exact coupling between spatial and temporal frequencies does not, therefore, exist, as we claimed in Chapter 7. An exact coupling occurs only as $L_s \to \infty$ so that $L_s \operatorname{sinc}[(\alpha - \alpha_k)L_s] \to \delta(\alpha - \alpha_k)$; all the signal energy is then concentrated at one sample position in the spatial frequency plane. The key point is that spatial diffraction is due to integration over a finite range at the space plane. All light associated with diffraction due to the aperture function must therefore have the same temporal frequency as the underlying cw signal.

To complete the mixed transform for the cw input signal, the spatial frequency transform given by Equation (10.8) is used in Equation (10.7) to produce the mixed transform of the cw signal:

$$\boxed{\begin{aligned} F_{+}(\alpha, f) &= L_s \operatorname{sinc}[(\alpha - \alpha_k) L_s] \int_{-\infty}^{\infty} e^{-j2\pi(f - \alpha_k v)t}\, dt \\ &= L_s \operatorname{sinc}[(\alpha - \alpha_k) L_s]\, \delta(f - \alpha_k v). \end{aligned}} \qquad (10.9)$$

This result shows that the temporal frequency consists of a delta function centered at $f_k = \alpha_k v$, which implies that the temporal frequency is not dependent on the probe position. The $\operatorname{sinc}[(\alpha - \alpha_k)L_s]$ function shows that the finite spatial aperture causes spectral spreading in the spatial frequency domain, whereas $\delta(f - f_k)$ shows that the temporal frequency content of the signal is pure. The purity of the temporal frequency arises because the detected signal is not truncated in time by the acousto-optic cell or by any other system component. In most experimental instruments, such as in an electronic spectrum analyzer, the temporal integration is constrained to the time range $|t| \leq T_e/2$, so that Equation (10.9) becomes

$$\begin{aligned} F_{+}(\alpha, f) &= L_s \operatorname{sinc}[(\alpha - \alpha_k) L_s] \int_{-T_e/2}^{T_e/2} e^{-j2\pi(f - f_k)t}\, dt \\ &= L_s T_e \operatorname{sinc}[(\alpha - \alpha_k) L_s] \operatorname{sinc}[(f - f_k) T_e]. \qquad (10.10) \end{aligned}$$

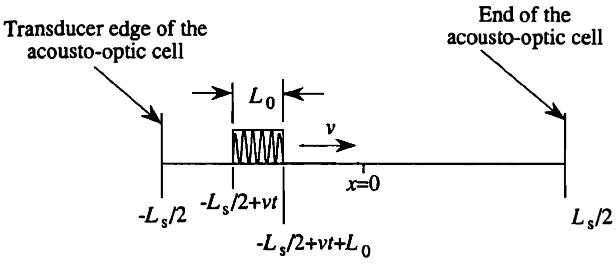
Transducer edge of the acousto-optic cell
End of the acousto-optic cell
L_0
v
x=0
$-L_s/2$
$-L_s/2+vt$
$-L_s/2+vt+L_0$
$L_s/2$

Figure 10.2. Short-pulse input signal.

This result shows that a conventional spectrum analyzer produces "temporal diffraction" if the signal has a finite time duration, similar to the spatial diffraction produced in the optical spectrum analyzer. When $T_e = L/v$, the spatial and temporal frequency spreads are equal.

10.3.2. A Short Pulse

The second signal is a *short pulse* of duration $T_0 \ll T_s$ and carrier frequency f_c that is completely within the acousto-optic cell. This signal, illustrated in Figure 10.2, exists within the cell for the time period $0 < t < (T_s - T_0)$. Using Equation (10.2), we find that the amplitude distribution at plane P_3 at some instant in time is

$$\begin{aligned} F_+(\alpha, t) &= jm \int_{-L_s/2+vt}^{-L_s/2+vt+L_0} e^{j2\pi f_c(t-T_s/2-x/v)} e^{j2\pi\alpha x}\, dx \\ &= jme^{j2\pi\alpha v t} L_0 \operatorname{sinc}[(\alpha-\alpha_c)L_0], \qquad 0 \le t \le (T_s - T_0), \quad (10.11) \end{aligned}$$

where we again ignore unimportant phase terms. The spatial spectrum of a short pulse is a sinc function, centered at α_c, whose magnitude and width are functions of the pulse length L_0.

The mixed transform for a short-pulse is found by substituting the result from Equation (10.11) into Equation (10.7) and noting that the effective integration time is $(T_s - T_0) \approx T_s$ seconds because the signal exists in the cell for only this time period:

$$\boxed{\begin{aligned} F_+(\alpha, f) &= L_0 \operatorname{sinc}[(\alpha-\alpha_c)L_0] \int_0^{T_s} e^{-j2\pi(f-\alpha v)t}\, dt \\ &= L_0 T_s \operatorname{sinc}[(\alpha-\alpha_c)L_0] \operatorname{sinc}[(f-\alpha v)T_s]. \end{aligned}} \qquad (10.12)$$

The temporal frequencies for the short pulse are also distributed according to a sinc function because the pulse also has finite time duration. This example shows most clearly that the temporal frequencies for a pulse that exists for a finite *time* duration are spread in the same way as the spatial frequencies are spread when a signal exists over a finite *space* interval. For a probe at any spatial frequency α, the mixed transform reveals that there is a temporal frequency sinc function centered at $f = \alpha v$ and that the temporal frequency spread is given by sinc$[(f - \alpha v)T_s]$.

10.3.3. The Evolving Pulse

The third signal is a pulse moving into the cell as shown in Figure 10.3; this pulse has duration $T_0 \gg T_s$ and carrier frequency f_c. When t is slightly larger than zero, that part of the signal within the cell behaves as a short pulse, concentrated near the transducer edge of the acousto-optic cell. When $t = T_s/2$ the signal fills half the cell and when $t > T_s$ the signal completely fills the cell so that it behaves as a cw signal. We now discuss the spatial/temporal characterization of the mixed transform as the signal evolves from a short pulse to a cw signal.

If the time of arrival of the leading edge of the pulse is $t = 0$, the leading edge moves to $x = (-L_s/2 + vt)$ for $0 < t \leq T_s$. For a unit amplitude pulse, Equation (10.2) becomes

$$F_+(\alpha, t) = jm \int_{-L_s/2}^{-L_s/2+vt} e^{j2\pi f_c(t - T_s/2 - x/v)} e^{j2\pi\alpha x}\, dx$$
$$= jme^{j2\pi(\alpha - \alpha_c)vt/2}\{vt \operatorname{sinc}[(\alpha - \alpha_c)vt]\}, \qquad (10.13)$$

where we ignore unimportant phase terms. When we apply the same

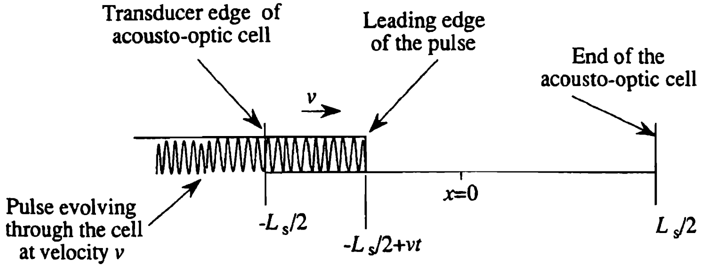
Transducer edge of acousto-optic cell
Leading edge of the pulse
End of the acousto-optic cell
v
Pulse evolving through the cell at velocity v
x=0
-L_s/2
-L_s/2+vt
L_s/2

Figure 10.3. Evolving-pulse input signal.

interpretation to Equation (10.13) as we did to the cw signal, we find that the spatial spectrum is a sinc function centered at α_c. However, the magnitude of the sinc function increases linearly as t increases and its width decreases. This behavior reflects the fact that the pulse width, within the cell, increases linearly with time.

The temporal frequency cannot be so easily deduced just from the phasor factor in Equation (10.13), because the linear term vt introduces additional temporal frequencies that are not accounted for by the simple phasor notation. The interesting relationship between the temporal and spatial frequencies can be appreciated only by completing the mixed transform. The mixed transform for the evolving pulse is found by substituting the spatial transform as given by Equation (10.13) into the mixed transform as given by Equation (10.7):

$$F_+(\alpha, f) = \int_0^{T_s} vt\,\mathrm{sinc}[(\alpha - \alpha_c)vt]\,e^{j\pi(\alpha+\alpha_c)vt}e^{-j2\pi ft}\,dt, \quad (10.14)$$

where T_s is the time duration of the acousto-optic cell. The integration time is over just that time integral during which the pulse evolves. We express the sinc function as $\sin[\pi(\alpha - \alpha_c)vt]/[\pi(\alpha - \alpha_c)vt]$, cancel the terms in vt, apply the Euler expansion, and perform the integration to produce

$$\boxed{F_+(\alpha, f) = \frac{T_s}{\alpha - \alpha_c}\{\mathrm{sinc}[(f - \alpha v)T_s] - e^{j\phi(\alpha, f)}\mathrm{sinc}[(f - \alpha_c v)T_s]\},} \quad (10.15)$$

where $\phi(\alpha, f)$ is a phase term. For a probe at $\alpha_c + \Delta\alpha$, the result shows two temporal frequencies: one at $f = f_c$ and one at $f_m = f_c + \Delta f$, as shown in Figure 10.4.

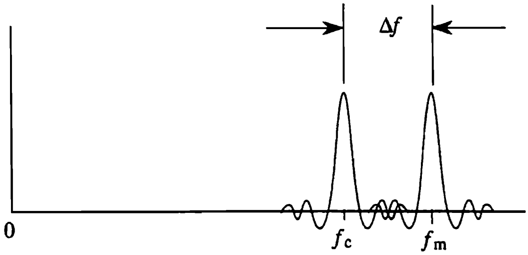

Figure 10.4. Mixed transform of the evolving pulse for a probe at $\Delta\alpha = \Delta f/v$ away from α_c.

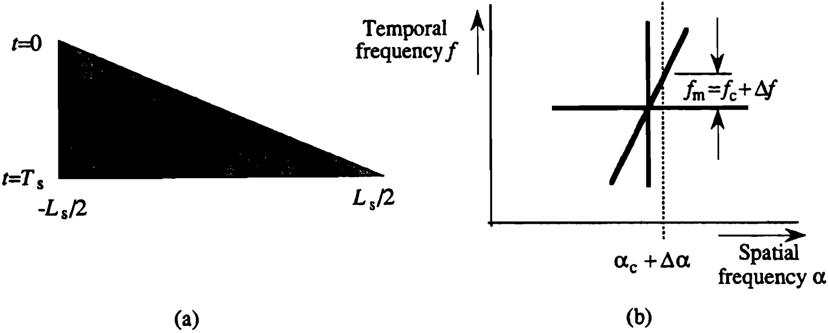

Figure 10.5. Two-dimensional representation of the mixed transform of an evolving pulse: (a) pulse length increases as time increases; (b) the spectrum of the triangle has strong diffraction perpendicular to t.

An alternative way to find the mixed transform is to plot the two-dimensional Fourier transform of the space/time representation of the evolving pulse as shown in Figure 10.5(a). At $t = 0$ the pulse length is zero, and at $t = T_s$ the pulse length is $L_s = vT_s$. The mixed transform of the pulse is found by calculating the two-dimensional transform of the shaded area in Figure 10.5(a) and translating the center of the Fourier transform to the coordinate (α_c, f_c) in the (α, f) domain to account fc. the spatial and temporal carrier frequencies. The two-dimensional Fourier transform consists of three main ridges of high intensity, as shown in Figure 10.5(b); each ridge is perpendicular to one of the edges of the shaded triangle. If we place a photodetector at $\alpha_c = \Delta\alpha$, as shown by the dotted line in Figure 10.5(b), the distance between the horizontal ridge and the diagonal ridge corresponds to $f_m = f_c + \Delta f$, exactly as predicted by Equation (10.15).

This temporal frequency behavior also becomes apparent if we continue the result from the spatial part of the analysis one more step to reveal the temporal behavior of the signal as it would be displayed on an oscilloscope. For example, if we add a reference beam to $F_+(\alpha, t)$, carry out the square-law detection, and take the real part of Equation (10.13), as required to complete the analysis of the cross-product term, we produce a time signal

$$F_+(\alpha, t) = vt\cos[2\pi(\alpha + \alpha_c)vt/2]\operatorname{sinc}[(\alpha - \alpha_c)vt/2], \qquad 0 \le t \le T_s. \tag{10.16}$$

As above, we expand the sinc function to obtain

$$F_+(\alpha,t) = \frac{1}{\alpha - \alpha_c} \sin[2\pi(\alpha - \alpha_c)vt/2]\cos[2\pi(\alpha + \alpha_c)vt/2], \tag{10.17}$$

where we again ignore unimportant constants. Consider the situation where the reference probe is located at $\alpha_c + \Delta\alpha$. We find that

$$F_+(\alpha,t) = \frac{1}{\Delta\alpha} \sin[2\pi(\Delta\alpha/2)vt]\cos[2\pi(\alpha_c + \Delta\alpha/2)vt];$$

$$0 \le t \le T_s, \tag{10.18}$$

which clearly shows that the output has temporal frequency $f_c + \Delta f/2$, modulated by a signal whose frequency is $\Delta f/2$. Its temporal frequency decomposition, by use of trigonometric identities, is exactly that of two frequencies separated by an interval Δf.

To illustrate the time waveform represented by Equation (10.18), we place the photodetector probe outside the mainlobe of the sinc function due to the signal and observe the amplitude modulation on an oscilloscope (103). The acousto-optic cell has a time duration $T_s = 10$ μsec. We use a 20-μsec pulse signal so that we can show (1) the output signal as the pulse evolves into the system for the first 10-μsec interval, (2) its temporal behavior as a cw signal for the next 10 μsec, and (3) its response as it once again becomes an evolving pulse leaving the cell during the last 10-μsec interval. The amplitude modulation for each portion of the output signal is seen in Figure 10.6 for a photodetector position corresponding to $\Delta f = 345$ kHz away from f_c. The frequency of the amplitude modulation at the beginning and end of the output is measured from the oscilloscope as 182 kHz. Because the expected value of the modulation frequency is $\Delta f/2 = 172.5$ kHz, the error of the measured value is 5.2%, which is reasonable for such measurements. The oscilloscope trace also shows a sharp transition to the response expected of a cw signal at 10 μsec, when the pulse fills the cell, and then back to the evolving pulse signal 10 μsec later as the trailing edge of the pulse passes through the cell. This result graphically shows how the temporal frequencies change as the input signal changes its form.

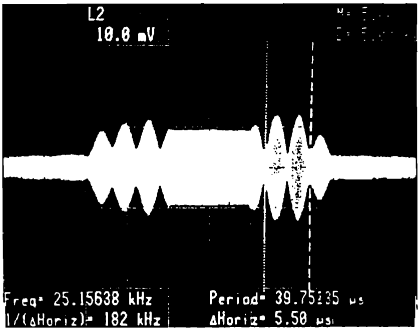

Figure 10.6. Amplitude of output for a 20-μsec pulse (103).

10.4. THE DISTRIBUTED LOCAL OSCILLATOR

At the end of Chapter 9, we discussed methods for implementing an optical radio. If the reference beam is scanned across the spectrum and if the resulting intensity is detected by a single photodetector, the result is a scanning spectrum analyzer. Such a system would be called a superheterodyne receiver if it were implemented electronically; it suffers from the fact that not all frequencies are monitored at all times. To implement a mo.̈ practical heterodyne spectrum analyzer and to take full advantage of the parallel nature of the optical system, we want to generate a reference beam that produces a constant-output IF frequency for all spatial frequency positions. If we can fix the offset temporal frequency at f_d for all detected spatial frequencies, we can use identical photodetectors and bandpass filters to select the desired cross-product term. Because f_d does not need to be a high frequency to separate the cross-product term from the bias terms, a substantial reduction in the photodetector bandwidth is possible, from several hundred to about 10 MHz, or even less in some applications.

10.4.1. The Ideal Reference Signal

The reference waveform at the Fourier plane plays an important role in the performance of the heterodyne spectrum analyzer. The desired characteristics of $R_+(\alpha, t)$ are that (1) the magnitude should be equal at all photodetector positions so that the magnitudes of the spatial frequencies due to the signal are measured accurately, (2) the spatial and temporal frequencies should be coupled so that, with a relative geometric displacement between the reference waveform and the signal spectrum, equal temporal offset frequencies are produced at all photodetector locations to simplify the postdetection circuitry, as shown in Chapter 9, Section 9.4.2, Method 5, (3) the magnitude should be constant over time to avoid measurement errors, and (4) the duty cycle of the drive signal $r(t)$ should be high so that light is efficiently used.

The reference signal must contain at least N frequency components, where N is of the order of $3M$ and the number of resolvable frequencies M is of the order of T_sW. As in Chapter 9, we consider each frequency in the reference signal at plane P_3 of Figure 10.1 as a probe that we use to measure the frequency content of $F_+(\alpha, t)$. The ideal reference signal is generated by summing N equal magnitude frequencies (102):

$$\boxed{r(t) = \sum_{n=N_1}^{N_2} \cos(2\pi n f_0 t - \phi_n),} \tag{10.19}$$

where f_0 is the fundamental frequency and where $f_1 = N_1 f_0$ and $f_2 = N_2 f_0$ are the lowest and highest frequencies in the signal. By definition, $r(t)$ is composed of exactly $N = N_2 - N_1 + 1$ frequency components, chosen so that there is exactly one probe for each photodetector at the Fourier plane of the spectrum analyzer.

Because $r(t)$ contains N discrete frequencies, each a harmonic of the fundamental frequency f_0, it is a repetitive signal with repetition period $T_r = 1/f_0$. The repetition period is also equal to L_r/v, where L_r is the length of the acousto-optic cell in the reference beam. We can generate a surprising variety of waveforms by specifying the phases appropriately. We begin by finding the waveform that $r(t)$ assumes when the phases are all zero; Equation (10.19) can then be written as

$$r(t) = \sum_{n=0}^{N_2} \cos(2\pi n f_0 t) - \sum_{n=0}^{N_1 - 1} \cos(2\pi n f_0 t), \tag{10.20}$$

which is the sum of two geometric series. The sum of the terms is given by

$$r(t) = \tfrac{1}{2}\left\{ \frac{1 - e^{j2\pi(N_2+1)f_0 t}}{1 - e^{j2\pi f_0 t}} - \frac{1 - e^{j2\pi N_1 f_0 t}}{1 - e^{j2\pi f_0 t}} \right\} + \text{c.c.}, \tag{10.21}$$

where we use Euler's formula to expand the cosine terms and c.c.

represents the complex conjugate of all the preceding terms. The terms in Equation (10.21) are combined to give

$$\begin{aligned} r(t) &= \tfrac{1}{2}\frac{e^{j2\pi(N_2+1)f_0t} - e^{j2\pi N_1 f_0 t}}{e^{j2\pi f_0 t} - 1} + \text{c.c.} \\ &= \tfrac{1}{2}\frac{e^{j\pi(N_2+N_1+1)f_0t}\left[e^{j\pi(N_2-N_1+1)f_0t} - e^{-j\pi(N_2-N_1+1)f_0t}\right]}{e^{j\pi f_0 t}\left[e^{j\pi f_0 t} - e^{-j\pi f_0 t}\right]} + \text{c.c.} \\ &= \tfrac{1}{2}e^{j\pi(N_2+N_1+1)f_0t}\frac{\sin[\pi(N_2 - N_1 + 1)f_0t]}{\sin(\pi f_0 t)} + \text{c.c.} \\ &= \cos[\pi(N_2 + N_1 + 1)f_0t]\frac{\sin[\pi(N_2 - N_1 + 1)f_0t]}{\sin(\pi f_0 t)}. \qquad (10.22) \end{aligned}$$

We set $N = N_2 - N_1 + 1$ as the number of cosine terms in $r(t)$ and find that Equation (10.22) becomes

$$r(t) = \cos[\pi(N + 2N_1)f_0t]\frac{\sin(\pi N f_0 t)}{\sin(\pi f_0 t)}. \qquad (10.23)$$

This result describes the reference waveform as an impulse train tha' modulates a temporal carrier frequency of $(N + 2N_1)f_0/2$. As an asiue, the impulse train is the temporal equivalent of the spatial Fourier transform of an N-slit grating as derived in classical optical texts (14).

If we set the phases ϕ_n as a linear function of n (e.g., $\phi_n = n\phi_0$), the impulse train is simply advanced or delayed according to the sign and magnitude of ϕ_0. If the phases are quadratic in n,

$$\phi = \frac{d\pi\, n^2}{N}, \qquad (10.24)$$

so that $r(t)$ becomes a repetitive chirp function, the period of which is T_r, the duty cycle of which is d, and the frequency range of which is from f_1 to f_2.

An example of the behavior of $r(t)$, which shows the transition from an impulse train to a chirp train as a function of the parameter d, is given in Figure 10.7. The upper trace shows two periods of $r(t)$ when $d = 0$ so that the phase is zero for all n. The result is an impulse train that modulates a carrier frequency f_c. The presence of the carrier changes the signal

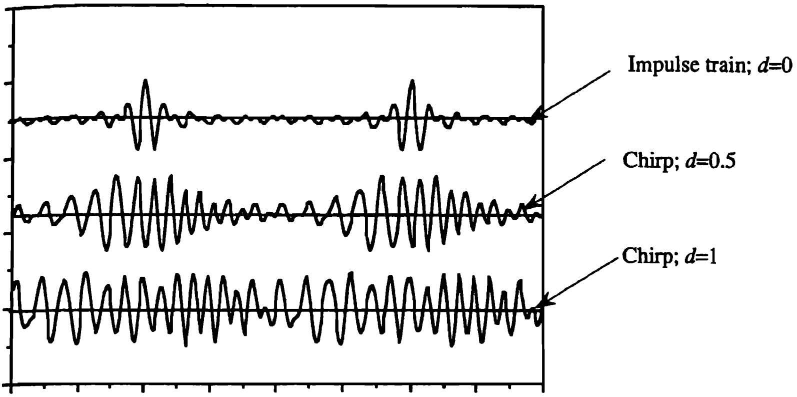

Figure 10.7. Chirp functions with duty cycles of 0, 0.5, and 1.

waveform somewhat from the expected impulse response, because there are only three cycles of the carrier underneath the impulse train envelope. Three carrier cycles per impulse arise from the fact that we require that $N_2 = 2N_1$ to produce an octave bandwidth and that the carrier frequency is $(N_1 + N_2)f_0/2 = (3/2)N_1 f_0$. The traces of Figure 10.7 are therefore accurate representations of the appearance of the signal on a test oscilloscope.

The middle trace is that for a quadratic phase function, according to Equation (10.24), but with $d = 1/2$; we note that the signal has become a repetitive chirp function with a duty cycle of 50%. The lower trace shows the chirp function when $d = 1$; the chirp now has a 100% duty cycle. Thus, we find a smooth progression from an impulse train to a full duty cycle chirp as d is changed from 0 to 1. Each of these signals is a suitable reference signal; the preferred choice is to use a high duty cycle chirp so that the light power is efficiently used. For example, the 100% duty cycle chirp signal produces reference probes at the Fourier plane whose intensities are N times those produced by the impulse train because the impulses intercept only $1/N$ of the input light intensity.

Other useful reference waveforms can be generated by a proper choice of the phases of $r(t)$. A repetitive pseudorandom sequence of length $N = 2^r - 1$, where r is an integer, can be produced if the phases for the various frequencies are suitably chosen (104). If the ϕ_n are random, the resulting signal simulates a bandlimited noise source that nevertheless retains a repetitive feature.

10.4.2. The Mixed Transform of the Reference Signal

The amplitude profile of the illuminating beam, the acoustic attenuation, the size limitations of the cell, and any other weighting factors combine to form a reference-beam aperture weighting function $b(x)$. These features of the interaction can be incorporated with the reference beam in the form $b(x)r(t - x/v)$, where we ignore the time-delay factor $T_r/2$ in this section. The reference signal corresponding to the positive diffracted order is

$$r_+(x,t) = b(x) \sum_{n=N_1}^{N_2} e^{j[2\pi n f_0(t-x/v)-\phi_n]}, \qquad (10.25)$$

and the mixed transform of $r(x, t)$ is

$$R_+(\alpha, f) = \iint_{-\infty}^{\infty} r(x,t) e^{j[2\pi(\alpha x - ft)]}\, dx\, dt, \qquad (10.26)$$

where α is the spatial frequency and f is the temporal frequency. We calculate the spatial transform first to find that

$$R_+(\alpha, t) = \int_{-\infty}^{\infty} b(x) \sum_{n=N_1}^{N_2} e^{j[2\pi n f_0(t-x/v)-\phi_n]} e^{j2\pi\alpha x}\, dx. \qquad (10.27\text{\`{}}$$

By separating the time- and space-dependent terms and by performing the integration over space, we find that

$$R_+(\alpha, t) = \sum_{n=N_1}^{N_2} B(\alpha - nf_0/v) e^{j[2\pi n f_0 t - \phi_n]}, \qquad (10.28)$$

where $B(\alpha)$ is the Fourier transform of the aperture weighting function $b(x)$. We see that the Fourier transform of the reference signal consists of a sequence of aperture functions $B(\alpha)$ that are centered at each of N photodetector positions. Each probe has an associated pure frequency that is a harmonic of f_0. Because each frequency component of the reference signal behaves as a cw signal, the entire aperture function oscillates at the same temporal frequency.

We complete the mixed transform by calculating the temporal frequency content:

$$R_+(\alpha, f) = \int_{-\infty}^{\infty} R_+(\alpha, t) e^{-j2\pi f t}\, dt. \qquad (10.29)$$

We substitute Equation (10.28) into Equation (10.29) to find that

$$R_+(\alpha,f) = \sum_{n=N_1}^{N_2} e^{-j\phi_n} B(\alpha - nf_0/v)\delta(f - nf_0), \tag{10.30}$$

which can be expressed in an equivalent form as

$$\boxed{R_+(\alpha,f) = B(\alpha - f/v) \sum_{n=N_1}^{N_2} e^{-j\phi_n}\delta(f - nf_0).} \tag{10.31}$$

We see that $R_+(\alpha,f)$ consists of a two-dimensional function $B(\alpha - f/v)$ that is sampled by a set of phase-weighted delta functions, creating N discrete probes. There is one probe at each photodetector position, shifted by the desired temporal frequency nf_0 and spatial frequency nf_0/v with a shape described by $B(\alpha)$. Because of the nature of the sampled function $B(\alpha - f/v)$, we find that the *magnitude of the mixed transform is independent of ϕ_n and, therefore, the specific repetitive reference signal $r(t)$.* This remarkable result states that the performance of the spectrum analyzer is completely independent of the specific reference signal, provided that it can be represented by Equation (10.19).

Figure 10.8 shows the magnitude of $R_+(\alpha,f)$ when $b(x) = \text{rect}(x/L_r)$. For any value n, the spatial frequency response is a sinc function centered at $\alpha = nf_0/v$. The mixed transform shows that the sinc function is also

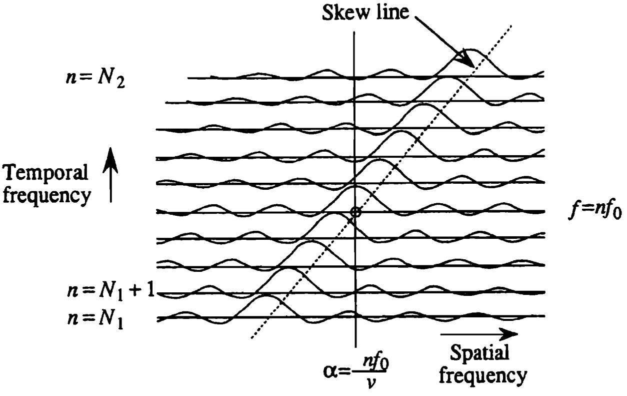

Figure 10.8. Magnitude of mixed transform for an arbitrary signal.

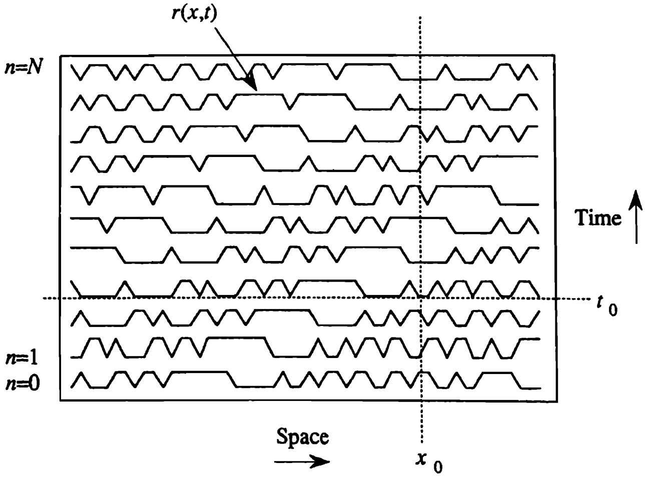

Figure 10.9. Reference signal envelope expressed as a function of space and time.

displayed in the second dimension at $f = nf_0$; as n increases from N_1 to N_2, we find that the sinc functions are centered on a skew line in the α ˆ plane.

A similar two-dimensional frequency display would result if we were to use the y axis of a conventional Fourier-transforming system to display the time-shifted versions of the reference signal as it passes through the acousto-optic cell. In Figure 10.9, we illustrate such a signal, shifted progressively in space as time increases in the vertical direction. For any spatial position x_0, we find the temporal function by reading the values along a vertical line positioned at x_0. At any time t_0, we find the spatial function resident within the acousto-optic cell by reading the values along a horizontal line through t_0. From the two-dimensional space/time representation of Figure 10.9, we could also obtain the mixed transform of Figure 10.8, provided that the optical aperture of a Fourier-transform system is limited to $\pm L_r/2$ in the space dimension and is unlimited in the time dimension.

10.5. PHOTODETECTOR GEOMETRY AND BANDWIDTH

The mixed transform provides considerable guidance about the design of the photodetector array, the nature of the bandpass filter, and the ex-

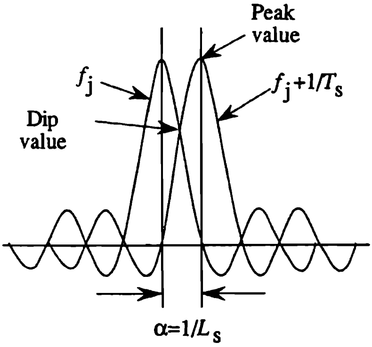

Figure 10.10. Frequency-resolution geometry for a spectrum analyzer.

pected performance levels of the spectrum analyzer. The major task in spectrum analysis is to accurately and reliably detect cw frequencies. We must be able to resolve spatial frequencies at intervals of approximately $1/L_s$, as shown in Figure 10.10. The resolution criterion is generally stated in terms of a required dip between frequencies of about 3 dB. Another consideration is that we wish to measure the signal magnitude to within a specified degree of accuracy. The photodetectors must therefore be spaced so that at least one of them is close to the peak value.

We now discuss how the reference acousto-optic cell length L_r is related to that of the signal cell whose length is L_s. Figure 10.11 shows the light distribution in the Fourier plane caused by a set of equal-magnitude

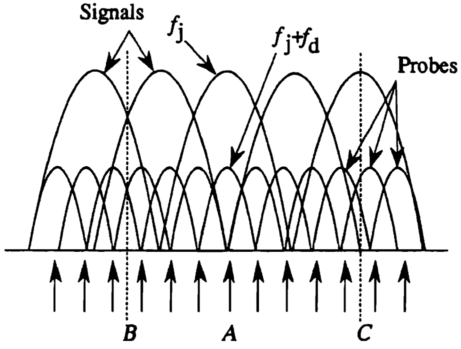

Figure 10.11. Signal spectrum for equal-strength cw signals plus reference probes.

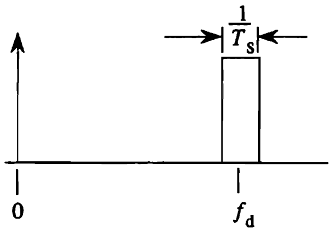

Figure 10.12. Bandpass filter for photodetector output.

cw signals generated from an acousto-optic cell of time duration T_s. For clarity, we show only the central lobes of the Fourier components, which are represented by $\mathrm{sinc}[(f - f_j)T_s]$ in the temporal frequency domain or by $\mathrm{sinc}[(\alpha - \alpha_j)L_s]$ in the spatial frequency domain. The reference beam is represented by a set of sinc-function probes that are spaced at intervals of f_0 in the temporal frequency domain or intervals of $\alpha_0 = f_0/v$ in the spatial frequency domain. The reference probes must be narrower than the cw-signal mainlobes so that the cw signals are sampled accurately. Furthermore, the temporal frequency of the probes is offset by an amount f_d through a geometric displacement at the Fourier plane of the reference beam relative to the signal beam. For example, in the region near point A in Figure 10.11, the cw signal frequency is f_j, whereas that of the central probe is $f_j + f_d$. The frequencies associated with adjacent probes are $f_j + f_d \pm nf_0$, where n is an integer.

We associate one photodetector with each of the reference probes. If we have R photodetectors per resolvable frequency, the interval between them is $1/RT_s$, which, by definition, is equal to f_0. For the moment, we let the photodetectors be point elements to clarify the key principles and identify the centers of the photodetectors by arrows. For this idealized case, a point detector at A detects only the cross product between one probe and the signal because all adjacent probes, as well as adjacent frequencies, have zero crossings at A. The output is therefore at the offset frequency f_d, which is accepted by a bandpass filter as shown in Figure 10.12. The shape of the bandpass filter is a function of the frequency resolution and required measurement accuracy.

10.5.1. The Bandpass Filter Shape

To find the minimum number of photodetectors per frequency to resolve signal frequencies spaced by $1/T_s$ and to accurately measure the signal

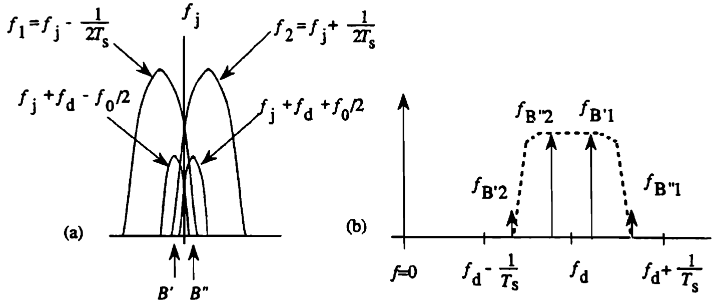

Figure 10.13. Worst-case resolution: (a) position of the probes relative to the signals; (b) the four major frequencies generated by the geometry of part (a).

magnitude is a somewhat more complicated procedure than that used in Chapter 4 in connection with power spectrum analyzers. With heterodyne detection, we must consider how the temporal frequencies generated by the interference between the signal and reference beams affect the output signal. The shape of the postdetection bandpass filter is influenced by the need (1) to control crosstalk, (2) to achieve a given frequency resolution, and (3) to detect the signals with a reasonable degree of accuracy.

In Figure 10.11 we show the case where $R = 2.5$, a value just above that required to satisfy the Nyquist sampling rate criterion. This case conveniently illustrates both the best- and worst-case conditions for detection, depending on the relative positions of the probes with respect to the signals. For example, the worst-case condition for resolving two frequencies occurs when the midpoint between the frequencies coincides with the midpoint between two photodetectors (as near point B in Figure 10.11). Figure 10.13(a) shows this situation with greater detail. Suppose that the temporal frequency associated with the midpoint is f_j. The two frequencies to be resolved are therefore $f_1 = f_j - 1/2T_s$ and $f_2 = f_j + 1/2T_s$. The point photodetectors are identified as being at the positions B' and B''; the frequencies of the associated probes are $f_j + f_d - f_0/2$ and $f_j + f_d + f_0/2$.

The probe/detector at B' produces outputs from both signal frequencies f_1 and f_2. After square-law detection, we find that the associated difference frequencies are

$$f_{B'1} = \left| f_1 - (f_j + f_d - f_0/2) \right| = f_d + \frac{1}{2T_s} - f_0/2 \qquad (10.32)$$

and

$$f_{B'2} = \left| f_2 - (f_j + f_d - f_0/2) \right| = f_d - \frac{1}{2T_s} - f_0/2. \qquad (10.33)$$

These two frequencies are sketched in Figure 10.13(b). In a similar fashion, the photodetector at B'' produces outputs at the frequencies

$$f_{B''1} = \left| f_1 - (f_j + f_d + f_0/2) \right| = f_d + \frac{1}{2T_s} + f_0/2 \qquad (10.34)$$

and

$$f_{B''2} = \left| f_2 - (f_j + f_d + f_0/2) \right| = f_d - \frac{1}{2T_s} + f_0/2, \qquad (10.35)$$

which are also shown in Figure 10.13(b). The magnitude of these frequency components are the same as those at B'. Note that both frequencies $f_{B'1}$ and $f_{B''2}$ do not pass through the bandpass filter associated with any one photodetector, but rather that any photodetector must be pr^ pared to accept any frequency within the specified range. When these requirements are met, we can use identical bandpass filters for each photodetector.

One task for the bandpass filter is to control the frequency content of the postdetection signal. The filter, which is identical for each photodetector circuit, must severely attenuate the unwanted frequency components represented by $f_{B''1}$ and $f_{B'2}$, while accepting the desired frequency components represented by $f_{B'1}$ and $f_{B''2}$. Because the maximum frequency spread about f_d produced by a desired signal is $\pm 1/(2T_s)$, the ideal filter shape is a rectangular passband, centered at f_d, with total bandwidth $1/T_s$, as shown in Figure 10.12.

10.5.2. Crosstalk

Crosstalk considerations for a heterodyne spectrum analyzer are much the same as those for a power spectrum analyzer because crosstalk affects the system dynamic range and the accuracy to which the frequency components are measured. Recall that the design procedure in a power spectrum analyzer is to select an aperture function $a(x)$ so that the sidelobes of a strong signal are sufficiently suppressed at the spatial frequency corresponding to a weak signal. The sidelobes in a power spectrum analyzer are

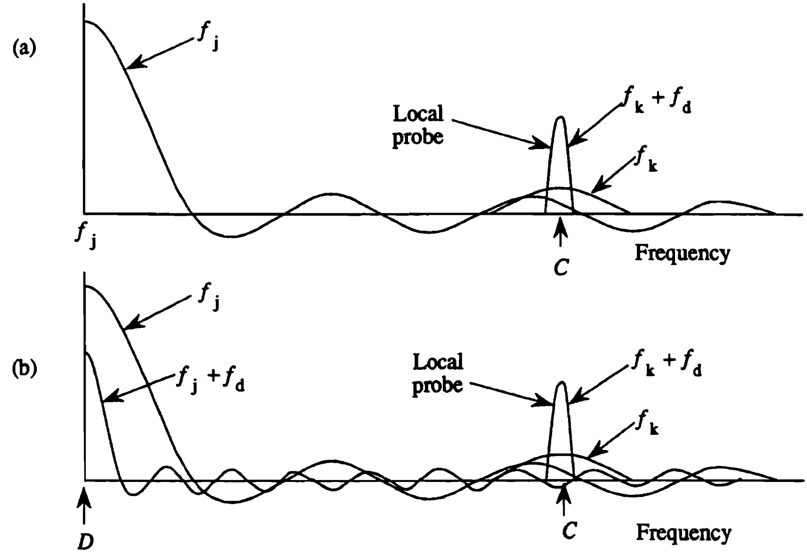

Figure 10.14. Geometry for cross-talk: (a) interference of local probe and strong signal and (b) interference of local probe and reference probe.

proportional to $|A(\alpha)|^2$, and the mainlobe width increases as the sidelobe levels are suppressed. As a result the frequency resolution is reduced.

One difference in the heterodyne spectrum analyzer is that the bandpass filter helps to suppress, in effect, some of the energy due to the sidelobes of a strong signal. The optical intensity that contributes to the crosstalk level in a heterodyne spectrum analyzer is proportional to the product of $A(\alpha - \alpha_j)$, due to the strong-signal frequency at f_j, and of $B(\alpha - \alpha_k)$, due to the reference probe at the weak-signal frequency f_k. Suppose, for example, that $A(\alpha - \alpha_j)$ is a sinc function, as shown in Figure 10.14(a), centered at f_j. At position C, we wish to detect a weak cw signal, whose frequency is f_k, in the presence of the strong signal at f_j. Because the probe associated with the detector at C has frequency $f_k + f_d$, there is no problem in extracting the desired weak-signal information. Even though the sidelobe level from $A(\alpha - \alpha_j)$ is high at C, the bandpass filter will not pass the energy because its frequency $|f_k + f_d - f_j|$ falls outside the passband. There is a special condition, however, when an alias signal slips through the bandpass filter. This condition arises when $f_k - f_j = -2f_d$ (i.e., when the strong signal is at a higher frequency relative to the weak signal). But because the signals are then spread farther apart, the sidelobe levels are lower so that crosstalk is less of a problem.

The bandpass filter does not completely eliminate crosstalk, however. Figure 10.14(b) shows the same situation as in Figure 10.14(a), but it also shows the probe associated with the detector at D. This probe at frequency $f_j + f_d$ along with the signal energy at f_j produces energy at f_d at all spatial frequency positions. The photodetector at C will therefore respond to the output produced by the sidelobes of a strong signal and its associated probe; we still need to use aperture weighting functions to help fight crosstalk as we did in power spectrum analyzers. Fortunately, in the heterodyne spectrum analyzer we have the advantage of being able to independently control $b(x)$ to reduce the sidelobe levels. Because we can control sidelobe levels almost entirely by the aperture weighting function of the reference beam, we do not suffer a loss in system resolution.

The bandpass filter also is effective in reducing the effects of scatter noise, which tends to limit the performance of power spectrum analyzers. The strongest scattered light at the photodetector plane is due to the undiffracted light from the signal and reference acousto-optic cells. These scattered light components do not, however, interfere to produce a signal at the offset frequency f_d. The interference occurs, instead, at baseband where it is removed by the bandpass filter.

10.5.3. Resolution, Accuracy, and Photodetector Size

After the aperture function $b(x)$ has been chosen to control the sidelobe level, we determine the system resolution in much the same way as in Chapter 4. In this case, we begin by convolving the aperture response $A(\alpha)$ from the signal branch with the aperture response $B(\alpha)$ from the reference branch, keeping track of the associated temporal frequencies as a function of the spatial frequency displacement. We then modify the resulting signal by the bandpass characteristics of a filter, accounting for the fact that the band-edge responses of the filter are not perfectly sharp in practice. Based on this information, we determine if the dip between frequencies meets the specification. If not, we iterate the design process until the dip specification is met. We find that $R = 3$ is generally adequate to provide the desired frequency resolution and measurement accuracy.

10.6. TEMPORAL FREQUENCIES OF THE REFERENCE BIAS TERM

So far we have focused on how the characteristics of the cross-product term affect the shape of the bandpass filter and the temporal frequency content of the resulting output signal. The bias term $I_2(\alpha, t)$, due to the reference function $|R_+(\alpha, t)|^2$, can also produce energy within the passband of the filter under certain conditions. We now examine the origin of this energy for the most general case.

From Equation (10.28), we find that the intensity $I_2(\alpha, t)$ due only to the reference beam is

$$\begin{aligned} I_2(\alpha,t) &= |R(\alpha,t)|^2 \\ &= \sum_{n=N_1}^{N_2} \sum_{m=N_1}^{N_2} e^{j2\pi(n-m)f_0 t} e^{j(\phi_n-\phi_m)} B(\alpha - nf_0/v) B^*(\alpha - mf_0/v). \end{aligned} \tag{10.36}$$

The mixed transform for the bias term is readily obtained by finding the temporal transform of Equation (10.36):

$$\begin{aligned} I_2(\alpha,f) &= \int_{-\infty}^{\infty} \sum_{n=N_1}^{N_2} \sum_{m=N_1}^{N_2} e^{j2\pi(n-m)f_0 t} e^{j(\phi_n-\phi_m)} \\ &\quad \times B(\alpha - nf_0/v) B^*(\alpha - mf_0/v) e^{-j2\pi ft}\, dt \\ &= \sum_{n=N_1}^{N_2} \sum_{m=N_1}^{N_2} e^{j(\phi_n-\phi_m)} B(\alpha - nf_0/v) \\ &\quad \times B^*(\alpha - mf_0/v) \int_{-\infty}^{\infty} e^{-j2\pi[f-(n-m)f_0]t}\, dt \\ &= \sum_{n=N_1}^{N_2} \sum_{m=N_1}^{N_2} e^{j(\phi_n-\phi_m)} B(\alpha - nf_0/v) \\ &\quad \times B^*(\alpha - mf_0/v) \delta[f-(n-m)f_0]. \end{aligned} \tag{10.37}$$

The conclusion that we reach from Equation (10.37) is that the bias term, in general, contributes energy at all integer multiples of f_0. Unfortunately, one or more integer multiples of f_0 must fall within the passband of the filter because its width is of the order of $2f_0$ to $3f_0$ if we use two to three probes per signal frequency.

There is a special set of conditions, however, for which $I_2(\alpha, f)$ has energy only at $f = 0$. This set of conditions is

1. That $b(x) = \mathrm{rect}(x/L_r)$.
2. That L_r is equal to an integer multiple of L_s.
3. That point photodetectors are placed at integer multiples of f_0/v so that all photodetectors are at nulls of adjacent sinc functions.

In this special case, we find that the sums in Equations (10.36) and (10.37) have value only for $n = m$; the result is that the power spectrum of $r_+(x, t)$ is *constant in time and at all photodetector positions.* In addition to placing all the point detectors at the nulls of sinc-function probes, we must have an integer number of probes for each resolvable cw signal (for example, $R = 3$). As a result, there is no opportunity for the heterodyne frequency to "walk off" from $f_d \pm nf_0$; this vernier effect can be seen in Figure 10.11, where we set $R = 2.5$.

Because this special set of conditions is impossible to implement in practice, we must find alternative methods to remove energy from the reference bias term. Other practical problems are that we may not be able to generate $N \approx 3M$ reference probes to synthesize $r(t)$ directly if N is large. These and other practical issues have been addressed in the literature (102).

10.7. DYNAMIC RANGE

We turn our attention to a calculation of the dynamic range of the heterodyne spectrum analyzer. The output signal, for a simple cosine of the form $f(x, t) = 0.5[1 + jm_s c_k \cos(2\pi f_k t)]$, is the same as we had ii. ᵗhe power spectrum analyzer discussed in Chapter 8, except that we need ιᴗ account for the beamsplitter and beam-combiner ratios. Suppose that the beamsplitter and beam combiner reflect a fraction γ and ρ of the incident light, respectively, and that the remainder is reflected. Any absorption of light by the beamsplitter or beam combiner is included in the value of A_s, along with other factors that affect the overall system efficiency. The Fourier transform of the signal beam is then

$$F_+(\alpha, t) = \frac{A_s m_s c_k L_s \sqrt{\gamma(1-\rho)}}{4\sqrt{\lambda F}} \operatorname{sinc}\left[(\xi - \xi_k)\frac{L_s}{\lambda F}\right] e^{j2\pi f_k t}, \quad (10.38)$$

where $A_s = \sqrt{P_0 \varepsilon_s / L_s}$ is the effective amplitude of the illumination beam, P_0 is the laser power, ε_s is the overall efficiency of the signal beam, L_s is the length of the acousto-optic cell, and m_s is the modulation index for the signal beam cell necessary to achieve the required spur-free dynamic range. To facilitate the development of analytical solutions, we set $a(x) = \operatorname{rect}(x/L_s)$.

The appropriate reference frequency component for this signal is $r(x, t) = 0.5\{1 + jm_r \cos[2\pi(f_k + f_d)t]\}$, where m_r is the modulation index for the reference beam. We assume that all the frequencies in the reference beam have the same magnitude; for convenience, we include the offset frequency f_d in the reference beam. The Fourier transform of the reference beam is therefore

$$R_+(\alpha, t) = \frac{A_r m_r L_r \sqrt{\rho(1-\gamma)}}{4\sqrt{\lambda F}} \operatorname{sinc}\left[(\xi - \xi_k)\frac{L_r}{\lambda F}\right] e^{j2\pi(f_k + f_d)t}; \qquad (10.39)$$

the symbols have meanings similar to those in Equation (10.38). Recall that the intensity at the Fourier plane is $I(\alpha, t) = |F_+(\alpha, t) + R_+(\alpha, t)|^2$ and that the cross-product term produces a current $i_3(t)$:

$$i_3(t) = 2S \int_{-\infty}^{\infty} \operatorname{Re}\{F_+(\xi, t) R_+^*(\xi, t)\} P(\xi)\, d\xi, \qquad (10.40)$$

where S is the responsivity of the photodetector. The response $P(\xi)$ accounts for the width and center position of the photodetector and determines the region of integration by the photodetector in the Fourier plane. The integration in Equation (10.40) becomes

$$\begin{aligned} i_3(t) = {} & \frac{S A_s A_r m_s m_r L_s L_r c_k \sqrt{\gamma\rho(1-\gamma)(1-\rho)}}{8\lambda F} \cos(2\pi f_t) \\ & \times \int_{-\infty}^{\infty} \operatorname{sinc}\left[(\xi - \xi_k)\frac{L_s}{\lambda F}\right] \operatorname{sinc}\left[(\xi - \xi_k)\frac{L_s}{\lambda F}\right] P(\xi)\, d\xi. \qquad (10.41) \end{aligned}$$

The photodetector length is equal to $\xi_r/2$, where $\xi_r = \lambda F/L_r$ is the distance to the first zero of the reference probe so that

$$P(\xi) = \operatorname{rect}\left[\frac{(\xi - \xi_k)L_r}{\lambda F}\right]. \qquad (10.42)$$

To solve the integral in Equation (10.41), we must find the product of two sinc functions. We express the sinc function in a power series:

$$\operatorname{sinc}(ax) = 1 - \frac{(ax)^2}{3!} + \frac{(ax)^4}{5!} + \qquad (10.43)$$

so that

$$\begin{aligned} \operatorname{sinc}(ax)\operatorname{sinc}(bx) = {} & 1 - \frac{(ax)^2}{3!} - \frac{(bx)^2}{3!} + \frac{a^2 b^2 x^4}{5!} \\ & + \frac{(a^4 + b^4)x^4}{5!} + \qquad (10.44) \end{aligned}$$

The integral of the product of two sinc functions is therefore

$$\int \operatorname{sinc}(ax)\operatorname{sinc}(bx)\,dx = x - \frac{(a^2+b^2)x^3}{3\cdot 3!} + \tag{10.45}$$

where we retain just the leading terms of the expansion. For the photodetector size as given by Equation (10.42), the value of the integral of the two sinc functions given by the leading term of Equation (10.45) is equal to $\lambda F/L_r$. The photocurrent is therefore

$$\boxed{i_3(t) = \tfrac{1}{8}SP_0\sqrt{\varepsilon_r\varepsilon_s\gamma\rho(1-\gamma)(1-\rho)}\,m_s m_r c_k\sqrt{L_s/L_r}\,\cos(2\pi f_d t).} \tag{10.46}$$

We estimate the value of m_r by noting that the overall efficiency of the reference beam is of the order of 0.5 in intensity. Each frequency will therefore have a diffraction efficiency of $\eta_r = 0.5/N$ so that $m_r = \sqrt{0.5/N}$ The final result for the cross-product term is that

$$i_3(t) = \frac{SP_0\sqrt{\varepsilon_r\varepsilon_s\gamma\rho(1-\gamma)(1-\rho)L_s/L_r}\,m_s c_k}{11\sqrt{N}}\cos(2\pi f_d t). \tag{10.47}$$

We now calculate the photocurrent due to the bias terms; these terms are due to the signal and reference beams acting alone. First, the current $i_2(t)$ due to the reference is obtained by integrating Equation (10.39) over the photodetector area:

$$i_2(t) = S\int_{-\infty}^{\infty}\left|\frac{A_r m_r L_r\sqrt{\rho(1-\gamma)}}{4\sqrt{\lambda F}}\operatorname{sinc}[(\xi-\xi_k)L_r/\lambda F]\right|^2 P(\xi)\,d\xi, \tag{10.48}$$

where the symbols have the same meanings as before. Following the same procedure as for calculating $i_3(t)$, we find that

$$\boxed{i_2(t) = \frac{SP_0\varepsilon_r\rho(1-\gamma)}{32N}.} \tag{10.49}$$

Similarly, the photocurrent due to the signal beam acting alone is obtained by integrating Equation (10.38):

$$i_1(t) = S\int_{-\infty}^{\infty}\left|\frac{A_s m_s c_k L_s\sqrt{\gamma(1-\rho)}}{4\sqrt{\lambda F}}\operatorname{sinc}[(\xi - \xi_k)L_s/\lambda F]\right|^2 P(\xi)\,d\xi, \tag{10.50}$$

which becomes

$$\boxed{i_1(t) = \frac{SP_0\varepsilon_s m_s^2\gamma(1-\rho)L_s/L_r}{16}c_k^2.} \tag{10.51}$$

Recall that $m_s^2 = \eta_f$ is the maximum diffraction efficiency per frequency to avoid exceeding the spur-free dynamic range specification.

The signal-to-noise ratio, following the analysis given in Chapter 4, is

$$\mathrm{SNR} = \frac{\langle i_3^2(t)\rangle}{2eB\left(i_d + \bar{i}_1 + \bar{i}_2\right) + 8\pi kTBf_{\mathrm{co}}c_d}. \tag{10.52}$$

This result is similar to that obtained for the power spectrum analyzer except that the shot noise contains the additional average current term $\bar{i}_2$ produced by the local oscillator. The minimum signal is found by using Equation (10.47) in Equation (10.52) to find that

$$\begin{aligned} c_{k\,\mathrm{min}}^2 &= \frac{2eB\left(i_d + \bar{i}_1 + \bar{i}_2\right) + 8\pi kTBf_{\mathrm{co}}c_d}{\left\langle\left[\frac{1}{8}SP_0\sqrt{\varepsilon_r\varepsilon_s\gamma\rho(1-\gamma)(1-\rho)L_s/L_r}\,m_s m_r\cos(2\pi f_d t)\right]^2\right\rangle} \\ &= \frac{2eB(i_d + SP_0\varepsilon_r\rho(1-\gamma)/32N) + 8\pi kTBf_{\mathrm{co}}c_d}{S^2P_0^2\varepsilon_r\varepsilon_s\gamma\rho(1-\gamma)(1-\rho)\eta_f L_s/256NL_r}. \end{aligned} \tag{10.53}$$

In passing from the first to the second line of Equation (10.53), we (1) used the fact that $\bar{i}_1$ is negligible relative to the other currents when c_k is small, (2) used the value of $\bar{i}_2$ from Equation (10.49), and (3) distributed the reference-beam energy over the N probes so that the diffraction efficiency m_r^2 is equal to $0.5/N$. The dynamic range is, following the procedure established in Chapter 8, equal to

$$\boxed{\mathrm{DR} = 10\log\left[\frac{S^2P_0^2\varepsilon_r\varepsilon_s\gamma\rho(1-\gamma)(1-\rho)\eta_f L_s/256NL_r}{2eB\big(i_d + SP_0\varepsilon_r\rho(1-\gamma)/32N\big) + 8\pi kTBf_{\mathrm{co}}c_d}\right].} \tag{10.54}$$

From Equation (10.54), we see that the system is thermal-noise limited unless the laser power is so large that the shot-noise term prevails. The dynamic range increases as the square of the laser power until the shot-noise limit is reached and increases linearly thereafter. The number of resolvable frequencies plays an important role in the dynamic range calculation, as expected.

From Equation (10.54) we also see that $\rho = \gamma = 0.5$ optimizes the dynamic range when the system is thermal-noise limited. However, when the laser power is increased so that the system becomes shot-noise limited, we find that the dynamic range becomes

$$\mathrm{DR} = 10\log\left[\frac{S^2P_0^2\varepsilon_r\varepsilon_s\gamma(1-\rho)\eta_f L_s/256NL_r}{2eB(SP_0\varepsilon_r/32N)}\right], \tag{10.55}$$

provided that the local-oscillator current dominates the dark current. In this case we find that the factor $\rho(1-\gamma)$ cancels, leaving just the factor $\gamma(1-\rho)$ in the numerator. This result suggests that γ should be made large and ρ should be made small to maximize the dynamic range, a condition that favors directing more of the laser power to the signal branch of the interferometer. Carrying this process to an extreme, however, would return us to the condition where the local-oscillator current no longer dominates the dark current, as can be seen from Equation (10.54). We generally set the beamsplitting and beam-combining ratios to 0.5, which is also the easiest to achieve with commonly available devices, because the maximum improvement in dynamic range is only 3 dB.

As an example of calculating the dynamic range, suppose that we need to detect 100 frequencies separated by 25 kHz. We therefore need 300 probes and discrete photodetector elements in the output array so that $N = 3M = 300$ and $L_s/L_r = \frac{1}{3}$. Consider a system with the following parameters: $P_0 = 100$ mW, $\varepsilon_r = \varepsilon_s = 0.5$, $\gamma = \rho = 0.5$, $S = 0.5$ A/W, $i_d = 10$ nA, $c_d = 1$ pF, $\eta_f = 0.01$, $f_{\mathrm{co}} = 1$ MHz, and $B = 25$ kHz. Substituting these values into Equation (10.52), we confirm that i_1 can be ignored when calculating the dynamic range. The other values become

$\bar{i}_2 = 5.2\ (10^{-7})$ and $i_3(t) = 1.5(10^{-6})c_k \cos(2\pi f_d t)$ so that the signal-to-noise ratio becomes

$$\text{SNR} = \frac{0.5\left[1.5(10^{-6})c_k\right]^2}{4.2(10^{-21}) + 2.6(10^{-21})}, \tag{10.56}$$

and we see that the shot noise is slightly more than the thermal noise. We solve Equation (10.56) for $c_{k\,\min}^2$ when the signal-to-noise ratio is equal to 1 and find that $c_{k\,\min}^2 = 9.4(10^{-9})$ so that the dynamic range is

$$\text{DR} = 10 \log\left[\frac{c_{k\,\max}^2}{c_{k\,\min}^2}\right] = 10 \log\left[\frac{1}{9.4(10^{-9})}\right] = 80.2\ \text{dB}. \tag{10.57}$$

10.8. COMPARISON OF THE HETERODYNE AND POWER SPECTRUM ANALYZER PERFORMANCE

If we had used a power spectrum analyzer with the same frequency parameters as given in the last section except for setting $f_{\text{co}} = B$, the system would produce a dynamic range of 55.5 dB. To compare the performance of the heterodyne and power spectrum analyzers under a wide range of conditions, we calculate the gain in the dynamic range, given by Gain = $\text{DR}_{\text{hsa}} - \text{DR}_{\text{psa}}$. Recall that the dynamic range for a power spectrum analyzer, given by Equation (8.35), is

$$\text{DR}_{\text{psa}} = 10 \log\left[\frac{0.02 P_0 \varepsilon S \eta_f}{\sqrt{2eBi_d + 8\pi kTBf_{\text{co}} c_d}}\right]. \tag{10.58}$$

We use Equations (10.54) and (10.58) to find that

$$\text{Gain} = \text{DR}_{\text{hsa}} - \text{DR}_{\text{psa}}$$

$$= 10 \log\left[\frac{\dfrac{S^2 P_0^2 \varepsilon_r \varepsilon_s \gamma\rho(1-\gamma)(1-\rho)\eta_f L_s/256 N L_r}{2eB(i_d + S P_0 \varepsilon_r \rho(1-\gamma)/32N) + 8\pi kTBf_{\text{co}} c_d}}{0.2 P_0 \varepsilon S \eta_f/\sqrt{2eBi_d + 8\pi kTBf_{\text{co}} c_d}}\right]. \tag{10.59}$$

We simplify Equation (10.59) by canceling similar factors to find that

$$\boxed{\text{Gain} = 10\log\left[\frac{\{SP_0\varepsilon_r\varepsilon_s\gamma\rho(1-\gamma)(1-\rho)L_s/256NL_r\}\sqrt{2eBi_d + 8\pi kTBf_{\text{co}}c_d}}{0.02\varepsilon\{2eB[i_d + SP_0\varepsilon_r\rho(1-\gamma)/32N] + 8\pi kTBf_{\text{co}}c_d\}}\right].} \tag{10.60}$$

From this general result we can consider several different operating conditions.

10.8.1. Both Systems Thermal-Noise Limited

We first consider the case where both analyzers are thermal-noise limited so that Equation (10.60) becomes

$$\text{Gain} = 10\log\left[\frac{\{SP_0\varepsilon_r\varepsilon_s\gamma\rho(1-\gamma)(1-\rho)L_s/256NL_r\}}{0.02\varepsilon\sqrt{8\pi kTBf_{\text{co}}c_d}}\right]. \tag{10.61}$$

The gain in performance is strongly proportional to the laser power and the number of frequencies that must be resolved, but it is less strongly dependent on the cutoff frequency and postdetection bandwidth.

10.8.2. Both Systems Shot-Noise Limited

Consider the situation when both systems are shot-noise limited so that Equation (10.60) becomes

$$\text{Gain} = 10\log\left[\frac{\{SP_0\varepsilon_r\varepsilon_s\gamma\rho(1-\gamma)(1-\rho)L_s/256NL_r\}\sqrt{2eBi_d}}{0.02\varepsilon\{2eB[i_d + SP_0\varepsilon_r\rho(1-\gamma)/32N]\}}\right]. \tag{10.62}$$

This case can be further subdivided into two cases. In the first and fairly unlikely case, we might find that the current produced by the local oscillator is less than that produced by the dark current. In this case, Equation (10.62) becomes

$$\text{Gain} = 10\log\left[\frac{\{SP_0\varepsilon_r\varepsilon_s\gamma\rho(1-\gamma)(1-\rho)L_s/256NL_r\}}{0.02\varepsilon\sqrt{2eBi_d}}\right], \tag{10.63}$$

so that the gain in performance is most highly dependent on the laser power and the number of frequencies that must be resolved, and the gain is independent of the cutoff frequency f_{co}. The somewhat more likely case occurs when the local-oscillator dominates the dark current in the heterodyne system so that the gain in performance becomes

$$\begin{aligned} \text{Gain} &= 10\log\left[\frac{\{SP_{0}\cdot\,.\varepsilon_s\gamma\rho(1-\gamma)(1-\rho)L_s/256NL_r\}\sqrt{2eBi_d}}{0.02\varepsilon\{2eB[SP_0\varepsilon_r\rho(1-\gamma)/32N]\}}\right] \\ &= 10\log\left[\frac{\{\varepsilon_s\gamma(1-\rho)L_s/256L_r\}\sqrt{2eBi_d}}{0.02\varepsilon(2eB/32)}\right]. \end{aligned} \tag{10.64}$$

We now see that the gain in performance is completely independent of the laser power, of the cutoff frequency, and of the number of frequencies to be resolved. The gain in performance in this case is completely determined by the parameters of the system and the postdetection bandwidth.

10.8.3. Power Spectrum Analyzer Thermal-Noise Limited; Heterodyne Spectrum Analyzer Shot-Noise Limited

The most likely scenario is that the power spectrum analyzer will be thermal-noise limited if the readout rate is fairly high, and the heterodyne spectrum analyzer will be shot-noise limited. In this case the gain in performance is

$$\text{Gain} = 10\log\left[\frac{\{SP_0\varepsilon_r\varepsilon_s\gamma\rho(1-\gamma)(1-\rho)L_s/256NL_r\}\sqrt{8\pi kTBf_{\text{co}}c_d}}{0.02\varepsilon\{2eB[i_d + SP_0\varepsilon_r\rho(1-\gamma)/32N]\}}\right]. \tag{10.65}$$

Here we see that the general nature of the gain in performance is the same as for Equation (10.61), aside from some different constants.

10.8.4. Power Spectrum Analyzer Using a CCD Array

In all the comparisons made so far, we have assumed that the power spectrum analyzer also uses discrete photodetectors at its output. In many applications, however, the power spectrum analyzer uses a CCD photodetector array, whose characteristics limit the linear dynamic range to about 35 dB, independent of how much laser power is available. Some of the nonlinear CCD arrays now provide dynamic ranges of about 50 dB or so.

The gain comparisons, in these cases, should be based on the dynamic range of a power spectrum analyzer as limited by the CCD array.

In general, we find that the performance of the heterodyne spectrum analyzer is significantly better than that of a comparable power spectrum analyzer. The additional performance comes at the price of needing a discrete photodetector array with more complicated detection circuitry. In Chapter 11, we discuss ways to partially overcome this disadvantage by using a decimated photodetector array.

10.9. HYBRID HETERODYNE SPECTRUM ANALYZERS

Aside from the improved dynamic range that can be obtained from a heterodyne spectrum analyzer, we find that certain postprocessing operations produce further frequency resolution. Suppose, for example, that we want to achieve a 1-kHz frequency resolution over a 100-MHz frequency band. We therefore need to resolve 10^5 frequency components, a performance level beyond that obtainable from conventional one-dimensional acousto-optic cells. In Chapter 4, we showed how two-dimensional falling raster recording formats could easily generate the required frequency resolution, but that system does not operate in real time.

Real-time spectrum analysis with the required resolution can be achieved by using a two-dimensional acousto-optic cell configuration, as discussed in Chapter 15. Here we briefly describe a *hybrid approach* that can perform the spectrum analysis in near-real time. Suppose that we use a heterodyne spectrum analyzer to divide the spectrum of the incoming 100-MHz signal into 100 frequency channels, each 1 MHz wide. We do so by creating 100 reference probes/photodetectors, each with a rectangular shape, to generate the required number of channels. The output of each photodetector is then analog-to-digital converted at a sample rate of 2 MHz; this data is fed to a DFT module that computes the Fourier transform of the narrowband signals. A 1024-point transform with 16-bit magnitude response can be computed in 1 msec, consistent with the required 1-KHz final frequency resolution. Note that the DFT computes the spectrum on a batch processing basis, as opposed to the continuous, sliding window processing available optically, as discussed in Chapter 15.

PROBLEMS

10.1. We design a heterodyne spectrum analyzer which requires a two-tone spur-free dynamic range of 45 dB. Assume that we have 300 reference-beam probes. The other system parameters are

$$\begin{aligned} P_0 &= 30\,\text{mW}, \\ i_d &= 10\,\text{nA}, \\ c_d &= 4\,\text{pF}, \\ \varepsilon_s &= \varepsilon_r = 0.5, \\ S &= 0.4\,\text{A/W}, \\ T &= 300\,\text{K}, \\ B &= 1\,\text{MHz}, \\ f_{\text{co}} &= 10.7\,\text{MHz}. \end{aligned}$$

(a) Calculate the local oscillator current. (b) Calculate the value of η_f. (c) Determine whether the system is shot-noise or thermal-noise limited. (d) Calculate the dynamic range for the heterodyne spectrum analyzer.

10.2. We design a heterodyne spectrum analyzer which requires a two-tone spur-free dynamic range of 55 dB and a single-tone dynamic range of 70 dB. We require 150 reference-beam probes. The other system parameters are

$$\begin{aligned} i_d &= 10\,\text{nA}, \\ c_d &= 2\,\text{pF}, \\ \varepsilon_s &= \varepsilon_r = 0.5, \\ S &= 0.4\,\text{A/W}, \\ T &= 300\,\text{K}, \\ B &= 500\,\text{kHz}, \\ f_{\text{co}} &= 3\,\text{MHz}. \end{aligned}$$

(a) Calculate the value of η_f. (b) Calculate the required laser power. (c) Calculate the local-oscillator current. (d) Determine whether the system is shot-noise or thermal-noise limited.

10.3. A heterodyne spectrum analyzer, used in a radar threat warning receiver, must resolve 30 frequencies with a resolution of 20 MHz. In this case, two-tone intermodulation products are not important, nor is the crosstalk between channels. You elect to use LiNbO_3 as the interaction medium and set the center frequency at 1000 MHz. The Fourier-transform lens has a focal length of 100 mm. On the assumption that the aperture weighting functions are such that

$a(x)$ and $b(x)$ are rectangular functions, calculate (a) the length of the signal and reference-beam cells, (b) the time bandwidth product for each cell, and (c) the complete geometry of the photodetector array (i.e., how many detectors, their size, their spacing, their position at the Fourier plane, and so forth).

10.4. Given the same system parameters as in Problem 10.2, (a) calculate the laser power required to make the shot-noise level twice that of the thermal-noise level, (b) calculate the resulting dynamic range for the heterodyne spectrum analyzer, using the power level found in part (a), (c) calculate the loss in dynamic range had this system been set up as a power spectrum analyzer (i.e., compare $\mathrm{DR}_{\mathrm{hsa}}$ to $\mathrm{DR}_{\mathrm{psa}}$). Is the power spectrum analyzer shot-noise or thermal-noise limited? (d) Calculate the laser power required for the power spectrum analyzer to produce the dynamic range obtained from the heterodyne spectrum analyzer in part (b).

11

Decimated Arrays and Cross-Spectrum Analysis

11.1. INTRODUCTION

As we discussed in Chapter 10, heterodyne spectrum analysis is information preserving because each photodetector is read out on an instantaneous basis. Heterodyne detection, however, places severe demands on the circuitry associated with each photodetector because the rf electronics are not easily implemented with integrated circuits. In this chapter we describe spectrum analyzers that support the sampling rate required to avoid missing signals and yet operate with a significantly reduced number of photodetector elements. The basic idea is to *decimate* an N-element photodetector array by retaining only every Mth element. We then time share the remaining elements by scanning the spectrum across the decimated array. Each photodetector therefore produces, as a time sequence, the spectral content of the received signal over a small frequency range.

In this chapter we also introduce a signal-processing operation called cross-spectrum analysis to determine the angle of arrival of a signal. For example, if we use two antenna elements to receive a signal from a common source, we can use a dual-channel acousto-optic cell to determine the source direction relative to the receiver geometry through a phase-comparison technique. The phase information, obtained by forming the cross spectrum of the signals received, provides a measure of the angle of arrival of cw emitters at each frequency.

11.2. BACKGROUND FOR THE HETERODYNE SPECTRUM ANALYZER

Because the detailed operation of the heterodyne spectrum analyzer was described in Chapter 10, we review only the major points here. The heterodyne spectrum analyzer consists of a conventional spectrum analyzer, modified to include a reference function at the Fourier plane.

References

1. N. Wiener, "Optics and the Theory of Stochastic Processes," *J. Opt. Soc. Am.*, Vol. 43, p. 225 (1953).
2. P. Elias, "Optics and Communication Theory," *J. Opt. Soc. Am.*, Vol. 43, p. 229 (1953).
3. P. Fellget, "Concerning Photographic Grain, Signal-to-Noise Ratio, and Information," *J. Opt. Soc. Am.*, Vol. 43, p. 271 (1953).
4. E. H. Linfoot, "Information Theory and Optical Imagery," *J. Opt. Soc. Am.*, Vol. 43, p. 808 (1955).
5. G. Toraldo di Francia, "The Capacity of Optical Channels in the Presence of Noise," Opt. Acta, Vol. 2, p. 5 (1955).
6. E. L. O'Neill, "Spatial Filtering in Optics," *IRE Trans. Inf. Theory*, Vol. IT-2, p. 56 (1956).
7. A. Marachal and P. Croce, "Un Filtre de Frequencies Spatiales Pour l'Amelioration du Contraste des Images Optiques," *C.R. Acad. Sci.*, Vol. 127, p. 607 (1953).
8. L. J. Cutrona, E. N. Leith, C. J. Palermo, and L. J. Porcello, "Optical Data Processing and Filtering Systems," *IRE Trans. Inf. Theory*, Vol. IT-6, p. 386 (1960).
9. A. VanderLugt, "Signal Detection by Complex Spatial Filtering," *IRE Trans. Inf. Theory*, Vol. IT-10, p. 139 (1964).
10. M. Born and E. Wolf, *Principles of Optics*, Pergamon Press, New York, 1964.
11. F. A. Jenkins and H. E. White, *Fundamental of Optics*, McGraw Hill, New York, 1957.
12. R. S. Longhurst, *Geometrical and Physical Optics*, Longmans, Green, & Co., London, 1967.
13. H. H. Hopkins, *Wavefront Theory of Aberrations*, University Microfilms, Ann Arbor, MI, 1952.
14. B. D. Guenther, *Modern Optics*, Wiley, New York, 1990.
15. A. Papoulis, *Systems and Transforms with Applications in Optics*, McGraw Hill, New York, 1968, p. 322.
16. A. Sommerfeld, *Optics*, Academic, New York, 1964.

17. R. N. Bracewell, *The Fourier Transform and its Applications*, McGraw-Hill, New York, 1965.

18. J. D. Gaskill, *Linear Systems, Fourier Transforms, and Optics*, Wiley, New York, 1978.

19. D. Gabor, "Microscopy by Reconstructed Wave-Fronts," *Proc. R. Soc. London, Ser., A*, Vol. 197, p. 454 (1951); "Microscopy by Reconstructed Wave-Fronts—II," *Proc. Phys. London*, Vol. 64, p. 449 (1951).

20. E. N. Leith and J. Upatnieks, "Reconstructed Wavefronts and Communication Theory," *J. Opt. Soc. Am.*, Vol. 52, p. 1123 (1962).

21. J. W. Goodman, *Introduction to Fourier Optics*, McGraw-Hill, New York, 1968.

22. W. T. Cathy, *Optical Information Processing and Holography*, Wiley, New York, 1974.

23. R. J. Collier, C. B. Bunkhardt, and L. H. Lin, *Optical Holography*, Academic, New York, 1971.

24. M. Abramowitz and I. A. Stegun, *Handbook of Mathematical Functions*, National Bureau of Standards, Applied Mathematics Series No. 55, U.S. Government Printing Office, Washington, DC.

25. A. B. Porter, "On the Diffraction Theory of Optical Images," *Philos. Mag.*, Vol. 11, p. 154 (1906).

26. A. VanderLugt, "Operational Notation for the Analysis and Synthesis of Optical Data Processing Systems," *Proc. IEEE*, Vol. 54, p. 1055 (1966).

27. F. P. Carlson and R. E. Francois, Jr., "Generalized Linear Processors for Coherent Optical Computers," *Proc. IEEE*, Vol. 65, p. 10 (1977).

28. A. VanderLugt, "Design Relationships for Holographic Memories," *Appl. Opt*. Vol. 12, p. 1675 (1973).

29. A. VanderLugt, "Packing Density in Holographic Systems," *Appl. Opt.*, Vol. 14, p. 1081, (1975).

30. D. R. Scifres, C. Lindstrom, R. D. Burnham, W. Streifer, and T. Paoli, "Phase-Locked (GaAl)As Laser Diode Emitting 2.6W cw from a Single Mirror," *Electron. Lett.*, Vol. 19, p. 169 (1983).

31. R. S. Kardar, "A Study of the Information Capacities of a Variety of Emulsion Systems," *Photogr. Eng.*, Vol. 6, p. 190 (1955).

32. D. Casasent, "Spatial Light Modulators," *Proc. IEEE*, Vol. 65, p. 143 (1977).

33. A. R. Tanguay, Jr., "Materials Requirements for Optical Processing and Computing Devices," *Opt. Eng.*, Vol. 24, p. 2 (1985).

34. Special issue, "*Spatial Light Modulators for Optical Information Processing*," Applied Optics, Vol. 28, 1989.

35. N. George, J. Thomasson, and A. Spindel, "Photodetector for Real Time Pattern Recognition," U.S. Patent No. 3, 689,772 (1970).

36. J. T. Thomasson, T. J. Middleton, and N. Jensen, "Photogrammetric Uses of the Optical Power Spectrum," Proc. Soc. Photo-Opt. Instrum. Eng., Vol. 45, p. 257 (1974).

37. See, for example, A. Yariv, *Optical Electronics*, Holt, Rinehart and Winston, New York, 1985.

38. Carlton E. Thomas, "Optical Spectrum Analysis of Large Space Bandwidth Signals," *Appl. Opt.*, Vol. 5, p. 1782 (1966).

39. G. Lebreton, "Power Spectrum of Raster-Scanned Signals," *Opt. Acta*, Vol. 29, p. 413 (1982).

40. W. M. Brown, *Analysis of Linear Time-Invariant Systems*, McGraw-Hill, New York, 1963.

41. W. B. Davenport, Jr. and W. L. Root, *An Introduction to the Theory of Random Signals and Noise*, McGraw-Hill, New York, 1958.

42. A. Papoulis, *Probability, Random Variables and Stochastic Processes*, McGraw-Hill, New York, 1984.

43. H. L. VanTrees, *Detection, Estimation, and Modulation Theory*, Wiley, New York, 1968.

44. A. VanderLugt, "A Review of Optical Data-Processing Techniques," *Opt. Acta*, Vol. 15, p. 1 (1968).

45. A. VanderLugt, "Coherent Optical Processing," *Proc. IEEE*, Vol. 62, p. 1300 (1974).

46. Special Issue on Optical Computing, *Proc. IEEE*, Vol. 65, pp. 1-176 (1977).

47. Special Issue on Optical Computing, *Proc. IEEE*, Vol. 72, pp. 753–992 (1984).

48. Special Issue on Optical Pattern Recognition, *Opt. Eng.*, Vol. 23, pp. 687–838 (1984).

49. P. L. Jackson, "Analysis of Variable-Density Seismograms by Means of Optical Diffractions," *Geophys.*, Vol. 30, p. 5 (1965).

50. M. B. Dobrin, A. L. Ingalls, and J. A. Long, "Velocity and Frequency Filtering of Seismic Data Using Laser Light," *Geophys.*, Vol. 30, p. 1144 (1965).

51. D. G. Falconer, "Optical Processing of Bubble Chamber Photographs," *Appl. Opt.*, Vol. 5, p. 1365 (1966).

52. P. L. Jackson, "Diffractive Processing of Geophysical Data," *Appl. Opt.*, Vol. 4, p. 419 (1965).

53. H. J. Pincus and M. B. Dobrin, "Geological Application of Optical Data Processing," *J. Geophys. Res.*, Vol. 71, p. 4861 (1966).

54. A. Kozma and D. L. Kelly, "Spatial Filtering for Detection of Signals Submerged in Noise," *Appl. Opt.*, Vol. 4, p. 387 (1965).

55. B. R. Brown and A. W. Lohmann, "Complex Spatial Filtering with Binary Masks," *Appl. Opt.*, Vol. 5, p. 967 (1966).

56. A. W. Lohmann, D. P. Paris, and H. W. Werlich, "Binary Fraunhofer Holograms Generated by Computer," *Appl. Opt.*, Vol. 6, p. 1139 (1967).

57. F. Zernike, "Das Phasenkontrastverfahren bei der mikroskopischen Beobachtung," *Z. Tech. Phys.*, Vol. 16, p. 454 (1935).

58. J. Tsujiuchi, "Correction of Optimal Images by Compensation of Aberrations and by Spatial Frequency Filtering," in E. Wolf, ed., *Progress in Optics*, North-Holland, Amsterdam, 1963, Vol. II.

59. J. L. Horner, "Light Utilization in Optical Correlators," *Appl. Opt.*, Vol. 21, p. 4511 (1982).

60. P. D. Gianino and J. L. Horner, "Additional Properties of the Phase-Only Correlation Filter," *Opt. Eng.*, Vol. 23, p. 695 (1984).

61. A. Kozma, "Photographic Recording of Spatially Modulated Coherent Light," *J. Opt. Soc. Am.*, Vol. 56, p. 428 (1966).

62. C. S. Weaver and J. W. Goodman, "A Technique for Optically Convolving Two Functions," *Appl. Opt.*, Vol. 5, p. 1248 (1966).

63. W-H. Lee, "Sampled Fourier Transform Hologram Generated by Computer," *Appl. Opt.*, Vol. 9, p. 639 (1970).

64. A. L. Ingalls, "The Effects of Film Thickness Variations on Coherent Light," *Photogr. Sci. Eng.*, Vol. 4, p. 135 (1960).

65. E. N. Leith, "Photographic Film as an Element of a Coherent Optical System," *Photogr. Sci. Eng.* Vol. 6, p. 75 (1962).

66. R. E. Swing and M. C. H. Shin, "The Determination of Modulation Transfer Characteristics of Photographic Emulsions in a Coherent Optical System," *Photogr. Sci. Eng.* Vol. 7, p. 350 (1963).

67. J. H. Altman, "Microdensitometry of High Resolution Plates by Measurement of the Relief Image," *Photogr. Sci. Eng.* Vol. 10, p. 156 (1966).

68. A. VanderLugt, F. B. Rotz, and A. Klooster, Jr., "Character Reading by Optical Spatial Filtering," in Tippett et al., eds. *Optical and Electro-Optical Information Processing*, MIT Press, Cambridge, 1965.

69. G. L. Turin, "An Introduction to Matched Filters," *IRE Trans. Inf. Theory*, Vol. IT-10, p. 311 (1960).

70. A. VanderLugt and F. B. Rotz, "The Use of Film Nonlinearities in Optical Spatial Filtering," *Appl. Opt.*, Vol. 9, p. 215 (1970).

71. A. VanderLugt, *The Theory of Optical Techniques for Spatial Filtering and Signal Recognition*, Ph.D. thesis, University of Reading 1969.

72. F. B. Rotz and M. O. Greer, "Photogrammetry and Reconnaissance Applications of Coherent Optics," *Proc. Soc. Photo-Opt. Instrum. Eng.*, Vol. 45, p. 139 (1974).

73. A. VanderLugt, "The effects of Small Displacements of Spatial Filters," *Appl. Opt.* 6, 1221 (1967).

74. Y. W. Lee, *Statistical Theory of Communication*, Wiley, New York, 1960.

75. L. Brillouin, "Diffusion de la Luimiere et des Rayons X par un Corps Transparent Homogene," *Ann. Phys.* (*Paris*), Vol. 17, p. 88 (1922).

76. P. Debye and F. W. Sears, "Scattering of Light by Supersonic Waves," *Proc. Nat. Acad. Sci.*, Vol. 18, p. 409 (1932).

77. R. Lucas and P. Biquard, "Proprietes Milieux Solides et Liquides Soumis aux Vibrations Elastiques Ultra Sonores," *J. Phys. Radium*, Vol. 3, p. 464 (1932).

78. C. V. Raman and N. S. Nagendra Nath, "The Diffraction of Light by High Frequency Sound Waves: Parts I and II," *Proc. Indian Acad. Sci. Sect. A*, Vol. 2, p. 406 (1935); "Part III-Doppler Effect and Coherent Phenomena," *Proc. Indian Acad. Sci., Sect. A*, p. 75 (1936); "Part IV-Generalized Theory," *Proc. Indian Acad. Sci. Sect. A*, Vol. 3, p. 119 (1936); "Part V-General Considerations-Oblique Incidence and Amplitude Changes," *Proc. Indian Acad. Sci., Sect. A*, Vol. 3, p. 359 (1936).

79. A. Korpel, *Acousto-Optics*, Marcel Dekker, New York, 1988.

80. E. H. Young, Jr., and S-K. Yao, "Design Considerations for Acousto-Optic Devices," *Proc. IEEE*, Vol. 69, p. 54 (1981).

81. A. Korpel, "Acousto-Optics—A Review of Fundamentals," *Proc. IEEE*, Vol. 69, p. 48 (1981).

82. I. Fuss and D. Smart, "Cryogenic Large Bandwidth Acousto-Optic Deflector," *Appl. Opt.*, Vol. 26, p. 1222 (1983).

83. M. Amano, G. Elston, and J. Lucero, "Materials for Large Time Aperture Bragg cells," *Proc. SPIE*, Vol. 567, p. 142 (1985).

84. A. VanderLugt, "Bragg Cell Diffraction Patterns," *Appl. Opt.*, Vol. 21, p. 1092 (1982).

85. H. N. Roberts, J. W. Watkins, and R. H. Johnson, "High Speed Holographic Recorder," *Appl. Opt.*, Vol. 13, p. 841 (1974).

86. A. H. Rosenthal, "Application of Ultrasonic Light Modulation to Signal Recording, Display, Analyses and Communication," *IRE Trans. Ultrason. Eng.*, Vol. SU-8, p. 1 (1961).

87. R. M. Wilmotte, "Light Modulation System for Analysis of Information," U.S. Patent No. 3,509,453 (1970).

88. L. B. Lambert, "Wideband Instantaneous Spectrum Analyzers Employing Delay-Line Light Modulators," *IRE Int. Conv. Rec.*, Vol. 10, p. 69 (1962).

89. D. L. Hecht, "Multifrequency Acousto-Optic Spectrum Analysis," *IEEE Trans. Sonics Ultrason.*, Vol. SU-24, p. 7 (1977).

90. D. R. Pape, "Minimization of Nonlinear Acousto-Optic Bragg Cell Intermodulation Products," 1989 Ultrasonics Symposium Proceedings, p. 509.

91. G. A. Coquin, J. P. Griffin, and L. K. Anderson, "Wideband Acousto-Optic Deflectors Using Acoustic Beam Steering," *IEEE Trans. Sonics Ultrason.*, Vol. SU-17, p. 34 (1970).

92. R. B. Brown, A. E. Craig, and J. N. Lee, "Predictions of Stray Light Modeling on the Ultimate Performance of Acousto-Optic Processors," *Opt. Eng.*, Vol. 28, p. 1299 (1989).

93. E. N. Leith and J. Upatnieks, "Wavefront Construction with Diffused Illumination and Three-Dimensional Objects," *J. Opt. Soc. Am.*, Vol. 54, p. 1295 (1964).

94. M. King, W. R. Bennett, L. B. Lambert, and M. Arm, "Real-Time Electro-Optical Signal Processors with Coherent Detection," Appl. Opt., Vol. 6, p. 1367 (1967).

95. L. Slobodin, "Optical Correlation Technique," *Proc. IEEE*, Vol. 51, p. 1782 (1963).

96. R. Whitman, A. Korpel, and S. Lotsoff, "Application of Acoustic Bragg Diffraction to Optical Processing Techniques," *Symposium on Modern Optics*, Polytechnic Institute of Brooklyn, 1967, p. 243.

97. R. L. Whitman and A. Korpel, "Probing of Acoustic Surface Perturbations by Coherent Light," *Appl. Opt.*, Vol. 8, p. 1567 (1969).

98. A. Korpel and R. L. Whitman, "Visualization of a Coherent Light Field by Heterodyning with a Scanning Laser Beam," *Appl. Opt.*, Vol. 8, p. 1577 (1969).

99. A. VanderLugt, "Interferometric Spectrum Analyzer," *Appl. Opt.*, Vol. 20, p. 2770 (1981).

100. G. W. Anderson, B. D. Guenther, J. A. Hynecek, R. J. Keyes, and A. VanderLugt, "Role of Photodetectors in Optical Signal Processing," *Appl. Opt.*, Vol. 27, p. 2871 (1988).

101. G. M. Borsuk, "Photodetectors for Acousto-Optic Signal Processors," *Proc. IEEE*, Vol. 69, p. 100 (1981).

102. A. VanderLugt and A. M. Bardos, "Spatial and Temporal Spectra of Periodic Functions for Spectrum Analysis," *Appl. Opt.*, Vol. 23, p. 4269 (1984).

103. P. H. Wisemann and A. VanderLugt, "Temporal Frequencies of Short and Evolving Pulses in Interferometric Spectrum Analyzers," *Appl. Opt.*, Vol. 28, pp. 3800 (1989).

104. S. W. Golomb, *Shift Register Sequences*, Holden-Day, San Francisco, 1967, p. 86.

105. M. D. Koontz, "Miniature Interferometric Spectrum Analyzer," *Proc. SPIE*, Vol. 639, p. 126 (1986).

106. J. L. Erickson, "Linear Acousto-Optic Filtering with Heterodyne and Frequency-Plane Control," Ph.D. thesis, Stanford University (University Microfilms, 1981).

107. R. W. Brandstetter and P. G. Grieve, "Recursive Optical Notching Filter," *Proc. SPIE*, Vol. 1154, p. 206 (1989).

108. P. J. Roth, "Optical Excision in the Frequency Plane," *Proc. SPIE*, Vol. 352, p. 17 (1982).

109. T. P. Karnowski and A. VanderLugt, "Generalized Filtering in Acousto-Optic Systems Using Area Modulation," *Appl. Opt.*, Vol. 30, p. 2344 (1991).

110. C. S. Anderson and A. VanderLugt, "Hybrid Acousto-Optic and Digital Equalization for Microwave Digital Radio Channels," *Opt. Lett.*, Vol. 15, p. 1182 (1990).

111. M. Arm, L. Lambert, and I. Weissman, "Optical Correlation Technique for Radar Pulse Compression," *Proc. IEEE*, Vol. 52, p. 842 (1964).

112. E. B. Felstead, "A Simple Real-Time Incoherent Optical Correlator," *IEEE Trans. Aerosp. Electron. Syst.*, Vol. AES-3, p. 907 (1967).

113. E. B. Felstead, "A Simplified Coherent Optical Correlator," *Appl. Opt.*, Vol. 7, p. 105 (1968).

114. C. Atzeni and L. Pantani, "A Simplified Optical Correlator for Radar-Signal Processing," *Proc. IEEE*, Vol. 57, p. 344 (1969).

115. C. Atzeni and L. Pantani, "Optical Signal-Processing Through Dual-Channel Ultrasonic Light Modulators," *Proc. IEEE*, Vol. 58, p. 501 (1970).

116. R. M. Montgomery, "Acousto-Optic Signal Processing System," U.S. Patent No. 3,634,749 (1972).

117. R. A. Sprague and C. L. Koliopoulos, "Time Integrating Acousto-Optic Correlator," *Appl. Opt.*, Vol. 15, p. 89 (1976).

118. R. Manasse, R. Price, and R. M. Lerner, "Loss of Signal Detectability in Band-Pass Limiters," *IRE Trans. Inf. Theory*, Vol. IT-4, p. 34 (1958).

119. C. R. Cohn, "A Note on Signal-to-Noise Ratio in Band-Pass Limiters," *IRE Trans. Inf. Theory*, Vol. IT-7, p. 39 (1961).

120. F. B. Rotz, "Time-Integrating Optical Correlator," *Proc. SPIE*, Vol. 202, p. 163 (1979).

121. P. Kellman, "Time Integrating Optical Processing," Ph.D. thesis, Stanford University (1979).

122. D. Mergerian, E. C. Malarkey, P. P. Pautienus, J. C. Bradley, G. E. Marx, L. D. Hutcheson, and A. L. Kellner, "Operational Integrated Optical RF Spectrum Analyzer," *Appl. Opt.*, Vol. 19, p. 3033 (1980).

123. M. W. Casseday, N. J. Berg, and I. J. Abramovitz, "Space-Integrating Signal Processors Using Surface-Acoustic Wave Delay Lines," in N. J. Berg and J. N. Lee, eds., *Acousto-Optic Signal Processing*, Marcel Dekker, New York, 1983.

124. I. J. Abramovitz, N. J. Berg, and M. W. Casseday, "Coherent Time-Integration Processors," in N. J. Berg and J. N. Lee, eds., *Acousto-Optic Signal Processing*, Marcel Dekker, New York, 1983.

125. D. Mergerian and E. C. Malarkey, "Integrated Optics," in N. J. Berg and J. N. Lee, eds., *Acousto-Optic Signal Processing*, Marcel Dekker, New York, 1983.

126. J. M. Elson and J. M. Bennett, "Relation between the Angular Dependence of Scattering and the Statistical Properties of Optical Surfaces," *J. Opt. Soc. Am.*, Vol. 69, p. 31 (1979).

127. T. M. Turpin, "Time Integrating Optical Processing," *Proc. SPIE*, Vol. 154, p. 196 (1978).

128. T. M. Turpin, "Spectrum Analysis Using Optical Processing," *Proc. IEEE*, Vol. 69, p. 79 (1981).

129. W. T. Rhodes, "Acousto-Optic Signal Processing: Convolution and Correlation," *Proc. IEEE*, Vol. 69, p. 65 (1981).

130. J. D. Cohen, "Ambiguity Processor Architectures Using One-Dimensional Acousto-Optic Transducers," *Proc. SPIE*, Vol. 180, p. 134 (1979).

131. A. W. Lohmann and B. Wirnitzer, "Triple Correlations," *Proc. IEEE*, Vol. 72, p. 889 (1984).

132. R. A. K. Said and D. C. Cooper, "Crosspath Real-Time Optical Correlator and Ambiguity-Function Processor," *Proc. IEE*, Vol. 120, p. 423 (1973).

133. A. VanderLugt, "Crossed Bragg Cell Processors," *Appl. Opt.*, Vol. 23, p. 2275 (1984).

134. P. M. Woodward, *Probability and Information Theory, with Applications to Radar*, McGraw-Hill, New York, 1953.

135. D. Psaltis and K. Wagner, "Real-time Optical Synthetic Aperture Radar (SAR) Processor," *Opt. Eng.*, Vol. 21, p. 822 (1982).

136. Michael Haney and Demetri Psaltis, "Real-Time Programmable Acousto-Optic Synthetic Aperture Radar Processor," *Appl. Opt.*, Vol. 27, p. 1786 (1988).

137. A. VanderLugt, "Adaptive Optical Processor," *Appl. Opt.*, Vol. 21, p. 4005 (1982).

138. A. VanderLugt and A. M. Bardos, "Stability Considerations for Adaptive Optical Fitlering," *Appl. Opt.*, Vol. 25, p. 2314 (1986).

Bibliography

M. Amano and E. Roos, "32-Channel Acousto-Optic Bragg Cell for Optical Computing," *Proc. SPIE*, Vol. 753, p. 37 (1987).

Gordon Wood Anderson, Francis J. Kub, Rebecca L. Grant, Nicholas A. Papanicolaou, John A. Modolo, and Douglas E. Brown, "Programmable Frequency Excision and Adaptive Filtering with a GaAs/AlGaAs/GaAs Heterojunction Photoconductor Array," *Opt. Eng.*, Vol. 29, p. 1243 (1990).

B. Auld, *Acoustic Fields and Waves in Solids*, Wiley, New York, 1973.

T.R. Bader, "Acoustooptic Spectrum Analysis: A High Performance Hybrid Technique," *Appl. Opt.*, Vol. 10, p. 1668 (1979).

M. J. Bastiaans, "The Wigner Distribution Function Applied to Optical Signals and Systems," *Opt. Commun.*, Vol. 25, p. 26 (1978).

R. Barakat, "Application of the Sampling Theorem to Optical Diffraction Theory," *J. Opt. Soc. Am.*, Vol. 54, p. 920 (1964).

D. F. Barbe, "Imaging Devices Using the Charge-Coupled Concept," *Proc. IEEE*, Vol. 63, p. 38 (1975).

H. Bartelt, A. W. Lohmann and B. Wirnizter, "Phase and Amplitude Recovery from Bispectra," *Appl. Opt.*, Vol. 18, p. 3121 (1984).

W. R. Beaudet, M. L. Popek, and D. R. Pape, "Advances in Multi-Channel Bragg Cell Technology," *Proc. SPIE*, Vol. 639, p. 28 (1986).

N. J. Berg, J. N. Lee, M. W. Casseday, and E. Katzen, "Adaptive Fourier Transformation by Using Acousto-Optic Convolution," Proc. 1978 IEEE Ultrasonics Symp., IEEE No. 78CH1344-1, p. 91 (1978).

G. D. Boreman and E. R. Raudenbush, "Characterization of a Liquid Crystal Television Display as a Spatial Light Modulator for Optical Processing," *Proc. SPIE*, Vol. 639, p. 41 (1986).

Robert W. Brandstetter and Philip G. Grieve, "Excision of Interference from Radio Signals by Means of a Recursive Optical Notching Filter," *Opt. Eng.*, Vol. 29, p. 804 (1990).

H. J. Butterweck, "Principles of Optical Data-Processing," in E. Wolf, ed., *Progress in Optics*, North Holland, Amsterdam, 1981, Vol. XIX.

David Casasent, "Optical Information Processing Applications of Acousto-Optics," in N. J. Berg and J. N. Lee, eds., *Acousto-Optic Signal Processing*, Marcel Dekker, New York, 1983.

David Casasent and Giora Silbershatz, "Product Code Processing on a Triple-Product Processor," *Appl. Opt.*, Vol. 21, p. 2076 (1982).

David Casasent and James Lambert, "General I and Q Data Processing on a Multichannel AO System," *Appl. Opt.*, Vol. 25, p. 1886 (1986).

S. G. Chamberlain and J. P. Y. Lee, "A Novel Wide Dynamic Range Silicon Photodetector and Linear Imaging Array," *IEEE Trans. Electron. Devices*, Vol. ED-31, p. 175 (1984).

I. C. Chang and S. Lee, "Efficient Wideband Acousto-Optic Cells," Proc. 1983 IEEE Ultrasonics Symp., IEEE No. 83CH 1947-1, p. 427 (1983).

J. D. Cohen, "Incoherent Light Time Integrating Processors," in N. J. Berg and J. N. Lee, eds., *Acousto-Optic Signal Processing*, Marcel Dekker, New York, 1983.

M. G. Cohen, "Optical Study of Ultrasonic Diffraction and Focusing in Anisotropic Media," *J. Appl. Phys.*, Vol. 38, p. 3821 (1967).

L. J. Cutrona, E. N. Leith, L. J. Porcello, and W. E. Vivian, "On the Application of Coherent Optical Processing Techniques to Synthetic Aperture Radar," *Proc. IEEE*, Vol. 54, p. 1026 (1966).

R. W. Dixon, "Photoelastic Properties of Selected Materials and their Relevance for Applications to Acoustic Light Modulators and Scanners," *IEEE J. Quantum Electron.*, Vol. QE-3, p. 85 (1967).

Jerry Erickson, "Linear Acousto-Optic Filters for Programmable and Adaptive Filtering," *Proc. SPIE*, Vol. 341, p. 173 (1982).

Jerry Erickson, "Optical Excisor Performance Limits Versus Improved Signal Detection," *Proc. SPIE*, Vol. 639, p. 232 (1986).

Michael W. Farn and Joseph W. Goodman, "Optical Binary Phase-Only Matched Filters," *Appl. Opt.*, Vol. 27, p. 4431 (1988).

E. B. Felstead, "Optical Fourier Transformation of Area-Modulated Spatial Functions," *Appl. Opt.*, Vol. 10, p. 2468 (1971).

T. K. Gaylord and M. G. Mohoram, "Analysis and Applications of Optical Diffraction Gratings," *Proc. IEEE*, Vol. 73, p. 894 (1985).

J. W. Goodman, "Operation Achievable with Coherent Optical Information Processing Systems," *Proc. IEEE*, Vol. 65, p. 39 (1977).

A. P. Goutzoulis and M. S. Gottlieb, "Design and Performance of Optical Activity Based Hg_2Cl_2 Bragg Cells," *Proc. SPIE*, Vol. 936, p. 119 (1988).

B. D. Guenther, C. R. Christensen, and J. Upatnieks, "Coherent Optical Processing: Another Approach," *IEEE J. Quantum Electron.*, Vol. 15, p. 1348 (1979).

D. L. Hecht, "Spectrum Analysis Using Acousto-Optic Devices," *Proc. SPIE*, Vol. 90, p. 148 (1976).

D. L. Hecht and G. W. Petrie, "Acousto-Optic Diffraction from Acoustic Anisotropic Shear Modes in Gallium Phosphide," Proc. 1980 IEEE Ultrasonics Symp., IEEE No. 80CH1602-2, p. 474, 1980.

W. R. Klein and B. D. Cook, "Unified Approach to Ultrasonic Light Diffraction," *IEEE Trans. Sonics Ultrason.*, Vol. SU-14, p. 723 (1967).

P. Kellman, H. N. Shaver, and J. W. Murray, "Integrating Acousto-Optic Channelized Receivers," *Proc. IEEE*, Vol. 69, p. 93 (1981).

A. Korpel, S. N. Lotsoff, and R. L. Whitman, "The Interchange of Time and Frequency in Television Displays," *Proc. IEEE*, Vol. 57, p. 160 (1969).

M. A. Krainak and D. E. Brown, "Interferometric Triple Product Processor (Almost Common Path)," *Appl. Opt.*, Vol. 24, p. 1385 (1985).

John N. Lee, N. J. Berg, M. W. Casseday, and P. S. Brody, "High-Speed Adaptive Filtering and Reconstruction of Broad-Band Signals Using Acousto-Optic Techniques," *1980 Ultrasonics Symposium*, p. 488 (1980).

J. N. Lee and A. D. Fisher, "Device Developments for Optical Information Processing," *Adv. Electron. Electron Phys.*, Vol. 69, p. 115 (1987).

J. N. Lee, "Optical Architectures for Temporal Signal Processing," in J. Horner, ed., *Optical Signal Processing*, Academic, Orlando, 1988.

E. N. Leith and A. L. Ingalls, "Synthetic Antenna Data Processing by Wavefront Reconstruction," *Appl. Opt.*, Vol. 7, p. 539 (1968).

J. P. Lindley, "Applications of Acousto-Optic Techniques to RF Spectrum Analysis," in N. J. Berg and J. N. Lee, eds., *Acousto-Optic Signal Processing*, Marcel Dekker, New York, 1983.

H. K. Liu and T. H. Chao, "Liquid Crystal Television Spatial Light Modulators," *Appl. Opt.*, Vol. 28, p. 4772 (1989).

G. E. Lukes, "Cloud Screening from Aerial Photography Applying Coherent Optical Pattern Recognition Techniques," *Proc. Soc. Photo-Opt. Instrum. Eng.*, Vol. 45, p. 265 (1974).

R. J. Marks, J. F. Walkup, and M. O. Hagler, "A Sampling Theorem for Space-Variant Systems," *J. Opt. Soc. Am.*, Vol. 66, p. 918 (1976).

E. L. O'Neill and A. Walther, "The Question of Phase in Image Formation," *Opt. Acta*, Vol. 10, p. 33 (1963).

D. A. Pinnow, "Guide Lines for the Selection of Acousto-Optic Materials," *IEEE J. Quantum Electron.*, Vol. QE-6, p. 223 (1970).

Demetri Psaltis, "Acousto-Optic Processing of Two-Dimensional Signals," *J. Opt. Soc. Am.*, Vol. 71, p. 198 (1981).

J. E. Rau, "Real-Time Complex Spatial Modulation," *J. Opt. Soc. Am.*, Vol. 57, p. 798 (1967).

J. E. Rhodes, Jr., "Analysis and Synthesis of Optical Images," *Am. J. Phys.*, Vol. 21, p. 337, (1953).

J. F. Rhodes and D. E. Brown, "Adaptive Filtering with Correlation Cancellation Loops," *Proc. SPIE*, Vol. 341, p. 140 (1983).

J. F. Rhodes, "Adaptive Filter with a Time-Domain Implementation using Correlation Cancellation Loops," *Appl. Opt.*, Vol. 22, p. 282 (1983).

W. T. Rhodes and J. M. Florence, "Frequency Variant Optical Signal Analysis," *Appl. Opt.*, Vol. 15, p. 3073 (1976).

A. M. Tai, "Low-Cost Spatial Light Modulator with High Optical Quality," *Appl. Opt.*, Vol. 25, p. 1380 (1986).

David Slepian, "On Bandwidth," *Proc. IEEE*, Vol. 64, p. 292 (1976).

Robert Spann, "A Two-Dimensional Correlation Property of Pseudorandom Maximal Length Sequences," *IEEE Trans. Inform. Theory*, Vol. 11, p. 2137 (1965).

N. Uchida and N. Niizeki, "Acousto-Optic Deflection Materials and Techniques," *Proc. IEEE*, Vol. 61, p. 1073 (1973).

Jean-Charles Vienot, Jean-Pierre Goedgebuer, and Alain Lacourt, "Space and Time Variables in Optics and Holography: Recent Experimental Aspects," *Appl. Opt.*, Vol. 16, p. 454 (1977).

A. VanderLugt, G. S. Moore, and S. S. Mathe, "Multichannel Bragg Cell Compensation for Acoustic Spreading," *Appl. Opt.*, Vol. 22, p. 3906 (1983).

A. Walther, "The Question of Phase Retrieval in Optics," *Opt. Acta*, Vol. 10, p. 41 (1963).

Index